COMPUTER MODELLING OF DIESEL SPRAY DISPERSION AND EVAPORATION

by

KARAM RAMZY BESHAY
B.Sc., M.Sc.

THESIS SUBMITTED FOR THE DEGREE
OF DOCTOR OF PHILOSOPHY
IN THE FACULTY OF ENGINEERING
UNIVERSITY OF LONDON
AND
FOR THE DIPLOMA OF
IMPERIAL COLLEGE

Fluids Section
Mechanical Engineering Department
Imperial College of Science and Technology
London. SW7 2BX

APRIL 1985

ABSTRACT

The prediction of the unsteady axisymmetric motion of diesel-like liquid sprays injected into a gaseous environment is the main objective of this study. To achieve this goal, two sets of differential conservation equations are solved, one for each phase. The motion of the gas phase, which is considered as a continuum, is described in terms of the ensemble-averaged Eulerian differential equations governing the conservation of mass, momentum and energy. Closure of the turbulent fluxes appearing in these equations is effected with the aid of the k-ε turbulence model. A finite-volume numerical scheme is used to solve the equations. A hybrid of upwind and central differencing schemes is employed in space and the temporal differencing is semi-implicit.

The liquid spray is mathematically represented using the discrete droplet model. In this, each computational droplet represents a 'parcel' of droplets possessing the same initial size, velocity, temperature, etc. The trajectories, masses, velocities and temperatures of the droplets are obtained by solving the Lagrangian conservation equations of mass, momentum and energy for each computational droplet. The droplets interact with the gas phase in a two-way manner, exchanging mass, momentum and energy with it and also displacing it.

The mathematical formulations for the gas and liquid phases are completed by specifying the conditions at the boundaries of the solution domain and the initial conditions of the injected droplets as well as the gas phase. The two sets of equations are solved simultaneously.

The gas-phase solution procedure is first assessed in isolation by predicting steady and starting isothermal and non-isothermal gas jets and comparing the results with the available experimental measurements.

The spray model is assessed against four sets of data: all involve experiments in which diesel fuel is injected into a high pressure/high temperature chamber containing inert gases. It is found that the predicted spray shape agrees well with the measured one but the penetration agreement differs from one case to another. Finally, the results of the sensitivity analysis and parametric study are presented.

ACKNOWLEDGEMENTS

First and foremost, I would like to express my deep gratitude to my supervisor, Dr. A.D. Gosman, who devoted many hours in making valuable suggestions, encouragement, guidance and criticisms throughout this research project.

I would like also to thank Dr. A.P. Watkins whose keen interest and helpful comments have greatly contributed to the completion of this work.

I am indebted to past and present colleagues at Imperial College including Dr. S.S. Koussa, Dr. A. Abbas, Dr. H. Moneib, Dr. M. Hassan, Mr. W. Attia, Mr. M. Ismail, Dr. H. Younan, Mr. M. Abdelrahman and Mr. B. Tabrizi for sharing everyday college life.

I am grateful to Dr. A. Yule for providing experimental data and the financial support of the Joint Research Committee is gratefully acknowledged.

Many thanks to the typist for her work on this difficult manuscript.

Finally, I would like to take this opportunity to extend my deepest gratitude to my family and Miranda for their support and encouragement.

CONTENTS

		Page
ABSTRACT		i
ACKNOWLEDGEMENTS		iii
CONTENTS		iv
CHAPTER 1	INTRODUCTION	1
1.1	Motivation for Diesel Spray Modelling Research	1
1.2	Objective, Scope and Contribution of the Present Study	3
1.3	Outline of the Thesis	5
CHAPTER 2	PREVIOUS AND RELATED WORK	8
2.1	Introduction	8
2.2	Spray Measurements	9
	2.2.1 Spray Formation	9
	2.2.2 Overall Spray Structure	12
	2.2.3 Droplet Size Distribution in Diesel Sprays	15
	a - Mean droplet diameter	15
	b - Measurements of droplet sizes	16
	c - Effect of the operating conditions on droplet size	19
	2.2.4 Spray Cone Angle	21
	2.2.5 Spray Penetration	24
	Parameters Influencing Penetration	27
	a - Effect of injection pressure	27
	b - Effect of ambient pressure	28
	c - Effect of ambient temperature	29
	d - Effect of injector diameter	30
	e - Effect of fuel properties	30

		Page
2.3	Spray Models	31
	Spray Submodels	40
	i - Droplet drag coefficient	40
	ii - Heat and mass transfer coefficients	43
2.4	Closure	46
CHAPTER 3	THE MATHEMATICAL MODEL	57
3.1	Introduction	57
3.2	Equations Governing Instantaneous Motion of Gas Phase	58
	3.2.1 Mass Conservation Equation	59
	3.2.2 Momentum Conservation Equation	60
	3.2.3 Energy Conservation Equation	61
	3.2.4 Fuel Vapour Mass Fraction Equation	63
3.3	Averaging Process	63
	3.3.1 Introduction	63
	3.3.2 Ensemble Averaging Procedure	64
	3.3.3 Favre Averaging Procedure	70
3.4	The Turbulence Model	75
	3.4.1 Introduction	75
	3.4.2 Choice of the Turbulence Model	76
	i - Zero-equation model	77
	ii - One-equation models	78
	iii - Two-equation models	78
	3.4.3 Transport Equation for Turbulent Kinetic Energy	79
	3.4.4 Dissipation Equation	81

		Page
3.5	Modelled Form of the General Transport Equation	82
3.6	Moving Co-ordinate Frame Transformation	83
3.7	Droplet-Phase Equations	88
	a - Introduction	88
	b - Model Assumptions	89
	c - Droplet Motion and Trajectory	91
	d - Droplet Evaporation	94
	e - Thermodynamic Properties	98
3.8	Turbulent Droplet Dispersion	103
3.9	Closure	106
CHAPTER 4	THE NUMERICAL SOLUTION PROCEDURES	114
4.1	Introductory Remarks	114
4.2	Computational Grid System and Notation	115
4.3	Finite-Difference Approximation	116
	4.3.1 Transport Equations	116
	4.3.2 Differencing of the Gas-Phase Source Terms	126
4.4	Differencing Practices	128
	4.4.1 Spatial Differencing Schemes	128
	4.4.2 Temporal Differencing Schemes	130
4.5	Solution of Continuity and Momentum Equations	137
4.6	Droplet Equations and Interaction Source Terms	144
4.7	Solution Algorithms	147
	4.7.1 Fully Implicit Solution Algorithm	147
	4.7.2 Semi-Implicit Solution Algorithm	153
4.8	Boundary and Initial Conditions	168
	4.8.1 Axis of Symmetry	168
	4.8.2 Outflow Boundary	169
	4.8.3 Free Stream Boundary	170

		Page
	4.8.4 Inflow Boundary	171
	4.8.5 Initial Conditions	174
4.9	Closure	178
CHAPTER 5	PRELIMINARY TESTING OF GAS JET AND SPRAY CALCULATION PROCEDURES	185
5.1	Introduction	185
5.2	Assessment of Accuracy of Fully Implicit Scheme	186
5.3	Assessment of the Semi-Implicit Scheme	190
5.4	Droplet Trajectory Calculations	193
5.5	Spray Calculations	196
	a - Effect of the grid size	196
	b - Effect of the time step	197
	c - Effect of the droplet number	199
	d - Stochastic variations	201
5.6	Concluding Remarks	212
CHAPTER 6	ASSESSMENT OF THE PROCEDURE GAS PHASE	214
6.1	Introduction	214
6.2	Steady Laminar Round Free Jet	215
6.3	Transient Laminar Round Free Jet	217
6.4	Steady-State Turbulent Free Jet	219
6.5	Impulsively Started Turbulent Round Jets	225
	a - Isothermal jets	225
	b - Non-isothermal jet	231
6.6	Parametric Study and Scaling Laws	236
	a - Parametric Study	236
	b - Scaling Laws	246
6.7	Concluding Remarks	249

		Page
CHAPTER 7	ASSESSMENT OF THE SPRAY CALCULATION PROCEDURE	251
7.1	Introduction	251
7.2	Isothermal Sprays	252
	7.2.1 Comparison With Measurements	252
	i - The experiments of Yule et al (1985a,b)	252
	ii - The experiments of Hiroyasu and Kadota (1974)	270
	7.2.2 Sensitivity Analysis	275
	7.2.2.1 Computational Sensitivity	277
	7.2.2.2 Modelling Sensitivity	284
	7.2.3 Parametric Study	296
7.3	Evaporating Spray	304
	7.3.1 Comparison With Measurements	304
	i - The experiments of Yule et al (1985a,b)	304
	ii - Simulation of Kuniyoshi et al (1980) experiments	305
	7.3.2 Parametric Study	323
7.4	Concluding Remarks	340
CHAPTER 8	SUMMARY AND CONCLUSIONS	342
8.1	Summary of Achievement and Findings	342
8.2	Recommendations for Future Work	346
REFERENCES		350
NOMENCLATURE		373

CHAPTER 1

INTRODUCTION

1.1 Motivation for Diesel Spray Modelling Research

Increased concern with long term energy reserves and environmental quality has given impetus to effort to enhance the efficiency and reduce the undesirable emission of the automotive internal combustion engines. The diesel engine, being the most economical engine type, has gained popularity in many applications, including heavy and medium duty vehicles. More recently it has been considered as a replacement for its main rival, namely the conventional petrol engine, in some passenger cars. The high thermal efficiency of the diesel engine is mainly a consequence of the relatively high compression ratios required to produce the autoignition, the lower pumping losses as a result of the absence of a throttle valve and the overall lean mixture (Henein (1976)).

The extent of the success of the combustion process inside the combustion chamber of a diesel engine depends on the air motion within the cylinder which is influenced by the intake port and piston bowl designs. Also, the combustion process depends on the quality of the hetrogenious mixture formed as a result of the mixing process. The production of nitrogen oxides during combustion is determined to a great extent by the high gas temperature which occurs whenever the heat-release rate is large and this in turn depends upon the fuel quantity and quality, the gas temperature and the air mixing process. The fuel quality and gas temperature determine the duration of the ignition delay period, defined as the period between the start of injection and the start of combustion, during which the fuel heats,

evaporates and the resulting vapour diffuses into the air to form a combustible mixtures (at several locations in the combustion chamber) and undergoes chemical reactions until at the end of this period, the mixture formed commences burning: meanwhile, in some other locations the fuel may still be in the liquid phase(Henein(1976)). After this essentially premixed-burning stage, the combustion rate is governed largely by the rate of mixing of the remaining fuel and the surrounding air. Mixture formation is in turn a very complex process involving two phase media and the quality of the mixture formed in the combustion chamber depends to some extent, on the characteristics of the fuel spray injected, namely the structure, penetration, droplet sizes, dispersion and evaporation.

In diesel engines, pressurized liquid fuel is injected through a small nozzle into the compressed combustion gasses and passes through a sequence of stages. The fuel leaves the nozzle as an intact liquid core, and then breaks down into ligaments, sheets or droplets of different sizes according to the operating conditions and the nozzle design. The effect of atomization is to drastically increase the surface area of the injected liquid and consequently leads to greatly increased rates of mass, momentum and energy transfer between it and the surrounding gas. Hence, the mixture formation process is improved.

The complicated mechanisms of the above processes and the fact that accurate measurements of them cannot be made even with the present day advanced measuring techniques has impeded understanding and analysis of spray behaviour. Also, the experimental 'cut and try' development testing of diesel engines becomes more costly when faced with a muliplicity of goals such as measuring the drop size and

velocity distributions of sprays in diesel engines using a non-intrusive light scattering techniques. These experimental measurement difficulties have created new interest in the development of mathematical models, which can, in principle, provide much more detailed information than it is possible to obtain experimentally, and thereby aid in the identification of the flow patterns. However, it is necessary to assess such models by comparison with a carefully chosen matrix of experimental data before they can be used with a high degree of confidence.

This thesis is concerned with the assembly of a numerical calculation procedure for predicting the behaviour of axisymmetric isothermal and evaporating diesel sprays injected into a gaseous medium, either quiescent or in (axisymmetric) motion. The method developed is not necessarily restricted to diesel sprays, but these are the focus of the present study.

1.2 Objective, Scope and Contribution of the Present Study

The present study describes a computer-based procedure for solving the Eulerian partial differntial equations governing the conservation of mass, momentum and energy for the gas phase using the finite-difference technique. In conjuction with these the Lagrangian equations of motion, evaporation and energy for representative droplets which pass through and interact with the gas phase are solved using Euler's method. The droplets are deemed to interact with the gas in a two-way manner by exchanging mass, momentum and energy with it and by displacing the gas. The momentum

equations of the gas and droplet phases are coupled together, as in the original method of Dukowicz(1980), to enable a simultaneous solution for the gas and droplet velocities. The specific contributions of this study are:

1. Assembly of a procedure to prevent the spray calculation method from producing non-physical (overshooting or undershooting) results.
2. Solution of the droplet energy and vaporization equations simultaneously with a truncated form of the gas energy equation to yield an accurate calculation of the mass and energy interaction source terms.
3. Calculation of the gas turbulent viscosity from a two-equation turbulence model which incorporates differential equations for the turbulent kinetic energy k and its dissipation rate ε.
4. Modelling the turbulent droplets dispersion in a stochastic way and using the gas turbulent kinetic energy and dissipation rate to calculate the turbulent interaction time.
5. Application of the gas-phase solution procedure to laminar and turbulent jet flow test cases. These comprises steady and unsteady laminar and turbulent isothermal round free jets and a non-isothermal starting jet. In all cases comparisons are made with experimental data.
6. Validation of the spray calculation procedure by comparisons with data from four different experiments: two for isothermal sprays and two for evaporating sprays and identification of the capabilities and limitations of the model.
7. Performing parametric study to test the sensitvity of the spray solution procedure to the various features it contains.

1.3 Outline of the Thesis

Chapter 2 reviews the previous experimental and theoretical work on diesel spray behaviour. Included are measurements of spray formation, structure, cone angle and penetration which are used later in the thesis for the purpose of assessing the theoretical model developed. The different theoretical models that have been devised to represent the spray behaviour including both empirical correlations and detailed numerical models are discussed with emphasis on the advantage and disadvantage of each. Finally, the drag, heat and mass transfer correlations which are used in these models are reviewed.

Chapter 3 deals with the assembly of the differential equations that govern the flow, heat and mass transfer of both the gas and liquid phases. It commences with the assembly of the turbulent gas-phase governing equations in an unsteady, two-dimensional axisymmetric co-ordinates and the two-equation model which is used to represent the effects of turbulence. The droplet-phase governing equations are presented in Lagrangian form and a description is given of the method employed to model the effects of the gas turbulence on the droplet trajectories.

Chapter 4 describes the numerical procedures employed to solve the equation presented. Finite difference approximations to the gas-phase differential equations are derived by integrating the latter in space and in time in a finite volume fashion. The difference equations are firstly presented in a general form such that the fully implicit and semi-implicit schemes are easily extracted and discussed from the viewpoint of stability and accuracy. The solution procedure for the droplet field equations is then presented and

combined with the gas-phase equations to enable simultaneous solution for the gas and droplet velocities and temperatures.

Chapter 5 is concerned with the tests which are performed to determine the accuracy and reliability of the numerical methods of chapter 4. The effect of the grid spacing and time step on the solution are quantified for the fully implicit scheme for unsteady turbulent round free jet. The semi-implicit scheme is assessed by comparing its predictions with those of the well estblished fully implicit one for both starting laminar and turbulent round free gaseous jets. Then tests are made of the spray procedure in which the effects of grid spacing, time step, number of droplet parcels introduced per unit time and stochastic variation are assessed.

The gas-phase solution procedure is then assessed in chapter 6 by predicting single-phase gas jets and comparing the results with the available measurements. These include steady laminar round free jet, steady turbulent round free jet, starting laminar and turbulent isothermal jets and starting non-isothermal turbulent round jet. Finally, a parametric study including the effect of the jet Reynolds number, input level of turbulent kinetic energy and dissipation rate and the scaling laws of the gas jets are presented.

Chapter 7 deals with the assessment of the spray calculation procedure, using four sets of experimental data obtained from various sources. These comprise two experiments on isothermal sprays injected into different charge pressures and two evaporating spray cases where the injection is at different charge pressures and temperatures. The sensitivity of the prediction to the various modelling parameters such as droplet dispersion and initial spray cone angle and the

computational parameters such as the initial level of turbulence quantities, initial velocity profile of the droplets and residual effects in pulsed spray experiments is presented. Also discussed are the effects on penetration of the different input parameters including intial droplet sizes, size distribution function, injection rate history, injection velocity and droplet introduction temperature.

Finally, in chapter 8, the achievements of this study are summerized and suggestion are made for improvements and extensions.

CHAPTER 2

PREVIOUS AND RELATED WORK

2.1 Introduction

The performance of most high intensity combustion systems which use liquid fuels depends on the process of atomization as an essential intermediate stage between injection and combustion. The term 'atomization' here refers to the process of the breaking up of the liquid fuel jet into a large number of tiny droplets, producing a greatly increased surface area of the liquid and hence more rapid evaporation.

Sprays inside diesel combustion chambers are generated with the aid of an injector. The function of the injector is to introduce the liquid fuel at high velocity in order to create sufficient turbulence inside the spray to satisfy better atomization and dispersion and also to obtain the optimum spray penetration.

Due to its importance, diesel spray behaviour has been extensively studied, both experimentally and theoretically, by many investigators. This chapter gives a comprehensive review of this work, starting in section (2.2) with the experimental investigations. Here such aspects as the formation, structure, dispersion and penetration of diesel sprays will be examined. The effect of the operating conditions on the spray penetration will also be discussed.

Section (2.3) deals with the different theoretical models that have been devised to represent the spray behaviour. These include both empirical correlations and detailed numerical models.

Finally, the empirical expressions of drag, heat and mass transfer are reviewed.

2.2 Spray Measurements

2.2.1 Spray Formation

Due to the importance of sprays in technological applications, a vast amount of literature has accumulated on this subject, including reviews and books (e.g. Tate (1969), Lapple et al (1967), Giffen and Muraszew (1953), Borodin et al (1967) and Levich (1962)). In spite of this profusion of literature, many important aspects of spray formation are still poorly understood.

The process of spray formation and the related mechanism of liquid jet disintegration have been extensively studied during the last six decades. In the jet breakup process the liquid, which accelerated through a small orifice into the compressed gas, is dynamically broken up in a finite distance called the 'breakup length' into a large number of droplets. There exists controversy about the magnitude of the jet breakup length. Haenlein (1932)* studied the process of spray formation of water jets injected from a circular orifice of diameter 0.00051 m into atmospheric air. He reported the results in the form of a 'breakup curve' which gives the breakup length x_B as a function of jet velocity U_o as shown

*The operating conditions of the different experimental work reviewed in this chapter are listed in table (2.1).

in Fig. (2.1). For very low velocities, drops are formed at the orifice (drip). The following four regimes of breakup are encountered as the injection velocity is progressively increased (Reitz (1978)):

Regime 1 - Rayleigh jet breakup which occurs many jet diameter downstream of the nozzle. It is caused by the growth of axisymmetric oscillations of the jet surface, induced by surface tension.

Regime 2 - First wind induced breakup regime which occurs many jet diameters downstream of the injector. In this case, the surface tension effect is augmented by the relative motion of the ambient gas and the jet.

Regime 3 - Second wind induced breakup regime which occurs some jet diameters downstream of the nozzle. Droplet formation in this regime results from the unstable growth of waves, assisted by air friction.

Regime 4 - Atomization regime which results in a complete and immediate disruption of the liquid jet.

Most authors (e.g. Haenlein(1932), Reitz (1978) and Hiroyasu et al (1982)) agree on the shape of this curve in the low velocity region (up to the end of regime 3). Beyond this point however, there remains some confusion about the shape of the curve and the mechanism of droplet formation. DeJuhasz (1931) (cited in Giffen et al (1953)) proposed that jet breakup process occurs within the nozzle itself, on the basis that his photographic study showed this. This result would imply that the curve of Fig. (2.1) goes suddenly to zero at the end of zone 3. He

suggested that liquid turbulence may play an important part in the jet breakup process.

Castleman (1931) as cited in Reitz (1978) (operating conditions are not specified) claimed that the breakup occurs over some jet diameters from the orifice and it is due to aerodynamic interaction between the liquid and gas phases. He argued that this interaction leads to the formation of ligaments or liquid columns which have one end attached to the jet surface, and, once formed rupture according to Rayleigh's (1878) classical breakup theory.

Bergwerk (1959) paid particular attention to the nature of the flow field within the injection nozzle and its influence on the jet breakup process. He observed from photographs that cavitation occurred inside the nozzle which he tested and this led him to conclude that this could be responsible for the breakup process.

Reitz (1978) made an extensive study on the process of breakup of water and glycerol mixtures injected through single hole nozzles of diameter of 0.34 mm and different length to diameter ratios. The ambient charge pressures (air, nitrogen) were 0.1 - 4.0 MPa. He concluded that aerodynamic effects, supplemented by liquid cavitation effects, combine to produce atomization. He also showed that the breakup length tends to zero for an injection pressure of 10 MPa and an ambient gas density of 12 kg/m^3. On the other hand Hiroyasu et al (1982) and Negus (1983) showed that the atomization process start at about 20 mm from the nozzle tip for an ambient charge density of 3 kg/m^3 and for high injection velocity ($\simeq$ 120 m/s).

Hiroyasu et al (1982) claimed that in direct injection passenger car diesel engines, the breakup length and the distance from the nozzle to the combustion chamber wall are almost the same. For this reason they conducted an experiment to study the effect of various operating conditions on x_B. In their experiment, they injected water at various rates from a 0.3 mm diameter nozzle into a gas of pressures up to 4 MPa. The breakup length was found to increase with increasing jet velocity until U_o = 50 m/s after-which it gradually decreases and then reaches a constant value as shown in Fig. (2.2). They also found that x_B decreases with an increase in the ambient pressure and then becomes constant at about 20 mm for injection velocities higher than 100 m/s. Further, they concluded that the length to diameter ratio of the nozzle has little effect on x_B at high ambient pressure (3 MPa).

2.2.2 Overall Spray Structure

The structure produced by the atomization process consists of a multitude of droplets of different diameters interspersed with the gas and contained within a narrow conical jet (Fig. (2.3)) of included angle in the range 3 - 20^o (dependent on the operating conditions). There is remarkably little information, much of which is controversial, on the structure of the pulsed sprays produced by diesel engine injection systems. This is due to difficulties of making measurements near (up to 100 mm) the injector, which is the region of practical interest. Fujimoto et al (1977), (1979)

and (1981), Kuniyoshi et al (1980), Sato et al (1982) and Jong-Yul Ha et al (1983) used high speed photography to observe the spray structure produced by injection from a single hole nozzle of diameters 0.30 mm into high pressure (up to 7.95 MPa) and room temperature nitrogen gas. They all found that the spray possesses two distinct zones of atomized droplets. In the interior of the spray (on the axis of symmetry), which they call the 'main jet region', the number density and velocity of the droplets are rather high, while in the spray envelope, which is termed the 'mixing flow region', the number density and velocity of the droplets are lower.

Boulderstone et al (1981) used the light scattering technique to measure the droplet size distribution in the first 100 mm of pulsed diesel sprays injected into atmospheric pressure and temperature surrounding. They used a 0.46 single hole nozzle and they found that the spray appears to develop a double structure with increasing distance downstream. The front of the spray pulse is very poorly atomized, with a significant proportion of liquid ligaments, while the main body of the spray is generally well atomized, typically with a mean diameter near 20 microns.

Yule et al (1985a) made a spark photomicrographic study of diesel spray structure using a lucas 0.46 mm diameter single hole nozzle operating at 12 MPa needle lift pressure and injecting 56 mm^3 of fuel per pulse. The measurements were obtained in a quiescent bomb at pressures up to 6 MPa and at room temperature. They found that the first 50 mm of the spray consists of an extremely dense core

containing a very high proportion of the liquid volume surrounded by a dilute well atomized sheath of droplets. As their optical technique could not penetrate the dense core zone, they caused the spray to pass through a thin slit thereby removing all but a thin slice: however even this was still too dense to transmit light. Ishikawa et al (1982) used a similar technique to slice the spray and they reported that there are many entangled ligaments in the dense core zone.

Turning now to sprays injected into high pressure and temperature environments, Kuniyoshi et al (1980) reported, for diesel sprays injected into nitrogen charge of P = 6.28 MPa and T up to 960 K, that vaporization takes place in the so called mixing flow region allowing the main flow region to be more clearly seen but making it difficult to identify the spray envelope. Yule et al (1985a) performed experiments at high temperature (373 K) and high pressures (up to 6 MPa) and found that vaporization occurs in the dilute spray zone with little change in the appearance of the dense core. Matsuoka (1983) reported that at P = 3.34 MPa and T = 670 K, almost instantaneous vaporization of the droplets occurs at the spray prepheries as soon as it is injected, but a core with high droplet concentration remains along the axis. By contrast, Negus (1983) showed that droplets, injected into a nitrogen charge of 2.7 MPa pressure and a temperature near the boiling temperature of the pure liquid fuel, exhibit the first signs of vaporization at the spray edge. As the charge temperature is increased towards the critical temperature of the liquid fuel, the liquid core shrinks and rapid vaporization occurs.

2.2.3 Droplet Size Distribution in Diesel Sprays

a. Mean droplet diameter

The degree of atomization is usually measured by some mean droplet diameter. There are at least six types of mean diameter D_{qp} which are commonly used according to the field of application. They are all contained in the general definition (see Elkotb (1982b)):

$$D_{qp} = \left[\frac{\int_{D_{min}}^{D_{max}} D_d^q \, dn}{\int_{D_{min}}^{D_{max}} D_d^p \, dn} \right]^{\frac{1}{q-p}} \qquad (2.1)$$

where: D_{min} and D_{max} are the minimum and maximum droplet diameters in the spray; q and p are constants associated with the particular mean used; dn represents the ratio of the number of droplets having diameter between $D - \frac{dD}{2}$ and $D + \frac{dD}{2}$ to the total number of droplets; and dD is the increment of droplet diameter.

The Sauter Mean Diameter (SMD), D_{32}, is of importance in combustion as it expresses the diameter of a droplet that has the same volume to surface area ratio as that of the total spray. According to equation(2.1) D_{32} is given by :

$$D_{32} = \frac{\int_{D_{min}}^{D_{max}} D_d^3 \, dn}{\int_{D_{min}}^{D_{max}} D_d^2 \, dn} \qquad (2.2)$$

b. Measurement of droplet sizes

The experimental determination of the droplet sizes in diesel engines is extremely difficult. Most of the experiments have therefore been done on pulsed or continuous fuel sprays in constant volume vessels (see e.g. Boulderstone et al (1981) and Tishkoff (1982)). Studies of this kind under conditions which simulate diesel injection have been made by many investigators. Hiroyasu et al (1974) and (1980) measured droplet sizes in pulsed diesel sprays using the liquid immersion sampling technique. This involved the use of a small transparent cell about 2 mm in thickness, filled with immersion liquid and was located at a distance of 650 mm from the injector. A sample of the spray was collected in the immersion cell and photographed images of the collected droplets were measured and counted. They found that their results for various charge pressures (in the range 0.1 - 5 MPa) were well correlated with the 'Chi-square' distribution:

$$\frac{dV}{V} = 13.5\left(\frac{D_d}{D_{32}^4}\right)^3 \exp\{-3\left(\frac{D_d}{D_{32}}\right)\}\, d\left(\frac{D_d}{D_{32}}\right) \qquad (2.3)$$

where V is the total volume of the spray and dV is the volume of the droplets between D_d and $D_d + dD_d$. This was found to apply to normal, pintle and throttle pintle nozzles. The Sauter mean diameter was also measured and an empirical relationship was derived relating this to the operating conditions as follows:

$$D_{32} = A(\Delta P)^{-0.135}(\rho_g)^{0.121}(Q)^{0.131} \qquad (2.4)$$

where ΔP = the mean effective pressure drop across the nozzle (MPa)

ρ_g = gas density (kg/m^3)

Q = amount of fuel injected (mm^3/stroke)

and A is a constant which depends on the nozzle used (A = 25.5 for the pintle nozzle, 23.9 for the hole nozzle and 22.4 for the throttle pintle nozzle).

Elkotb (1982a) and (1982b) and Elkotb et al (1982) measured the droplet size distribution of sprays injected through a 0.55 mm diameter pintle nozzle using the slide sampling technique. They measured the droplet sizes at a location of 60 mm from the nozzle tip and at charge pressures ranging from 0.1 to 0.7 MPa, while the temperature was held constant at 293 K. The measured droplet sizes ranged from 2 to 90 μm and were best fitted by either Chi-square distribution:

$$\frac{dV}{V} = 1953\left(\frac{D_d}{D_{32}}\right)^{7.5} \exp\left\{-7.5\left(\frac{D_d}{D_{32}}\right)\right\} d\left(\frac{D_d}{D_{32}}\right) \qquad (2.5)$$

or a Tanasawa-Tesima (1958) distribution

$$\frac{dn}{n} = 10\left(\frac{D_d}{D_{32}}\right)^{2.4} \exp\left\{-2.4\left(\frac{D_d}{D_{32}}\right)^{2}\right\} d\left(\frac{D_d}{D_{32}}\right) \qquad (2.6)$$

They also reported a correlation relating the Sauter mean diameter to the operating conditions, expressed in non-dimensional form:

$$D_{32}/d_j = 107\ Re^{-1.183} We^{-0.442} C_Q^{-0.442} \left(\frac{\rho_d}{\rho_g}\right)^{-0.05} \qquad (2.7)$$

where d_j is the nozzle diameter, Re is the Reynolds number $\left(\frac{\rho_g D_d u_d}{\mu}\right)$ We is the Weber number $\left(\frac{\rho_g |u-u_d|^2 D_d}{2\sigma_d}\right)$ and C_Q is the discharge coefficient.

Although the collection methods of measuring droplet size distributions have been commonly used, their accuracy is uncertain and they are intrusive, i.e. they may influence the behaviour of the spray. They also suffer from the following additional problems: (a) Large droplets may be produced by impingement and coalescence of droplets when they are captured (see Karasawa et al (1982)). (b) When the sampling device is used, a percentage of small droplets may fail to pass through the shutter due to the differing drag/inertia ratios of large and small droplets and (c) Droplets can break into smaller ones at the moment of impact. Concerning (a) Karasawa et al (1982) showed evidence that mean diameter deviates markedly from the true value when coalescence of droplets occurs in the immersion sampling liquid. The most important point is that the measurement position of these intrusive techniques is well downstream and this may not be representative of the first 50 mm of the spray where atomization and/or agglomeration is in progress.

Boulderstone et al (1981) overcame the above three problems by using a non-intrusive light scattering technique. This was employed to measure droplet size distribution at locations 32, 64 and 96 mm from the nozzle of a pulsed diesel spray injected into atmospheric pressure surroundings. They found that the droplet size distribution changes along the spray. For the measurements taken at x = 64 mm they reported that the droplet size distributions were generally well approximated by the Rosin-Rammler function:

$$\frac{dV}{V} = n \frac{D_d^{n-1}}{\bar{D}^n} e^{-\{(D_d/\bar{D})^n\}} dD_d \qquad (2.8)$$

where $\bar{D}$ and n are the mean diameter and an empirical parameter respectively which were reported as functions of time for both single hole and pintle nozzles as shown in Fig. (2.4).

More recently, Negus (1983) measured the droplet sizes at the edge of pulsed diesel sprays injected into a room pressure and temperature air charge, using a laser diffraction technique. The measurements were carried out well downstream of the injector (i.e. > 50 mm). He reported that, for a 0.2 mm nozzle diameter, the droplet sizes were approximated by a Rosin-Rammler distribution with $\bar{D}$ = 39 μm and n = 3.5.

c. Effect of the operating conditions on droplet size

The effect of the different operating conditions on the droplet sizes which result from the atomization process is discussed here. Those include the effective pressure (that is, the pressure drop across the nozzle), medium density, nozzle diameter and fuel viscosity. As far as the effective pressure ΔP is concerned, Hiroyasu et al (1974) showed that an increase in ΔP (for a charge pressure of 3 MPa) decreases the mean diameter of the spray for the three types of nozzles they investigated. They postulated that it was due to the accompanying increase in the injection velocity. ElKotb et al (1982) noted the same tendency as Hiroyasu et al (1974) (the Sauter mean diameter of the diesel fuel spray injected into atmospheric condition decreases from 70 μm at ΔP = 7.3 MPa to 52 μm at ΔP = 11.7 MPa) but they attributed this

effect to the high turbulence intensity created in the gas at high injection pressure, causing an increase of the available 'specific energy of atomization'.

According to Giffen and Muraszew (1953), the effect of the increased charge density (increased pressure at constant room temperature) is to reduce the measured drop size i.e. for a nozzle of 0.56 mm diameter and an injection pressure of 20.4 MPa, the mean diameter decreases from 40 μm at ρ_g = 12.8 kg/m^3 to 5 μm at ρ_g = 38.7 kg/m^3. However, Hiroyasu et al (1974) and ElKotb et al (1982) found that the Sauter mean diameter of the spray increases with an increase in the charge density as shown in Fig. (2.5). They believed that this can be attributed to the agglomeration of droplets due to the reduced penetration which is a characteristic of higher density. A third group (Kuniyoshi et al (1980)) measured the droplet sizes of diesel spray injected from a 0.3 mm diameter single hole nozzle and injection pressure of 37.3 MPa into a nitrogen charge of various pressures (densities). They claimed that the Sauter mean diameter is constant although the charge pressure is varied from 1.08 to 9.91 MPa.

The effect of nozzle orifice diameter on droplet sizes has been investigated by Hiroyasu and Kadota (1974) using 0.2, 0.25, 0.3 and 0.5 mm diameter nozzles for injection and charge pressures of 9.9 and 0.1 MPa respectively. No appreciable difference was noted on the Sauter mean diameter produced by these nozzles.

In general, it is believed (Reitz (1978)) that an increase in the liquid fuel viscosity is to damp any tendency for deformation

of the liquid surface. This contention is supported by the experimental findings of ElKotb et al (1982) that droplet size increases with increasing liquid viscosity. In their experiments they measured the size distributions of sprays of different fuels e.g. gasoline, kerosene, light diesel fuel and diesel fuel injected from 0.55 mm single hole nozzle into atmospheric condition. (They noted that the variations of both the surface tension and density between the above fuels are small compared to the variation in the viscosity). Their measurements showed that the distribution curve for gasoline, which has the lowest viscosity, has a sharp and high peak at small sizes indicating a nearly homogeneous distribution as shown in Fig. (2.6). On the other hand, the curve for diesel fuel, which has the highest viscosity, was rather flat distribution with a peak at larger sizes indicating an inhomogeneous distribution.

2.2.4 Spray Cone Angle

The cone angle of a spray is usually defined as the angle between the tangents to the spray envelope at the nozzle exit as shown in Fig. (2.3). Wakuri et al (1960) measured the cone angle (2β) of diesel sprays injected through 0.31, 0.34, 0.38 mm diameter hole nozzles. They noted that the semi-angle β is affected by the ratio of the charge density to the fuel density, nozzle diameter and injection velocity. They proposed the following dimensionless correlation:

$$\beta = f\left(\frac{\rho_d}{\rho_g}, \frac{\rho_d d_j U_o}{\mu_g}\right) \tag{2.9}$$

where ρ_d, ρ_g are the fuel and gas densities respectively, μ_g is the gas viscosity, d_j the nozzle diameter and U_o is the injection velocity.

Hiroyasu et al (1980) correlated their measurements of cone angle to effective injection pressure, gas and liquid densities, gas viscosity and nozzle diameter with the aid of the dimensional analysis of Wakuri et al (1960) to obtain:

$$\beta = 0.66\left(\frac{d_j^2 . \rho_g^3 . \Delta P}{\rho_d^2 \mu_g^2}\right)^{\frac{1}{4}} \tag{2.10}$$

Reitz (1978) measured the cone angle of water-glycerol mixtures with a wide range of density ratios (ρ_g/ρ_d). He also used 9 nozzles of different geometries with sharp exit edges (length to diameter ratio L/d_j = 0.5 - 85) and he found that β follows the simple relationship:

$$\tan \beta = \frac{1}{A} 4\pi \left(\frac{\rho_g}{\rho_d}\right)^{\frac{1}{2}} \frac{\sqrt{3}}{6} \tag{2.11}$$

where A is constant for a given nozzle geometry.

Wu et al (1983) continued the experiments of Reitz (1978) but with a wider range of operating conditions. They used 13 nozzles with sharp and rounded exit edges and liquids with broader ranges of viscosities and surface tensions (water-n-hexane and n-tetradecane). They used also higher injection pressure than Reitz's as shown in

table (2.1). They reported that the surface tension, nozzle diameter and the injection pressure have no discernable effect on β and they proposed the following correlation:

$$\tan \beta = \frac{1}{A} 4\pi \left(\frac{\rho_g}{\rho_d}\right)^{\frac{1}{2}} f\left\{\left(\frac{\rho_d}{\rho_g}\right)\left(\frac{Re_d}{We_d}\right)\right\} \qquad (2.12)$$

Thus it can be concluded from the above investigations that β is mostly affected by the density ratio (ρ_g/ρ_d) and the geometry of the nozzle. Giffen and Muraszew (1953), Reitz (1978), Hirayasu et al (1980) and Wu et al (1983) found, for a given nozzle geometry, liquid and injection pressure, that β increases as the charge pressure increases up to a certain level, whereafter the rate of increase in β with increasing P_g diminishes as shown in Fig. (2.7).

Concerning the effect of nozzle geometry on spray cone angle, Wu et al (1983) showed that for nozzles of a given diameter but different length and for a given injection pressure and density ratio, the spray angle increases with decreasing L/d_j. However at L/d_j around 10 a maximum value of β is reached and it then falls as L/d_j is further reduced as shown in Fig. (2.8). Hiroyasu et al (1982) found a similar trend but obtained the maximum at around $L/d_j = 20$ whereas Reitz (1978) observed that the angle increases monotonically with decreasing L/d_j.

The transient variation of β for pulsed sprays injected into high pressure/or high temperature charges has been studied by Takeuchi et al (1983) and Yule et al (1985b). No obvious trends were seen for β at the early injection times due to the irregular shape of the spray, while later on, the spray takes the typical

conical form with clear and identified boundary, β takes nearly a constant value.

2.2.5 Spray Penetration

The distance which the fuel spray penetrates into the combustion chamber is clearly important to the formation of a combustible mixture. The penetration length or 'penetration' of a spray is defined as the distance between the nozzle and the furthest droplets at a given moment.

Spray penetration has been the subject of intensive investigations during the last six decades. Schweitzer (1937) made measurements for fuel oil sprays injected through single hole nozzles with diameters of 0.18, 0.34, 0.64 mm. The injection pressure varied between 6.8 - 54.4 MPa, while the charge (air) pressures were 0.1 - 1.7 MPa and air temperature was 293 K. He showed that the spray penetrates quickly in the early stages but slows down later. A correlation was proposed of the following form:

$$\frac{\ell}{d_j}\left(\frac{\rho_g}{\rho_d}\right)^{0.75} = 2265 \ln\left\{\frac{1}{115.5}\frac{t}{d_j}\frac{\rho_g}{\rho_d}\sqrt{\frac{\Delta P}{\rho_d}} + 1\right\} \qquad (2.13)$$

where ℓ is the penetration length at time t.

Burt and Troth (1970) measured the spray penetration of gasoline, kerosine and heavy gas oil injected from a 0.25 mm single hole nozzle into a high pressure (0.56 - 2.7 MPa) and room

temperature charge. The fuel injection pressures were 13.6, 20.4 and 28.9 MPa. They found that their data, over the range of experimental density conditions, are fitted by the following equation:

$$\ell = (a - b\rho_g)\tanh ct \tag{2.14}$$

where a, b and c are constants (their values are not given).

Hiroyasu et al (1980) made measurements of diesel spray injected into nitrogen charges with pressures ranging from 0.1 to 3 MPa and temperature within the range 293 - 593 K. The injection pressure varied between 7 to 15 MPa. They found that the penetration is proportional to the time in the early stage of injection (a period of $\simeq$ 0.3 - 1 ms depending on the injection condition), and then becomes proportional to the square root of the time viz:

$$\begin{aligned} \ell &= 0.39\sqrt{\frac{2\Delta P}{\rho_d}}\, t \qquad && 0 < t < t_{trans} \\ \ell &= 2.95\, (\frac{\Delta P}{\rho_g})^{\frac{1}{4}} \sqrt{d_j t} \qquad && t > t_{trans} \end{aligned} \tag{2.15}$$

where t_{trans} is the transition time from linear penetration to the situation where the penetration varies as $\sqrt{t}$ and it is given by

$$t_{trans} = \frac{15.8\rho_d d_j}{0.55\sqrt{\rho_g \Delta P}}$$

Fujimoto et al (1981) conducted similar experiments but over a broader range of charge pressures (1.08 - 9.9 MPa) and temperature (283 - 960 K). They noted similar trends in that the

penetration was nearly linear with time within a period of 0.5 ms after the start of injection and then followed the law:

$$\ell = 27.1\ t^{0.38}(\rho g)_g^{0.092} \log t - 0.41 U_o^{0.5}\ d_j^{0.5} \qquad (2.16)$$

where U_o is the mean discharge velocity of the fuel at the outlet of the nozzle ($180 < U_o < 250$ m/s).

Varde et al (1983) made measurements to study diesel spray penetration at high fuel injection pressures (up to 150 MPa) and also to evaluate how nozzle dimensions and the ambient pressure influence the penetration. For this purpose they used different single hole nozzles having different orifice diameters (0.18 - 0.42 mm) and L/d_j ratios (from 2.2 to 11). They found that the spray penetration is correlated by:

$$\ell = 1.1\left(\frac{\Delta P \rho_d d_j^2}{\mu_d^2}\right)^{0.3} \left(\frac{Re^2}{We}\right)^{-0.008} \left(\frac{\rho_d}{\rho_g}\right)^{0.5} \left(\frac{L}{d_j}\right)^{0.16} t^{0.55} \qquad (2.17)$$

where μ_d is the viscosity of the fuel.

Recently, Yule (1984) made penetration measurement of diesel sprays using three injectors with hole size ranging from 0.21 mm to 0.46 mm with 12 MPa needle lift pressure. Sprays were investigated in a constant volume bomb pressurized with carbon dioxide to produce pressures up to 6 MPa and the charge temperature ranging from 293 - 700 K. A non-intrusive spark photography technique was used to measure spray structure. A photodiode technique was used to measure spray penetration at any time. Also the jitter effect was examined by use of transient recorder to average many spray pulses at each

time. In addition to studying the spray structure and penetration, the transient spray cone angle versus time characteristics were measured. Also recorded were the fuel flow rate versus time characteristics.

Parameters Influencing Penetration

a. Effect of injection pressure

The effect of injection pressure on spray penetration has been the subject of many experiments. It is not obvious at first sight whether the penetration should increase or decrease with an increase in injection pressure, because the latter is accompanied by a simultaneous decrease in droplet size (as noted earlier), and hence by an increase in drag on the droplets.

Burt and Troth (1970) showed that the penetration of the spray, injected into a high pressure (2.7 MPa) and room temperature nitrogen charge, at t = 3 ms increases from 45 mm to 68 mm corresponding to an increase in the injection pressure from 13.6 to 28.9 MPa.

Hiroyasu et al (1980) and Varde et al (1983) also observed that the an increase of injection pressure, for the same nozzle and charge condition, increases the penetration and Giffen and Muraszew (1953) emphasised that at higher injection pressures (> 40 MPa), the increase in penetration with increased injection pressure becomes smaller.

b. Effect of ambient pressure

The gas density has been considered by many investigator as the most important factor affecting penetration. In most investigations the change in density has usually been produced by altering the charge pressure at a constant temperature.

Burt and Troth (1970) showed that, for gasoline spray at injection pressure of 13.6 MPa, increasing the charge pressure at a constant temperature increases the penetration rate, e.g. at t = 3 ms the penetration decreases from 100 mm at P = 0.56 MPa to 45 mm at P = 2.7 MPa.

Hiroyasu et al (1974) reported that the penetration of diesel oil spray at injection pressure of 9.9 MPa decreases with an increase in the charge pressure, for example at t = 3 ms the penetration decreases from 100 mm to 50 mm corresponding to an increase in the charge pressure from 1.1 to 5 MPa respectively. Kuniyoshi et al (1980) and Yule et al (1985b) also observed the same trend that the penetration decreases with increasing the charge pressure due to the decrease of the spray tip velocity which is attributed to the increased drag on the droplets. It was also observed that the decrease in spray tip penetration with ambient gas pressure becomes smaller with higher ambient pressures.

c. Effect of ambient temperature

As the charge temperature is increased the evaporation accelerates, causing a gradual decrease of droplet size especially for small droplets; this in turn would decrease the drag on droplets and increase the penetration. On the other hand there are effects in the opposite direction due to the increase in charge temperature. Hiroyasu et al (1980) noted that at low charge pressure (1 MPa) the penetration did not significantly change when the ambient temperature was raised from 295 K to 593 K. By contrast, Kuniyoshi et al (1980) found that, at high pressures (6.28 MPa), increasing ambient temperature from 530 to 750 K increases penetration, but at values higher than 750 K, the penetration decreases due to the high rate of evaporation. (In fact there is some ambiguity in their definition of spray penetration, which they deduced from photographs. They stated that the density of the spray was less than the intensity of the transmitted light of the measuring technique due to the extensive vaporization of the spray. They added that the spray tip was made clear by the scattered light of the flame produced when the spray ignites. These data are claimed to be well correlated by equation (2.16)).

d. Effect of injector diameter

The penetration of sprays injected from hole atomizers depends on the nozzle diameter d_j and the nozzle L/d_j ratio for the same injection velocity and charge conditions. Giffen and Muraszew (1953) showed that the penetration increases linearly with d_j. They argued that this can be explained by the fact that the momentum of the discharged fuel increases approximately in proportion with d_j^2 while the area of the jet exposed to air resistance increases in proportion with d_j. However, the correlations of Hiroyasu et al (1980) equation (2.15) and Kuniyoshi et al (1980) equation (2.16) show that the penetration increases in proportion with $\sqrt{d_j}$.

The effect of nozzle length expressed as L/d_j has also been investigated. Giffen and Muraszew (1953) noted that the penetration decreases with increasing L/d_j until a value of ~2, after which it decreases.

e. Effect of fuel properties

The effect of the physical properties of different liquids on spray penetration has been studied by several research workers. In spite of this, however, there are some contradictory views regarding the effect of viscosity on penetration. Schweitzer (1937) showed that increasing the fuel viscosity from 6 to 13.5 cS. had

no effect on spray penetration at t = 1 ms, and produced less than 10% increase at t = 4 ms. Tham (1982) observed the same tendency and he reported that the spray penetration is 11% greater for diesel oil (compared to gasoline) at ambient pressure of 4.5 MPa. Giffen and Muraszew (1953) argued that fuels with high viscosity cause both a reduction in the cone angle and an increase in droplet sizes, which combine to cause an increase in the velocity and penetration of the spray.

Burt and Troth (1970) carried out experiments involving a wide variation of fuel viscosity, produced either from selection of different fuels or from changing the fuel temperature. They reported no measurable effect on the spray penetration and stated that the explanation lies in the flow condition in the nozzle at the high pressure of diesel sprays which causes the spray atomization.

2.3 Spray Models

The theoretical analysis of spray behaviour started with the development of simple global, penetration-oriented empirical correlations. Such models stemmed from the need to know spray penetration characteristics in diesel engines since overpenetration can lead to excessive fuel deposition on the cylinder walls while underpenetration can cause poor mixing and combustion (Varde et al

(1983)). Hay and Jones (1972) reviewed the penetration correlations which are based on analytical models as those of Lyshevskiy (1956), Wakuri et al (1960), Rusinov (1963), Sitkei (1964), Ogaswara and Sami (1966), Oz (1969) and Dent (1971) and those based on experimental study such as those of Schweitzer (1937), Parkes et al (1966), Burt and Troth (1969) and Taylor and Walsham (1970). Hay and Jones (1972) evaluated these correlations and recommended that of Dent (1971) under all conditions apart from exceptionally large charge densities (equal to or more than 10 MPa) where it tends to overpredict. This correlation takes the form:

$$\ell = 3.1 \{(\frac{\Delta P}{\rho_g})^{\frac{1}{2}} d_j t\}^{\frac{1}{2}} (\frac{294}{T_g})^{\frac{1}{4}} \qquad (2.18)$$

where ΔP is the effective injection pressure (MPa) and T_g is the gas temperature (K).

Although such penetration correlations are simple, they suffer from two severe limitations. Firstly, they are only valid for the conditions of the experiments they were based on or tested for. Secondly, they provide no detailed information about the spray such as drop velocities and the distributions of the fuel vapour concentration.

One approach to the prediction of details of the latter kind is to solve numerically differential conservation equations for the gas and droplet phases. Three different formulations of these equations are reported in the literature namely, the 'spray equation' model, the 'continuous droplet' model and the 'discrete droplet' model.

In the spray equation approach, developed by Williams (1965), the droplet field is described by a continuous statistical distribution function defined at all positions in the flow field. The distribution function $f_d(D_d, \vec{x}_d, \vec{u}_d, t)dD_d d\vec{x}_d d\vec{u}_d$ represents the number of droplets with diameter in the range dD_d about D_d, located in the volume $d\vec{x}_d$ about $\vec{x}_d$, with velocities in the range $d\vec{u}_d$ about $\vec{u}_d$, at time t. An equation governing the rate of change of f_d is derived by Williams (1965) as:

$$\frac{\partial f_d}{\partial t} + \frac{\partial}{\partial D}(\dot{R}_d f_d) + \nabla_x \cdot (\vec{u}_d f_d) + \nabla_{\vec{u}_d} \cdot (\vec{F}_d f_d) = S \qquad (2.19)$$

where $\dot{R}_d$ is the droplet vaporization rate, $\vec{F}_d$ is the sum of the external body forces and the aerodynamic drag forces acting on each droplet and S is the generalized source and droplet interaction terms. Solution of this equation has been obtained by Bracco (1974), Bracco et al (1976) and Westbrook (1976), all of whom computed the spray evolution in prespecified gas flows (i.e. the droplets were assumed not to influence the gas field). Westbrook (1977), Haselman and Westbrook (1978) and Gupta and Bracco (1978) refined the above approach by solving the spray equation along with the gas phase conservation equations and taking into consideration the coupling of the two phases through inclusion of appropriate droplet interaction source terms in the gas phase equations.

A fundamental practical difficulty with the spray equation approach is the large number of independent variables involved. For a three-dimensional transient problem, the distribution function involves eight dimensions (three space, three velocity, one size

and one temperature co-ordinates), even with the simplifying assumption that the droplets are a pure liquid evaporating at the wet bulb conditions (Faeth (1983)). This problem is compounded when additional factors, such as droplet temperature variations, are considered. Furthermore, the drop temperatures, velocities etc. vary rapidly in the near-injector region, imposing requirements for closely spaced grids for all the dimensions of f_d if numerical errors are to be avoided. This would require prohibitive amounts of computer time and storage.

The 'continuum' droplet model treats the droplets as a continuous fluid interpenetrating and interacting with the gas field. Travis et al (1976) showed that the continuum model is equivalent to taking appropriate moments of the spray equation. Integration of the resulting equations over the entire range of D_d and u_d values gives the conservation equations of the droplet phase, which are linked to the equivalent transport equations for gas phase properties, e.g. the axial momentum equations for both phases are written as:

$$\frac{\partial}{\partial t}(\rho u)_g + \frac{\partial}{\partial x}(\rho u^2)_g + \frac{1}{r}\frac{\partial}{\partial r}(r\rho uv)_g = -\frac{\partial P}{\partial x} + \frac{B_d}{\theta\rho_g}(u_p - u_g)$$

$$\frac{\partial}{\partial t}(\rho u)_d + \frac{\partial}{\partial x}(\rho u^2)_d + \frac{1}{r}\frac{\partial}{\partial r}(r\rho uv)_d = -\frac{\partial P}{\partial x} + \frac{B_d}{(1-\theta)\rho_d}(u_g - u_d) \qquad (2.20)$$

where u and v are the axial and radial components of the velocity, θ is the void fraction and B_d represents the drag function. This model has been used by many investigators e.g. Murray (1965),

Soo (1967), Anderson and Jackson (1967), Harlow and Amsden (1975) and Gosman et al (1976a). It is also widely employed in calculations of two-phase flows in nuclear reactors (see Dehaye et al (1981)). This approach yields a particularly concise formulation when a single droplet size is adequate to describe the process. Sprays, however are polydispersed, i.e. they possess a range of droplet sizes and this can only be represented in the continuum model by defining discrete size ranges and solving a set of continuum equations for each range. Thus, in these circumstances the continuum approach effectively replaces the large number of discretized independent variables of the spray equation by a large number of transport equations (according to the number of size ranges used), so it too becomes costly in terms of computer time and storage requirements. A second disadvantage of the continuum appraoch is that it is prone to numerical diffusion errors when the narrow, high velocity spray is oblique to the computing mesh.

There exists a subclass of continuum models employed by Shearer and Faeth (1977), Khalil et al (1977), Shearer et al (1978) and Faeth (1979) among others usually termed 'locally homogeneous flow models'. The basic premise of this model is that interactions between phases are fast in comparison to the development of the flow field as a whole. This implies that at each point in the flow both phases have the same velocity and are in thermodynamic equilibrium. This requirement is most easily met when the dispersed phase is a gas and the continuous phase is a liquid, due to the relatively low inertia and thermal capacity of bubbles. The validity of this model for spray applications is however questionable, unless

the droplet sizes are small, the densities of the phases are nearly the same and the rate of flow development is slow. None of these conditions are met in real diesel sprays.

The major advantage of the locally homogeneous flow model is that fewer equations are required for spray calculations since the theory is equivalent to a single-phase flow. The main disadvantage involves the inaccuracies inherent in the assumption of infinitely fast interactions (see Shearer et al (1978)).

The most popular method is the 'discrete' droplet model in which the spray is statistically represented by a finite number of discrete droplets, rather than by continuous distribution. Conventionally the droplet behaviour is described by Lagrangian conservation equations as (for axial direction):

$$\frac{dx_d}{dt} = u_d$$

$$\frac{du_d}{dt} = B_d(u_g - u_d) - \frac{1}{\rho_d}\frac{\partial P}{\partial x} \qquad (2.21)$$

while an Eulerian formulation is retained for the gas motion: however the latter practice is a matter of choice rather than necessity. The application of the discrete droplet model involves dividing the liquid emanating from the nozzle (or more generally, the atomization zone) into a finite number of droplet classes or parcels whose initial properties (i.e. size, velocity, temperature etc.) are assumed known. Each parcel is considered to represent a group of droplets all possessing the same initial characteristics. The life history of each parcel is then computed as it traverses

the flow field and exchanges mass, momentum and energy with the surrounding gas. The effect of the droplets on the gas phase is considered by introducing appropriate interaction source terms in its equations of motion. This interaction source term is given by the following:

$$S_{\phi_{i,j}} = \sum_k N_{d,k}\{(m_d\phi_d)_k^{n+1} - (m_d\,\phi_d)_k^n\} \qquad (2.22)$$

where i,j designates the computational cell, $N_{d,k}$ is the total number of droplets in the parcel k, m_d is the mass of the droplet in the parcel and ϕ_d is a general property which represents u, v, T and 1 for mass source. The superscript n+1 and n designate new and old time levels respectively.

A summary of the properties of the recent discrete droplet models is listed in table (2.2). The list is by no means complete and the various investigations in this list have been selected to represent typical features of current models, a range of applications and the extent and limitation of the various model predictions.

The applications considered by the models listed in table (2.2) involve both evaporating and combusting sprays (e.g. Crowe et al (1977), Mongia et al (1978), ElBanhawy and Whitelaw (1980), Gosman et al (1980a) and Boyson et al (1981)). In these calculations it was assumed either explicitly or implicitly that the spray is 'dilute'. It is meant by this term that interactions between droplets as well as the volume occupied by droplets are both negligible.

It was also assumed in the above-mentioned studies that the droplets respond only to the time-averaged velocity field, which effectively ignores the possibility of turbulent diffusion of the droplets. Some workers, such as Abbas et al (1980) represented the effect of gas-phase turbulence in a deterministic way, by working out from the droplet concentrations a 'diffusion' velocity which is added to that obtained from the original Lagrangian equations of motion. An alternative, and probably more correct approach is the stochastic one devised by Dukowicz (1980) and elaborated by Gosman and Ioannides (1981), in which the gas turbulence is randomly sampled during each droplet's flight and allowed to influence its motion.

The first reciprocating engine applications of the discrete droplet model were made by Butler et al (1980) and Gosman and Johns (1980b). The former predicted the spray evolution in a direct-injection stratified-charge engine. The numerical model was used to simulate the compression and expansion strokes, including the effects of fuel injection, mixing, ignition, combustion and nitric oxide formation. In their calculations, they used a constant eddy diffusivity to represent the gas turbulence and did not model the effect of this on droplet dispersion. Gosman and Johns (1980b) predicted the spray characteristics in an open-chamber direct-injection engine, in the absence of combustion, using the k-ε model for the gas phase turbulence. They too ignored droplet dispersion due to gas turbulence. This methodology was later extended by Gosman and Harvey (1982) to include a combustion model, of a kind which allows in an approximate way for both chemical-kinetic and turbulence effects on the burning rate.

An improved numerical technique (within the discrete droplet model) was developed by Dukowicz (1980) for computing the behaviour of atomized non-evaporating diesel sprays injected into a constant volume vessel containing quiescent gas. The gas and droplet momentum equations were solved by a coupled and implicit method that eliminated iteration for the droplet-gas interaction terms due to the strong coupling of the droplets and gas phase velocities. In his analysis, the gas phase turbulence was simulated by an empirical eddy diffusivity relation devised for gaseous jets. This methodology was later extended by O'Rourke et al (1980) and Kuo et al (1982a) who considered the dense spray phenomena which included the effect of non-unity void fraction on interphase transport rates (drag, heat and mass transfer coefficients); the effect of droplet collision and agglomeration; and allowance for non-unity void fraction in the governing equations of the gas phase.

The main advantage of the discrete droplet model is the elimination of the numerical diffusion (due to Eulerian smearing) in the droplet calculations. Also, the computer storage and computational time are smaller than those of the other spray models examined earlier, because, in practice, the number of droplet parcels required to achieve satisfactory representation of the spray is not excessive, typically 200 parcels/ms. (Dukowicz (1980)).

A serious difficulty when using the discrete droplet models is the lack of data on detailed injector characteristics, such as droplet size and velocity distributions. This is inherently associated with the complex and incompletely understood area of spray atomization as discussed earlier.

The discrete droplet models, as the spray equation and continuum models, requires the specification of the submodels for droplet interaction with the gas phase, such as the drag coefficient, heat and mass transfer correlations. These correlations will be discussed in the next subsection.

Finally, it can be concluded from the above discussion that the discrete droplet models have been favoured by recent workers since the computational time and computer storage are smaller than those of the spray equation model (the number of droplets representing the spray using the discrete droplet model is much less than the number of cells needed in the spray equation model). Also the discrete droplet model eliminates the problems of numerical diffusion for the droplet calculation. Therefore, the discrete droplet model will be used to mathematically model the liquid phase in the present study.

Spray Submodels

i. Droplet drag coefficient

A knowledge of the drag coefficient of the droplets (which constitute the entire spray) is essential for the calculation of spray behaviour.

Since the droplets are spherical in form, some information on the drag forces for liquid droplets may be inferred from experiments on solid spheres. The total drag on a solid sphere may be divided into two components, the friction (Stokes) drag associated with the viscous shear stress tangential to the surface

and the form drag associated with the variation of pressure over the surface. At low droplet Reynolds number friction drag dominates while at high Reynolds number the form drag dominates as a result of the local decrease in pressure in the separation region (see Graves and Scull (1960)).

Ingebo (1956) measured the drag coefficient (C_D) of an accelerating droplet in an airstream and he found that C_D is related to the Reynolds number in the range $6 < Re < 400$, as:

$$C_D = 27/Re^{0.84} \tag{2.23}$$

where $Re = \frac{\rho V_{rel} D_d}{\mu}$ and V_{rel} is the relative velocity of the droplet to the main body of the airstream. Ingebo showed that correlation (2.23) lies between Stokes drag (24/Re) and the standard drag (the drag of smooth inert spheres moving in steady state conditions).

Rabin et al (1960) observed that the flattering of the droplet at high Reynolds number causes an increase in the drag coefficient. They obtained, for Reynolds number in the range $80 - 10^4$, the following correlation:

$$C_D = 0.271(Re)^{0.217} \tag{2.24}$$

while they recommended Ingebo's correlation for Reynolds number less than 80.

Eisenklam et al (1967) investigated the influence of evaporation on the drag coefficient. They reported that evaporation reduces the friction drag due to a thickening of the boundary layer and they correlated their results by

$$C_D = C_D'/(1 + B) \qquad 0.1 < Re < 40 \tag{2.25}$$

here B is the transfer number defined as $c_p(T_g - T_d)/L$ where c_p is the specific heat and L is the latent heat of vaporization. C_D' is the standard drag, proposed by Wallis (1969) for $0 < Re < 10^3$ as:

$$C_D' = \frac{24}{Re}(1 + 0.15\ Re^{0.687}) \tag{2.26}$$

Yuen and Chen (1976) assumed that the difficulty with the drag coefficient of an evaporating droplets arises due to variable property effects in the film surrounding the droplets. They found that the drag coefficient obtained from their results together with that obtained by Eisenklam et al (1967) correlates well with the "standard drag" provided that Reynolds number is calculated in terms of the free stream velocity and density while the viscosity is determined at an average film temperature.

Finally, it can be concluded from the above discussion that the standard drag (correlation (2.26)) describes well the drag of non-evaporating droplets as well as the evaporating ones when proper averaging of the film properties is used to calculate Reynolds number. It is also a simple equation which covers the range of interest of Reynolds number. Therefore it will be used in the present study.

ii. Heat and mass transfer coefficients

Droplet vaporization theory has been extensively studied by many investigators. Classical droplet vaporization theory describes a fuel droplet in a spherically-symmetric gas field, and then correct the results with an empirical correlation for convection. For constant fluid properties, in the absence of convection, the heat and mass transfer coefficients for a spherical droplet are given by (see Faeth (1977)):

$$Nu = \frac{hD}{\kappa} = 2$$

$$Sh = \frac{h'RT_m D_d}{D} = 2 \qquad (2.27)$$

where Nu is the Nusselt number, h is the heat transfer coefficient, κ is the thermal conductivity, Sh is the Sherwood number, R is the gas constant, T_m is the mean film temperature and D is the diffusivity.

The effect of forced convection (due to the relative motion between the droplets and the gas phase) and free convection (due to the diffusivity of the vapour away from the surface of the vaporizing droplet), is then treated by an additive correction which is a function of Reynolds, Prandtl (Pr) and Schmidt (Sc) numbers. A popular and well-established correlation of this type is due to Ranz and Marshall (1952) who indicated that the Nusselt number and vaporization rate for vaporization from wetted porous spheres increase by a factor of $1 + 0.3\ Re^{1/2}Pr^{1/3}$ due to convection. A similar

correction was also used to evaluate the mass transfer rate, where the Sherwood and Schmidt numbers replace the Nusselt and Prandtl numbers, thus:

$$Nu = 2 + 0.6\ Re^{1/2}Pr^{1/3}$$

$$Sh = 2 + 0.6\ Re^{1/2}Sc^{1/3} \qquad (2.28)$$

Here, the thermodynamic properties of the dimensionless numbers are evaluated at the mean film temperature and composition and Reynolds number is based on the relative velocity of the droplet, gas density and viscosity. In their experiments, they used low gas temperature (less than 473 K) which produced low vapour concentration. At high gas temperature as that encountered in diesel engine (at the time of fuel injection), the vaporization rate becomes high which in turn influences the heat and mass transfer coefficients.

Rowe et al (1965) (cited in Yuen and Chen (1978)), obtained an experimental correlation for the heat transfer coefficient at high temperature in the range of Re from 60 to 1800 as

$$Nu = 2 + 0.69\ Re^{1/2}Pr^{1/3} \qquad (2.29)$$

The heat transfer rates obtained from the above correlations are higher than those obtained from equation (2.28) for the same Reynolds number. This is not physically realistic since the high evaporation rates associated with high temperature decrease the heat transfer to the droplets.

Natarjan and Brzustowski (1970) carried out experiments at high pressures and temperatures and they correlated their results by:

$$Nu = 0.146\ Re^{1/2}/B_E \tag{2.30}$$

where $B_E = 1 + (h_\infty - h_s)/L$ and h_∞ and h_s are the enthalpy at the free stream and the droplet surface respectively. This equation has asymptotically incorrect limits at low Reynolds number.

At free stream temperature up to 1233 K and for Reynolds number ranging from 200 to 1800, Yuen and Chen (1978) showed that the heat transfer rate correlates well with

$$Nu = (2 + 0.6\ Re^{1/2}Pr^{1/2})/B_E \tag{2.31}$$

In the above equation (and similar equation for the mass transfer rate), all properties are evaluated at the film condition except the density in the Reynolds number which is the free stream density.

However, Faeth (1977) proposed a general correlation as

$$(Nu \text{ or } Sh) = \{2 + \frac{0.555\ Re^{1/2}(Pr \text{ or } Sc)^{1/3}}{(1 + 1.232/(Re(Pr \text{ or } Sc)^{4/3}))^{1/2}}\} \left(\frac{B_E}{\ell n(1+B_E)}\right) \tag{2.32}$$

which approaches the correct limiting values at low Reynolds number at low values of B_E. The above correlation contains experimental uncertainties at high Reynolds number, uncertainties in the form of mass transfer correction at finite B_E, and uncertainties in the selection of the reference state for the physical properties (Faeth (1977)).

From the above discussion, it can be concluded that Ranz and Marshall correlations (equation (2.28)) represents the well-established and tested correlations of heat and mass transfer rate

for evaporating droplets at low gas temperature. It will be used in the present study with some modification to account for the effect of mass transfer from the droplets at high gas temperature, as will be shown in chapter 3.

2.4 Closure

In this chapter, a comprehensive review of the experimental work on spray characteristics is given. The spray characteristics include spray formation, structure, droplet mean diameter, cone angle and penetration.

It has been shown, by many investigators, that the atomization of the high speed liquid jet is not completed at once after the jet emerges from the nozzle, but that the jet disintegration occurs over some jet diameters from the nozzle due to the aerodynamic effects supplemented by liquid cavitation effects. It has also been found that the breakup length depends mainly on the operating conditions of the experiments.

As far as the spray structure is concerned, it has been found that diesel sprays possess a double structure: a dense core of poorly atomized ligaments surrounded by a dilute and well atomized zone (see e.g. Kuniyoshi et al (1980), Boulderstone et al (1981),

Negus (1983) and Yule et al (1985b)). This structure also depends to a great extend on the operating conditions of the experiments.

The effects of the different operating conditions on the spray characteristics can be summarised as:

1. An increase in the effective pressure decreases the mean droplet diameter, increases the spray cone angle and the penetration.
2. Increased air density results in shorter sprays of larger droplet size and cone angle.
3. Increased nozzle diameter has no appreciable effect on the mean droplet size and the cone angle while it increases the spray tip penetration.
4. Increased liquid viscosity results in a more compact jet which is more difficult to disperse and gives a spray with larger droplet size and longer penetration.

Also, this chapter reviews the different spray models which are used to represent the spray behaviour. These include the global, penetration-oriented correlations and the detailed numerical models. The latter class of models involves the spray equation model, the continuous droplet models and the discrete droplet models. The discrete droplet models are the favoured ones since the computational time and computer storage are less than those of the other spray models.

Finally, it has been shown that the droplet drag coefficient is very close to the standard drag curve for solid spheres provided that the Reynolds number is based upon an average viscosity, while

the heat and mass transfer coefficients of Ranz and Marshall (1952) are limited to droplets evaporating at low gas temperature. Therefore, a correction is needed to account for the high mass transfer from the droplets which evaporate at high gas temperatures.

Table (2.1) Summary of the operating conditions of the various experimental work.

Reference	Liquid → medium	nozzle diameter (mm)	injection pressure (MPa)	charge pressure (MPa)	charge temperature (K)
Bergwerk (1959)	shell oil → air	0.2 - 0.25	10 - 23	0.1 - 9.5	293
Boulderstone et al (1981)	diesel fuel oil → air	0.46	12	0.1	293
Burt and Troth (1970)	gasoline, kerosine and gas oil → nitrogen	0.25	13.6, 20.4 28.9	0.56 - 2.74	293 - 873
ElKotb (1982a) ElKotb (1982b) ElKotb (1982)	diesel fuel oil, kerosine → air	0.55	11.8	0.1 - 0.8	293
Fujimoto et al (1977), (1979) and (1981)	heavy fuel oil →nitrogen	0.3	37.3	1.08 - 7.95	293 - 806
Hoenlein (1932)	water → air	0.51	-	0.1	293
Hiroyasu et al (1974)	diesel fuel oil → nitrogen	0.2 - 0.5	9.9	0.1 - 5	293

Table(2.1) Cont'd.

Reference	liquid→ medium	nozzle diameter (mm)	injection pressure (MPa)	charge pressure (MPa)	charge temperature (K)
Hiroyasu et al (1980)	diesel fuel oil→ nitrogen	0.3	7 - 15	0.1 - 5	293 - 593
Hiroyasu et al (1982)	water → nitrogen	0.3	up to 70	0.1 - 4	293
Ishikawa et al (1982)	diesel fuel oil → air	0.32 - 0.34	12	0.1	293
Jong-Yule Ha et al (1983)	diesel fuel oil → CO_2	0.32 - 0.36	22 - 49	0.49 - 0.89	298
Kuniyoshi et al (1980)	diesel fuel oil →nitrogen	0.3	37.3	1.08 - 9.95	293 - 960
Negus (1983)	diesel fuel oil → air	0.28	18	0.1 - 0.34	293 - 673
Reitz (1978)	water, Glycerol → air, nitrogen, helium	0.34	3.3 - 16.6	0.1 - 4	293
Sato et al (1982)	heavy fuel oil →nitrogen	0.29	37.3	1.08 - 7.95	298
Schweitzer (1937)	diesel fuel oil→ air	0.18,0.34,0.64	6.8 - 54.4	0.1 - 1.7	293
Varde et al (1983)	diesel fuel oil→nitrogen	0.18 - 0.42	24 - 150	2 - 4.2	293
Wakuri et al (1960)	fuel oil → nitrogen	0.31,0.34,0.38	40 - 75	0.1 - 4	293
Wu et al (1983)	water,n-hexane and n-tetradecane → nitrogen	0.25,0.34,0.66	11.1 - 107.6	0.1 - 0.42	293
Yule (1984) Yule et al (1985, a,b)	fuel oil → CO_2	0.21 - 0.46	12	0.1 - 6	288- 700

Table (2.2) Summary of representative discrete droplet models of sprays

Reference	Application and dimensions	Turbulence model	Droplet dispersion model	Collision model
Crowe et al (1977)	Evaporating sprays, steady 2-D	k-ε	None	None
ElBanhawy et al (1980)	Combusting sprays in cylindrical furnaces, steady 2-D	k-ε	None	None
Gosman et al (1980a)	Combusting sprays, steady 2-D	k-ε	None	None
Abbas et al (1980)	Combusting sprays in furnaces, steady 2-D	k-ε	Deterministic model	None
Ioannides et al (1980)	Combusting sprays in furnaces, steady 2-D	k-ε	Stochastic model	None
Mongia et al (1978)	Combusting sprays in gas turbine combustors, steady 3-D	k-ε	None	None
Boyson et al (1981)	Combusting sprays in gas turbine combustors, steady 3-D	k-ε	None	None
Butler et al (1981)	Combusting sprays in DISC engines, transient 2-D	Scalar eddy diffusivity	None	None

Table(2.2) Cont'd.

Reference	Application and dimensions	Turbulence model	Droplet dispersion model	Collision model
Gosman and Johns (1980b)	Evaporating sprays in DISC engines, transient 2-D	k-ε	None	None
Gosman et al (1982)	Combusting sprays in DISC engines, transient 2-D	k-ε	None	None
Dukowicz (1980)	Isothermal sprays, transient 2-D	Scalar eddy diffusivity	Stochastic model	None
O'Rourke (1980)	Isothermal sprays, transient 2-D	Scalar eddy diffusivity	Stochastic model	Yes

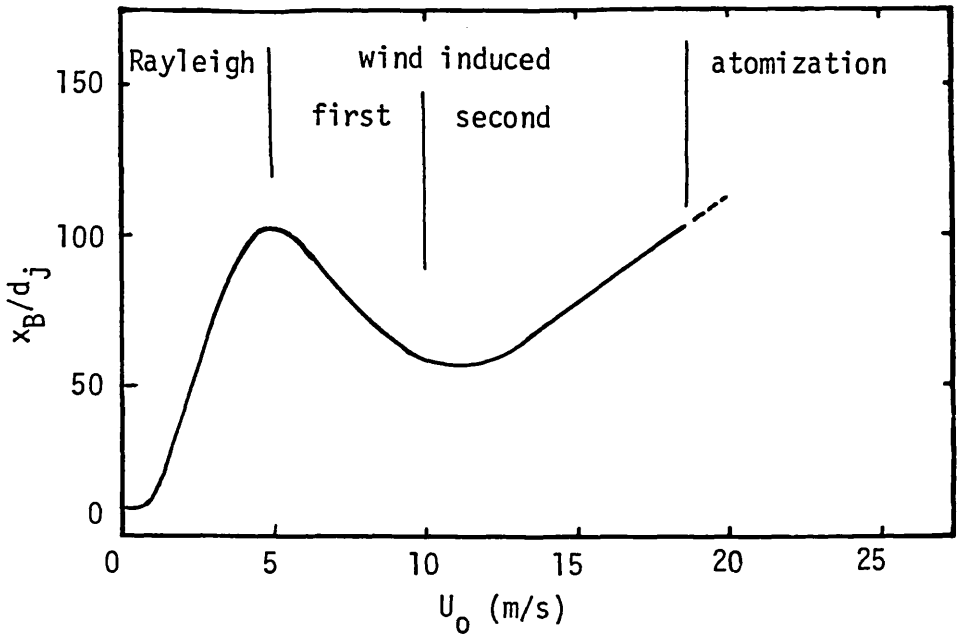


Fig. (2.1) Jet breakup length as a function of jet velocity from Haenlein (1932)

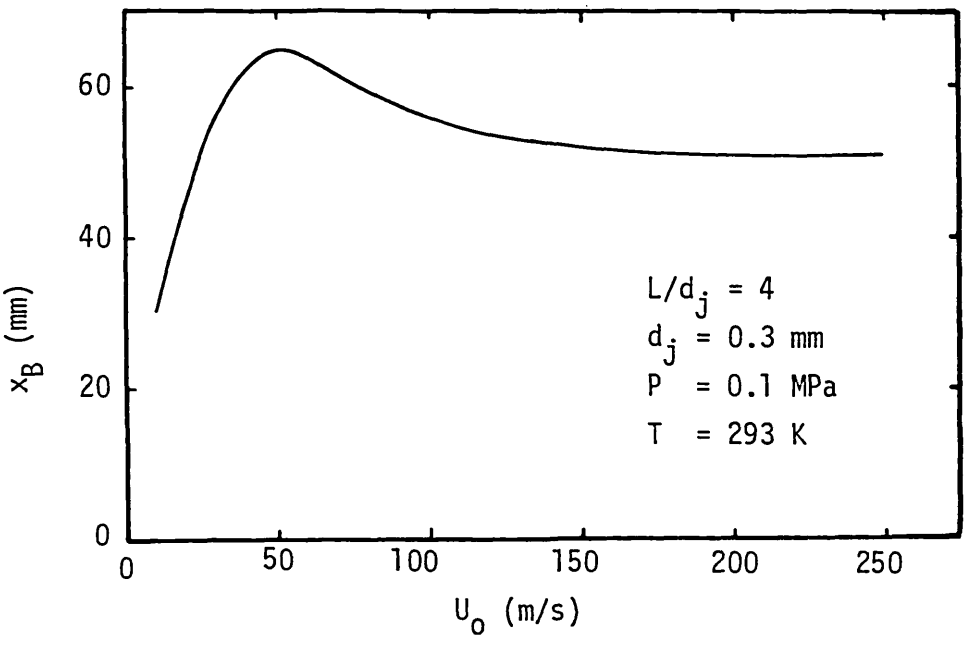
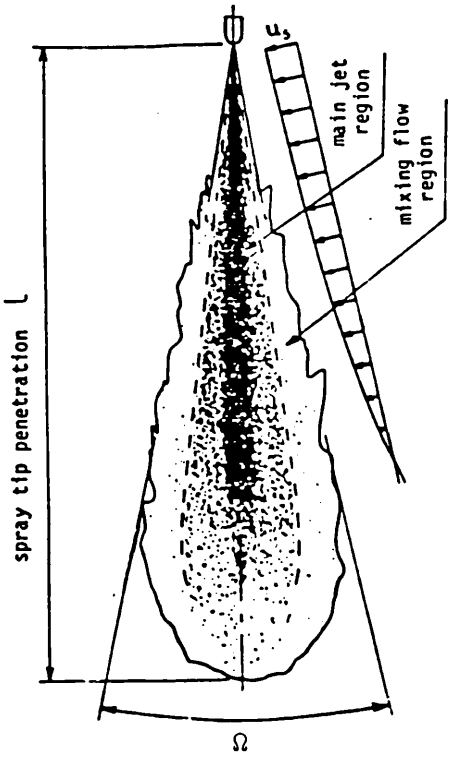


Fig. (2.2) Effect of the injection velocity on the breakup length from Hiroyasu et al (1982)



Ω spray cone angle

u_s entrained air velocity

Fig. (2.3) Structure and shape of diesel spray from Kuniyoshi et al (1980)

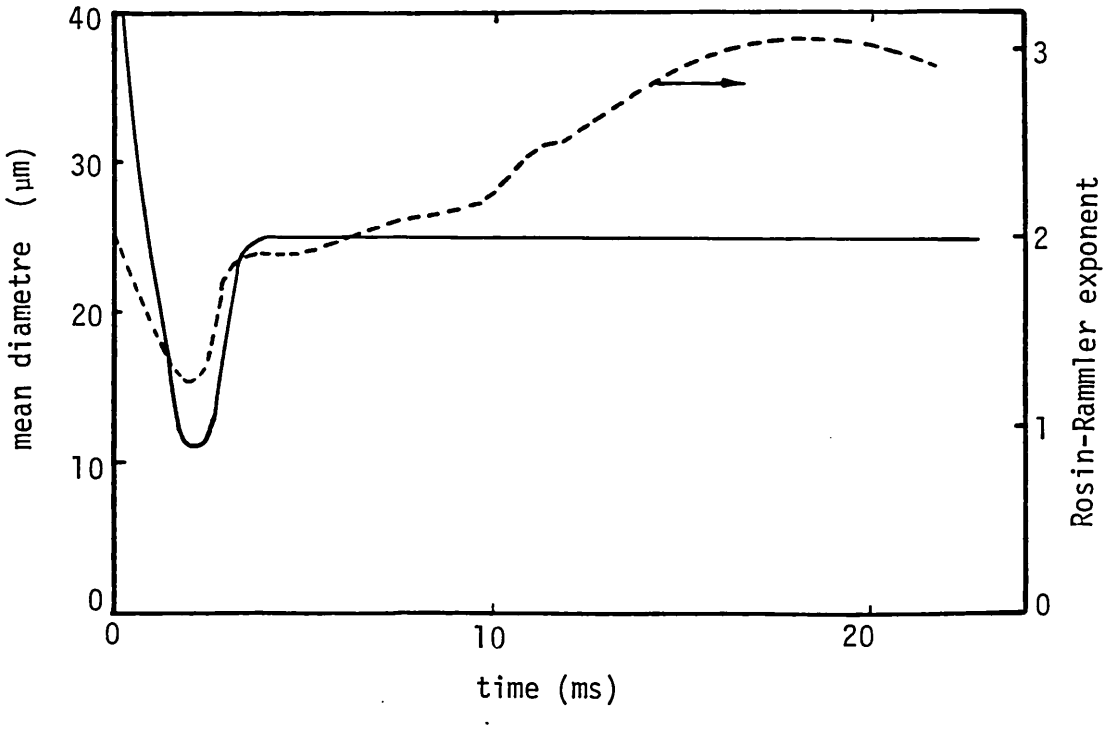


Fig. (2.4) Mean diameter and exponent of Rosin Rammler distribution as a function of time from Boulderstone et al (1981)

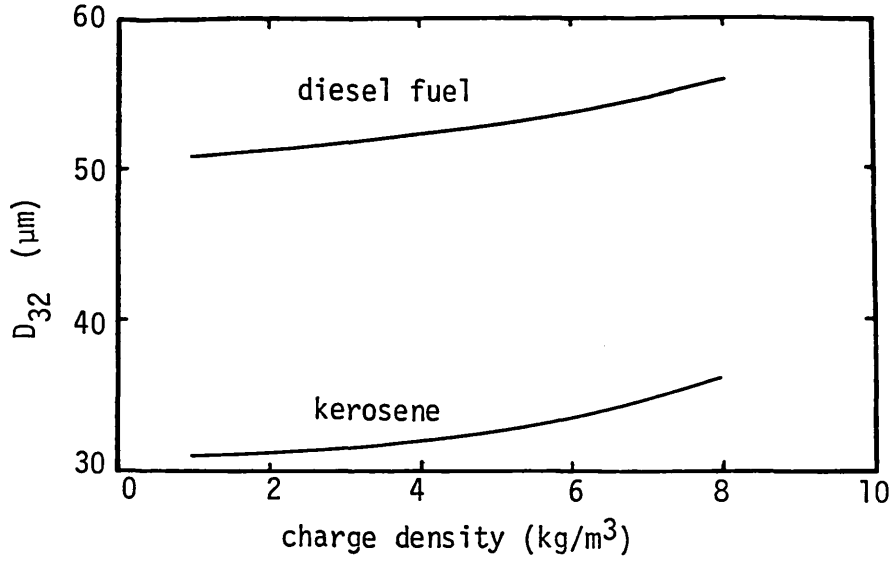


Fig. (2.5) Effect of the charge density on the Sauter mean diameter from Elkotb et al (1982)

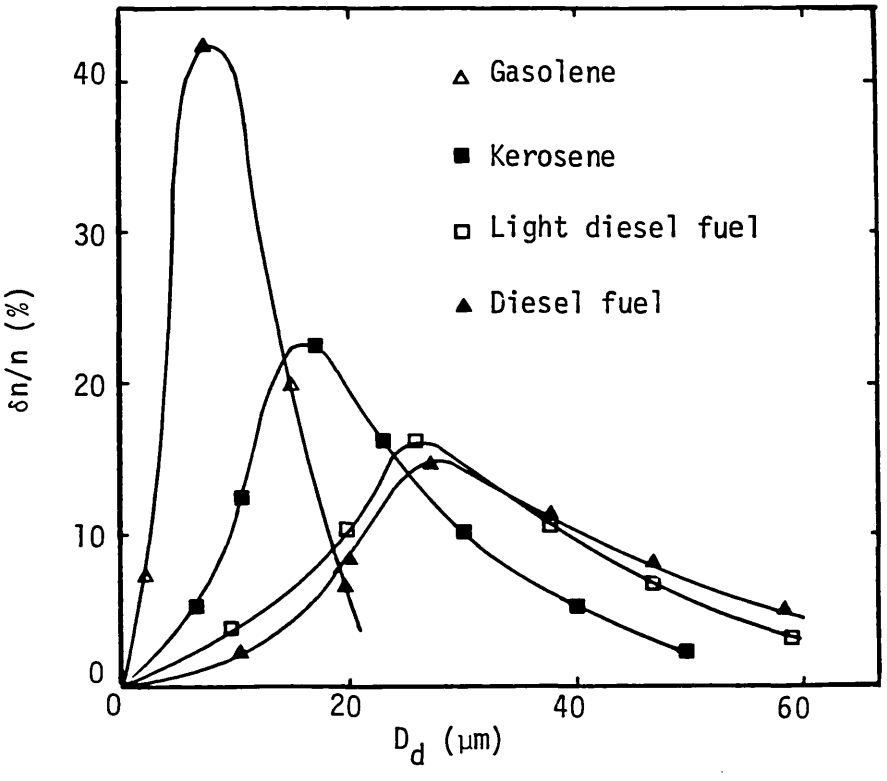


Fig. (2.6) Droplet size distribution of various fuels from ElKotb et al (1982)

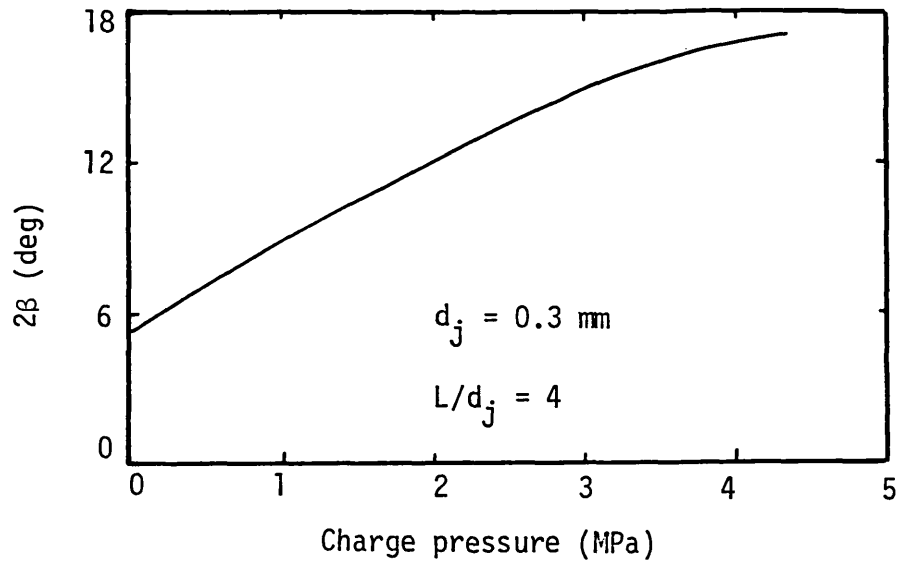


Fig. (2.7) Effect of the charge pressure on the spray cone angle from Hiroyasu et al (1982)

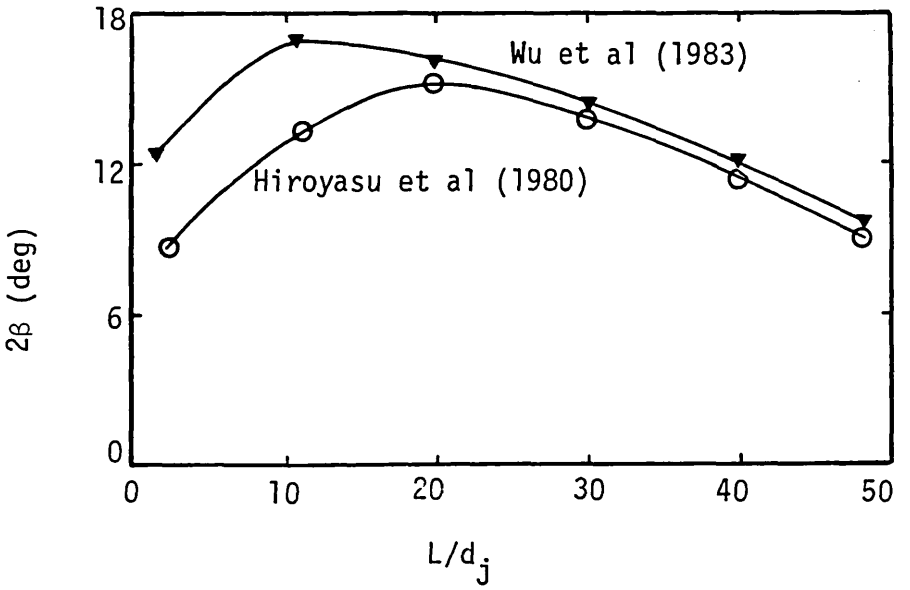


Fig. (2.8) Effect of L/d_j on the spray cone angle

CHAPTER 3

THE MATHEMATICAL MODEL

3.1 Introduction

The predictions of the hydrodynamic and thermal characteristics of liquid sprays in diesel engines require consideration of interacting gas and liquid phases in the flow field. This requires dealing with two sets of equations, one set for the gas and the other for the droplet. These equations are coupled primarily by two mechanisms; the displacement of gas by the volume occupied by the droplets and mass, momentum and energy interchange between droplets and the gas.

This chapter deals with the assembly of the differential equations that govern the flow, heat and mass transfer processes of both phases. Section 3.2 presents the instantaneous gas phase equations conventionally expressed as Eulerian differential equations, and their ensemble-average forms are then given in section 3.3.

Section 3.4 discusses the effects of turbulence on the gas phase and reviews the different turbulence models that may be employed to represent these effects. Also, it covers the modelling of the Reynolds stresses and the turbulent shear fluxes generated from the ensemble-averaging process. The modelled forms of the gas-phase equations employed in the present study are given in section (3.5). Finally, the working versions of these

equations are obtained through a co-ordinate transformation in section (3.6).

The derivation of the droplet-phase governing equations including the underlying assumptions and fuel and film properties are presented in section (3.7). Then the method employed to model the effects of the gas turbulence on the droplet trajectories is discussed in section (3.8).

3.2 Equations Governing Instantaneous Motion of Gas Phase

In the present study, the Eulerian differential equations governing the conservation of mass, momentum and energy form the basis for the analysis of a general, compressible, non-reacting gas phase flow, heat and mass transfer. The equations are first written below in the form appropriate to a time-dependent, two-dimensional axially symmetric flow.

3.2.1 Mass Conservation Equation

Defining a variable $\rho(x,t)$ as the density of the gas occupying a volume V which contains k droplet parcels, the conservation of mass states that the rate of change of the mass of gas in the volume V must equal the mass flux crossing its surface plus the rate of mass transfer from the droplets (Travis et al (1976)). This is expressed mathematically as follows:

$$\frac{\partial}{\partial t}(\rho\theta) + \frac{\partial}{\partial x}(\rho\theta u) + \frac{1}{r}\frac{\partial}{\partial r}(r\rho\theta v) = S_{m,d} \qquad (3.1)$$

where θ is the 'void fraction', defined as the fraction of the volume occupied by the gas and u and v are the gas velocities in x and r directions, respectively. $S_{m,d}$ is the rate of evaporation of the droplets. The presence of the void fraction in this equation accounts for the displacement effect of the droplets and is related to the droplet mass $m_{d,k}$ and droplet density $\rho_{d,k}$ of parcel number k as

$$\theta = 1 - \frac{1}{\rho_{d,k} V} \sum_k m_{d,k} \qquad (3.2)$$

3.2.2 Momentum Conservation Equation

The equations of motion of the gas phase also contain contributions from the droplets through the exchange of momentum with them as well as the displacement effect (Travis et al (1976)). The momentum equation in the axial direction is:

$$\frac{\partial}{\partial t}(\rho\theta u) + \frac{\partial}{\partial x}(\rho\theta uu) + \frac{1}{r}\frac{\partial}{\partial r}(r\rho\theta vu) =$$

$$-\{\frac{\partial}{\partial x}(\theta\tau_{xx}) + \frac{1}{r}\frac{\partial}{\partial r}(r\theta\tau_{rx})\} - \theta\frac{\partial P}{\partial x} + S_{u,d} \qquad (3.3)$$

and the radial momentum equation is

$$\frac{\partial}{\partial t}(\rho\theta v) + \frac{\partial}{\partial x}(\rho\theta vu) + \frac{1}{r}\frac{\partial}{\partial r}(r\rho\theta vv) =$$

$$-\{\frac{\partial}{\partial x}(\theta\tau_{xr}) + \frac{1}{r}\frac{\partial}{\partial r}(r\theta\tau_{rr})\} - \theta\frac{\partial P}{\partial r} + S_{v,d} \qquad (3.4)$$

In these equations, P stands for the pressure; τ_{xx}, τ_{rx}, τ_{xr} and τ_{rr} are the components of the stress tensor; and $S_{u,d}$ and $S_{v,d}$ represent the momentum exchanges with the droplets per unit volume. The stress components for a Newtonian compressible flow are linked to the velocity field by the following relations (see Goldstein (1957) and Bird et al (1968)):

$$\tau_{xx} = -2\mu\frac{\partial u}{\partial x} + \frac{2}{3}\mu(\nabla.\vec{u})$$

$$\tau_{rr} = -2\mu\frac{\partial v}{\partial r} + \frac{2}{3}\mu(\nabla.\vec{u}) \qquad (3.5)$$

$$\tau_{rx} = \tau_{xr} = -\mu(\frac{\partial u}{\partial r} + \frac{\partial v}{\partial x})$$

where μ is the gas viscosity and $\vec{u}$ is the velocity vector.

It is to be noted that in equations (3.3) and (3.4) the factor θ lies outside the pressure gradients so that the equation can represent the limiting case of static equilibrium for an inhomogeneous distribution of the dispersed phase (Harlow et al (1975)) i.e. P = constant; $u = v = 0$; $S_{u,d} = S_{v,d} = 0$ and $\theta \neq$ constant. Then if θ is inside the pressure gradient term, the equations reduce to $p \frac{\partial \theta}{\partial x} = 0$ which is not correct.

3.2.3 Energy Conservation Equation

The conservation of energy principle can be expressed as

$$\frac{\partial}{\partial t}(\rho\theta h) + \frac{\partial}{\partial x}(\rho\theta uh) + \frac{1}{r}\frac{\partial}{\partial r}(r\rho\theta vh)$$

$$= \frac{\partial}{\partial x}(\theta \frac{\kappa}{c_p}\frac{\partial h}{\partial x}) + \frac{1}{r}\frac{\partial}{\partial r}(r\theta \frac{\kappa}{c_p}\frac{\partial h}{\partial r})$$

$$+ \frac{\partial P}{\partial t} + \frac{\partial}{\partial x}\{\theta(\mu - \frac{\kappa}{c_p})\frac{\partial}{\partial x}(\frac{u^2 + v^2}{2})\}$$

$$+ \frac{1}{r}\frac{\partial}{\partial r}\{r\theta(\mu - \frac{\kappa}{c_p})\frac{\partial}{\partial r}(\frac{u^2 + v^2}{2})\}$$

$$+ S_{h,d} \qquad (3.6)$$

where $S_{h,d}$ is the energy exchange with the droplets per unit volume and h is the stagnation enthalpy defined by:

$$h = c_p T + \left(\frac{u^2 + v^2}{2}\right) \tag{3.7}$$

Here T stands for the absolute temperature, κ is the thermal conductivity and c_p is the specific heat at constant pressure defined as

$$c_p = \left(\frac{\partial \hat{h}}{\partial T}\right)_P \tag{3.8}$$

In the above $\hat{h}$ is the instantaneous static enthalpy given by $\hat{h} = c_v T + P/\rho$.

The temperature, density and pressure are linked by the equation of state for an ideal gas i.e.

$$\rho = QP \tag{3.9}$$

$$\text{where } Q = \frac{m}{\bar{R}T} \tag{3.10}$$

$\bar{R}$ is the universal gas constant and m is the gas molecular weight.

Again, the droplet-phase contribution is made through the energy exchange term and the void fraction.

3.2.4 Fuel Vapour Mass Fraction Equation

The conservation of the fuel vapour mass fraction f can be expressed as:

$$\frac{\partial}{\partial t}(\rho\theta f) + \frac{\partial}{\partial x}(\rho\theta uf) + \frac{1}{r}(r\rho\theta vf)$$

$$= \frac{\partial}{\partial x}(\mu\theta \frac{\partial f}{\partial x}) + \frac{1}{r}\frac{\partial}{\partial r}(r\mu\theta \frac{\partial f}{\partial r}) + S_{m,d} \qquad (3.11)$$

The above equations (3.1), (3.3), (3.4), (3.6) and (3.11) are 'exact' and are thus applicable to both laminar and turbulent flows: however they are not solved in the form presented for the reasons given below.

3.3 Averaging Process

3.3.1 Introduction

The numerical method of solution employed to solve the gas-phase equations calculates the values of each dependent variable at a number of discrete points or 'nodes' throughout the field. For turbulent flows, the important details of turbulence properties have small time and length scales; for example, the sizes of the eddies responsible for the decay of turbulence in

a gaseous flow are typically about 0.1 mm (Launder and Spalding (1972)). It is impossible to resolve details of this order because such a large number of nodes would be required that it would strain the capabilities of even the largest present day computers. Fortunately for most engineering purposes, it is not necessary to consider the details of turbulence, since we are usually concerned with the averaged effects. The representation of these will now be considered.

3.3.2 Ensemble Averaging Procedure

The instantaneous value of any dependent variable ϕ (scalar or velocity component) can be represented by an averaged component $\overline{\phi}$ and a fluctuating component ϕ'. For a stationary or 'steady' flow, the average $\overline{\phi}$ is equal to the time average defined as (Hinze (1959)).

$$\overline{\phi}(\underline{x}_o) = \lim_{t_o \to \infty} \frac{1}{2t_o} \int_{t=-t_o}^{t=t_o} \phi(\underline{x}_o, t)dt \qquad (3.12)$$

where $\underline{x}_o$ is a certain point in space and t_o is the time interval. However this procedure renders $\overline{\phi}$ independent of time, it is therefore only appropriate for quasi-steady flows in which the averaged quantities can be expected to be time-independent. This is clearly not the case for the flow considered in the

present study where the averaged quantities will vary throughout the spray pulse. For such unsteady flow, the averaged quantities are defined through ensemble averaging over a large number of repeated pulses or experiments as (see e.g. Bendat and Piersol (1967)):

$$\overline{\phi}(\underline{x}_o, t) = \lim_{m\to\infty} \frac{1}{2m+1} \sum_{n=-m}^{n=m} \phi(\underline{x}_o, nt_o + t) \qquad (3.13)$$

Here n stands for the number of identically repeated experiments if the flow is not cyclically repetitive while it represents the number of cycles or pulses in case the flow is cyclically or pulsating repetitive; t is the time after the start of each experiment or pulse of period t_o and $\underline{x}_o$ is some fixed point in space.

Equation (3.13) is used in the present work to ensemble-average the conservation equations, so their solutions are therefore deemed to be representative of the average number of experiments in which the averaged quantities are repeated.

The averaged equations are thus derived by replacing each of the instantaneous values of the variable in equations (3.1), (3.3), (3.4), (3.6) and (3.11) by the sum of their ensemble-average value (represented by the overbar) and a fluctuating part (represented by '), e.g.

$$\rho = \overline{\rho} + \rho' \ , \quad u = \overline{u} + u' \ , \ \theta = \overline{\theta} + \theta' \text{ etc.}$$

and then ensemble averaging the equation. This process produces the following, with the overbar indicating ensemble averaging.

Continuity

$$\frac{\partial}{\partial t}(\bar{\rho}\,\bar{\theta} + \overline{\rho'\theta'}) + \frac{\partial}{\partial x}(\bar{\rho}\,\bar{\theta}\,\bar{u} + \bar{\rho}\,\overline{\theta'u'} + \bar{\theta}\,\overline{\rho'u'}$$

$$+ \bar{u}\,\overline{\rho'\theta'} + \overline{\rho'\theta'u'}) + \frac{1}{r}\frac{\partial}{\partial r}\{r(\bar{\rho}\,\bar{\theta}\,\bar{v}$$

$$+ \bar{\rho}\,\overline{\theta'v'} + \bar{\theta}\,\overline{\rho'v'} + \bar{v}\,\overline{\rho'\theta'} + \overline{\rho'\theta'v'})\} = \bar{S}_{m,d} \qquad (3.14)$$

Axial Momentum

$$\frac{\partial}{\partial t}(\,\overline{\rho\theta}\,\bar{u} + \bar{\rho}\,\overline{\theta'u'} + \bar{\theta}\,\overline{\rho'u'} + \bar{u}\,\overline{\rho'\theta'} + \overline{\rho'\theta'u'}\,)$$

$$+ \frac{\partial}{\partial x}(\,\bar{\rho}\,\bar{\theta}\,\bar{u}\,\bar{u} + 2\,\bar{\rho}\,\bar{u}\,\overline{\theta'u'} + 2\,\bar{\theta}\bar{u}\,\overline{\rho'u'} + \bar{u}\,\bar{u}\,\overline{\rho'\theta'} + \bar{\rho}\bar{\theta}\,\overline{u'u'} +$$

$$2\bar{u}\,\overline{\rho'\theta'u'} + \bar{\rho}\,\overline{\theta'u'u'} + \bar{\theta}\,\overline{\rho'u'u'} + \overline{\rho'\theta'u'u'}\,)$$

$$+ \frac{1}{r}\frac{\partial}{\partial r}\{r(\bar{\rho}\bar{\theta}\,\bar{u}\bar{v} + \bar{u}\,\bar{v}\overline{\rho'\theta'} + \bar{\rho}\bar{v}\,\overline{\theta'u'} + \bar{\rho}\bar{u}\,\overline{\theta'v'} + \bar{\theta}\,\bar{u}\,\overline{\rho'v'} +$$

$$\bar{\theta}\,\bar{v}\,\overline{\rho'u'} + \bar{\rho}\bar{\theta}\,\overline{u'v'} + \bar{\rho}\,\overline{\theta'u'v'} + \bar{\theta}\,\overline{\rho'u'v'} + \bar{u}\,\overline{\rho'\theta'v'} +$$

$$\bar{v}\,\overline{\rho'\theta'u'} + \overline{\rho'\theta'u'v'})\} = -\,\bar{\theta}\,\frac{\partial\bar{P}}{\partial x} - \overline{\theta'\,\frac{\partial P'}{\partial x}}$$

$$-\frac{\partial}{\partial x}(\bar{\theta}\,\bar{\tau}_{xx} + \overline{\theta'\tau'_{xx}}) - \frac{1}{r}\frac{\partial}{\partial r}\{r\,(\bar{\theta}\,\bar{\tau}_{rx} + \overline{\theta'\tau'_{rx}})\} + \bar{S}_{u,d} \qquad (3.15)$$

Radial Momentum

$$\frac{\partial}{\partial t}\left(\bar{\rho}\bar{\theta}\bar{v} + \bar{\rho}\,\overline{\theta'v'} + \bar{\theta}\,\overline{\rho'v'} + \bar{v}\,\overline{\rho'\theta'} + \overline{\rho'\theta'v'}\right)$$

$$+ \frac{\partial}{\partial x}\left(\bar{\rho}\bar{\theta}\bar{u}\bar{v} + \bar{u}\bar{v}\,\overline{\rho'\theta'} + \bar{\rho}\bar{v}\,\overline{\theta'u'} + \bar{\rho}\bar{u}\,\overline{\theta'v'} + \bar{\theta}\bar{u}\,\overline{\rho'v'} +\right.$$

$$\bar{\theta}\bar{v}\,\overline{\rho'u'} + \bar{\rho}\bar{\theta}\,\overline{u'v'} + \bar{\rho}\,\overline{\theta'u'v'} + \bar{\theta}\,\overline{\rho'u'v'} + \bar{u}\,\overline{\rho'\theta'v'} +$$

$$\left.\bar{v}\,\overline{\rho'\theta'u'} + \overline{\rho'\theta'u'v'}\right) + \frac{1}{r}\frac{\partial}{\partial r}\{r(\bar{\rho}\bar{\theta}\bar{v}\bar{v} + 2\bar{\rho}\bar{v}\,\overline{\theta'v'} +$$

$$2\bar{\theta}\bar{v}\,\overline{\rho'v'} + \bar{v}\bar{v}\,\overline{\rho'\theta'} + \bar{\rho}\bar{\theta}\,\overline{v'v'} + 2\bar{v}\,\overline{\rho'\theta'v'} +$$

$$\bar{\rho}\,\overline{\theta'v'v'} + \bar{\theta}\,\overline{\rho'v'v'} + \overline{\rho'\theta'v'v'})\} =$$

$$-\bar{\theta}\frac{\partial\bar{P}}{\partial r} - \overline{\theta'\frac{\partial P'}{\partial r}} - \frac{\partial}{\partial x}(\bar{\theta}\,\bar{\tau}_{xr} + \overline{\theta'\tau'_{xr}})$$

$$-\frac{1}{r}\frac{\partial}{\partial r}\{r(\bar{\theta}\,\bar{\tau}_{rr} + \overline{\theta'\tau'_{rr}})\} + \bar{S}_{v,d} \qquad (3.16)$$

Energy Equation

If the fluctuations of the molecular viscosity, thermal conductivity and specific heat are ignored, this runs

$$\frac{\partial}{\partial t}(\bar{\rho}\bar{\theta}\bar{h} + \bar{\rho}\,\overline{\theta'h'} + \bar{\theta}\,\overline{\rho'h'} + \bar{h}\,\overline{\rho'\theta'} + \overline{\rho'\theta'h'})$$

$$+ \frac{\partial}{\partial x}(\bar{\rho}\bar{\theta}\bar{u}\bar{h} + \bar{u}\bar{h}\,\overline{\rho'\theta'} + \bar{\rho}\bar{h}\,\overline{\theta'u'} + \bar{\rho}\bar{u}\,\overline{\theta'h'} + \bar{\theta}\bar{u}\,\overline{\rho'h'} +$$

$$\bar{\theta}\bar{h}\,\overline{\rho'u'} + \bar{\rho}\bar{\theta}\,\overline{u'h'} + \bar{\rho}\,\overline{\theta'u'h'} + \bar{\theta}\,\overline{\rho'u'h'} + \bar{u}\,\overline{\rho'\theta'h'} +$$

$$\bar{h}\,\overline{\rho'\theta'u'} + \overline{\rho'\theta'u'h'}) + \frac{1}{r}\frac{\partial}{\partial r}\,[r(\bar{\rho}\bar{\theta}\bar{v}\bar{h} + \bar{v}\bar{h}\,\overline{\rho'\theta'} +$$

$$\bar{\rho}\bar{h}\,\overline{\theta'v'} + \bar{\rho}\bar{v}\,\overline{\theta'h'} + \bar{\theta}\bar{v}\,\overline{\rho'h'} + \bar{\theta}\bar{h}\,\overline{\rho'v'} + \bar{\rho}\bar{\theta}\,\overline{v'h'} +$$

$$\bar{\rho}\,\overline{\theta'v'h'} + \bar{\theta}\,\overline{\rho'v'h'} + \bar{v}\,\overline{\rho'\theta'h'} + \bar{h}\,\overline{\rho'\theta'v'} + \overline{\rho'\theta'v'h'})] =$$

$$\frac{\partial}{\partial x}\left[\frac{\bar{\kappa}}{\bar{c}_p}\left(\bar{\theta}\,\frac{\partial\bar{h}}{\partial x} + \overline{\theta'\,\frac{\partial h'}{\partial x}}\right)\right] + \frac{1}{r}\frac{\partial}{\partial r}\left[r\,\frac{\bar{\kappa}}{\bar{c}_p}\left(\bar{\theta}\,\frac{\partial\bar{h}}{\partial r} + \overline{\theta'\,\frac{\partial h'}{\partial r}}\right)\right] +$$

$$\bar{\theta}\,\frac{\partial\bar{p}}{\partial t} + \overline{\theta'\,\frac{\partial p'}{\partial t}} + \frac{\partial}{\partial x}\left\{\left(\bar{\mu} + \frac{\bar{\mu}}{\bar{c}_p}\right)\left[\bar{\theta}\,\frac{\partial}{\partial x}\left(\Sigma\,\frac{\vec{\bar{u}}^{\,2}}{2} + k\right) +\right.\right.$$

$$\left.\left.\theta'\,\frac{\partial}{\partial x}\left(\Sigma\,\frac{\vec{\bar{u}}^{\,2}}{2} + k\right)\right]\right\} + \frac{1}{r}\frac{\partial}{\partial r}\left\{r\left(\bar{\mu} + \frac{\bar{\kappa}}{\bar{c}_p}\right)\left[\bar{\theta}\,\frac{\partial}{\partial r}\left(\Sigma\,\frac{\vec{\bar{u}}^{\,2}}{2} + k\right) +\right.\right.$$

$$\left.\left.\theta'\,\frac{\partial}{\partial r}\left(\Sigma\,\frac{\vec{\bar{u}}^{\,2}}{2} + k\right)\right]\right\} + \bar{S}_{h,d} \qquad (3.17)$$

where $\vec{\bar{u}}$ is the velocity vector and $k = \Sigma\,\frac{\overline{u'^2}}{2}$ is the turbulent kinetic energy.

Fuel Vapour Mass Fraction Equation

$$\frac{\partial}{\partial t}(\overline{\rho\theta f} + \overline{\rho}\ \overline{\theta' f'} + \overline{\theta}\ \overline{\rho' f'} + \overline{f}\ \overline{\rho'\theta'} + \overline{\rho'\theta' f'})$$

$$+ \frac{\partial}{\partial x}(\overline{\rho\theta u f} + \overline{uf}\ \overline{\rho'\theta'} + \overline{\rho f}\ \overline{\theta' u'} + \overline{\rho u}\ \overline{\theta' f'} + \overline{\theta u}\ \overline{\rho' f'} +$$

$$\overline{\theta f}\ \overline{\rho' u'} + \overline{\rho\theta}\ \overline{u' f'} + \overline{\rho}\ \overline{\theta' u' f'} + \overline{\theta}\ \overline{\rho' u' f'} + \overline{u}\ \overline{\rho'\theta' f'} +$$

$$\overline{f}\ \overline{\rho'\theta' u'} + \overline{\rho'\theta' u' f'}) + \frac{1}{r}\frac{\partial}{\partial r}\left[r(\overline{\rho\theta v f} + \overline{vf}\ \overline{\rho'\theta'} + \right.$$

$$\overline{\rho f}\ \overline{\theta' v'} + \overline{\rho v}\ \overline{\theta' f'} + \overline{\theta v}\ \overline{\rho' f'} + \overline{\theta f}\ \overline{\rho' v'} + \overline{\rho\theta}\ \overline{v' f'} +$$

$$\left.\overline{\rho}\ \overline{\theta' v' f'} + \overline{\theta}\ \overline{\rho' v' f'} + \overline{v}\ \overline{\rho'\theta' f'} + \overline{f}\ \overline{\rho'\theta' v'} + \overline{\rho'\theta' v' f'})\right] =$$

$$\frac{\partial}{\partial x}\left[\overline{\mu}(\overline{\theta}\frac{\partial \overline{f}}{\partial x} + \theta'\frac{\partial f'}{\partial x})\right] + \frac{1}{r}\frac{\partial}{\partial r}\left[r\overline{\mu}(\overline{\theta}\frac{\partial \overline{f}}{\partial r} + \theta'\frac{\partial f'}{\partial r})\right]$$

$$+ \overline{S}_{m,d} \qquad (3.18)$$

3.3.3 Favre Averaging Procedure

The ensemble averaging approach used above results in double and triple correlations involving density and velocity fluctuations e.g. $\overline{\rho' u'}$ and $\overline{\rho' u' \phi'}$ etc., as can be seen in equations (3.14) to (3.18). These terms could be significant in reacting (Libby et al (1977)) and non-reacting flows (Bradshaw et al (1971)) and the modelling of these terms is difficult and uncertain (Sayed (1977)).

Favre (1969) introduced an alternative method of averaging usually called 'density-weighted averaging' which eliminates the forementioned correlations and therefore, results in considerably simpler equations (Libby (1973), Bilger (1975), Pope (1976) and Jones (1980)).

The density-weighted averaging procedure involves decomposition of the instantaneous variables thus,

$$\begin{aligned} u &= \tilde{u} + u'' \\ v &= \tilde{v} + v'' \\ \theta &= \tilde{\theta} + \theta'' \\ \phi &= \tilde{\phi} + \phi'' \end{aligned} \tag{3.19}$$

where $\tilde{u}$, $\tilde{v}$, $\tilde{\theta}$ and $\tilde{\phi}$ are the density-weighted average values defined by

$$\tilde{\phi}(\underline{x}_o, t) = \frac{1}{\overline{\rho}} \left[\lim_{m \to \infty} \frac{1}{2m+1} \sum_{n=-m}^{n=m} \rho(\underline{x}_o, nt_o + t) \phi(\underline{x}_o, nt_o + t) \right] \tag{3.20}$$

and $\overline{\rho}$ is the ensemble-average density.

Comparison of equation (3.13) and (3.20) yields the relation between $\tilde{\phi}$ and the ensemble-average $\overline{\phi}$ and the fluctuation ϕ' as

$$\tilde{\phi} = \overline{\phi} + \frac{\overline{\rho'\phi'}}{\overline{\rho}} \tag{3.21}$$

and also it can be shown that

$$\phi'' = \phi' - \frac{\overline{\rho'\phi'}}{\overline{\rho}} \tag{3.22}$$

It should be noted that

$$\overline{\rho u''} = \overline{\rho v''} = \overline{\rho\theta''} = \overline{\rho\phi''} = 0$$

and $\quad \overline{u''} \neq 0$

$$\overline{\phi''} \neq 0$$

The Favre averaged forms of the governing equations, after noting that density weighting is not to be applied to either the pressure or density (see Jones (1980)), can be written as:

Continuity

$$\frac{\partial}{\partial t}(\overline{\rho}\tilde{\theta}) + \frac{\partial}{\partial x}(\overline{\rho}\tilde{\theta}\tilde{u} + \overline{\rho}\,\widetilde{\theta''u''})$$

$$+ \frac{1}{r}\frac{\partial}{\partial r}\left|r(\overline{\rho}\,\tilde{\theta}\tilde{v} + \overline{\rho}\,\widetilde{\theta''v''})\right| = \overline{S}_{m,d} \tag{3.23}$$

Axial momentum

$$\frac{\partial}{\partial t}(\bar{\rho}\tilde{\theta}\tilde{u} + \bar{\rho}\,\overline{\theta''\tilde{u}''}) + \frac{\partial}{\partial x}(\bar{\rho}\,\tilde{\theta}\tilde{u}\tilde{u} + \bar{\rho}\,\tilde{\theta}\,\overline{u''\tilde{u}''}$$

$$+ 2\bar{\rho}\tilde{u}\,\overline{\theta''\tilde{u}''} + \bar{\rho}\,\overline{\theta''u''\tilde{u}''}) + \frac{1}{r}\frac{\partial}{\partial r}\left[r(\bar{\rho}\tilde{\theta}\tilde{u}\tilde{v}\right.$$

$$\left. + \bar{\rho}\,\tilde{\theta}\,\overline{u''\tilde{v}''} + \bar{\rho}\tilde{u}\,\overline{\theta''\tilde{v}''} + \bar{\rho}\,\tilde{v}\,\overline{\theta''\tilde{u}''} + \bar{\rho}\,\overline{\theta''u''\tilde{v}''})\right]$$

$$= -\bar{\theta}\frac{\partial \bar{P}}{\partial x} - \overline{\theta'\frac{\partial P'}{\partial x}} - \frac{\partial}{\partial x}(\bar{\theta}\,\bar{\tau}_{xx} + \overline{\theta'\tau'_{xx}}) -$$

$$\frac{1}{r}\frac{\partial}{\partial r}\left[r(\bar{\theta}\,\bar{\tau}_{rx} + \overline{\theta'\tau'_{rx}})\right] + \bar{S}_{u,d} \qquad (3.24)$$

Radial momentum

$$\frac{\partial}{\partial t}(\bar{\rho}\,\tilde{\theta}\tilde{v} + \bar{\rho}\,\overline{\theta''\tilde{v}''}) + \frac{\partial}{\partial x}(\bar{\rho}\,\tilde{\theta}\,\tilde{u}\tilde{v} + \bar{\rho}\,\tilde{\theta}\,\overline{u''\tilde{v}''}$$

$$+ \bar{\rho}\tilde{u}\,\overline{\theta''\tilde{v}''} + \bar{\rho}\,\tilde{v}\,\overline{\theta''\tilde{u}''} + \bar{\rho}\,\overline{\theta''u''\tilde{v}''}) + \frac{1}{r}\frac{\partial}{\partial r}\left[r(\bar{\rho}\,\tilde{\theta}\tilde{v}\tilde{v}\right.$$

$$\left. + \bar{\rho}\,\tilde{\theta}\,\overline{v''\tilde{v}''} + 2\bar{\rho}\,\tilde{v}\,\overline{\theta''\tilde{v}''} + \bar{\rho}\,\overline{\theta''v''\tilde{v}''})\right] = -\bar{\theta}\,\frac{\partial \bar{P}}{\partial x} - \theta'\,\frac{\partial P'}{\partial x}$$

$$- \frac{\partial}{\partial x}(\bar{\theta}\,\bar{\tau}_{xr} + \overline{\theta'\tau'_{xr}}) - \frac{1}{r}\frac{\partial}{\partial r}\left[r(\bar{\theta}\,\bar{\tau}_{rr} + \overline{\theta'\tau'_{rr}})\right]$$

$$+ \bar{S}_{v,d} \qquad (3.25)$$

Energy

$$\frac{\partial}{\partial t}(\bar{\rho}\tilde{\theta}\tilde{h} + \bar{\rho}\,\overline{\theta'''\tilde{h}'''}) + \frac{\partial}{\partial x}(\bar{\rho}\tilde{\theta}\tilde{u}\tilde{h} + \bar{\rho}\tilde{\theta}\,\overline{u'''\tilde{h}'''} + \bar{\rho}\tilde{u}\,\overline{\theta'''\tilde{h}'''}$$

$$+ \bar{\rho}\tilde{h}\,\overline{\theta'''\tilde{u}'''} + \bar{\rho}\,\overline{\theta'''\tilde{u}'''\tilde{h}'''}) + \frac{1}{r}\frac{\partial}{\partial r}\,[r(\bar{\rho}\tilde{\theta}\tilde{v}\tilde{h}$$

$$+ \bar{\rho}\tilde{\theta}\,\overline{v'''\tilde{h}'''} + \bar{\rho}\tilde{v}\,\overline{\theta'''\tilde{h}'''} + \bar{\rho}\tilde{h}\,\overline{\theta'''\tilde{v}'''} + \bar{\rho}\,\overline{\theta'''\tilde{v}'''\tilde{h}'''})]$$

$$= \frac{\partial}{\partial x}\{\frac{\bar{\kappa}}{\bar{c}_p}(\bar{\theta}\frac{\partial\bar{h}}{\partial x} + \theta'\frac{\partial h'}{\partial x})\} + \frac{1}{r}\frac{\partial}{\partial r}\{r\frac{\bar{\kappa}}{\bar{c}_p}(\bar{\theta}\frac{\partial\bar{h}}{\partial r} + \theta'\frac{\partial h'}{\partial r})\} +$$

$$\bar{\theta}\frac{\partial\bar{p}}{\partial t} + \overline{\theta'\frac{\partial p'}{\partial t}} + \frac{\partial}{\partial x}\{(\bar{\mu} + \frac{\bar{\kappa}}{\bar{c}_p})\,[\bar{\theta}\frac{\partial}{\partial x}(\Sigma\frac{\bar{u}_i^2}{2} + k) +$$

$$\theta'\frac{\partial}{\partial x}(\Sigma\frac{\bar{u}_i^2}{2} + k)]\} + \frac{1}{r}\frac{\partial}{\partial r}\{r(\bar{\mu} + \frac{\bar{\kappa}}{\bar{c}_p})\,[\bar{\theta}\frac{\partial}{\partial r}(\Sigma\frac{\bar{u}_i^2}{2} + k) +$$

$$\theta'\frac{\partial}{\partial r}(\Sigma\frac{\bar{u}_i^2}{2} + k)]\} + \bar{S}_{h,d} \qquad (3.26)$$

Fuel Vapour Mass Fraction

$$\frac{\partial}{\partial t}(\bar{\rho}\tilde{\theta}\tilde{f} + \bar{\rho}\,\overline{\theta'''\tilde{f}'''}) + \frac{\partial}{\partial x}(\bar{\rho}\tilde{\theta}\tilde{u}\tilde{f} + \bar{\rho}\tilde{\theta}\,\overline{u'''\tilde{f}'''} + \bar{\rho}\tilde{u}\,\overline{\theta'''\tilde{f}'''}$$

$$+ \bar{\rho}\tilde{f}\,\overline{\theta'''\tilde{u}'''} + \bar{\rho}\,\overline{\theta'''\tilde{u}'''\tilde{f}'''}) + \frac{1}{r}\frac{\partial}{\partial r}\,[r(\bar{\rho}\tilde{\theta}\tilde{v}\tilde{f} + \bar{\rho}\tilde{\theta}\,\overline{v'''\tilde{f}'''} + \bar{\rho}\tilde{v}\,\overline{\theta'''\tilde{f}'''}$$

$$+ \bar{\rho}\tilde{f}\,\overline{\theta'''\tilde{v}'''} + \bar{\rho}\,\overline{\theta'''\tilde{v}'''\tilde{f}'''})] = \frac{\partial}{\partial x}\,[\bar{\mu}(\bar{\theta}\frac{\partial\bar{f}}{\partial x} + \overline{\theta'\frac{\partial f'}{\partial x}})] +$$

$$\frac{1}{r}\frac{\partial}{\partial r}\,[r\bar{\mu}(\bar{\theta}\frac{\partial\bar{f}}{\partial r} + \overline{\theta'\frac{\partial f'}{\partial r}})] + \bar{S}_{m,d} \qquad (3.27)$$

It should be noted that Favre averaging is applied only to terms containing density. Inspection shows that the Favre averaged forms are simpler than the ensemble averaged forms due to the elimination of the correlation involving density fluctuation as already mentioned. However, when comparison of calculations with the measurements is made, it should be known whether the measuring instrument records $\rho\phi$ or ϕ whose respective statistical averages are $\tilde{\phi}$ or $\overline{\phi}$. (Laser-Doppler and hot-wire anemometers measure unweighted variables while the pitot tube measures density-weighted variables, see Jones (1980)).

Nevertheless there are some grounds for selecting the ensemble-averaged forms of the equations. Firstly, the Favre average equations contain some unweighted averaged variables like $\overline{\tau}_{xx}$, $\overline{h}$ and $\overline{f}$; and the determination of these requires modelling of the density fluctuation correlations (c.f. equation (3.21)). Secondly, Favre averaging like ensemble averaging does not eliminate correlations involving fluctuations in the void fraction. These correlations could be significant but unfortunately there is no experimental or theoretical evidence of their magnitudes. There is also little experimental information about the importance of ρ'-containing correlations like $\overline{\rho' u'}$ and $\overline{\rho' \phi'}$ in multiphase flows. For these reasons, in the present study, the ensemble-averaged forms of the equations are used with the correlations involving density and void fraction fluctuations omitted, in the knowledge that their effects may be significant.

3.4 The Turbulence Model

3.4.1 Introduction

As can be seen, the process of ensemble averaging, gives rise to similar equations to those for the instantaneous quantities but with some extra terms involving fluctuating velocities e.g. $\overline{\rho}\,\overline{\theta}\ \overline{u'u'}$, $\overline{\rho}\,\overline{\theta}\ \overline{u'v'}$ and $\overline{\rho}\,\overline{\theta}\ \overline{u'\phi'}$. These terms, commonly interpreted as diffusional fluxes of momentum, energy etc. due to turbulent motion, play a significant role in all turbulent flows. In order to solve the ensemble-averaged equations therefore additional relations are needed connecting these unknown to calculable quantities. Unfortunately, there is no exact way of determining the magnitude of these terms; therefore, their effects must be approximated or 'modelled' and the process of formulating equations for the unknown correlations is termed 'turbulence modelling'. As has been stated earlier, modelling of correlations involving density fluctuations is hindered by the lack of measurements, hence their effects are neglected (as well as terms containing θ'). However, the turbulence model based on the characteristic of constant density flows has been used for the calculation of turbulent reacting flows (see for example Khalil et al (1975), Gosman et al (1976b), Salooja (1978), Megahed (1979), El Banhawy et al (1980) and Abbas et al (1981)).

3.4.2 Choice of the Turbulence Model

The determination of the turbulent fluxes constitutes the main problem in turbulent flow calculations. A possible approach to determining the values of the Reynolds stress $\bar{\rho}\,\overline{u_i' u_j'}$ and the turbulent fluxes $\bar{\rho}\,\overline{u_i' \phi'}$ is to represent them as the dependent variables in conservation equations. This can readily be achieved but with the consequence that higher order correlations will appear (see e.g. Harlow and Nakayama (1967), Lumley (1975) and Reynolds (1976)). The same approach can be taken again and the conservation equations written for the higher order correlations will contain a further higher order correlations. Closure approximations are therefore introduced to limit this approach and relate these higher order terms to lower order 'known' terms in order to produce a closed set of equations (Launder et al (1975)). This approach, known as 'Reynolds stress closure', requires for three-dimensional flows, the solution of at least seven differential equations to obtain values for $\bar{\rho}\,\overline{u_i' u_j'}$ terms.

Another approach which sometimes termed 'mean field closure' or 'effective viscosity' modelling relates the Reynolds stresses to the mean rate of strain through the Boussinesq (1877) equation:

$$-\bar{\rho}\,\bar{\theta}\,\overline{u_i' u_j'} = \bar{\theta}\,\mu_t \left[\frac{\partial \bar{u}_i}{\partial x_j} + \frac{\partial \bar{u}_j}{\partial x_i} - \frac{2}{3}\,\nabla.\vec{u}\,\delta_{ij}\right] - \frac{2}{3}\,\bar{\rho}\,\bar{\theta}\,k\,\delta_{ij} \qquad (3.28)$$

where i and j are the co-ordinate directions and δ_{ij} is the Kroneker delta = 1 if i = j and 0 if $i \neq j$.

The correlations of the velocities and scalar fluctuations ($\overline{\rho}\,\overline{\theta}\,\overline{u'\phi'}$) are analogously expressed in terms of gradients of average quantities (see Launder and Spalding (1972)) i.e.

$$-\overline{\rho}\,\overline{\theta}\,\overline{u_i'\phi'} = \frac{\theta\mu_t}{\sigma_\phi}\frac{\partial\overline{\phi}}{\partial x_i} \tag{3.29}$$

where μ_t is the turbulent viscosity and σ_ϕ is the Prandtl or Schmidt number (experimentally determined). The introduction of μ_t provides a framework for constructing a turbulence model. A convenient classification of 'effective viscosity' turbulence model uses the number of equations to be solved in addition to the continuity, momentum and scalar equations, i.e. zero, one and two equations models (Launder et al (1972) and Reynolds (1976)). These models relate the turbulent viscosity to known or calculable quantities as:

i. Zero-equation model:

The turbulent viscosity is determined through an algebraic expression which relates it to a prescribed turbulent length scale ℓ_t and a characteristic velocity scale $\ell_t(\partial u/\partial r)$ (Prandtl (1925)) i.e.:

$$\mu_t = \overline{\rho}\,\ell_t^2\left|\frac{\partial u}{\partial r}\right| \tag{3.30}$$

This model does not need any extra differential equation to solve turbulent flow, hence it is called a zero equation model.

ii. One-equation models

In this class, Prandtl (1945) has suggested that the velocity scale is well represented by the square root of the turbulent kinetic energy, $k(= \frac{1}{2}\Sigma\overline{u_i'^2})$. Substituting $k^{\frac{1}{2}}$ as the velocity scale in equation (3.30), thus:

$$\mu_t = \rho k^{\frac{1}{2}} \ell_t \tag{3.31}$$

ℓ_t is specified algebraically but k is determined from the solution of differential transport equation.

iii. Two-equation models

This more general and popular class of model, solves partial differential equations for the turbulent kinetic energy and a quantity ε related to ℓ_t. The turbulent energy dissipation rate ε is expressed (Jones and Launder (1972)) as:

$$\varepsilon = c_\mu k^{3/2}/\ell_t \tag{3.32}$$

where c_μ is an empirical coefficient, usually ascribed a constant value. Upon substitution in equation (3.31), the turbulent viscosity becomes:

$$\mu_t = c_\mu \rho k^2/\varepsilon \tag{3.33}$$

The conservation equations of the turbulent kinetic energy and its dissipation rate are given next.

3.4.3 Transport Equation for Turbulent Kinetic Energy

The equation for the turbulent kinetic energy k can be derived by subtracting the ensemble-averaged momentum equations (3.15) and (3.16) from their instantaneous counterpart equations expressed in terms of mean and fluctuating components after substituting the values of τ from equation (3.5), multiplying the resultant equations by u' and v' respectively, summing the two equations and averaging the final equation. Introducing the definition $k = \frac{1}{2}\overline{u_i'^2}$, the resulting equation will contain some new unknown (e.g. $\overline{u_i u_i}$, $\overline{\rho' u_j'}$) which must be modelled in terms of known or calculable quantities (details of the derivation and modelling of these unknown terms are given by Watkins (1977)). The final form of the k equation is then given by

$$\frac{\partial}{\partial t}(\bar{\theta}\bar{\rho}k) + \frac{\partial}{\partial x}(\bar{\theta}\bar{\rho}\bar{u}k) + \frac{1}{r}\frac{\partial}{\partial r}(r\bar{\rho}\bar{\theta}\bar{v}k)$$

$$= \frac{\partial}{\partial x}(\theta \frac{\mu_{eff}}{\sigma_k}\frac{\partial k}{\partial x}) + \frac{1}{r}\frac{\partial}{\partial r}(\theta r \frac{\mu_{eff}}{\sigma_k}\frac{\partial k}{\partial r})$$

$$+ \bar{\theta}G_t - \bar{\theta}\bar{\rho}\varepsilon + \mathfrak{D}_k + \mathfrak{L}_k \qquad (3.34)$$

where the effective viscosity μ_{eff} is the sum of the laminar and turbulent viscosities i.e.

$$\mu_{eff} = \mu + \mu_t \qquad (3.35)$$

and σ_k is the turbulent Prandtl number, and the generation rate of the turbulent energy G_t is given by

$$G_t = \mu_t \{2 [(\frac{\partial \bar{u}}{\partial x})^2 + (\frac{\partial \bar{v}}{\partial r})^2 + (\frac{\bar{v}}{r})^2] + (\frac{\partial \bar{u}}{\partial r} + \frac{\partial \bar{v}}{\partial x})^2\}$$

$$- \frac{2}{3} \nabla.\vec{u}(\mu_t \nabla.\vec{u} + \bar{\rho}k) \qquad (3.36)$$

The turbulent kinetic energy equation (3.34) contains two extra terms $\mathfrak{D}_k$ and $\mathfrak{L}_k$. The first one comprises a large number of terms involving density and void fraction fluctuations. As already noted earlier in connection with the equations of the mean motion, there is no guidance currently available on how to model such effects: they are neglected here as well.

The last term $\mathfrak{L}_k$ (and a similar term in ε equation) has been added by Buckingham et al (1981) to account for the effects of the droplets on the turbulence properties. These effects are mainly in the form of added dissipation, i.e.

$$\mathfrak{L}_k = a_1 G_t - a_2 \bar{\rho}\varepsilon + a_3 [(\bar{u}_{d,i} - \bar{u}_i)\overline{\theta' u_i'} + \overline{(u_{d,i}' - u_i')u_i'\theta}$$

$$+ \overline{u_i'\theta'(u_{d,i}' - \bar{u}_i)}] \qquad (3.37)$$

where the (empirical) coefficients a_1, a_2 and a_3 are required to vanish when $\theta = 1$; and $u_{d,i}'$ is the droplet velocity fluctuation. This modified k-ε model was applied to flows containing sparse small solid particles (see Buckingham et al (1981)): the results suggested that the particles tend to damp turbulent motions primarily due to inertial effects. The computations were not compared directly with experiments and more extensive evaluation of this model will be required in order to adequately establish its validity. For this reason the term $\mathfrak{L}_k$ is also ignored in the present study.

3.4.4 Dissipation Equation

An exact equation for ε can be derived (following Harlow and Nakayama (1967)) by taking the derivative of the equation for the fluctuating velocity u' with respect to x_ℓ, multiplying the resulting equation by $\mu \frac{\partial u_i'}{\partial x_\ell}$ and averaging (details of derivation are given by Watkins (1977)). After modelling the unknown terms generated, the final form is:

$$\frac{\partial}{\partial t}(\overline{\rho\theta}\varepsilon) + \frac{\partial}{\partial x}(\overline{\rho\theta u}\varepsilon) + \frac{1}{r}\frac{\partial}{\partial r}(r\overline{\rho\theta v}\varepsilon)$$

$$= \frac{\partial}{\partial x}(\overline{\theta}\frac{\mu_{eff}}{\sigma_\varepsilon}\frac{\partial \varepsilon}{\partial x}) + \frac{1}{r}\frac{\partial}{\partial r}(r\overline{\theta}\frac{\mu_{eff}}{\sigma_\varepsilon}\frac{\partial \varepsilon}{\partial r})$$

$$+ c_1\frac{\overline{\theta}}{k}G_t + c_2\overline{\theta\rho}\frac{\varepsilon^2}{k} - \overline{\rho\theta}\varepsilon\nabla.\vec{u} + \mathfrak{D}_\varepsilon + \mathfrak{Y}_\varepsilon \qquad (3.38)$$

where c_1, c_2, σ_k and σ_ε are empirical coefficients whose values are given in table (3.1) and are taken from Gosman and Pun (1974).

As with the k equation, $\mathfrak{D}_\varepsilon$ contains a large number of terms involving density and void fraction fluctuations which are neglected in the present study.

The last term $\mathfrak{Y}_\varepsilon$ added by Buckingham et al (1981) to account for the effects of the droplets on the turbulence structure of the gas phase, is

$$\mathfrak{Y}_\varepsilon = a_1\overline{\rho}G_t + a_2\overline{\rho}\frac{\varepsilon^2}{k} + a_3\overline{(u_{d,i}' - u_i')u_i'\theta} \qquad (3.39)$$

This term is also ignored in the present study for the reasons mentioned earlier.

3.5 Modelled Form of the General Transport Equation

The modelling of the Reynolds stress terms in the ensemble-averaged momentum equations has been indicated in section (3.4) (equations (3.28) and (3.29)). The only remaining terms to be modelled are of the form $\overline{\rho\theta}\ \rho\overline{u_i'h'}$ which appear in the energy equation. Following Launder and Spalding (1973) and others, these terms are modelled as a diffusion process, typically:

$$- \overline{\rho\theta}\ \overline{u_i'h_i'} = \overline{\theta}\,\frac{\mu_t}{\sigma}\,\frac{\partial\overline{h}}{\partial x_i} = \overline{\theta}\mu_t\{\frac{1}{\sigma_h}\frac{\partial\overline{h}}{\partial x_i} + (1 - \frac{1}{\sigma_h})\frac{\partial}{\partial x_i}(\Sigma\,\frac{\overline{u_i}^2}{2})$$

$$+ (\frac{1}{\sigma_k} - \frac{1}{\sigma_h})\frac{\partial k}{\partial x_i}\} \qquad (3.40)$$

where

$$\overline{h} = \overline{c_p T} + \frac{\Sigma\overline{u_i}^2}{2} + k \qquad (3.41)$$

The ensemble-averaged forms of the equations have the same structure and can all be expressed by the following general transport equation for any variable ϕ

$$\frac{\partial}{\partial t}(\rho\theta\phi) + \frac{\partial}{\partial x}(\rho\theta u\phi) + \frac{1}{r}\frac{\partial}{\partial r}(r\rho\theta v\phi)$$

$$= \frac{\partial}{\partial x}(\theta\Gamma_\phi\frac{\partial\phi}{\partial k}) + \frac{1}{r}\frac{\partial}{\partial r}(\theta r\Gamma_\phi\frac{\partial\phi}{\partial r}) + S_\phi + S_{\phi,d} \qquad (3.42)$$

where ϕ stands for u, v, h, f, k, ε (the overbar has been omitted) or in the case of mass conservation, unity. The exchange coefficient Γ_ϕ is given by:

$$\Gamma_\phi = \frac{\mu_{eff}}{\sigma_\phi} \tag{3.43}$$

The definitions of Γ_ϕ and the associated source term, S_ϕ, are given in table (3.2).

3.6 Moving Co-ordinate Frame Transformation

The equations assembled and modelled so far are for an Eulerian co-ordinate frame. For flows with moving boundaries, transformation of the Eulerian co-ordinate system to a more flexible system that moves with the boundaries is required. As the transient gas jets and the liquid sprays of the present study penetrate further with time, then using a fixed grid system will be inefficient in computer time and storage because the jet or the spray occupies a small proportion of the total flow domain in the early stages of injection. Therefore, a solution domain which expands with expansion of the jet is used for the calculation of the transient laminar and turbulent isothermal gas jets. A fixed grid system is employed for spray calculations because there is a restriction on the minimum size of the cells as will be discussed in chapter 5.

Transformation formulae have been derived by Watkins (1973) for the case of an internal combustion engine with a flat topped piston, while Johns (1980) have derived the transformation formulae

for a translating and expanding/contracting co-ordinate frame to accommodate with the complex shape of the piston bowls. A simplified form of the derivation employed by Johns will be used here.

New independent variables x' and r' are introduced which are functions of the Eulerian co-ordinate frame i.e.

$$x' = f_1(x, r, t)$$

$$r' = f_2(x, r, t) \tag{3.44}$$

From differential calculus:

$$dx' = \frac{\partial x'}{\partial x} dx + \frac{\partial x'}{\partial r} dr + \frac{\partial x'}{\partial t} dt$$

$$dr' = \frac{\partial r'}{\partial x} dx + \frac{\partial r'}{\partial r} dr + \frac{\partial r'}{\partial t} dt \tag{3.45}$$

A variable ϕ can be expressed in either co-ordinate system as:

$$\phi(x, r, t) = \phi(x', r', t) \tag{3.46}$$

differentiation of this equation yields:

$$\frac{\partial \phi}{\partial x} dx + \frac{\partial \phi}{\partial r} dr + \frac{\partial \phi}{\partial t} dt = \frac{\partial \phi}{\partial x'} dx' + \frac{\partial \phi}{\partial r'} dr$$

$$+ \frac{\partial \phi}{\partial t} dt \tag{3.47}$$

Substituting from equation (3.45) yields:

$$\frac{\partial\phi}{\partial x}\,dx + \frac{\partial\phi}{\partial r}\,dr + \frac{\partial\phi}{\partial t}\,dt = \frac{\partial\phi}{\partial x'}\frac{\partial x'}{\partial x}\,dx + \frac{\partial\phi}{\partial x'}\frac{\partial x'}{\partial r}\,dr$$

$$+ \frac{\partial\phi}{\partial x}\frac{\partial x'}{\partial t}\,dt + \frac{\partial\phi}{\partial r'}\frac{\partial r'}{\partial x}\,dx + \frac{\partial\phi}{\partial r'}\frac{\partial r'}{\partial r}\,dr$$

$$+ \frac{\partial\phi}{\partial r'}\frac{\partial r'}{\partial t}\,dt + \frac{\partial\phi}{\partial t}\,dt \qquad (3.48)$$

By inspection, the general transformation formulae between the two frames are as follows:

$$\frac{\partial\phi}{\partial x} = \frac{\partial\phi}{\partial x'}\frac{\partial x'}{\partial x} + \frac{\partial\phi}{\partial r'}\frac{\partial r'}{\partial x}$$

$$\frac{\partial\phi}{\partial r} = \frac{\partial\phi}{\partial x'}\frac{\partial x'}{\partial r} + \frac{\partial\phi}{\partial r'}\frac{\partial r'}{\partial r} \qquad (3.49)$$

$$\frac{\partial\phi}{\partial t} = \frac{\partial\phi}{\partial x'}\frac{\partial x'}{\partial t} + \frac{\partial\phi}{\partial r'}\frac{\partial r'}{\partial t} + \frac{\partial\phi}{\partial t}$$

The dependence functions f_1 and f_2 of equation (3.44) are here specified as:

$$x' = f_1 = \frac{x}{\xi_1}$$

$$r' = f_2 = \frac{r}{\xi_2} \qquad (3.50)$$

where ξ_1 and ξ_2 are time-varying distances (here taken as the jet penetrations in axial and radial directions respectively). Hence, the solution domain, defined in the new (x', r', t) co-ordinate frame, is always bounded by the injected jet.

Differentiation of equation (3.50) with respect to x, r and t yields:

$$\frac{\partial x'}{\partial x} = \frac{1}{\xi_1}$$

$$\frac{\partial x'}{\partial r} = 0$$

$$\frac{\partial x'}{\partial t} = -\frac{x}{\xi_1^2}\frac{\partial \xi_1}{\partial t} = -\frac{x'}{\xi_1}\frac{\partial \xi_1}{\partial t} \qquad (3.51)$$

$$\frac{\partial r'}{\partial x} = 0$$

$$\frac{\partial r'}{\partial r} = \frac{1}{\xi_2}$$

$$\frac{\partial r'}{\partial t} = -\frac{r}{\xi_2^2}\frac{\partial \xi_2}{\partial t} = -\frac{r'}{\xi_2}\frac{\partial \xi_2}{\partial t}$$

Insertion of the above expressions into the general transformation formulae (3.49) yields the final form of these formulae for that particular transformation (equation (3.50)) as:

$$\frac{\partial \phi}{\partial x} = \frac{1}{\xi_1}\frac{\partial \phi}{\partial x'}$$

$$\frac{\partial \phi}{\partial r} = \frac{1}{\xi_2}\frac{\partial \phi}{\partial r'} \qquad (3.52)$$

$$\frac{\partial \phi}{\partial t} = \frac{\partial \phi}{\partial t} - \frac{x'}{\xi_1}\frac{\partial \xi_1}{\partial t}\frac{\partial \phi}{\partial x'} - \frac{r'}{\xi_2}\frac{\partial \xi_2}{\partial t}\frac{\partial \phi}{\partial r'}$$

Application of these relations to the general transport equation (3.42) produces:

$$\frac{\partial}{\partial t}(\rho\theta\phi) - \frac{x'}{\xi_1}\frac{\partial \xi_1}{\partial t}\frac{\partial}{\partial x'}(\rho\theta\phi) - \frac{r'}{\xi_2}\frac{\partial \xi_2}{\partial t}\frac{\partial}{\partial r'}(\rho\theta\phi)$$

$$+ \frac{1}{\xi_1}\frac{\partial}{\partial x'}(\rho\theta u\phi) + \frac{1}{(\xi_2 r')}\frac{1}{\xi_2}\frac{\partial}{\partial r'}\left[(\xi_2 r')\rho\theta v\phi\right]$$

$$= \frac{1}{\xi_1}\frac{\partial}{\partial x'}\left[\theta\Gamma_\phi \frac{\partial \phi}{\xi_1 \partial x'}\right] + \frac{1}{(\xi_2 r')}\frac{1}{\xi_2}\frac{\partial}{\partial r'}\left[(\xi_2 r')\theta\Gamma_\phi \frac{\partial \phi}{\xi_2 \partial r'}\right]$$

$$+ S'_\phi + S_{\phi,d} \qquad (3.53)$$

where S'_ϕ is also transformed. With some further manipulation, the transformed equation takes the form:

$$\frac{1}{\xi_1\xi_2(\xi_2 r')}\frac{\partial}{\partial t}\left[\xi_1\xi_2(\xi_2 r')\rho\theta\phi\right] + \frac{\partial}{\xi_1 \partial x'}\left[\rho\theta\phi(u - x'\frac{\partial \xi_1}{\partial t})\right]$$

$$+ \frac{1}{\xi_2 r'}\frac{1}{\xi_2}\frac{\partial}{\partial r'}\left[(\xi_2 r')\rho\theta\phi(v - r'\frac{\partial \xi_2}{\partial t})\right]$$

$$- \frac{1}{\xi_1}\frac{\partial}{\partial x'}\left[\theta\Gamma_\phi \frac{\partial \phi}{\xi_1 \partial x'}\right] - \frac{1}{\xi_2 r'}\frac{1}{\xi_2 \partial r'}\left[(\xi_2 r')\,\phi\Gamma_\phi \frac{\partial \phi}{\xi_2 \partial r'}\right]$$

$$= S'_\phi + S_{\phi,d} \qquad (3.54)$$

The quantities $x'\frac{\partial \xi_1}{\partial t}$ and $r'\frac{\partial \xi_2}{\partial t}$ are the local co-ordinate frame velocities in direction x' and r' respectively. Hence, by dropping the primes, the above equation can be written more compactly as:

$$\frac{1}{\xi_1\xi_2\,(\xi_2 r)}\left\{\frac{\partial}{\partial t}\left[\xi_1\xi_2(\xi_2 r)\,\rho\theta\phi\right] + \frac{\partial}{\partial x}\left[\xi_2(\xi_2 r)\rho\theta u_r\phi\right]\right.$$

$$+\frac{\partial}{\partial r}\left[\xi_1(\xi_2 r)\,\rho\theta v_r\theta\right] - \frac{\partial}{\partial x}\left[\xi_2(\xi_2 r)\theta\Gamma_\phi\,\frac{\partial\phi}{\xi_1\partial x}\right]$$

$$\left.-\frac{\partial}{\partial r}\left[\xi_1\xi_2 r\,\theta\Gamma_\phi\,\frac{\partial\phi}{\xi_2\partial r}\right]\right\} = S_\phi + S_{\phi,d} \qquad (3.55)$$

where $u_r = u - \xi_1\dfrac{\partial\xi_1}{\partial t}$

$$v_r = v - \xi_2\frac{\partial\xi_2}{\partial t} \qquad (3.56)$$

The transformed source terms for each variable are given in table (3.3).

3.7 Droplet-Phase Equations

a. Introduction

Spray vaporization and combustion studies are of primary importance in predicting and improving the performance of systems utilizing spray injection. Jet engines, industrial furnaces and diesel engines are typical examples of these systems. The introduction of fuel into a combustion chamber (either as a prevaporized gas often diluted with air or in liquid form) is the

key step in the combustion process since its results determine the overall combustion rate, fuel efficiency and emission of chemical pollutants, therefore an accurate prediction of the spray behaviour is necessary.

The approach which is employed here to mathematically model the liquid-phase is identified as 'discrete droplet model'. In this model, the spray is represented by discrete computational parcels. Each parcel represents a group of droplets possessing the same size, temperature, velocity, etc. The trajectories of the computational parcels and their masses, velocities and temperatures are obtained from the Lagrangian conservation equations of mass, momentum and energy for each parcel (Crowe et al (1977), Crowe (1978), Gosman et al (1980a),Gosman et al (1982), Dukowizc (1980) and O'Rourke (1981)). The limitations in the above model constitute the topic of the next subsection.

b. Model Assumptions

The various assumptions included in the spray model of the present study are:

1. The spray is considered to be fully atomized and secondary droplet break up is assumed to take place. Droplet break-up occurs whenever the Weber number exceeds a critical value. The Weber number is defined as the ratio of the inertia body force to the surface tension force and is given by:

$$We = \frac{\rho D_d V_{rel}^2}{\sigma} \qquad (3.57)$$

where ρ is the gas density, D_d is the droplet diameter, V_{rel} is the relative speed = $|u - u_d|$ and σ is the surface tension. Henein (1976) reports that the critical Weber number associated with the secondary droplet break-up is 15. In the present study, for the maximum droplet diameter of 50 μm and a typical relative velocity of ≈10 m/s, the Weber number is less than the critical value.

2. The droplet is assumed to be spherical. It is well known that moving drops deform in shape; however, the existing correlations for drag and heat transfer incorporate this effect implicitly, treating the droplet as an equivalent sphere (see Yuen et al (1976)).
3. Phenomena such as droplet collision, coalescence and droplet vibration are neglected (Borman et al (1962)).
4. The fluid motion in the droplet interior and the flow around the drop (in the gas-phase boundary layer) are considered to be quasi-steady i.e. the flow immediately adjusts to the local boundary conditions at each instant of time (Faeth (1983) and Sirignano (1983)).
5. The radial velocity of the liquid surface due to the evaporation of the liquid is neglected (Sirignano(1983)). Also, the liquid surface is assumed to be in thermodynamic equilibrium, with negligible temperature jump due to finite rates of evaporation (Faeth (1983)).

6. Thermal diffusion is neglected and only concentration diffusion is considered. (El Wakil et al (1954)).
7. The liquid is a pure hydrocarbon having infinite effective conductivity because of rapid circulation within the droplet to maintain uniform droplet temperature (Borman et al (1962)).
8. Effect of turbulence on drop transport properties e.g. drag coefficient, heat and mass transfer rates, is ignored. (Butler et al (1980) and Gosman et al (1980a)).

Under the above assumptions, the Lagrangian set of equations that describe the droplet behaviour i.e. its motion, heating and evaporation are discussed next.

c. Droplet Motion and Trajectory

The history of a non-rotating droplet of mass $m_d = \frac{\pi}{6} \rho_d D_d^3$ and velocity vector $\vec{u}_d$ in a gaseous field of velocity vector $\vec{u}$ and density ρ is obtained by writing Newton's second law of motion as (Borman and Johnson (1962)):

$$m_d \frac{d\vec{u}_d}{dt} = \vec{F} \tag{3.58}$$

where $\vec{F}$ is the sum of the forces acting on the droplets. These forces are as follows

1. The drag force, which represents the flow resistance connected with the motion of the droplet relative to the fluid. This is usually written for ith direction as:

$$F_{d,i} = \frac{1}{2} C_D \rho A_d (\vec{u} - \vec{u}_d) |u_i - u_{d,i}| \tag{3.59}$$

where A_d is the droplet cross-sectional area and C_D is the drag coefficient. The latter is a function of the droplet Reynolds number Re_d which is defined as:

$$Re_d = \frac{\rho |\vec{u} - \vec{u}_d| D_d}{\mu} \tag{3.60}$$

here D_d represents the droplet diameter. This force has the most significant effect on the droplet motion (Ioannides and Gosman (1978)).

2. Apparent mass force; when a droplet is accelerated relative to the surrounding fluid, it induces a flow around it. This induced mass requires an additional force to be accelerated over that for the droplet (Wallis (1969)). Since the liquid droplet is surrounded by gas of low density compared to the droplet density ($\rho/\rho_d \simeq 3\%$ at typical diesel engine conditions), then this force will be small compared to the inertia force of the droplet and can be neglected (Zubar (1964)).
3. The pressure gradient force; this is due to the static pressure gradients in the flow in the direction of motion $\frac{\partial P}{\partial x_i}$ and is equal to:

$$F_{p,i} = - \frac{m_d}{\rho_d} \frac{\partial P}{\partial x_i} \tag{3.61}$$

this term has been retained in the present study because it can be of significant value in thick sprays (O'Rourke (1981)).

4. The gravity force; defined as

$$F_{g,i} = m_d g(\rho_d - \rho)/\rho_d \tag{3.62}$$

where g is the gravitational acceleration ($g = 9.81\ m/s^2$). As already shown, $\rho/\rho_d \simeq 3\%$ implying that $F_{g,i} \simeq m_d g$. This force is small compared to the drag force and, therefore, is neglected (Williams (1962)).

5. Several additional forces such as Bassett force, Saffman lift and Magnus force. These forces are neglected in the present study since they only have a secondary effect on the spray behaviour (Faeth (1983)).

The preceding discussion shows that the most influential forces are the drag and the pressure gradient forces. Substitution of the expressions for these into the momentum equation (3.58) gives, for the axial and radial directions respectively:

$$\frac{du_d}{dt} = \frac{3}{4}\frac{\rho}{\rho_d D_d} C_D(u - u_d)|\vec{u} - \vec{u}_d| - \frac{1}{\rho_d}\frac{\partial P}{\partial x}$$

$$\frac{dv_d}{dt} = \frac{3}{4}\frac{\rho}{\rho_d D_d} C_D(v - v_d)|\vec{u} - \vec{u}_d| - \frac{1}{\rho_d}\frac{\partial P}{\partial r} \tag{3.63}$$

where u_d and v_d are the droplet velocity in axial and radial directions respectively. Integration of the above equations

gives u_d and v_d. The trajectory of the droplets is then obtained from a further integration, of the following equations:

$$\frac{dx_d}{dt} = u_d$$

$$\frac{dr_d}{dt} = v_d \qquad (3.64)$$

where x_d and r_d are the axial and radial position of the droplet respectively.

The drag coefficient C_D of an evaporating droplet, and as already discussed in chapter 2, is well correlated by the standard drag of solid spheres when the average film viscosity is used to evaluate Reynolds number (equation (3.60)) (Yuen and Chen (1976)). The standard drag, proposed by Wallis (1969), is

$$C_D = \frac{Re_d}{24}(1 + 0.15\ Re_d^{0.687}) \quad \text{for } Re_d < 1000$$

$$C_D = 0.44 \quad \text{for } Re_d > 1000 \qquad (3.65)$$

d. Droplet Evaporation

It is known that liquid droplets behave in an unsteady fashion during droplet vaporization (Sirignano (1983)). Heat is transferred from the hot gas to the liquid surface. Some of the heat from the gas will be required to overcome the latent heat of vaporization while some is transferred to the interior of the

droplet to heat it. The droplet energy equation in its fundamental form can be written as follows (El Wakil et al (1954)):

$$\frac{d}{dt}(m_d\bar{h}_d) = h_{vs}\frac{dm_d}{dt} + q \tag{3.66}$$

where $\bar{h}_d$ is the average droplet specific enthalpy, h_{vs} is the vapour enthalpy at the droplet surface and q is the total heat supplied by the gas to the droplet. The latent heat of vaporization is defined as

$$L = h_{vs} - h_{ds} \tag{3.67}$$

where h_{ds} is the liquid enthalpy at the droplet surface. Substitution into equation (3.66) yields

$$\frac{d}{dt}(m_d\bar{h}_d) - h_{ds}\frac{dm_d}{dt} = L\frac{dm_d}{dt} + q \tag{3.68}$$

with some further manipulations and for a uniform droplet temperature, equation (3.68) can finally be written as:

$$m_d c_{p_d}\frac{dT_d}{dt} = L\frac{dm_d}{dt} + q \tag{3.69}$$

Here, c_{p_d} is the droplet specific heat and T_d is its temperature.

El Wakil et al (1954) derived an expression for the heat supplied to the droplet of surface area A_a, q as:

$$q = hA_a(T - T_d)\frac{z}{e^z - 1} \tag{3.70}$$

where h is the convective heat transfer coefficient through the film surrounding the droplet in the absence of mass transfer and the factor $z/(e^z - 1)$ represents a correction factor to the heat transfer coefficient to account for mass transfer from the droplet. z is defined by

$$z = - \frac{c_{p_v} \frac{dm_d}{dt}}{\pi D_d \bar{\kappa} Nu} \tag{3.71}$$

where c_{p_v} is the fuel vapour specific heat and $\bar{\kappa}$ is the thermal conductivity of the film. The heat transfer coefficient is obtained via the Nusselt number defined as

$$Nu = \frac{hD_d}{\bar{\kappa}} \tag{3.72}$$

Substituting from equations (3.70) and (3.72) into equation (3.69) gives the final form of the droplet energy equation as:

$$\frac{dT_d}{dt} = \frac{\pi D_d \bar{\kappa}(T - T_d)}{m_d c_{p_d}} \frac{z}{(e^z - 1)} Nu + \frac{L}{m_d c_{p_d}} \frac{dm_d}{dt} \tag{3.73}$$

By analogy with the heat transfer equation, a semi-empirical relationship was derived for the mass transfer by El Wakil et al (1954) thus:

$$\frac{dm_d}{dt} = - A_a h' P_t \ell n \left\{ \frac{P_t - P_{v,\infty}}{P_t - P_{v,s}} \right\} \tag{3.74}$$

Here, h' is the mass transfer coefficient, P_t is the total pressure, $P_{v,\infty}$ is the partial pressure of the fuel vapour at the edge of the film (away from the droplet) and $P_{v,s}$ is the partial pressure of the vapour at the droplet surface. The mass transfer coefficient is obtained through knowledge of the Sherwood number Sh defined as:

$$Sh = \frac{D_d R T_m h'}{D} \tag{3.75}$$

where T_m represents the mean film temperature ($=(T + T_d)/2$), D is the diffusivity and R is the gas constant. Substituting h' from equation (3.75) into equation (3.74) yields the final form of the mass transfer equation:

$$\frac{dm_d}{dt} = - \pi D_d D \frac{P_t}{R T_m} \ln\left(\frac{P_t - P_{v,\infty}}{P_t - P_{v,s}}\right) Sh \tag{3.76}$$

The Nusselt and Sherwood numbers are evaluated from the expressions given by Ranz and Marshall (1952) as

$$\begin{aligned} Nu &= 2. + 0.6\ Re_d^{0.5}\ Pr^{0.33} \\ Sh &= 2. + 0.6\ Re_d^{0.5}\ Sc^{0.33} \end{aligned} \tag{3.77}$$

where

$$\begin{aligned} \text{Prandtl number } Pr &= \frac{c_{p_m} \mu_m}{\overline{\kappa}} \\ \text{Schmidt number } Sc &= \frac{\mu_m}{\rho D} \end{aligned} \tag{3.78}$$

with the subscript m denotes mean film properties. Equations (3.77) are valid for Reynolds number in the range of interest in diesel sprays as already shown in the review given in Chapter 2.

In the present study, the fuel is assumed to be the pure substance n-dodecane ($C_{12}H_{26}$) which has approximately the same molecular weight as diesel fuel. The fuel properties, fuel vapour and air properties are given below.

e. Thermodynamic Properties

a. Liquid phase

i. Density

The density of the n-dodecane decreases as the temperature increases (as shown in Fig. (3.1)), according to Rose et al (1977):

$$\rho_d = 840/\{1 + 0.00067(T_d - 288)\} \tag{3.79}$$

ii. Specific Heat

The specific heat of the liquid fuel at constant pressure at different temperatures is obtained from the data of Maxwell (1956) and fitted by:

$$c_{p_d} = 803.42 + 5.076T_d - 2.212 \times 10^{-3}T_d^2 + 1.673 \times 10^{-6}T_d^3 \tag{3.80}$$

which is applicable in the temperature range 300 K - 650 K. For higher temperatures, c_{p_d} is obtained by extrapolation of the above equation in the absence of any other information. The temperature variation of c_{p_d} is shown in Fig. (3.1).

iii. Latent Heat of Vaporization

The latent heat of vaporization of the liquid fuel is given by the following fit to Maxwell's (1956) data

$$L = 3.288 \times 10^5 + 1.882 \times 10^3 T_d - 10.99 T_d^2 + 2.104 \times 10^{-2} T_d^3 - 1.446 \times 10^{-5} T_d^4 \quad (3.81)$$

which is valid in the temperature range 300K - 640K. The temperature variation of L (Fig. (3.1)) shows a sharp decrease at $T_d \simeq 660$ K after which the droplet reaches the critical point, for which L = 0.

b. Gas-phase (air and vapour)

i. Fuel Vapour Partial Pressures

The partial pressure of the fuel vapour at the droplet surface is expressed as a function of droplet temperature (see Borman and Johnson (1962)) as:

$$P_{v,s} = 6894.757 e^{\{12.12767 - 3743.84/(T_d - 93.022)\}} \quad (3.82)$$

It should be noted that when $P_{v,s} = P_t$ (the gas pressure) T_d becomes the saturation temperature of the fuel. Figure (3.2) is a graphical representation of the above formula, from which it is seen that $P_{v,s}$ is limited by the value of the gas pressure i.e. $P_{v,s)_{max}} \leq P_t$.

The partial pressure of the fuel vapour in the ambient droplet surroundings $P_{v,\infty}$ is given by:

$$P_{v,\infty} = \frac{m_m}{m_f} f P_t \tag{3.83}$$

where m_m is the mean molecular weight defined below, m_f is the fuel molecular weight (= 170.3) and f is the ambient fuel vapour mass fraction.

ii. Viscosities

The viscosity of air is a fit to the data reported by Hilsenrath (1960):

$$\mu_a = 6.829 \times 10^{-6} + 4.529 \times 10^{-8} T - 1.0687 \times 10^{-11} T^2 \tag{3.84}$$

The viscosity of the fuel vapour, as fitted to the data given by Maxwell (1956) is given by:

$$\mu_v = 1.69387 \times 10^{-7} + 1.30959 \times 10^{-8} T + 6.6482 \times 10^{-12} T^2 - 9.238 \times 10^{-15} T^3 \tag{3.85}$$

iii. Specific Heats

The equation for the specific heat of air at constant pressure is obtained from the data reported by Hilsenarth (1960) for the temperature range 600 K - 950 K as:

$$c_{p_a} = 888.4 + 0.2885T - 3.527 \times 10^{-5} T^2 \tag{3.86}$$

The fuel vapour specific heat is obtained from the data reported by the National Bureau of Standard (1952) for the temperature range 360 K - 840 K:

$$c_{p_v} = 303.57 + 3.8705T + 4.323 \times 10^{-3}T^2 - 8.648 \times 10^{-6}T^3 + 3.95 \times 10^{-9}T^4 \quad (3.87)$$

iv. Thermal Conductivity

The equation for the thermal conductivity of air is determined for the data of Hilsenarth (1960) as:

$$\kappa = 0.05128 - 9.885 \times 10^{-5}T + 2.1157 \times 10^{-7}T^2 - 9.4686 \times 10^{-11}T^3 \quad (3.88)$$

v. Diffusivity

The diffusion coefficient (diffusivity) of the fuel-air mixture is obtained from the following formula given by Borman et al (1962)

$$D = 1.218 \times 10^{-4} \frac{T^{3/2}}{P_t \Omega} \quad (3.89)$$

where $\Omega = 1.864 - 2.992 \times 10^{-3}T + 3.357 \times 10^{-6}T^2 - 1.394 \times 10^{-9}T^3$ (3.90)

Graphical representations of formulae (3.84) to (3.89) are given in Fig. (3.3).

C. Calculation of Film Properties

The computations of vaporization rate described earlier require the calculation of μ, c_p and κ of the vapour-air mixture in the film surrounding the droplet. The molal ratio of fuel vapour to air is approximated by the ratio of the partial pressure of the fuel vapour at droplet surface to the air pressure (see El Wakil et al (1954)). The properties then are calculated at the mean temperature T_m $(=(T + T_d)/2)$ and for a fuel vapour-air mixture of concentration equal to half the concentration at the droplet surface (assuming the concentration at the outer edge of the film is the ambient concentration which, generally, is a small fraction of that at the droplet surface). Thus the mean film properties can be written as:

$$\mu_m = (1 - \frac{P_{v,s}}{2P_t})\mu_a + \frac{P_{v,s}}{2P_t}\mu_v$$

$$c_{p_m} = \frac{(1 - \frac{P_{v,s}}{2P_t})m_a}{m_m} c_{p_a} + \frac{(\frac{P_{v,s}}{2P_t})m_f}{m_m} c_{p_v} \qquad (3.91)$$

$$m_m = (1 - \frac{P_{v,s}}{2P_t})m_a + \frac{P_{v,s}}{2P_t} m_f$$

$$= \frac{1}{(\frac{1-f}{m_a}) + (\frac{f}{m_f})}$$

and $R_m = \bar{R}/m_m$

where $\bar{R}$ is the universal gas constant and f is the fuel vapour mass fraction.

3.8 Turbulent Droplet Dispersion

In a non-isothermal turbulent environment of the kind of diesel sprays injected to, the droplets will experience time varying velocity, temperature and concentration fields due to the effects of the turbulent motions. Neglecting the effects of turbulence on droplet behaviour implies that drops follow deterministic trajectories prescribed by their initial conditions at the injector exit and mean gas properties throughout the flow field. The extent of droplet dispersion from their mean trajectories depends on their inertial properties and turbulence characteristics of the gas phase. Faeth (1983) showed, for the measurements of Yuu et al (1978) of a round air jet of diameter 8 mm containing a dust of nearly mono-dispersed particles having a diameter of 20 μm, that ignoring droplet dispersion leads to an under-estimation of the radial spread of the particles.

Two main methods have been employed to compute droplet dispersion in sprays. Abbas et al (1980) simulated the turbulence effects as an extra diffusion force added to the droplet equations of motion (equation 3.63)). In that case, the drag force is evaluated using the ensemble-averaged gas velocities. The diffusion force is obtained for each droplet using a droplet concentration gradient expression which employs a turbulent gas/droplet exchange coefficient. Some method of estimating the gas/droplet exchange coefficient is required in order to obtain a closed form solution. Lack of theoretical guidance on values of gas/droplet exchange coefficients is compounded by difficulties with existing measurements.

Yuu et al (1978) pointed out that measurements are often suspect, since the experiments were analysed assuming that mean gas and droplet velocities were the same which is rarely satisfied in practice.

Hotchkiss and Hirt (1972), cited by Dukowicz (1980) proposed another way for estimating the droplet diffusion coefficient to compute droplet dispersion. In this case, it is related to the variance of the probability density function of droplet position (assumed to be Gaussian) at the end of each computational time step. Given the variance, the distribution is randomly sampled to obtain the diffusional increment of droplet position. This procedure gives the diffusion coefficient very simply but it does not provide any real advantage over the next method discussed, the stochastic approach.

In the stochastic dispersion method employed by Gosman and Ioannides (1981), the instantaneous gas velocity $\bar{u} + u'$ replaces the mean velocity in the droplet equations of motion to yield, for the axial direction:

$$\frac{du_d}{dt} = \frac{3}{4} \frac{\rho}{\rho_d D_d} C_D(\bar{u} + u' - u_d)|\overrightarrow{\bar{u} + u'} - \vec{u}_d| - \frac{1}{\rho_d} \frac{\partial P}{\partial x} \qquad (3.92)$$

As droplets pass through the flow, they are assumed to interact with individual eddies. Each interaction deflects the droplet as dictated by the instantaneous velocity of the eddy and the droplet inertia. Therefore, the droplet trajectory is determined similar

to a random walk computation until the droplet passes out of the region under consideration.

In the present study the stochastic method is employed in the spirit of Gosman and Ioannides (1981). The instantaneous gas velocity within an eddy is obtained from the mean gas velocity and the turbulent kinetic energy k, which are known from the solution for the gas-phase properties. For this purpose, the turbulence is assumed to be isotropic with fluctuating velocity u' having a Gaussian distribution whose standard deviation σ_{sd} is given by:

$$\sigma_{sd} = (\frac{2}{3} k)^{\frac{1}{2}} \tag{3.93}$$

Random fluctuating velocities are selected from this distribution as follows (see Dukowicz (1980)):

$$u' = \sigma_{sd} \, sgn(X,Y) \, erf^{-1}(|X|, |Y|) \tag{3.94}$$

where X and Y are random variables, associated with the x and r co-ordinates, selected from uniform distributions in the range $-1<X,Y<1$.

Following Brown and Hutchinson (1979), a droplet is assumed to interact with an eddy for a time taken as the minimum of either the eddy life time t_e, or the transit time t_R required for the droplet to traverse the eddy. Estimates of the eddy and transit times are made under the assumption that the characteristic size of the randomly sampled eddy is the dissipation length scale ℓ_e given by:

$$\ell_e = c_\mu^{1/2} k^{3/2} / \varepsilon \tag{3.95}$$

The eddy life time is then estimated as:

$$t_e = \ell_e / |\vec{u}'| \tag{3.96}$$

The transit time is simply given as

$$t_R = \ell_e / |\vec{u} - \vec{u}_d| \tag{3.97}$$

where $|\vec{u} - \vec{u}_d|$ is the local slip velocity vector.

3.9 Closure

In this chapter, the instantaneous form of the gas-phase governing equations has been presented in an unsteady, two-dimensional axisymmetric co-ordinates. Ensemble-averaged form of the equations is derived and a turbulence model which employs two additional differential equations for the kinetic energy of turbulence and its dissipation rate to form a closed set of equation is described. A transformation of the co-ordinate has been derived that allows it to move, for gas jet predictions. The equations that govern droplet motion and trajectory are presented. Droplet vaporization and diminution expressions are

presented to complete the droplet-phase equations. A summary of the fuel and film properties is given. Finally, a treatment of droplet diffusion using the stochastic dispersion method has been described.

Table 3.1 Turbulence model constants

Constant	Value
c_μ	0.09
c_1	1.44
c_2	1.92
σ_k	1.
σ_ε	1.2175
σ_h	0.9
σ_f	1.0

Table 3.2 Expressions for the exchange coefficient and the source terms appearing in the general transport equation

Dependent Variable	Γ_ϕ	S_ϕ
u	μ_{eff}	$-\theta\frac{\partial P}{\partial x} + \frac{\partial}{\partial x}(\theta\mu_{eff}\frac{\partial u}{\partial x}) + \frac{1}{r}\frac{\partial}{\partial r}(r\theta\mu_{eff}\frac{\partial v}{\partial x})$ $-\frac{2}{3}\frac{\partial}{\partial x}(\theta\mu_{eff}\nabla.\vec{u} + \rho\theta k)$
v	μ_{eff}	$-\theta\frac{\partial P}{\partial r} + \frac{\partial}{\partial x}(\theta\mu_{eff}\frac{\partial u}{\partial r}) + \frac{1}{r}\frac{\partial}{\partial r}(\theta r\mu_{eff}\frac{\partial v}{\partial r})$ $-2\mu_{eff}\theta\frac{v}{r^2} - \frac{2}{3}\frac{\partial}{\partial r}(\theta\mu_{eff}\nabla.\vec{u} + \rho\theta k)$
1	0	0
h	$\frac{\mu_{eff}}{\sigma_h}$	$\theta\frac{\partial P}{\partial t} + \frac{\partial}{\partial x}\{\theta\mu_{eff}(1-\frac{1}{\sigma_h})\frac{\partial}{\partial x}(\Sigma\frac{\overline{u_i}^2}{2})\}$ $+\frac{1}{r}\frac{\partial}{\partial r}\{r\theta\mu_{eff}(1-\frac{1}{\sigma_h})\frac{\partial}{\partial r}(\Sigma\frac{\overline{u_i}^2}{2})\}$ $+\frac{\partial}{\partial x}[\theta\mu_{eff}(\frac{1}{\sigma_k}-\frac{1}{\sigma_h})\frac{\partial k}{\partial x}] + \frac{1}{r}\frac{\partial}{\partial r}\{r\theta\mu_{eff}$ $(\frac{1}{\sigma_k}-\frac{1}{\sigma_h})\frac{\partial k}{\partial r}\}$
f	$\frac{\mu_{eff}}{\sigma_f}$	0
k	$\frac{\mu_{eff}}{\sigma_k}$	$\theta G_t - \rho\theta\varepsilon$
ε	$\frac{\mu_{eff}}{\sigma_\varepsilon}$	$\frac{\varepsilon}{k}(c_1\theta G_t - c_2\rho\theta\varepsilon) + \rho\theta\varepsilon\nabla.\vec{u}$

Table 3.3 Source terms in the transformed co-ordinate system

Dependent Variable	S_ϕ
u	$-\theta\frac{\partial P}{\xi_1\partial x'} + \frac{1}{\xi_1}\frac{\partial}{\partial x}(\theta\mu_{eff}\frac{\partial u}{\xi_1\partial x}) - \frac{1}{\xi_2 r}\frac{\partial}{\xi_2\partial r}[(\xi_2 r)\theta\mu_{eff}\frac{\partial v}{\xi_1\partial x}]$ $-\frac{2}{3}\frac{1}{\xi_1}\frac{\partial}{\partial x}[\theta\mu_{eff}\nabla.\vec{u} + \rho\theta k]$
v	$-\theta\frac{\partial P}{\xi_2\partial r} + \frac{1}{\xi_1}\frac{\partial}{\partial x}(\theta\mu_{eff}\frac{\partial u}{\xi_2\partial r}) + \frac{1}{\xi_2 r}\frac{\partial}{\xi_2\partial r}[(\xi_2 r)\theta\mu_{eff}\frac{\partial v}{\xi_2\partial r}]$ $-2\mu_{eff}\theta\frac{v}{(\xi_2 r)^2} - \frac{2}{3}\frac{1}{\xi_2}\frac{\partial}{\partial r}[\theta\mu_{eff}\nabla.\vec{u} + \rho\theta k]$
1	0
h	$\theta\frac{\partial P}{\partial t} + \frac{1}{\xi_1}\frac{\partial}{\partial x}[\theta\mu_{eff}(1-\frac{1}{\sigma_h})\frac{\partial}{\xi_1\partial x'}(\Sigma\frac{\overline{u_i}^2}{2})]$ $+\frac{1}{\xi_2 r}\frac{\partial}{\xi_2\partial r}[(\xi_2 r)\theta\mu_{eff}(1-\frac{1}{\sigma_h})\frac{\partial}{\xi_2\partial r}(\Sigma\frac{\overline{u_i}^2}{2})]$ $+\frac{1}{\xi_1\partial x}[\theta\mu_{eff}(\frac{1}{\sigma_k}-\frac{1}{\sigma_h})\frac{\partial k}{\xi_1\partial x}]$ $+\frac{1}{\xi_2 r}\frac{\partial}{\xi_2\partial r}[(\xi_2 r)\theta\mu_{eff}(\frac{1}{\sigma_k}-\frac{1}{\sigma_h})\frac{\partial k}{\xi_2\partial r}]$
f	0
k	$\theta G_t - \rho\theta\varepsilon$
ε	$\frac{\varepsilon}{k}(c_1\theta G_t - c_2\rho\theta\varepsilon) + \rho\theta\varepsilon\nabla.\vec{u}$

$$\nabla.\vec{u} = \frac{1}{\xi_1}\frac{\partial u}{\partial x} + \frac{1}{\xi_2}\frac{\partial v}{\partial r}$$

$$G_t = \mu_t\{2[(\frac{\partial u}{\xi_1\partial x})^2 + (\frac{\partial v}{\xi_2\partial r})^2 + (\frac{v^2}{\xi_2 r})^2] + [(\frac{\partial u}{\xi_2\partial r} + \frac{\partial v}{\xi_1\partial x})]^2\}$$

$$-\frac{2}{3}\nabla.\vec{u}(\mu_t\nabla.u + \rho k).$$

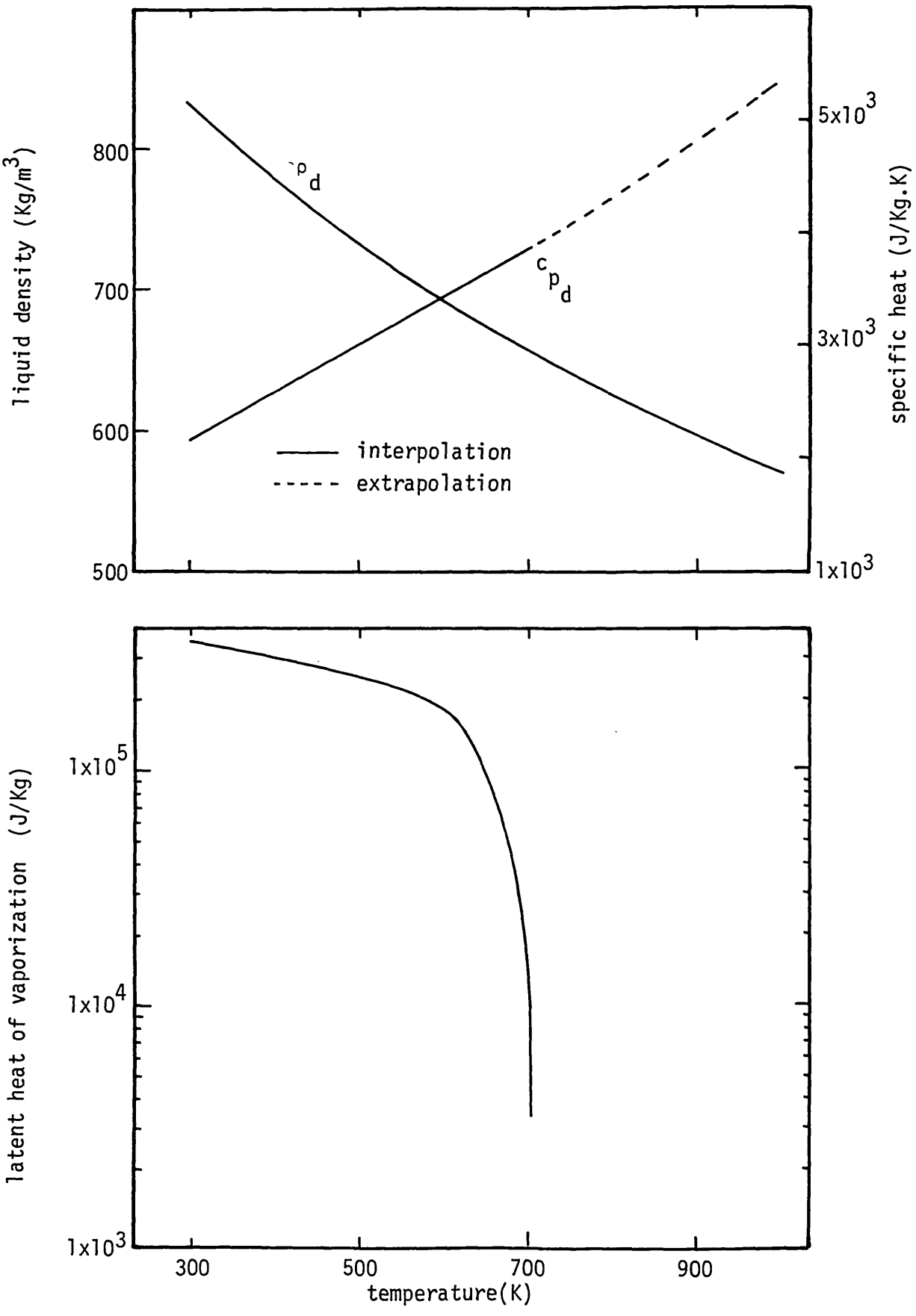


Fig.(3.1) Variation of the fuel properties with temperature.

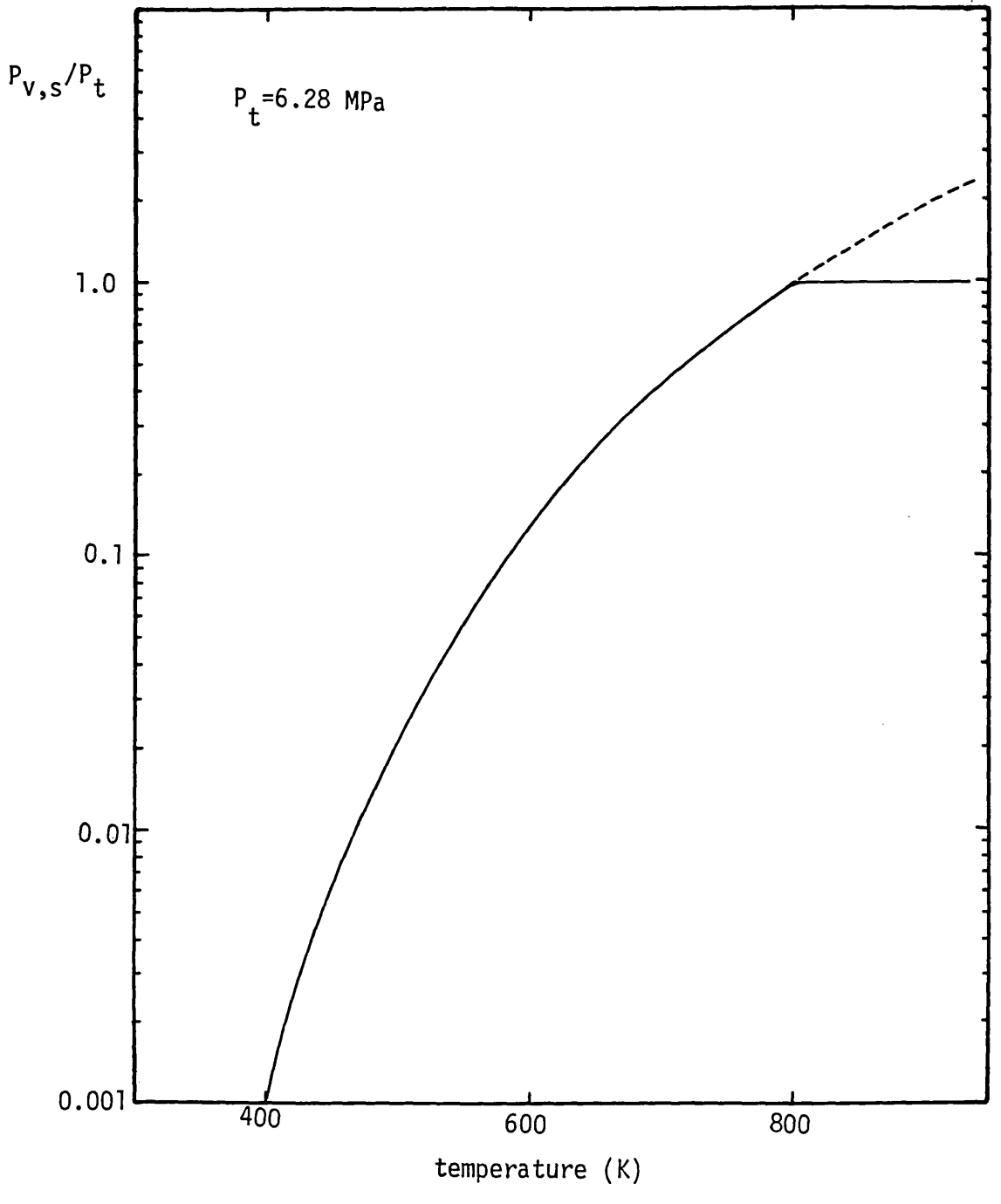


Fig.(3.2) Temperature variation of the partial pressure of the fuel vapour at droplet surface.

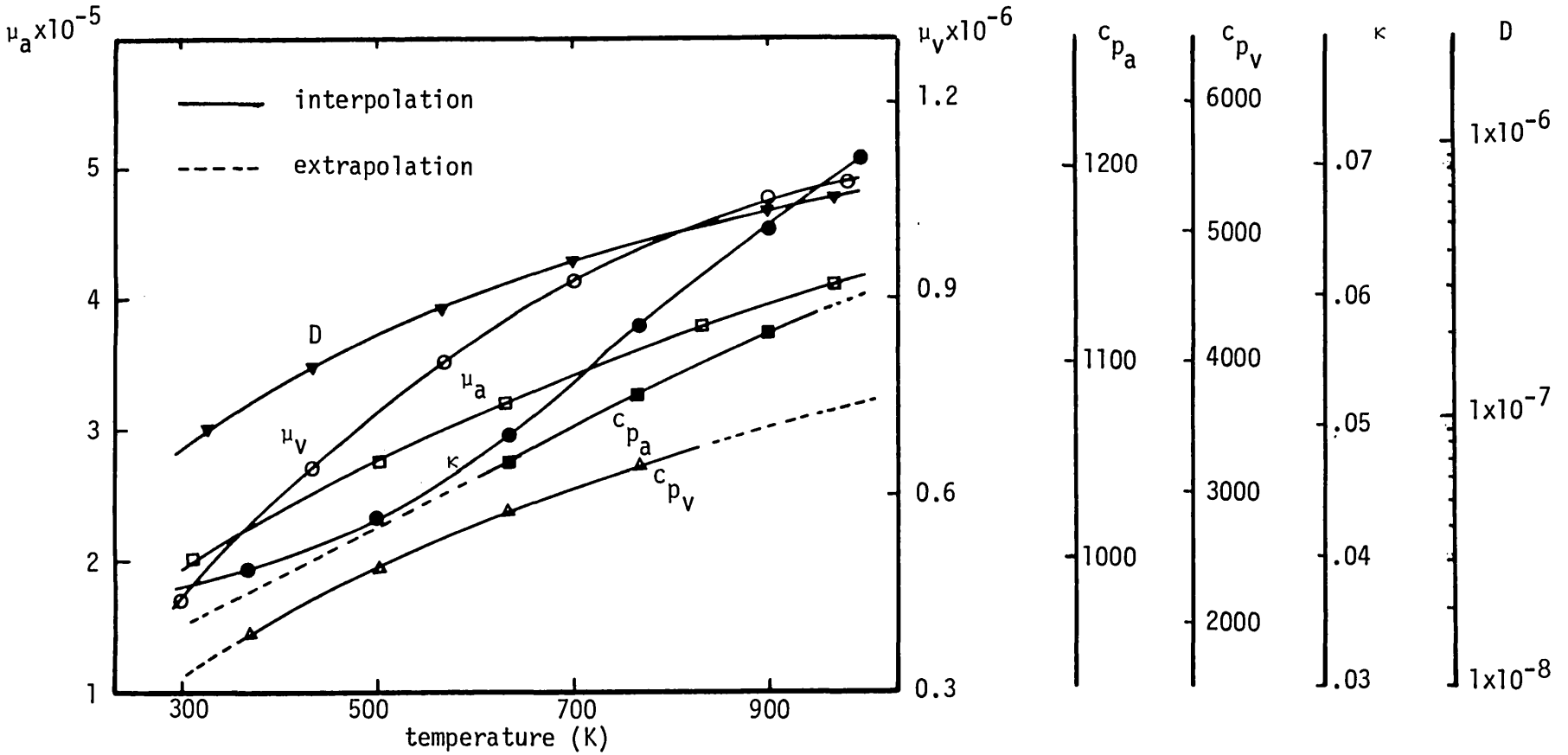


Fig.(3.3) Temperature variation of the thermodynamic properties of the gas phase

CHAPTER 4

THE NUMERICAL SOLUTION PROCEDURES

4.1 Introductory Remarks

The transport equations of the gas phase given in chapter 3 form a closed set of non-linear and strongly coupled partial differential equations, which are too complicated to be solved analytically. Hence numerical solution is required. One of the most popular and widely used numerical methods is the finite volume procedure, in which the solution domain is divided into a finite number of discrete volumes or 'cells' by a computational grid. The finite volume equations are derived by integrating the differential equations over such cells (see Patankar et al (1972)).

Furthermore, a numerical method of solution is also needed to integrate the ordinary differential equations governing the droplet motion, temperature and evaporation rate.

This chapter is concerned with procedures employed in the present study for solving both sets of the differential equations. In section 4.2, the location of the different variables within the computational mesh, are defined. The general transport equation is integrated both in space and in time in a finite-volume fashion in section 4.3. The alternative spatial and temporal differencing schemes are discussed from the viewpoint of stability and accuracy in section 4.4 and a provisional choice is made.

The procedure that links the continuity and momentum equations in order to obtain the pressure field is detailed in section 4.5.

In section 4.6, the Euler method used to integrate the droplet equations and evaluate the interaction terms is described.

Section 4.7 outlines the two different solution algorithms used to solve the gas phase equations. One is a fully implicit scheme, used for gas jet calculations, and the other is a semi-implicit scheme, used for spray predictions. In the latter case particular emphasis is placed on the coupling between the droplet and gas equations.

Finally, the incorporation of the boundary and initial conditions into the solution procedures is given in section 4.8.

4.2 Computational Grid System and Notation

The computational grid employed for the analysis is illustrated in Fig. (4.1). It consists of arbitrarily-spaced planes of constant x and r. All the scalar quantities including enthalpy, density, pressure, temperature, turbulence kinetic energy, dissipation rate, viscosity, fuel vapour mass fraction and void fraction are located at the centre of the cells. Following common practice, (e.g. Caretto et al (1972)) the axial and radial velocities, designated by the arrows in Fig. (4.2.), are displaced to lie on the boundaries of the 'scalar cell'. This positioning - which is

known as a 'staggered grid' - has two advantages: firstly, the velocities lie between the pressures, so providing a straightforward calculation of the pressure gradient terms in the momentum equations, and secondly, they are in a convenient position to calculate the convective flux across the scalar cell boundaries.

Figure (4.3) illustrates a portion of the computational grid showing a typical node P and its nearest neighbours, labelled N, E, S and W for scalar locations, while the velocities are located in the intervening cell boundaries denoted by n, e, s and w. These control volumes are formed by rotating the grid through unit angle about the symmetry axis.

4.3 Finite-Difference Approximation

4.3.1 Transport Equations

In accordance with the finite-volume approach of Gosman et al (1969), the general finite-difference equation is derived by integration of the general transport equation (3.55) over a typical control volume and a time interval δt to yield, after division by δt:

$$\frac{1}{\delta t}\int_{t}^{t+\delta t}\{\int_{V_p}\frac{\partial}{\partial t}(\xi_1\xi_2\xi_2 r\rho\theta\phi)dxdr$$

I

$$+ \int_{r_s}^{r_n} \xi_2\xi_2 r(\rho\theta u_r\phi - \theta\frac{\Gamma_\phi}{\xi_1}\frac{\partial\phi}{\partial x})_w^e \, dr$$

II

$$+ \int_{x_w}^{x_e} \xi_1\xi_2 r(\rho\theta v_r\phi - \theta\frac{\Gamma_\phi}{\xi_2}\frac{\partial\phi}{\partial r})_s^n \, dx$$

III

$$- \int_{V_p} \xi_1\xi_2\xi_2 r(S_\phi + S_{\phi,d})dxdr\} \, dt = 0 \qquad (4.1)$$

IV

where $\int_{V_p}$ denotes integration over the scalar control volume surrounding P, i.e. $\int_{V_p}(\xi_1\xi_2\xi_2 r\rho\theta\phi)dxdr = \int_s^n \int_w^e (\xi_1\xi_2\xi_2 r\rho\theta\phi)dxdr$.

The above expression is exact but in order to obtain the final result it is now necessary to introduce approximations. Thus, to evaluate the volume integral of term I the values of the variables at the central node are assumed to pertain throughout the volume, giving:

$$\frac{1}{\delta t}\int_t^{t+\delta t} \frac{\partial}{\partial t}\int_{V_p} (\xi_1\xi_2\xi_2 r\rho\theta\phi)dxdrdt$$

$$= \frac{\left[(\xi_1\xi_2 r)_P \delta x_{ew}\delta r_{ns}\rho\theta\phi\right]^{n+1} - \left[(\xi_1\xi_2 r)_P \delta x_{ew}\delta r_{ns}\rho\theta\phi\right]^n}{\delta t}$$

$$= \frac{(V\rho\theta\phi)_P^{n+1} - (V\rho\theta\phi)_P^n}{\delta t} \qquad (4.2)$$

where the superscripts n+1 and n denote new and old time levels respectively, separated by the time interval δt. V_p is the cell volume defined as:

$$V_p = (\xi_1 \xi_2 r)_p \delta x_{ew} \delta r_{ns} \tag{4.3}$$

and the cell face areas are evaluated by

$$a_n = (\xi_1 \xi_2 r)_n \delta x_{ew}$$

$$a_s = (\xi_1 \xi_2 r)_s \delta x_{ew} \tag{4.4}$$

$$a_e = a_w = a_{ew} = (\xi_2 r)_p \xi_2 \delta r_{ns}$$

Terms II and III of equation (4.1) represent the total flux of ϕ across the cell faces due to convection and diffusion in both axial and radial directions respectively. The cell wall values of $\frac{\partial \phi}{\xi_1 \partial x}$ are obtained by assuming a linear variation of ϕ between the bracketing points, e.g.:

$$\frac{1}{\xi_1} \frac{\partial \phi}{\partial x} \Big|_e \approx \frac{\phi_E - \phi_P}{\xi_1 \delta x_{EP}} \tag{4.5}$$

Hence, for example, term II of equation (4.1) is approximated as:

$$F_x = \int_{r_s}^{r_n} \xi_1 \xi_2 r(\rho\theta u_r\phi - \theta \frac{\Gamma_\phi}{\xi_1} \frac{\partial\phi}{\partial x})_w^e \, dr$$

$$\simeq a_{ew} \{ \rho\theta u_r\phi - \frac{\theta\Gamma_\phi}{\xi_1} \frac{(\phi_E - \phi_P)}{\delta x_{EP}} \}_e$$

$$- a_{ew} \{ \rho\theta u_r\phi - \frac{\theta\Gamma_\phi}{\xi_1} \frac{(\phi_P - \phi_W)}{\delta x_{PW}} \}_w \qquad (4.6)$$

If cell-boundary Peclet numbers Pe are defined thus:

$$Pe_e = \frac{(\rho u_r)_e \xi_1 \delta x_{EP}}{\Gamma_e}$$

$$Pe_w = \frac{(\rho u_r)_w \xi_1 \delta x_{PW}}{\Gamma_w} \qquad (4.7)$$

equation (4.6) may also be written as:

$$F_x = a_{ew}(\rho\theta u_r)_e \{ \phi_e - \frac{\phi_E - \phi_P}{Pe_e} \}$$

$$- a_{ew}(\rho\theta u_r)_w \{ \phi_w - \frac{\phi_P - \phi_W}{Pe_w} \} \qquad (4.8)$$

The cell-boundary void fractions, densities and diffusivities appearing in the above equation are evaluated as a weighted average of their values at the nearest neighbours, e.g.:

$$\rho_e = f_1 \rho_P + (1 - f_1)\rho_E \tag{4.9}$$

where f_1 is the spatial weighting factor, given by:

$$f_1 = \frac{\xi_1 \delta x_{Ee}}{\xi_1 \delta x_{EP}} \tag{4.10}$$

The values of ϕ at the cell faces are also expressed in terms of neighbouring nodal values, typically:

$$\phi_e - \frac{\phi_E - \phi_P}{Pe_e} \equiv (1 - \alpha_e)\phi_E + \alpha_e \phi_P$$

$$\phi_w - \frac{\phi_P - \phi_W}{Pe_w} \equiv \alpha_w \phi_W + (1 - \alpha_w)\phi_P \tag{4.11}$$

where α is a weighting factor, to be specified later. Substitution from equation (4.11) into equation (4.8) yields the following:

$$F_x = a_{ew}(\rho\theta u_r)_e \{(1 - \alpha_e)\phi_E + \alpha_e \phi_P\}$$

$$- a_{ew}(\rho\theta u_r)_w \{\alpha_w \phi_W + (1 - \alpha_w)\phi_P\} \tag{4.12}$$

To complete the integration of term II, a two time level differencing scheme is introduced with an arbitrary temporal weighting factor η such that

$$F_{x,t} = \frac{1}{\delta t} \int_t^{t+\delta t} F_x dt = \eta F_x^{n+1} + (1 - \eta)F_x^n \tag{4.13}$$

The specification of η will also be given later. The final form of term II is then

$$F_{x,t} \simeq \eta\, a_{ew}^{n+1}(\rho\theta u_r)_e^{n+1}\{(1-\alpha_e^{n+1})\phi_E^{n+1} + \alpha_e^{n+1}\phi_P^{n+1}\}$$

$$-\eta\, a_{ew}^{n+1}(\rho\theta u_r)_w^{n+1}\{\alpha_w^{n+1}\phi_W^{n+1} + (1-\alpha_w^{n+1})\phi_P^{n+1}\}$$

$$+ (1-\eta)a_{ew}^{n}(\rho\theta u_r)_e^{n}\{(1-\alpha_e^{n})\phi_E^{n} + \alpha_e^{n}\phi_P^{n}\}$$

$$- (1-\eta)a_{ew}^{n}(\rho\theta u_r)_w^{n}\{\alpha_w^{n}\phi_W^{n} + (1-\alpha_w^{n})\phi_P^{n}\} \qquad (4.14)$$

The third term of equation (4.1) is treated in a similar manner, to give:

$$F_{r,t} = \frac{1}{\delta t}\int_t^{t+\delta t}\int_{x_w}^{x_e} \xi_1\xi_2 r\left(\rho\theta v_r\phi - \frac{\Gamma_\phi}{\xi_2}\frac{\partial\phi}{\partial r}\right)_s^n dr\,dt$$

$$= \eta\, a_n^{n+1}(\rho\theta v_r)_n^{n+1}\{(1-\alpha_n^{n+1})\phi_N^{n+1} + \alpha_n^{n+1}\phi_P^{n+1}\}$$

$$-\eta a_s^{n+1}(\rho\theta v_r)_s^{n+1}\{\alpha_s^{n+1}\phi_S^{n+1} + (1-\alpha_s^{n+1})\phi_P^{n+1}\}$$

$$+ (1-\eta)a_n^{n}(\rho\theta v_r)_n^{n}\{(1-\alpha_n^{n})\phi_N^{n} + \alpha_n^{n}\phi_P^{n}\}$$

$$- (1-\eta)a_s^{n}(\rho\theta v_r)_s^{n}\{\alpha_s^{n}\phi_S^{n} + (1-\alpha_s^{n})\phi_P^{n}\} \qquad (4.15)$$

The remaining integral IV of equation (4.1) contains sources associated with gas and droplets respectively. It will be represented by:

$$\frac{1}{\delta t}\int_{t}^{t+\delta t}\int_{V_p}\xi_1\xi_2\xi_2 r(S_\phi + S_{\phi,d})dxdrdt$$

$$\simeq \overline{S}_\phi + \overline{S}_{\phi,d} \tag{4.16}$$

where $\overline{S}_\phi$ and $\overline{S}_{\phi,d}$ depend on the variable ϕ under consideration as will be discussed later in the chapter.

As a result of the above approximations, the general finite difference equation can now be assembled:

$$\frac{(\rho\theta\phi V)_P^{n+1} - (\rho\theta\phi V)_P^n}{\delta t}$$

$$+ \{\eta(1 - \alpha_e^{n+1})\dot{m}_e^{n+1}\phi_E^{n+1} + (1 - \eta)(1 - \alpha_E^n)\dot{m}_e^n\phi_E^n\}$$

$$- \{\eta\alpha_w^{n+1}\dot{m}_w^{n+1}\phi_W^{n+1} + (1 - \eta)\alpha_w^n\dot{m}_w^n\phi_W^n\}$$

$$+ \{\eta(1 - \alpha_n^{n+1})\dot{m}_n^{n+1}\phi_N^{n+1} + (1 - \eta)(1 - \alpha_n^n)\dot{m}_n^n\phi_N^n\}$$

$$- \{\eta\alpha_s^{n+1}\dot{m}_s^{n+1}\phi_S^{n+1} + (1 - \eta)\alpha_s^n\dot{m}_s^n\phi_S^n\}$$

$$+ \eta\{\alpha_e^{n+1}\dot{m}_e^{n+1} - (1 - \alpha_w^{n+1})\dot{m}_w^{n+1} + \alpha_n^{n+1}\dot{m}_n^{n+1} - (1 - \alpha_s^{n+1})m_s^{n+1}\}\phi_P^{n+1}$$

$$+ (1 - \eta)\{\alpha_e^n\dot{m}_e^n - (1 - \alpha_w^n)\dot{m}_w^n + \alpha_n^n\dot{m}_n^n - (1 - \alpha_s^n)\dot{m}_s^n\}\phi_P^n$$

$$= \overline{S}_\phi + \overline{S}_{\phi,d} \tag{4.17}$$

where $\dot{m}_e = (\rho\theta a u_r)_e$, $\dot{m}_n = (\rho\theta a v_r)_n$ etc. Equation (4.17) may be written in more compact form as

$$A_P^{n+1}\phi_P^{n+1} = \sum_c A_c^{n+1}\phi_c^{n+1} + \sum_c A_c^n\phi_c^n + A_P^n\phi_P^n + \overline{S}_\phi + \overline{S}_{\phi,d} \qquad (4.18)$$

where summations are over the four nodes surrounding point P (e.g. N, E, S and W in Fig. (4.3)) and the coefficients A_c are given by:

$$\begin{aligned}
A_N^{n+1} &= -\eta(1-\alpha_n^{n+1})\dot{m}_n^{n+1} \\
A_S^{n+1} &= \eta\alpha_s^{n+1}\dot{m}_s^{n+1} \\
A_E^{n+1} &= -\eta(1-\alpha_e^{n+1})\dot{m}_e^{n+1} \\
A_W^{n+1} &= \eta\alpha_w^{n+1}\dot{m}_w^{n+1} \\
A_N^n &= -(1-\eta)(1-\alpha_n^n)\dot{m}_n^n \\
A_S^n &= (1-\eta)\alpha_s^n\dot{m}_s^n \\
A_E &= -(1-\eta)(1-\alpha_e^n)\dot{m}_e^n \\
A_W^n &= (1-\eta)\alpha_w^n\dot{m}_w^n \\
A_P^{n+1} &= \eta\{\alpha_e^{n+1}\dot{m}_e^{n+1} - (1-\alpha_w^{n+1})\dot{m}_w^{n+1} + \alpha_n^{n+1}\dot{m}_n^{n+1} - (1-\alpha_s^{n+1})\dot{m}_s^{n+1}\} \\
&\quad + \frac{(\rho\theta V)_P^{n+1}}{\delta t} \\
A_P^n &= -(1-\eta)\{\alpha_e^n\dot{m}_e^n - (1-\alpha_w^n)\dot{m}_w^n + \alpha_n^n\dot{m}_n^n - (1-\alpha_s^n)\dot{m}_s^n\} \\
&\quad + \frac{(\rho\theta V)_P^n}{\delta t}
\end{aligned} \qquad (4.19)$$

The treatment of the momentum equations differs from the scalar equation integration in that the control volumes are centred on the velocity component in question and are thus effectively formed from two half scalar cells, as shown in Fig. (4.2). An example of a control volume for the axial component is shown in more detail in Fig. (4.4), along with the associated labelling. In this connection, it should be noted that the convention adopted is that the velocities assume the label of the scalar nodes at which they point. The axial momentum equation is written as

$$A_P^{n+1} u_P^{n+1} = \sum_c A_c^{n+1} u_c^{n+1} + \sum_c A_c^n u_c^n + A_P^n u_P^n + \bar{S}_u + \bar{S}_{u,d} \qquad (4.20)$$

where the A_c's, A_P^{n+1} and A_P^n are defined in equations (4.19) and the definitions of the mass flow rates appearing in these equations are illustrated by the following examples:

$$\dot{m}_e = (\rho\theta a)_P \frac{u_{r_E} + u_{r_P}}{2} \qquad (4.21)$$

and

$$\dot{m}_n = a_{n/nw} \{(\rho\theta)_P f_2 + (\rho\theta)_N (1 - f_2)\} v_{r_n}$$

$$+ a_{nw/wnn} \{(\rho\theta)_W f_2 + (\rho\theta)_{NW} (1 - f_2)\} v_{r_{wnw}} \qquad (4.22)$$

where f_2 is a linear interpolation factor given by:

$$f_2 = \frac{(\xi_2 \delta r)_{Nn}}{(\xi_2 \delta r)_{NP}} \qquad (4.23)$$

$a_{n/nw}$ represents the area bounded by the subscripts n and nw. $(\xi_2 \delta r)_{nP}$ is the radial distance from point n to point P (see Fig. (4.4)). Cell-boundary Peclet numbers which appear in the definition of the weighting factors α_e, α_w, etc. are given, for example, by:

$$Pe_n = \frac{\rho_{nw} v_{r_{nw}} (\xi_2 \delta r)_{NP}}{\Gamma_{nw}} \tag{4.24}$$

where ρ_{nw} and Γ_{nw} are evaluated from a weighted average of the surrounding values e.g.

$$\rho_{nw} = f_1 \{\rho_W f_2 + \rho_{NW}(1 - f_2)\} + (1 - f_1) \{\rho_P f_2 + \rho_N (1 - f_2)\} \tag{4.25}$$

Similarly, the integration of the radial momentum equation produces

$$A_P^{n+1} v_P^{n+1} = \Sigma_c A_c^{n+1} v_c^{n+1} + \Sigma_c A_c^n v_c^n + A_P^n v_P^n + \bar{S}_v + \bar{S}_{v,d} \tag{4.26}$$

4.3.2 Differencing of the Gas-Phase Source Terms

The final stage in the assembly of the difference equations for the individual variables is the assembly of the gas-phase source terms $\bar{S}_\phi$ and the interaction terms $\bar{S}_{\phi,d}$. The former are dealt with here, with the exception of the pressure gradient terms in the momentum equations, which are treated separately in section (4.5). The $\bar{S}_{\phi,d}$'s will be assembled later.

Momentum Equations

Many of the components of $\bar{S}_\phi$ for the momentum equations are similar in form, hence it will suffice to consider a representative example, taken to be the axial momentum sources, contained in $\bar{S}_\phi$: the differential expression for this is given in table (3.3). Firstly, the source term is differenced temporally as:

$$\bar{S}_u = \eta \bar{S}_u^{n+1} + (1 - \eta)\bar{S}_u^n \tag{4.27}$$

$\bar{S}_u$ is expressed in integral form (excluding the pressure gradient) as follows (the notation is that of Fig. (4.4)):

$$\bar{S}_u = a_{ew} \{(\theta\mu_{eff})_P \frac{u_E - u_P}{\xi_1 \delta x_{ew}} - (\theta\mu_{eff})_W \frac{u_P - u_W}{\xi_1 \delta x_{w/ww}}\}$$

$$+ (a\theta\mu_{eff}\xi_2 r \frac{\partial v}{\xi_1 \partial x})_{nw} - (a\theta\mu_{eff}\xi_2 r \frac{\partial v}{\xi_1 \partial x})_{sw}$$

$$-(P_P - P_W)a_{ew}(f_1\theta_W + (1 - f_1)\theta_P)$$

$$-\frac{2}{3}a_{ew}\{(\theta\mu_{eff}\nabla.\vec{u} + \rho\theta k)_P - (\theta\mu_{eff}\nabla.\vec{u} + \rho\theta k)_W\} \quad (4.28)$$

The cell faces values of $(\frac{\partial v}{\xi_1 \partial x})_{nw}, \theta_{nw}$ and μ_{eff} are evaluated by central differencing or linear interpolation, as appropriate. For example:

$$\frac{\partial v}{\xi_1 \delta x})_{nw} \simeq \frac{v_N - v_{NW}}{\xi_1 \delta x_{n/nwn}} \quad (4.29)$$

$$\theta_{NW} \simeq f_1\{v_W f_2 + v_{NW}(1 - f_2)\} + (1 - f_1)\{v_P f_2 + v_N(1 - f_2)\}$$

Turbulence Equations

The source terms for the turbulent kinetic energy and the dissipation rate equations are approximated by the expressions:

$$\overline{S}_k = \eta(\theta G_t - \rho\theta\varepsilon)_P^{n+1}V_P^{n+1} - (1 - \eta)(\theta G_t - \rho\theta\varepsilon)_P^n V_P^n \quad (4.30)$$

$$\overline{S}_\varepsilon = \eta\{\frac{\varepsilon}{k}(c_1\theta G_t - c_2\rho\theta\varepsilon) + \rho\theta\varepsilon\nabla.\vec{u}\}_P^{n+1}V_P^{n+1}$$

$$- (1 - \eta)\{\frac{\varepsilon}{k}(c_1\theta G_t - c_2\rho\theta\varepsilon) + \rho\theta\varepsilon\nabla.\vec{u}\}_P^n V_P^n \quad (4.31)$$

Energy Equations

The pressure work which appears in the source term of the energy equation plays a significant role in a gas undergoing compression. It has been neglected in the present study since no compression or expansion occurs. The other terms of the energy source term are small and they are neglected.

4.4 Differencing Practices

4.4.1 Spatial Differencing Schemes

The specification of the spatial weighting factors α_e and α_w (and by implication α_n and α_s) is very important, since it determines the accuracy, stability and economy of the solution procedure. Spalding (1972) and Raithby and Torrance (1974) showed that the use of solely central or upwind differencing can cause erroneous results if proper account is not taken of the value of the cell Peclet number (equation (4.7)). Therefore, the scheme which is used in the present study is a hybrid of central and upwind (donor-cell) differencing schemes.
This is:

$$\alpha_e = \begin{cases} \frac{1}{2} + \frac{1}{Pe_e} & , \text{ for } |Pe_e| \leq 2 \\ 1 & , \text{ for } Pe_e > 2 \\ 0 & , \text{ for } Pe_e < -2 \end{cases} \qquad (4.32)$$

Thus, when $|Pe| \leq 2$ ϕ can be assumed to vary linearly between adjacent grid nodes so that the cell face values of ϕ can be expressed in a central differencing formulation. Typically

$$\phi_e = \frac{\phi_P + \phi_E}{2}$$

For higher values of cell-face Peclet numbers, the central differencing scheme leads to unrealistic results (see for example, Spalding (1972) and Patankar (1980)). Because of this the upwind differencing scheme, firstly put forward by Courant et al (1952), is used in which the cell face values of ϕ are assigned the value of ϕ at the grid node from which the fluid has just passed. Thus, for example, $\phi_e = \phi_P$ for flow in the positive axial direction (i.e. from W to E) and $\phi_e = \phi_E$ for flow in the opposite direction.

The main advantage of the hybrid differencing scheme presented by equation (4.32) is that the numerical stability is enhanced, because the coefficient in the finite-difference equation (4.18) can then never be negative and thus the coefficient matrix is always diagonally dominant (Roache (1972)).

4.4.2 Temporal Differencing Schemes

The value of the temporal weighting factor η which appears in the discretized equations determines the time differencing scheme and hence, the type of the solution algorithm required. There are three well-known practices, being:

i. Fully implicit schemes ($\eta = 1$) which postulate that, at time t, ϕ suddenly changes from ϕ^n (the old time level value) to ϕ^{n+1} (the new one) and stays at that value over the whole time step δt. In those schemes, it can be seen from equation (4.18) that ϕ_P^{n+1} is related to neighbouring unknown field values (ϕ_E^{n+1}, ϕ_W^{n+1}, ϕ_N^{n+1} and ϕ_S^{n+1}). Hence simultaneous solution is required in order to solve the equations. The fully implicit approach is linearly stable for all δt because the coefficient A_P^n is always positive, as can be seen from equation (4.19). From the point of view of computation requirements, this scheme (as with the fully explicit scheme described below) requires coefficient evaluation at just one time level (A^{n+1}). Also, steady state solutions can be easily obtained with implicit schemes by using a very large time step (effectively infinite) (see Patankar (1980)).

ii. Fully explicit schemes ($\eta = 0$) essentially assume that the 'old' value of ϕ prevails throughout the entire time step except at time $t + \delta t$ where it takes the value ϕ^{n+1}. This produces especially simple equations for the ϕ_P^{n+1} since it relates them to the known old time level values

(ϕ^n), as can be seen from equation (4.18). Hence a straightforward solution is possible.

The convenience in this regard, is, however, offset by a serious limitation on the size of the allowable time step. It can be seen from equation (4.19) that the coefficient A_p^n can be negative, hence reducing the values of A_p in relation to the individual A_c's of the surrounding nodes and thus reduces the diagonal dominance of the coefficient matrix, this dominance is required for numerical stability reasons (Roache (1972)). Therefore, the size of the time step must be small enough to give positive A_p^n (equation (4.19)) and hence, produces a stable solution. Courant et al (1967) showed that if the momentum and continuity equations are all treated explicitly, then the time step must satisfy the following condition

$$\frac{(u_f + u_s)\delta t}{\delta x} < \lambda \qquad (4.33)$$

where u_f is the local fluid velocity, u_s is the sound speed, δx represents the cell spacing and λ is of order unity. The implied δt can be extremely small and hence, these schemes can be very expensive in terms of computation time.

Harlow and Amsden (1971) removed the sound speed component from equation (4.33) by differencing the pressure gradient terms of the momentum equations implicitly

(i.e. at the 'new' time level values) while retaining the explicit formulation for the remaining terms. Hence, with this 'semi-implicit' formulation the restriction on the time step becomes:

$$\frac{|u_f|\,\delta t}{\delta x} \tag{4.34}$$

iii. Time-centred 'Crank-Nicolson' schemes ($\eta = 0.5$). These assume a linear variation of ϕ between t and $t + \delta t$ and are formally second order in δt. Such schemes seem likely to be superior to both the fully implicit or explicit schemes for sufficiently small time step (see, e.g. Runchal (1977)). For such small δt it gives a more accurate solution than that of the fully implicit scheme. The Crank-Nicolson scheme is usually described as unconditionally stable. However, it does have the disadvantage that, in contrast to the fully implicit scheme, the coefficient A_p^n can become negative if δt is sufficiently large, producing oscillatory unbounded solution (see, e.g. Patankar and Baliga (1978) and Johns (1980)). It has also the disadvantage that the coefficients are required at both old and new time levels, giving rise to the need for more computer storage. This is by no means a trivial matter for multi-dimensional flows.

From the above discussion, it can be concluded that only the implicit scheme is free from constraints on δt other than those required for temporal accuracy. Hence it is the preferred choice when the latter constraint allows δt to be appreciably larger than that set by the Courant number limit (equation (4.34)) as in the case of the gas jets. For diesel spray computations, the temporal accuracy of the solution necessitates the use of smaller time steps due to the strong coupling of the gas and the droplets. Clearly, if it is necessary to work with a Courant number of order unity or less, the advantages of the implicit schemes are lost and it is more logical to imply a semi-implicit method since the latter requires no iteration.

Therefore, both the implicit and semi-implicit schemes will be given in some detail in the next section.

a. The implicit scheme

The substitution of $\eta = 1$ equation (4.19) yields:

$$
\begin{aligned}
A_N^{n+1} &= \dot{m}_n^{n+1}(\alpha_n^{n+1} - 1) \\
A_S^{n+1} &= \dot{m}_s^{n+1}\alpha_s^{n+1} \\
A_E^{n+1} &= \dot{m}_e^{n+1}(\alpha_e^{n+1} - 1) \\
A_W^{n+1} &= \dot{m}_w^{n+1}\alpha_w^{n+1} \\
A_P^{n+1} &= \frac{(\rho\theta V)_P^{n+1}}{\delta t} + \{\Sigma_c A_c^{n+1} + (\dot{m}_e - \dot{m}_w + \dot{m}_n - \dot{m}_s)^{n+1}\} \\
A_P^n &= \frac{(\rho\theta V)_P^n}{\delta t}
\end{aligned}
\qquad (4.35)
$$

The implicit form of the finite-difference mass conservation equation is obtained from equation (4.17) by putting $\phi = 0$, $\overline{S}_\phi = 0$ and $\overline{S}_{\phi,d} = \overline{S}_{m,d}$, thus:

$$\frac{(\rho\theta V)_P^{n+1} - (\rho\theta V)_P^n}{\delta t} + (\dot{m}_e - \dot{m}_w + \dot{m}_n - \dot{m}_s)^{n+1} = \overline{S}_{m,d} \qquad (4.36)$$

Introducing this equation into the coefficient A_P^{n+1} (equation (4.35)) yields:

$$A_P^{n+1} = \sum_c A_c^{n+1} + \frac{(\rho\theta V)_P^n}{\delta t} + \overline{S}_{m,d} \qquad (4.37)$$

The source term $\overline{S}_\phi$ is now expressed in the quasi-linear form as

$$\overline{S}_\phi = S_{\phi_E} + S_{\phi_I}\phi_P \qquad (4.38)$$

where the subscripts E and I refer to the 'explicit' and 'implicit' contributions respectively. An essential condition for stability is that S_{ϕ_I} is negative (Gosman and Pun (1974) and Patankar (1980)).

The final form of the discretized equation is therefore:

$$A'^{n+1}_P \phi_P^{n+1} = \sum_c A_c^{n+1}\phi_c^{n+1} + A_P^n\phi_P^n + S_{\phi_E}^{n+1} + \overline{S}_{\phi,d} \qquad (4.39)$$

where $A'_P = A_P^{n+1} - S_{\phi_I}^{n+1}$ (This will be written as A_P^{n+1} hereafter).

The above equations (4.39) relate the unknown values at point $P(\phi_P^{n+1})$ to the neighbouring unknown values (ϕ_c^{n+1}'s), hence an iterative solution is required.

b. The semi-implicit scheme

Setting $\eta = 0$ in equation (4.17) gives

$$\frac{(\rho\theta\phi V)_P^{n+1} - (\rho\theta\phi V)_P^n}{\delta t}$$

$$= (\alpha_e^n - 1)\dot{m}_e^n\phi_E^n + \alpha_w^n\dot{m}_w^n\phi_W^n$$

$$+(\alpha_n^n - 1)\dot{m}_n^n\phi_N^n + \alpha_s^n\dot{m}_s^n\phi_S^n$$

$$+ \{ - \alpha_e\dot{m}_e + (1 - \alpha_w)\dot{m}_w - \alpha_n\dot{m}_n + (1 - \alpha_s)\dot{m}_s \}^n\phi_P^n$$

$$+ \overline{S}_\phi + \overline{S}_{\phi,d} \qquad (4.40)$$

Here $\overline{S}_\phi$ is written for an unspecified time level because as will be shown later, the specification will vary according to the constituents.

Equation (4.40) can be written in a more compact form as

$$A_P^{n+1}\phi_P^{n+1} = \sum_c A_c^n\phi_c^n + A_P^n\phi_P^n + \overline{S}_\phi + \overline{S}_{\phi,d} \qquad (4.41)$$

where the subscript c denotes summation over the four nodes surrounding point P and the coefficients are given by:

$$A_N^n = (\alpha_n^n - 1)\dot{m}_n^n$$

$$A_S^n = \alpha_s^n\dot{m}_s^n$$

$$A_E^n = (\alpha_e^n - 1)\dot{m}_e^n$$

$$A_W^n = \alpha_w^n\dot{m}_w^n$$

$$A_P^n = \frac{(\rho\theta V)_P^n}{\delta t} - [(\dot{m}_e - \dot{m}_w + \dot{m}_n - \dot{m}_s)^n + \sum_c A_c^n]$$

$$A_P^{n+1} = \frac{(\rho\theta V)_P^{n+1}}{\delta t} \tag{4.42}$$

For the limiting case of inert particles moving without slip in a uniform field of ϕ and undergoing no other interaction with same, then the flux and source terms in equation (4.40) vanish and it reduces to

$$\phi_P^{n+1} = \frac{\theta_P^n}{\theta_P^{n+1}} \phi_P^n \tag{4.43}$$

From this it can be seen that an unphysical overshooting or undershooting may occur depending on the value of $\theta_P^n/\theta_P^{n+1}$. As a remedy for this problem, the continuity equation is differenced explicitly (by setting $\phi = 1$, $\overline{S}_\phi = 0$ and $\overline{S}_{\phi,d} = \overline{S}_{m,d}$ into equation (4.40)) as follows

$$\frac{(\rho\theta V)_P^{n+1} - (\rho\theta V)_P^n}{\delta t} = (\dot{m}_w - \dot{m}_e + \dot{m}_s - \dot{m}_s)^n + \overline{S}_{m,d} \tag{4.44}$$

Substitution from the above equation into equation (4.40) yields the same form of equation (4.41) with a modified definition of the coefficient A_P^n:

$$A_P^n = \frac{(\rho\theta V)_P^{n+1}}{\delta t} - \overline{S}_{m,d} - \sum_c A_c^n \tag{4.45}$$

with this treatment, equation (4.43) simply gives the typically acceptable result $\phi_P^{n+1} = \phi_P^n$.

Equation (4.41) can be easily solved for each variable since the right-hand side of the equation is given in terms of known values (old time level). In the momentum equations, the pressure gradients (which appear as part of the source term S_ϕ) are evaluated at new time level values (implicitly), hence their determination is necessary and constitute the main topic of the next section.

4.5 Solution of Continuity and Momentum Equations

For any Mach number flows, the pressure field strongly affects the local momentum balance. In a highly compressible (high Mach number) flows, its effect on the density can be significant and in such circumstances, the density may be regarded as one of the main dependent variables and can be extracted from the continuity equation. The pressure can then be obtained through the equation of state. Such an approach is not, however, helpful for constant-density flows because density is no longer a variable in the continuity equation.

In the present study, following Chorin (1968), Caretto et al (1972) and others, the pressure is calculated from its own equation formed by combining the continuity and momentum equations. For the sake of generality, the pressure correction equation will

be derived for a compressible flow although it is recognized that the flow in diesel engines is generally of low Mach number.

In the strategy of this algorithm each variable ϕ is expressed in terms of an approximation, labelled (ϕ^*), and a correction value, denoted (ϕ'), thus:

$$\begin{aligned} P &= P^* + P' \\ \rho &= \rho^* + \rho' = \rho^* + \left(\frac{\partial \rho}{\partial p}\right)_T P' \\ &= \rho^* + QP' \\ u &= u^* + u' \\ v &= v^* + v' \end{aligned} \tag{4.46}$$

In the first stage of the algorithm the approximate pressures P* are inserted into the momentum equations (4.20) and (4.26) which are solved to yield an approximate velocity field u*, v*, e.g.

$$A_P^{n+1} u_P^* = \Sigma_c A_c^{n+1} u_c^* + \Sigma_c A_c^n u_c^n + A_p^n u_P^n + \bar{S}_{u,d}$$

$$+ \tilde{S}_u - \{\eta \alpha_{ew}^{n+1}(P_P^* - P_W^*) + (1 - \eta)\alpha_{ew}^n (P_P^n - P_W^n)\} \tag{4.47}$$

where $\tilde{S}_u = \bar{S}_u - a_{ew}(P_P - P_W)$ (4.48)

Note that the superscript (n+1) has been dropped and those variables with (*), (') refer to the advanced time level value. The 'correct' pressure and velocity fields will satisfy:

$$A_P^{n+1}u_P = \sum_c A_c^{n+1}u_c + \sum_c A_c^n u_c^n + A_P^n u_P^n + \bar{S}_{u,d}$$

$$+\tilde{S}_u - \{\eta a_{ew}^{n+1}(P_P - P_W) + (1-\eta)a_{ew}^n(P_P^n - P_W^n)\} \qquad (4.49)$$

Subtraction of equation (4.47) from the above gives:-

$$A_P^{n+1}u_P' = \sum_c A_c^{n+1}u_c' - \eta a_{ew}^{n+1}(P_P' - P_W') \qquad (4.50)$$

If it is assumed that the major effect of changes in the pressure gradients is on the velocity at the node lying between the pressure nodes in question, then the term $\sum_c A_c^{n+1}u_c'$ can be ignored, yielding:

$$A_P^{n+1}u_P' \simeq -\eta a_{ew}^{n+1}(P_P' - P_W') \qquad (4.51)$$

hence, from (4.46):

$$u = u^* - \frac{\eta a_{ew}^{n+1}}{A_P^{n+1}}(P_P' - P_W')$$

or $$u_P = u_P^* - D_u(P_P' - P_W') \qquad (4.52)$$

similarly,

$$v_P = v_P^* - D_v(P_P' - P_S') \qquad (4.53)$$

where

$$D_u = \frac{\eta a_{ew}^{n+1}}{A_{P,u}^{n+1}}, \quad D_v = \frac{\eta(\frac{a_n + a_s}{2})^{n+1}}{A_{P,v}^{n+1}} \qquad (4.54)$$

Here it should be noted that the subscripts u and v have been attached to the coefficient A_p^{n+1} to associate them with the appropriate momentum component.

The finite-difference form of the continuity equation can be obtained from equation (4.17) by setting $\phi = 1$, $\overline{S}_{\phi} = 0$ and $\overline{S}_{\phi,d} = \overline{S}_{m,d}$;

$$\frac{(\rho\theta V)_P^{n+1} - (\rho\theta V)_P^n}{\delta t} + \eta\{(\rho\theta u_r a)_e^{n+1} - (\rho\theta u_r a)_w^{n+1} + (\rho\theta v_r a)_n^{n+1} - (\rho\theta v_r a)_s^{n+1}\} + (1 - \eta)\{(\rho\theta u_r a)_e^n - (\rho\theta u_r a)_w^n + (\rho\theta v_r a)_n^n - (\rho\theta v_r a)_s^n\} = \overline{S}_{m,d} \tag{4.55}$$

Substitution from equations (4.46), (4.52) and (4.53) into the above equation gives, after neglecting terms of order P'^2 and arrangement:

$$\frac{(\theta V Q P')_P^{n+1}}{\delta t} + \eta\theta_e^{n+1} a_{ew}^{n+1} \{u^*_{r,e} Q P'_e - \rho^*_e D_{u,e}(P'_E - P'_P)\} - \eta\theta_w^{n+1} a_{ew}^{n+1} \{u^*_{r,w} Q P'_w - \rho^*_w D_{u,w}(P'_W - P'_P)\} + \eta\theta_n^{n+1} a_n^{n+1} \{v^*_{r,n} Q P'_n - \rho^*_n D_{v,n}(P'_N - P'_P)\} - \eta\theta_s^{n+1} a_s^{n+1} \{v^*_{r,s} Q P'_s - \rho^*_s D_{v,s}(P'_P - P'_S)\} = - \frac{(\rho^*\theta V)_P^{n+1} - (\rho\theta V)_P^n}{\delta t} - \{\eta[(\rho^*\theta u^*_r a)_e^{n+1}$$

$$- (\rho^*\theta u_r^* a)_w^{n+1} + (\rho^*\theta u_r^* a)_n^{n+1} - (\rho^*\theta u_r^* a)_s^{n+1}]$$

$$+ (1 - \eta)\,[(\rho\theta v_r a)_e^n - (\rho\theta v_r a)_w^n + (\rho\theta v_r a)_n^n$$

$$- (\rho\theta v_r a)_s^n]\} + \overline{S}_{m,d} \tag{4.56}$$

Here the cell face quantities such as θ_e are obtained by linear interpolation as before. Defining the cell face 'Mach' number

$$Ma^2 = \frac{Qu_r^*}{D_u\rho^*} \quad \text{or} \quad \frac{Qv_r^*}{D_v\rho^*} \tag{4.57}$$

Equation (4.56) can be re-written as

$$\frac{(\theta VQP_P')^{n+1}}{\delta t} + \eta(\theta Qu_r a)_e^{n+1}\{P_e' - \frac{P_E' - P_P'}{Ma_e^2}\}$$

$$- \eta(\theta Qu_r a)_w^{n+1}\{P_w' - \frac{P_P' - P_W'}{Ma_w^2}\}$$

$$+ \eta(\theta Qv_r a)_n^{n+1}\{P_n' - \frac{P_N' - P_P'}{Ma_s^2}\}$$

$$- \eta(\theta Qv_r a)_s^{n+1}\{P_S' - \frac{P_P' - P_S'}{Ma_s^2}\} = (Su)_P \tag{4.58}$$

where $(Su)_P$ is the local mass imbalance in the mass conservation equation given by:

$$(Su)_P = -\{\frac{(\rho^*\theta V)_P^{n+1} - (\rho\theta V)_P^n}{\delta t}\} - \{\eta(\dot{m}_e^* - \dot{m}_w^* + \dot{m}_n^* - \dot{m}_s^*)^{n+1}$$

$$+ (1 - \eta)(\dot{m}_e - \dot{m}_w + \dot{m}_n - \dot{m}_s)^n\} + \overline{S}_{m,d} \tag{4.59}$$

By analogy with equation (4.11), the cell face values of P' are replaced by; for example,

$$P'_e - \frac{P'_E - P'_P}{Ma_e^2} = (1 - \alpha_e)P'_E + \alpha_e P'_P \tag{4.60}$$

After some manipulation, the final form of the P' equation is written in a compact form as:

$$A_P^{n+1} P'_P = \sum_c A_c^{n+1} P'_c + (Su')_P \tag{4.61}$$

where the coefficients are

$$A_E^{n+1} = - (1 - \alpha_e^{n+1})(\theta^{n+1} Q u_r^* a)_e$$

$$A_W^{n+1} = \alpha_w^{n+1} (\theta^{n+1} Q u_r^* a)_w$$

$$A_N^{n+1} = - (1 - \alpha_n^{n+1})(\theta^{n+1} Q v_r^* a)_n$$

$$A_S^{n+1} = \alpha_s^{n+1} (\theta^{n+1} Q v_r^* a)_s \tag{4.62}$$

$$A_P^{n+1} = \frac{(\theta Q V)_P^{n+1}}{\delta t} + \{ (\alpha^{n+1} \theta^{n+1} Q u_r^* a)_e - (1 - \alpha_w^{n+1})(\theta^{n+1} Q u_r^* a)_w$$

$$+ (\alpha^{n+1} \theta^{n+1} Q v_r^* a)_n - (1 - \alpha_s^{n+1})(\theta^n Q v_r^* a)_s \}$$

$$(Su')_P = - \{ \frac{(\theta \rho^* V)_P^{n+1} - (\theta \rho V)_P^n}{\delta t} \} - (\dot{m}_e^* - \dot{m}_w^* + \dot{m}_n^* - \dot{m}_s^*)^{n+1} + \overline{S}_{m,d}$$

In order that the above finite-difference equation (4.61) is diagonally dominant, it is necessary that the coefficient A_p^{n+1}

is equal to or greater than $\sum_c A_c^{n+1}$; this can be achieved by assuming that the factor

$$R = (Q\theta^{n+1}u_r^*a)_e - (Q\theta^{n+1}u_r^*a)_w + (Q\theta^{n+1}v_r^*a)_n - (Q\theta^{n+1}v_r^*a)_s \tag{4.63}$$

is equal to zero, yielding the final form of A_P^{n+1} as:

$$A_P^{n+1} = \sum_c A_c^{n+1} + \frac{\theta^{n+1} Q V_P^{n+1}}{\delta t} \tag{4.64}$$

The above assumption is not strictly correct but since equation (4.61) is an equation for corrections to P in which the final solution is obtained when $(Su')_P = 0$ and therefore all the P' 's are zero, no error is introduced.

As already indicated, the terms $\sum_c A_c^{n+1} u_c'$ are ignored. If they are retained they lead to considerable complication as discussed by Patankar (1980), it usually does not prevent the convergence of the solution procedure, although under-relaxation is often necessary.

The local mass imbalance $(Su')_P$ serves as a useful indicator of the convergence of the pressure correction equation. If $(Su')_P$ is everywhere zero, then the primed quantities are also equal to zero and a converged solution is obtained. This means that the starred values of the pressure and velocities (the last obtained values) will be the correct values which satisfy both the momentum and continuity equations. Thus any approximation made in the process of the derivation of the pressure correction equation is justified as long as the procedure converges.

4.6 Droplet Equations and Interaction Source Terms

Finite-difference forms of the Lagrangian droplet motion, heating and evaporating equations are used to calculate the behaviour of the spray. Equations (3.63), (3.64), (3.73) and (3.76) are integrated, as Dukowicz (1980), O'Rourke (1981) and Kuo (1982), using Euler's method. Thus:

$$x_d^{n+1} = x_d^n + u_d^n \delta t \tag{4.65}$$

$$r_d^{n+1} = r_d^n + v_d^n \delta t \tag{4.66}$$

$$u_d^{n+1} = u_d^n + B_d^n \delta t \left\{ \frac{(\rho\theta u)^{n+1}}{(\rho\theta)^n} + u'^n - u_d^{n+1} \right)\} - \frac{\delta t}{\rho_d^{n+1}} \frac{\delta p^{n+1}}{\delta x} \tag{4.67}$$

$$v_d^{n+1} = v_d^n + B_d^n \delta t \left\{ \frac{(\rho\theta v)^{n+1}}{(\rho\theta)^n} + v'^n - v_d^{n+1} \right)\} - \frac{\delta t}{\rho_d^{n+1}} \frac{\delta p^{n+1}}{\delta r} \tag{4.68}$$

$$T_d^{n+1} = T_d^n + \left(\frac{6\bar{\kappa}}{c_{p_d}\rho_d} \frac{z}{e^z - 1} Nu\right)^n \delta t \frac{(T^{n+1} - T_d^{n+1})}{(D_d^2)^{n+1}} + \left(\frac{3L}{c_{p_d}}\right)^n \frac{D_d^{n+1} - D_d^n}{D_d^{n+1}} \tag{4.69}$$

$$D_d^{n+1} = \{\left[m_d^n - \left(\frac{2\pi DP_t}{R_{mix}} \ell n\left(\frac{P_t - P_{v,\infty}}{P_t - P_{v,s}}\right) Sh\right)^n \frac{\delta t D_d^{n+1}}{(T + T_d)^{n+1}}\right] /$$

$$\left(\frac{\pi}{6} \rho_d^{n+1}\right)\}^{1/3} \tag{4.70}$$

where B_d is the 'drag function', given by:

$$B_d = \frac{3}{4} C_D \frac{\rho}{\rho_d} \frac{1}{D_d} |\vec{u} + \vec{u}' - \vec{u}_d| \tag{4.71}$$

It should be noted that, in the momentum equation (4.67) and (4.68) the drag function B_d is expressed in terms of old time level quantities in order that these equations contain only linear functions of the gas and droplet velocities. Similarly, the turbulent fluctuations $\overline{u}'$ and $\overline{v}'$ of the gas velocities, which would in general be non-linear function of mean flow velocities, are evaluated at old time level.

Evaluation of Interaction Terms

The void fraction θ and the interaction source terms $S_{\phi,d}$ appearing in the gas phase equations (see section (3.2)) are calculated for each appropriate cell by summing up the contributions from all droplets which reside at that cell at the end of each time step. The void fraction is:

$$\theta = 1 - \frac{1}{V_p} \sum_k \left(\frac{\pi}{6} D_{d,k}^3 N_{d,k}\right) \tag{4.72}$$

where $N_{d,k}$ is the number of droplets in parcel number k located in the scalar cell of volume V_p.

It should be pointed out that this and previous Lagrangian formulation contain no provision for recognizing that an assembly of droplet parcels cannot occupy more volume than that of the liquid they contain. Thus in situations where many parcels enter a given cell it is possible that the above equation can yield a negative void fraction.

The mass source term $\overline{S}_{m,d}$ appearing in the continuity equation (3.1) is given by

$$\overline{S}_{m,d} = -\frac{\pi}{6}\frac{N_{d,k}}{\delta t}\sum_k \{\rho_{d,k}^{n+1}(D_{d,k}^3)^{n+1} - \rho_{d,k}^{n}(D_{d,k}^3)^{n}\} \tag{4.73}$$

The momentum exchange rate for the axial momentum for the associated cell is:

$$\overline{S}_{u,d} = -\frac{\pi}{6}\frac{1}{\delta t}\sum_k N_{d,k}\{\rho_{d,k}^{n+1}(D_{d,k}^3)^{n+1}u_{d,k}^{n+1} - \rho_{d,k}^{n}(D_{d,k}^3)^{n}u_{d,k}^{n}\} \tag{4.74}$$

and similarly for the radial momentum as:

$$\overline{S}_{v,d} = -\frac{\pi}{6}\frac{1}{\delta t}\sum_k N_{d,k}\{\rho_{d,k}^{n+1}(D_{d,k}^3)^{n+1}v_{d,k}^{n+1} - \rho_{d,k}^{n}(D_{d,k}^3)^{n}v_{d,k}^{n}\} \tag{4.75}$$

Finally, the energy source term is given by:

$$\bar{S}_{h,d} = -\frac{\pi}{6}\frac{1}{\delta t}\sum_k N_{d,k}\{\rho_{d,k}^{n+1}(D_{d,k}^3)^{n+1}(c_{p_{d,k}}T_{d,k})^{n+1} - \rho_{d,k}^{n}(D_{d,k}^3)^{n}(c_{p_{d,k}}T_{d,k})^{n}\} \quad (4.76)$$

4.7 Solution Algorithms

4.7.1 Fully Implicit Solution Algorithm

As mentioned earlier in section (4.4), the fully implicit scheme is used for calculations of droplet-free gas jets. In such cases the void fraction θ is 1 and the interaction source terms $\bar{S}_{m,d}$, $\bar{S}_{u,d}$, $\bar{S}_{v,d}$ and $\bar{S}_{h,d}$ are, of course, zero. Hence, all the discretized equations, have the following form:

$$A_P^{n+1}\phi_P^{n+1} = \sum_c A_c^{n+1}\phi_c^{n+1} + A_P^n\phi_P^n + \bar{S}_\phi^{n+1} \quad (4.77)$$

They, therefore, consist of a set of non-linear coupled equations, thus, iterative solution is necessary. The particular method employed here is known as the SIMPLE algorithm. It advances through time in a series of steps. At each time step, the momentum equations are solved with the prevailing pressure $\bar{P}^*$

field inserted to yield velocity fields denoted by u* and v*. The pressure correction equation is then solved to provide a correction to the pressure field, for subsequent use in the momentum equations, and also corrections to the density and velocities are made through equations (4.46), (4.52) and (4.53) respectively. The remaining equations for the turbulent kinetic energy k, its dissipation rate ε, stagnation enthalpy h and fuel vapour mass fraction f are then solved and the temperatures and densities are recalculated from the enthalpy field and the equation of state. The whole cycle of solution, called 'outer' iteration, is then repeated until a converged solution is obtained (the convergence criteria will be given later in this subsection). The procedure then advances to the next time step. The main steps in the above solution algorithm is shown by the flow chart depicted in Fig. (4.5) and can now be summarised as follows:

1. Guess a pressure field P*.
2. Assemble and solve the momentum equations to obtain the starred velocities u* and v*.
3. Solve the pressure correction equation (4.61) to get P'.
4. Correct the density and velocities using equations (4.46), (4.52) and (4.53) respectively.
5. Solve the discretised equations for k, ε, h and f.
6. Recalculate the density from the enthalpy field and the equation of state.
7. Take the corrected pressures as the new guessed pressure field and return to step 2 unless a converged solution is obtained.

8. Start the next time step using the final ϕ values from the previous time step as guessed fields.

Solution of the Discretized Equations

The set of simultaneous equations for each variable is solved by a form of block iteration in which the equations for the grid nodes along each grid line are assembled to form a tri-diagonal matrix by temporarily assuming that the values on neighbouring lines are known (they are taken as the most recently calculated values, as in the Gauss-Seidel method). The tri-diagonal matrices are solved by Gaussian elimination using the 'Thomas algorithm' or 'Tri-Diagonal Matrix Algorithm' (TDMA). This practice is applied to the entire grid in an alternating direction fashion. These are called 'inner' iterations.

It should be noted that full convergence of these inner iterations is not necessary due to the need to continually update the coefficients of the discretized equations during the outer iterations and a few sweeps (number of inner iterations), typically three, suffices.

Convergence and Stability

During the course of the iteration, the solution is taken to be converged when the sums of the normalized absolute imbalances over the entire grid (here called the residuals), defined with respect to the general discretized equation (4.77) as:

$$R_\phi = \{\sum_c A_c^{n+1}\phi_c^{n+1} + A_P^n\phi_P^n + \bar{S}_\phi - A_P^{n+1}\phi_P^{n+1}\} \tag{4.78}$$

has fallen below a specified level, i.e.

$$\sum_F R_\phi < \gamma_1 N_\phi \tag{4.79}$$

$\sum_F$ denotes summation over all the control volumes of the flow domain, γ_1 is usually of the order 10^{-3} and N_ϕ is the normalization factor.

The normalization factors for the mass and momentum residuals are here taken as the total mass and momentum inflow evaluated at the nozzle exit. Hence, the mass normalization factor N_P, is given by:

$$N_P = \rho_o A_o U_o \tag{4.80}$$

in which ρ_o, A_o and U_o represent the exit density, area and velocity respectively. The momentum normalization factors N_u and N_v are evaluated as:

$$N_u = N_v = \rho_o A_o U_o^2 \tag{4.81}$$

The normalization factors for other variables are also evaluated from inflow properties. Hence, in the turbulent kinetic energy, it is the inflow of the kinetic energy of the jet and is given as:

$$N_k = \rho_o A_o U_o^3 \tag{4.82}$$

and for the enthalpy, the normalization factor N_h is

$$N_h = \rho_o A_o U_o c_{p_o} T_o \tag{4.83}$$

where c_{p_o} and T_o are the specific heat and the temperature of the gases at exit.

A further convergence criterion is applied in the form of a test on the rate of change of ϕ at a selected reference location in the solution domain. Convergence is assumed, together with the above criteria (equation (4.79)) if

$$|\phi^i - \phi^{i-1}| < \gamma_2 \phi^i \tag{4.84}$$

where γ_2 is of the order of 10^{-3} and the superscripts i and i-1 refer to values in successive iterations.

Because of the strong non-linearities in the partial differential equations and the coupling between the equations, numerical instability may develop, leading to divergence during the course of the calculation. This can usually be avoided by appropriate under-relaxation of the variable in the following manner:

$$\phi = \chi \phi^i + (1 - \chi)\phi^i \tag{4.85}$$

where χ is the specified under-relaxation factor (between 0 - 1). In the present study the procedure of Johns (1980) for the dynamic control of stability and convergence is used, in which the under-relaxation factors are adjusted during the calculation using the parameters ψ_1, ψ_2 and ψ_3 as follows:

a. A slight increase (3%) is made to the under-relaxation factor if the calculations are converging

$$\chi_\phi \rightarrow \psi_1 \chi_\phi \qquad (\phi = u \text{ or } v \text{ and } P')$$

where $\psi_1 = 1.03$.

b. A slight decrease is made if the residuals 'wander' about some mean level with no obvious trend

$$\chi_\phi \rightarrow \psi_2 \chi_\phi \qquad (\phi = u \text{ or } v \text{ and } P')$$

where $\psi_2 = 0.95$.

c. A substantial decrease is made if the calculation is diverging (residuals rapidly increasing)

$$\chi_\phi \rightarrow \psi_3 \chi_\phi \qquad (\phi = u \text{ or } v \text{ and } P')$$

where $\psi_3 = 0.5$.

Within the above procedure the relaxation factors also are constrained to lie in the range $0.3 < \chi < 0.7$, with the exception of that for P' whose upper bound is unity.

The under-relaxation factors specified for the other variables are summarized in the following table (4.1).

Table (4.1) The Under-relaxation factors for the scalar variables

Variable ϕ	k	ε	h	f	μ_t
χ_ϕ	0.7	0.7	0.7	0.7	0.7

4.7.2 Semi-Implicit Solution Agorithm

One possible semi-implicit method is to solve each of equations (4.67) and (4.68) in turn using u and v as old time level values. However, the coupling between the gas and droplet equations is so strong (because the droplet velocities appear in the right-hand side of the gas equations (4.20) and (4.26) and vice versa) that stability and accuracy would be impaired. It is better therefore to adopt a strategy of algebraically combining those equations at each mesh point in order to account for the interactions implicitly (Dukowicz (1980)). Similar comments apply to the energy equations of the two phases.

Coupled Gas and Momentum Equations

The discretization practice described in section (4.6) cause the new time level values of gas and droplet velocities to appear in linear form in droplet phase equations (4.67) and (4.68). Since in the semi-implicit formulation of the gas phase equations no other terms contain new time level velocities, it is possible to algebraically eliminate either the gas or droplet velocity, thus achieving a fully simultaneous solution without iteration. In the present analysis the new droplet velocities are eliminated from the gas phase momentum equations in the following manner.

Firstly axial and radial momentum equations for the gas are written in the following forms

$$\frac{(\rho\theta V)_P^{n+1}}{\delta t} u_P^{n+1} = \Sigma_c A_c^n u_c^n + A_P^n u_P^n - \theta_P^{n+1} a_{ew}(P_P - P_W)^{n+1}$$

$$+ (\tilde{S}_u)^n - \frac{\pi}{6}\frac{1}{\delta t}\Sigma_k N_{d,k}\{\rho_{d,k}^{n+1}(D_{d,k}^3)^{n+1} u_{d,k}^{n+1}$$

$$- \rho_{d,k}^n (D_{d,k}^3)^n u_{d,k}^n\} \qquad (4.86)$$

$$\frac{(\rho\theta V)_P^{n+1}}{\delta t} v_P^{n+1} = \Sigma_c A_c^n v_c^n + A_P^n v_P^n - \theta^{n+1}\frac{a_n + a_s}{2}(P_P - P_S)^{n+1}$$

$$+ (\tilde{S}_v)^n - \frac{\pi}{6}\frac{1}{\delta t}\Sigma_k N_{d,k}\{\rho_{d,k}^{n+1}(D_{d,k}^3)^{n+1} v_{d,k}^{n+1}$$

$$- \rho_{d,k}^n (D_{d,k}^3)^n v_{d,k}^n\} \qquad (4.87)$$

The droplet equations (4.67) and (4.68) can be arranged to give

$$u_{d,k}^{n+1} = \{u_{d,k}^{n} + \delta t B_d^n \left[\frac{(\rho\theta u)^{n+1}}{(\rho\theta)^n} + u'^n\right] - \frac{\delta t\, a_{ew}^{n+1}}{\rho_{d,k}^{n+1}(V_P)^{n+1}}(P_P - P_W)^{n+1}\}$$

$$/(1 + \delta t B_d^n)$$

$$v_{d,k}^{n+1} = \{v_{d,k}^{n} + \delta t B_d^n \left[\frac{(\rho\theta v)^{n+1}}{(\rho\theta)^n} + v'^n\right] - \frac{\delta t}{\rho_{d,k}^{n+1}(V_P)^{n+1}}$$

$$\left(\frac{a_n + a_s}{2}\right)^{n+1}(P_P - P_S)^{n+1}\}/(1 + \delta t B_d^n) \qquad (4.88)$$

where ρ, u, v, u' and v' are the gas density, the axial and radial mean gas velocities and the fluctuating components of same respectively in the cell where the droplet parcel k resides. Substitution of equations (4.88) into equation (4.86) yields, for the axial components

$$\frac{(\rho\theta V)_P^{n+1}}{\delta t} u_P^{n+1} = \sum_c A_c^n u_c^n + A_P^n u_P^n - \theta_P^{n+1} a_{ew}^{n+1}(P_P - P_W)^{n+1}$$

$$+ (\tilde{S}_u)_P^n - \frac{\pi}{6}\frac{1}{\delta t}\sum_k N_{d,k}\{\rho_{d,k}^{n+1}(D_{d,k}^3)^{n+1}\left[u_{d,k}^n + \right.$$

$$\delta t\, B_d^n \frac{(\rho\theta u)^{n+1}}{(\rho\theta)^n} - \delta t B_d^n (u')^n - \frac{\delta t}{\rho_{d,k}^{n+1}}\left(\frac{a_{ew}}{V_P}\right)^{n+1}(P_P - P_W)^{n+1}\Big]/$$

$$(1 + \delta t B_d^n) - \rho_{d,k}^n (D_{d,k}^3)^n u_{d,k}^n\} \qquad (4.89)$$

and after some manipulation the above equation takes the form:

$$\frac{(\rho\theta V)_P^{n+1}}{\delta t} u_P^{n+1} = \Sigma_c A_c^n u_c^n + A_P^n u_P^n - \theta_P^{n+1} a_{ew}^{n+1} (P_P - P_W)^{n+1} + (\tilde{S}_u)_P^n$$

$$+ \frac{\pi}{6} \frac{1}{\delta t} \Sigma_k N_{d,k} \{\rho_{d,k}^n (D_{d,k}^3) u_{d,k}^n - \rho_{d,k}^{n+1} (D_{d,k}^3)^{n+1} \frac{u_{d,k}^n + \delta t B_d^n u'^n}{1 + \delta t B_d^n}\}$$

$$- \frac{\pi}{6} \frac{1}{(\rho\theta)^n} \frac{1}{V_P^{n+1}} \Sigma_k N_{d,k} \rho_{d,k}^{n+1} (D_{d,k}^3)^{n+1} \frac{\delta t B_d^n}{1 + \delta t B_d^n} \frac{(\rho\theta V)_P^{n+1}}{\delta t} u_P^{n+1}$$

$$+ \frac{\pi}{6} \left(\frac{a_{ew}}{V_P}\right)^{n+1} \Sigma_k N_{d,k} (D_{d,k}^3)^{n+1} (P_P - P_W)^{n+1} \qquad (4.90)$$

Now define

$$AU = \frac{\pi}{6} \frac{1}{\delta t} \Sigma_k N_{d,k} \{\rho_{d,k}^n (D_{d,k}^3)^n u_{d,k}^n -$$

$$\rho_{d,k}^{n+1} (D_{d,k}^3)^{n+1} \frac{u_{d,k}^n + \delta t B_d u'^n}{1 + \delta t B_d^n}\} \qquad (4.91)$$

$$BU = \frac{\pi}{6} \frac{1}{(\rho\theta)^n} \frac{1}{V_P^{n+1}} \Sigma_k N_{d,k} \rho_{d,k}^{n+1} (D_{d,k}^3)^{n+1} \frac{\delta t B_d^n}{1 + \delta t B_d^n} \qquad (4.92)$$

$$CU = \frac{\pi}{6} \frac{1}{V_P^{n+1}} \Sigma_k N_{d,k} (D_{d,k}^3)^{n+1} \qquad (4.93)$$

With the introduction of these, equation (4.90) can be written as:

$$\frac{(\rho\theta V)_P^{n+1}}{\delta t} u_P^{n+1} = \Sigma_c A_c u_c^n + A_P^n u_P^n + (\tilde{S}_u)_P^n - \theta_P^{n+1} a_{ew}^{n+1} (P_P - P_W)^{n+1}$$

$$+ AU - BU \frac{(\rho\theta V)_P^{n+1}}{\delta t} u_P^{n+1}$$

$$+ CU\, a_{ew}^{n+1} (P_P - P_W)^{n+1} \qquad (4.94)$$

as after further arrangements

$$\frac{(\rho\theta V)_P^{n+1}}{\delta t} u_P^{n+1} = \{ \Sigma A_c^n u_c^n + A_P^n u_P^n + (\tilde{S}_u)_P^n$$

$$- (\theta^{n+1} - CU) a_{ew}^{n+1} (P_P - P_W)^{n+1}$$

$$+ AU \}/(1 + BU) \qquad (4.95)$$

The expressions AU, BU and CU are hereafter called the 'interaction source coefficients'. A similar result can be derived for the radial velocity component, thus:

$$\frac{(\rho\theta V)_P^{n+1}}{\delta t} v_P^{n+1} = \{ \Sigma_c A_c^n v_c^n + A_P^n v_P^n + (\tilde{S}_v)_P^n -$$

$$(\theta_P^{n+1} - CV) \frac{(a_n + a_s)^{n+1}}{2} (P_P - P_S)^{n+1} +$$

$$AV\}/(1 + BV) \qquad (4.96)$$

where

$$AV = \frac{\pi}{6}\frac{1}{\delta t}\sum_k N_{d,k}\{\rho_{d,k}^{n+1}(D_{d,k}^3)^n v_{d,k}^n - \rho_{d,k}^{n+1}(D_{d,k}^3)^{n+1}\frac{v_{d,k}^n + \delta t B_d^n v'^n}{1+\delta t B_d^n}\} \quad (4.97)$$

$$BV = \frac{\pi}{6}\frac{1}{(\rho\theta)^n}\frac{1}{V_P^{n+1}}\sum_k N_{d,k}\rho_{d,k}^{n+1}(D_{d,k}^3)^{n+1}\frac{\delta t B_d^n}{1+\delta t B_d^n} \quad (4.98)$$

$$CV = \frac{\pi}{6}\frac{1}{V_P^{n+1}}\sum_k N_{d,k}(D_{d,k}^3)^{n+1} \quad (4.99)$$

It should be noted that although equations (4.98) and (4.99) are formally the same as equations (4.92) and (4.93), the summations take place over the different cell volumes of the axial and radial velocity components. It should also be noted that the source coefficients are written in terms of known quantities apart from the new time level droplet diameters ($D_{d,k}^{n+1}$) and densities ($\rho_{d,k}^{n+1}$), whose determination is dealt with next

Simultaneous Solution of Gas and Droplet Energy and Evaporation Equations

The droplet energy and evaporation equations (4.69), and (4.70) are implicit in gas temperature, droplet temperature and droplet diameter. Here, with the help of a simplified version of the gas energy equation, the aforementioned equations are

solved simultaneously by iteration to give the new time level droplet temperature T_d^{n+1} and droplet diameter D_d^{n+1}. First, the gas energy equation is written as:

$$\frac{\partial}{\partial t}(\rho\theta h) = -\nabla.(\rho\theta\vec{u}h) + \nabla.(\theta\Gamma \text{grad } h) + \frac{1}{V_p}\frac{d}{dt}(m_d h_d) \qquad (4.100)$$

The relative importance of each of the above terms is investigated through the order of magnitude estimate given in table (4.2).

Table (4.2) Relative order of magnitude estimate of the different terms of the gas energy equation

term	order of magnitude	relative order of magnitude
$\frac{\partial}{\partial t}(\rho\theta h)$	$\frac{\rho\theta c_p T}{t}$	1
$\nabla.(\rho\theta\vec{u}h)$	$\frac{\rho\theta u c_p T}{L}$	$\frac{ut}{L}$
$\nabla(\Gamma\theta \text{grad } h)$	$\frac{\mu\theta c_p T}{L^2}$	$\frac{\mu t}{L^2\rho}$
$\frac{1}{V_p}\frac{d}{dt}(m_d h_d)$	$\frac{1-\theta}{t}\rho_d c_{p_d} T_d$	$\frac{1-\theta}{\theta}\frac{\rho_d}{\rho}\frac{c_{p_d}}{c_p}\frac{T_d}{T}$

Typical values of θ and t are 0.9 and 3×10^{-6} s. respectively while the values of gas and droplet properties as well as L (the

length) vary along the spray length. Therefore, the relative order of magnitude of the different terms of equation (4.100) at three locations along the spray is given in the following table:

term	near the injector	middle of spray	near spray tip
$\frac{\partial}{\partial t}(\rho\theta h)$	1	1	1
$\nabla.(\rho\theta\vec{u}h)$	0.2	0.08	0.024
$\nabla.(\Gamma\theta\text{grad } h)$	3×10^{-4}	1×10^{-4}	2×10^{-4}
$\frac{1}{V_p}\frac{d}{dt}(m_d T_d)$	5	5.7	6.1

From the above table, it is clear that the interaction source term is much larger than the convection term $\{\nabla.(\rho\theta\vec{u}h)\}$ and the diffusion term $\{\nabla.(\Gamma\theta\text{grad } h)\}$ in any location within the spray region, therefore, here, the gas energy equation is simplified by assuming that the droplet source term dominates the right-hand side of equation (4.100) (it is important to note that the full form of the gas energy equation is solved along with the other gas phase equations, as will be shown later in this section), thus:

$$T^{n+1} \simeq T^n - \left(\frac{\pi \rho_{d,k} N_{d,k} c_{p_{d,k}}}{6 \rho V_p c_{p_{mix}}}\right)^n \left\{ (D^3_{d,k})^{n+1} T^{n+1}_{d,k} - (D^3_{d,k})^n T^n_{d,k} \right\} \quad (4.101)$$

which can be expressed more compactly as:

$$T^{n+1} = F - E(D^3_{d,k})^{n+1} T^{n+1}_{d,k} \quad (4.102)$$

where

$$E = \left(\frac{\pi \rho_{d,k} N_{d,k} c_{p_{d,k}}}{6 \rho V_p c_{p_{mix}}}\right)^n$$

and

$$F = E\,(D^3_{d,k})^n T^n_{d,k} + T^n$$

The droplet energy equation (4.69) is written in the compact form as:

$$T^{n+1}_{d,k} = \frac{A}{(D^2_{d,k})^{n+1}} (T^{n+1} - T^{n+1}_{d,k}) - \frac{C}{D^{n+1}_{d,k}} + B \quad (4.103)$$

where

$$A = \left(\frac{6\bar{\kappa}}{c_{p_{d,k}} \rho_{d,k}} \frac{z}{e^z - 1} Nu\right)^n \delta t$$

$$B = \left(\frac{3L}{c_{p_{d,k}}}\right)^n + T^n_{d,k}$$

$$C = \left(\frac{3L}{c_{p_{d,k}}}\right)^n D^n_{d,k}$$

The droplet mass equation (4.70) is similarly treated:

$$D_{d,k}^{n+1} = \{ [m_d^n - G \frac{D_{d,k}^{n+1}}{(T + T_{d,k})^{n+1}}] / (\frac{\pi}{6} \rho_{d,k}^{n+1}) \}^{1/3} \qquad (4.104)$$

where

$$G = \{ \frac{2\pi D P_t}{R_{mix}} \ell n (\frac{P_t - P_{v,\infty}}{P_t - P_{v,s}}) Sh \}^n \delta t$$

Because equations (4.102), (4.103) and (4.104) are non-linear and coupled they are solved iteratively.

At low ambient pressure (lower than the critical pressure of the pure hydrocarbon fuel) the droplet temperature in restricted by the condition

$$T_d \leq T_{boil} \qquad (4.105)$$

where T_{boil} is the boiling temperature of the liquid i.e. the temperature at which the partial pressure of the fuel vapour at the droplet surface equals the charge pressure P_t, thus from equation (3.82) the boiling temperature is given as:

$$T_{boil} = \frac{3743.84}{12.12767 - \ell n(P_t/6894.757)} + 93.022 \qquad (4.106)$$

In the absence of other effects, at charge conditions at or higher than the thermodynamic critical point of the liquid fuel, the radial regression velocity of the liquid surface becomes comparable to the radial gas velocity since the densities of the two phases are the same and the gas mixtures in the film surrounding the droplet behave in a non-ideal manner (see e.g. Maltosz et al (1972) and Kadota et al (1976)).

However, the solubility of the liquid increases and at the critical condition itself all characteristics of both phases are the same; temperature, pressure and composition. Faeth (1983) reports that the presence of dissolved gases in the liquid fuel at high charge pressure tends to raise the critical conditions of the liquid. This trend was observed by Manrique et al (1969) who concluded that the droplets heat continuously without reaching the (presumably elevated) critical condition before they are completely evaporated. Therefore, in the present study, the droplets are assumed to heat up continuously. The upper temperature limit being the surrounding gas temperature. However, the partial pressure of the fuel vapour at droplet surface is restricted not to exceed the gas pressure i.e.

$$P_{v,s} \leq P_t \tag{4.107}$$

Since it would be unrealistic to extrapolate the equilibrium curve of the fuel vapour partial pressure beyond the charge pressure.

As far as the liquid and vapour properties at elevated pressure are concerned, and in the absence of any experimental information, they are here taken from the low pressure values, given in Chapter 3.

Solution of Equations

As already shown in section (4.4), in the semi-implicit scheme, all the unknown new field values of ϕ's (ϕ^{n+1}) are related to known old time level values (ϕ^{n}) except in the momentum equation (4.95) and (4.96) where the pressure gradients are given in terms of new quantities. Thus for a given pressure field, the discretized form of the gas conservation equations are solved point by point and no special provision is necessary for them.

The pressure correction equation (which is cast in fully implicit form) is solved by the same alternating direction line method used in the implicit algorithm and described in section (4.7.1).

The droplet equations are also explicit except for the mass and energy conservation equations which are non-linear, coupled and implicit, therefore, require iteration. However, since the droplets are non-interacting, the equation for each droplet can be treated in turn.

Order of Solution

In summary, each time step entails the following sequence of operations as also shown in the flow chart given in Fig. (4.6).

1. The new droplet positions are calculated from equations (4.65) and (4.66).

2. The new droplet temperatures, masses and hence sizes are obtained by iterative solution of equations (4.102), (4.103) and (4.104).
3. The new void fractions are obtained by inserting the new droplet sizes into equation (4.72), and the mass, momentum and energy transferred to the gas are evaluated through equations (4.73), (4.91)-(4.93), (4.97)-(4.99) and (4.76).
4. The momentum equations (4.95) and (4.96) are solved using the prevailing pressure field P* to give the starred velocities u* and v*.
5. The new fuel vapour mass fractions and gas enthalpies are obtained from equation (4.41) with ϕ equals f and h respectively. Calculate the gas density from the enthalpy field and the equations of state.
6. The new turbulent kinetic energy and its dissipation rate are calculated from equation (4.41) with ϕ = k and ε respectively.
7. The gas pressures, densities and velocities are corrected through solving the pressure correction equation (4.61) and then applying equations (4.46), (4.52) and (4.53).
8. The new droplet velocity components are obtained from equations (4.88).

Stability Requirements

The semi-implicit scheme adapted in the present study eliminates the need to observe the Courant sound speed restriction on the magnitude of the computational time step (see Harlow and Amsden (1971)). Also, the present simultaneous treatment of the gas and droplet equations obviates the need to use a very small time step due to the close coupling of both phases. However, there are still some restrictions on the time step that must be obeyed to ensure stability and accuracy of the solution.

As the convection terms in the gas momentum equations are differenced explicitly, stability requires that a fluid element cannot move by more than a cell dimension, giving (see Courant et al (1967)):

$$\max\left(\frac{|u|\delta t}{\delta x}, \frac{|v|\delta t}{\delta r}\right) < 1 \qquad (4.108)$$

A similar constraint applies to the diffusion of a fluid element, to the explicit treatment of the turbulent diffusion terms:

$$\max\left(\frac{\Gamma_\phi \delta t}{\rho \delta x^2}, \frac{\Gamma_\phi \delta t}{\rho \delta r^2}\right) < 1 \qquad (4.109)$$

Another time step constraint arises due to the fact that the source terms S_ϕ's are differential explicitly. In the momentum equations they are diffusion-like terms and are therefore, covered by equation (4.109). In the turbulence equations, the source term $\bar{S}_k$ (equation (4.30)) can become negative if the dissipation is higher than the generation G_t, thus producing negative values of

k. As a remedy, $\bar{S}_k$ and $\bar{S}_\varepsilon$ are manipulated with the help of equation (3.33) to give:

$$\bar{S}_k^n = (\theta G_t - \theta c_\mu \rho^2 k^2/\mu)^n \tag{4.110}$$

$$\bar{S}_\varepsilon^n = \left[c_1 c_\mu \rho\theta G_t \frac{k}{\mu} - c_2 \rho\theta \frac{\varepsilon^2}{k} + \rho\theta\varepsilon\nabla.\vec{u}\right]^n \tag{4.111}$$

With these practices temporal stability was found to be ensured by obedience to the foregoing constraints.

Another important condition for stability is that the void fraction at the cell under consideration must not become negative, which the Lagrangian droplet treatment does not ensure as was pointed out in connection with equation (4.72). It will be shown later that the avoidance of that situation effectively puts a constraint on the minimum cell size.

For the <u>accuracy</u> of computing the mass, momentum and energy interaction terms, the time step δt must be a fraction of the residence time of a parcel in a cell (O'Rourke (1981)), thus

$$\max.\left(\frac{|u_d|\delta t}{\delta x}, \frac{|v_d|\delta t}{\delta r}\right) < 1 \tag{4.112}$$

A further constraint on the time step is implied in order to obtain an <u>accurate</u> calculation of droplets behaviour using 'Euler' integration method as will be seen in Chapter 5.

4.8 Boundary and Initial Conditions

The complete representation of the mathematical problems requires the specification of the conditions at the boundaries of the domain of interest for each dependent variable. These boundary conditions are usually either specification of the variable itself, or the value of its normal gradient at the boundary, or a combination of the two.

This section describes the ways in which the conditions at the various boundaries are handled, as well as the specification of the initial conditions.

4.8.1 Axis of Symmetry

At the symmetry axis all the gas-phase properties are assumed to have zero radial gradient, apart from the radial velocity, which is set to zero. The assumption of zero radial gradient is imposed in the finite-difference equation (4.18) by setting the appropriate coefficients A_c to zero.

In spray computations, there is a possibility that the droplets attempt to stray across the axis of symmetry due to the present treatment of the turbulent dispersion of droplets, thereby causing a loss of mass and momentum of the liquid. In the present study a provision is made to reflect the droplets

which cross the axis; if the outcome of equation (4.66) is that $r_d^{n+1} < 0$, the reflection is imposed by setting $r_d^{n+1} \rightarrow - r_d^{n+1}$ and $v_d^{n+1} \rightarrow - v_d^{n+1}$.

4.8.2 Outflow Boundary

The fluid condition at the outlet section is not always known in advance, nevertheless, a boundary condition for each variable must be specified. However, provided that the outlet plane is located where the flow has a parabolic or boundary layer nature (high Peclet number), the effect of the outlet boundary condition on the upstream fluid is small. The normal practice is to assume that the gas-phase properties have zero gradients normal to the boundary except the axial velocity at the boundary u_B, which is obtained by some form of extrapolation from the interior velocities and then corrected to ensure that overall continuity is maintained. Thus:

$$u_B \rightarrow u_B + \delta u \tag{4.113}$$

where the velocity increment δu is calculated from:

$$\delta u = \frac{\dot{m}_{in} - \int_{A_B} \rho_B \vec{u}_{B-1} dA_B}{\int_{A_B} \rho_B dA_B} \tag{4.114}$$

where $\dot{m}_{in}$ is the total mass inflow and the subscripts B and B - 1 denote boundary and next to the boundary respectively while A_B represents the area of the boundary.

4.8.3 Free Stream Boundary

Provided that the freestream boundary shown in Fig. (4.1) does not intersect with the jet or the spray anywhere within the solution domain, all the gas-phase properties are assumed to have the free stream values i.e.

$$k = \varepsilon = 0$$

The velocity components are assumed to satisfy continuity at the free stream boundary, thus:

$$\frac{\partial u}{\partial x} = 0 \ ,$$

$$\frac{\partial rv}{\partial r} = 0 \qquad (4.115)$$

4.8.4 Inflow Boundary

a. Gas jets

Referring to Fig. (4.7) which shows the grid arrangement used in gas jet computations, the inlet boundary conditions across the jet exit ($r < r_j$) are:

$$u_{in} = U_o$$

$$v_{in} = 0$$

$$k_{in} = iU_o^2 \tag{4.116}$$

$$\varepsilon_{in} = k_{in}^{3/2}/\ell_o \tag{4.117}$$

where r_j stands for the nozzle or injector radius, U_o is the velocity at the nozzle exit and i and ℓ_o are the turbulence intensity and dissipation length scale respectively. ℓ_o is related to the jet diameter d_j through:

$$\ell_o = \lambda . d_j \tag{4.118}$$

The region of the inflow boundary on top of the nozzle ($r > r_j$) is treated as a no-slip wall for which:

$$u = v = k = \varepsilon = 0$$

As the flow adjacent to that wall which is mainly due to entrainment is laminar, it is not necessary to apply the 'wall functions' to estimate the values of v, k and ε adjacent to the wall (see Looney (1982)).

b. Spray computations

The inflow boundary conditions imposed on the gas-phase properties are those of a no-slip wall similar to the gas jets, except for the 'injection cell' which is located adjacent to the injection nozzle, as shown in Fig. (4.1). Following O'Rourke (1981), the gas and droplets are injected from the injection cell with the same axial velocity in the manner described below.

The present spray representation cannot simulate the process of the atomization of the liquid jet emerging from the nozzle: thus it is necessary to make some assumptions concerning the nature of the droplets produced and their effect on the gas flow, for use as the upstream boundary conditions in the calculations. In the present treatment, it is assumed that within the injection cell, the jet breaks up into non-interactive spherical droplets of known initial size and velocity, and the gas is assumed to be accelerated to this velocity.

With reference to Fig. (4.8), the liquid jet enters the cell from the nozzle whose radius is r_j. The droplet parcels exit from the cell within a cone of angle 2β. The exit radius r_s is evidently

$$r_s = r_j + \delta x \tan\beta \qquad (4.119)$$

where δx is the axial dimension of the injection cell which is chosen such that $r_s \leq \delta r$ (the radial dimension of the cell). The cell exit values of the droplet axial velocity U_{do} and the void fraction θ_o are determined from balances of liquid mass and

mixture axial momentum on the injection cell. It is assumed for this purpose that the axial velocity U_o of the gas is equal to U_{do}. This assumption is justified because the mass of liquid in the injection cell is much larger than that of the gas there and therefore only a small fraction of the liquid momentum need be transferred to the gas to bring the velocities into equilibrium. The equation for the conservation of liquid is:

$$\rho_d U_{inj} \pi r_j^2 = (1 - \theta_o)\rho_d U_{do} \pi r_s^2 \tag{4.120}$$

and that for the mixture axial momentum is

$$\rho_d U_{inj}^2 \pi r_j^2 = \rho_d (1 - \theta_o) U_{do}^2 \pi r_s^2$$

$$+ \rho U_{do} \pi \{\delta r^2 - (1 - \theta_o) r_s^2\} \tag{4.121}$$

where U_{inj} is the liquid injection velocity.
Equation (4.120) and (4.121) can be solved to give

$$\frac{U_{do}}{U_{inj}} = \frac{-(1 - \frac{\rho}{\rho_d}) + \sqrt{(1 - \frac{\rho}{\rho_d})^2 + 4\frac{\rho}{\rho_d}(\frac{\delta r}{r_j})^2}}{2\frac{\rho}{\rho_d}(\frac{\delta r}{r_j})^2} \tag{4.122}$$

and

$$\theta_o = 1 - \frac{U_{inj}}{U_{do}}(\frac{r_j}{r_s})^2 \tag{4.123}$$

The entrainment gas velocity v_o through the top of the cell is obtained from a conservation of the gas mass assuming

incompressibility, thus:

$$v_o = U_{do} \frac{(1 - \theta_o)r_s^2 - \delta r^2}{2\delta r \delta x} \tag{4.124}$$

The injection cell gas velocity components $u = U_{do}$ and v_o and the void fraction θ_o are calculated at the beginning of each time step using the measured time histories of the fuel injection rate and spray cone angle, as will be shown later, and they are used as boundary conditions at that time step.

4.8.5 Initial Conditions

a. Gas Jets

As the gas jets in the present study are injected into an initially quiescent medium, the ambient gas velocities are initially set to zero everywhere in the solution domain. The thermodynamic properties of the gas i.e. pressure, temperature and density are set initially in a fashion consistent with the equation of state. The initial turbulent kinetic energy and dissipation rate are set to give a level of turbulent viscosity equal to the molecular viscosity. For this purpose, a value of $k = 0.01\ k_{in}$ is used and ε is calculated from equations (4.117) and (4.118)

b. Spray Calculations

In order to simulate the conditions of the initially quiescent medium which the sprays are injected into, the gas velocity components are set initially to zero except for the injection cell which has its own treatment as described earlier. Since initially there is no liquid in the zone of interest the fuel vapour mass fraction is set to zero, and the thermodynamic properties of the gas are set in a similar manner to the gas jets. The turbulent kinetic energy and dissipation rate are initially set to give a level of viscosity equal to the molecular viscosity. i.e. $k = 1 \times 10^{-5} u_{av}^2$; where u_{av} is the average injection velocity and ε is calculated from equation (4.117) and (4.118).

The initial conditions of the injected droplet parcels are the subject of the next subsection.

Droplet Injection

As noted earlier the droplet parcels emerge from the injection cell with assigned velocities, sizes and temperatures.

Concerning the velocities, all droplets are assigned the axial value U_{do} as calculated from equation (4.122). The radial component is randomly assigned in the range $0 < v_{do} < U_{do} \tan\beta$, is an effort to simulate the observed effect of atomization to produce an initial spread. As explained later, β is obtained from measurements.

The mass injected at each time step δm_i (from time t_i to $t_i + \delta t$) is obtained from the injection rate diagram shown in

Fig. (4.9) and allocated to N_p droplet parcels (N_p is the number of droplet parcels introduced per time step). The diameters of the droplets are randomly chosen from the range

$$D_{d,min} < D_{d,k} < D_{d,max} \quad \text{for } 1 < k < N_p$$

and $D_{d,min}$ and $D_{d,max}$ are the assumed lower and upper bounds on D_d respectively.

The proportions of the total liquid mass in each parcel, and hence the number of droplets $N_{d,k}$ in same, is obtained from an assumed size distribution function that relates the probability σ_k of finding a droplet of volume $\frac{\pi}{6} D_{d,k}^3$ to the droplet diameter (as shown in Fig. (4.10)) thus:

$$N_{d,k} = \frac{\delta m_i \sigma_k}{\sum_{k=1}^{N_p} \sigma_k \frac{\pi}{6} \rho_d D_{d,k}^3} \tag{4.125}$$

The injection velocity U_{inj} of the droplets is calculated, at each time step, from the mass injected as:

$$U_{inj} = \frac{\delta m_i}{\pi \rho_d r_j^2 \delta t} \tag{4.126}$$

Alternatively, if the pressure drop ΔP across the nozzle and the discharge coefficient C_Q are known, then

$$U_{inj} = C_Q \sqrt{\frac{2\Delta P}{\rho_d}} \tag{4.127}$$

The spray cone angle (2β) must be provided for the injector in question by direct measurement or through empirical formula. Reitz (1978) has developed a semi-empirical method for calculating this angle, which is

$$\tan\beta = A\sqrt{\frac{\rho}{\rho_d}} \tag{4.128}$$

where A is a constant dependent on the nozzle used and ρ and ρ_d are the ambient gas and droplet densities respectively.

Finally, the droplet size distribution was measured downstream of the injector and the data were fitted by e.g. the Rosin-Rammler distribution (Boulderstone et al (1981)) as:

$$\frac{dV}{V} = n\,\frac{D_d^{n-1}}{\bar{D}}\,e^{-\{(D_d/\bar{D})^n\}}\,dD_d \tag{4.129}$$

where n and $\bar{D}$ are experimentally determined exponent and mean diameter respectively.

4.9 Closure

In this chapter, the partial differential equations of the gas phase have been discretized yielding algebraic expressions from which the values of velocities, pressure, energy, turbulence quantities and the fuel vapour mass fraction may be found at a finite number of points in the flow.

The discretized equations have been expressed in terms of general spatial and temporal difference functions. A hybrid of central and donor-cell spatial differencing has been selected for reasons of stability and accuracy and the implicit and semi-implicit temporal differencing schemes have been presented.

The pressure field and hence, the pressure gradient terms of the momentum equations have been obtained by linking the continuity and momentum equations.

The droplet equations have been differenced using Euler's method and combined with the gas-phase equations to enable simultaneous solution for the gas and droplet velocities. A method has also been developed to solve the droplet mass and energy equations simultaneously with the simplified gas energy equation.

Finally, the treatment of the initial and boundary conditions has been described with particular emphasis on the injection cell treatment.

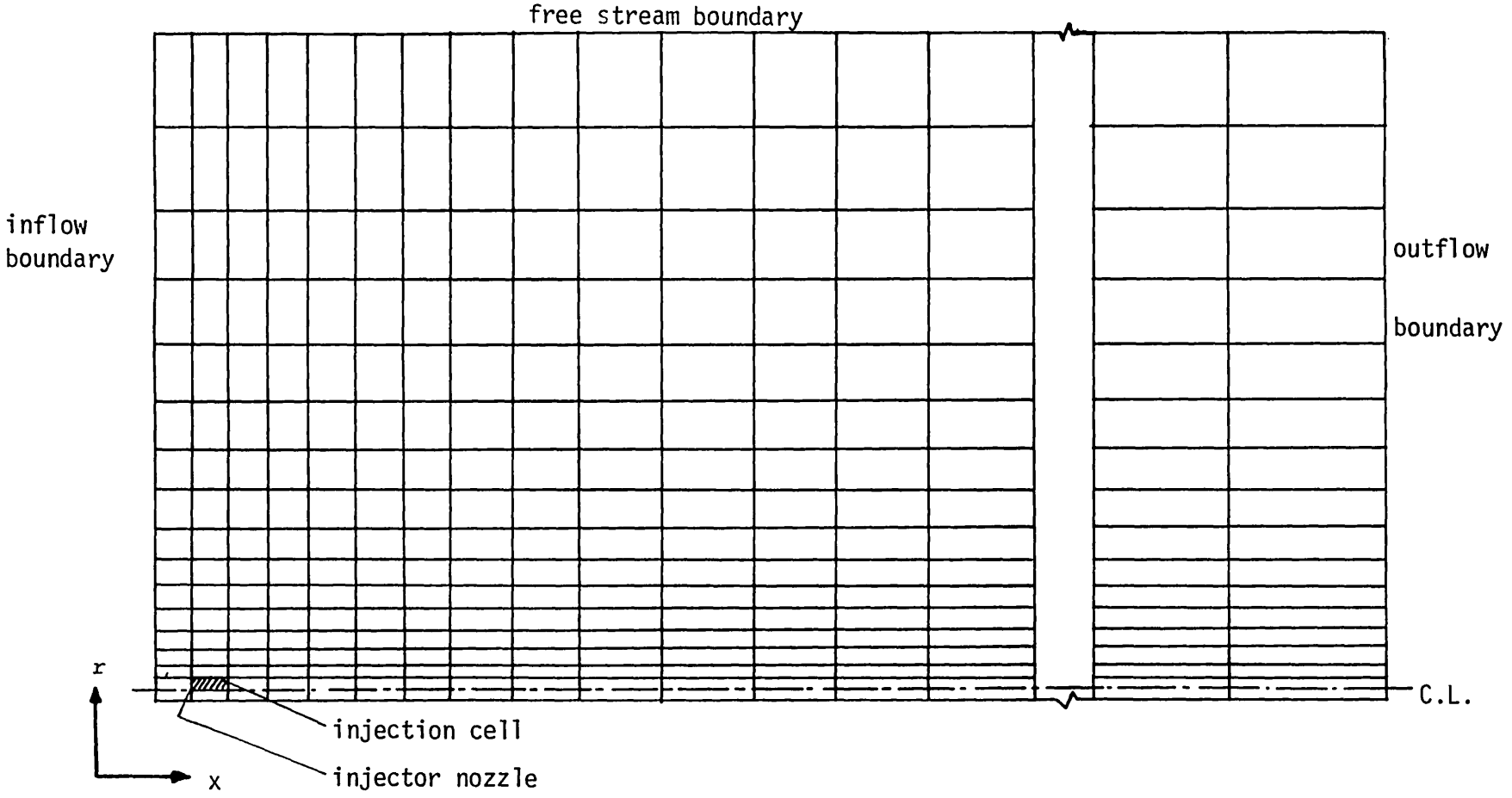


Fig. (4.1) The computational grid

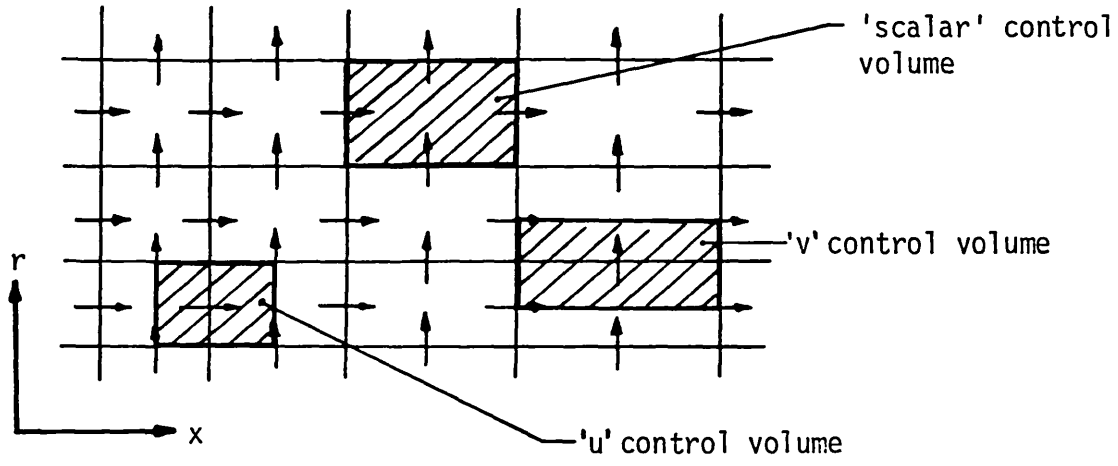


Fig. (4.2) The staggered grid arrangement

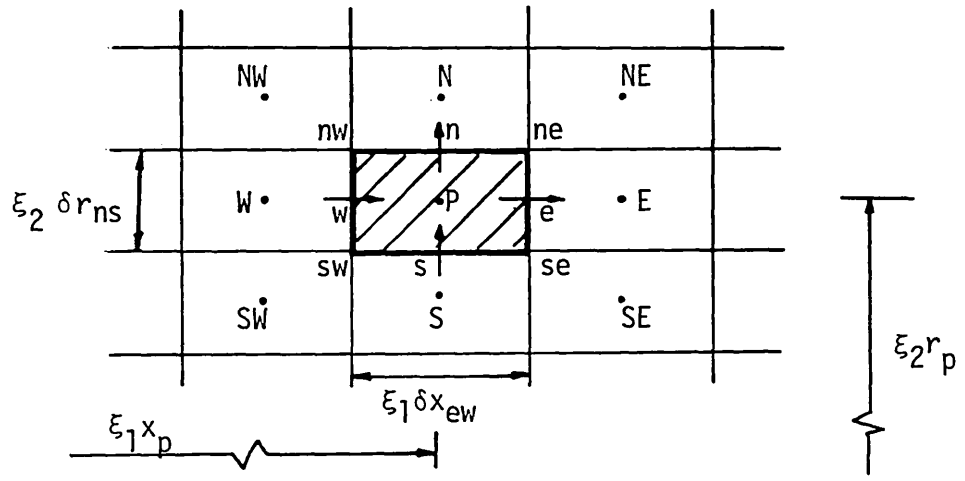


Fig. (4.3) Scalar control volume and notation

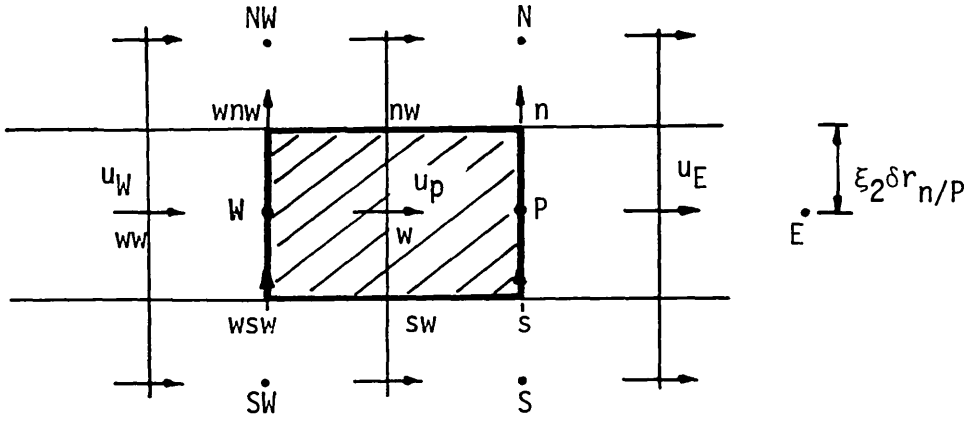


Fig. (4.4) Details of control volume for axial velocities

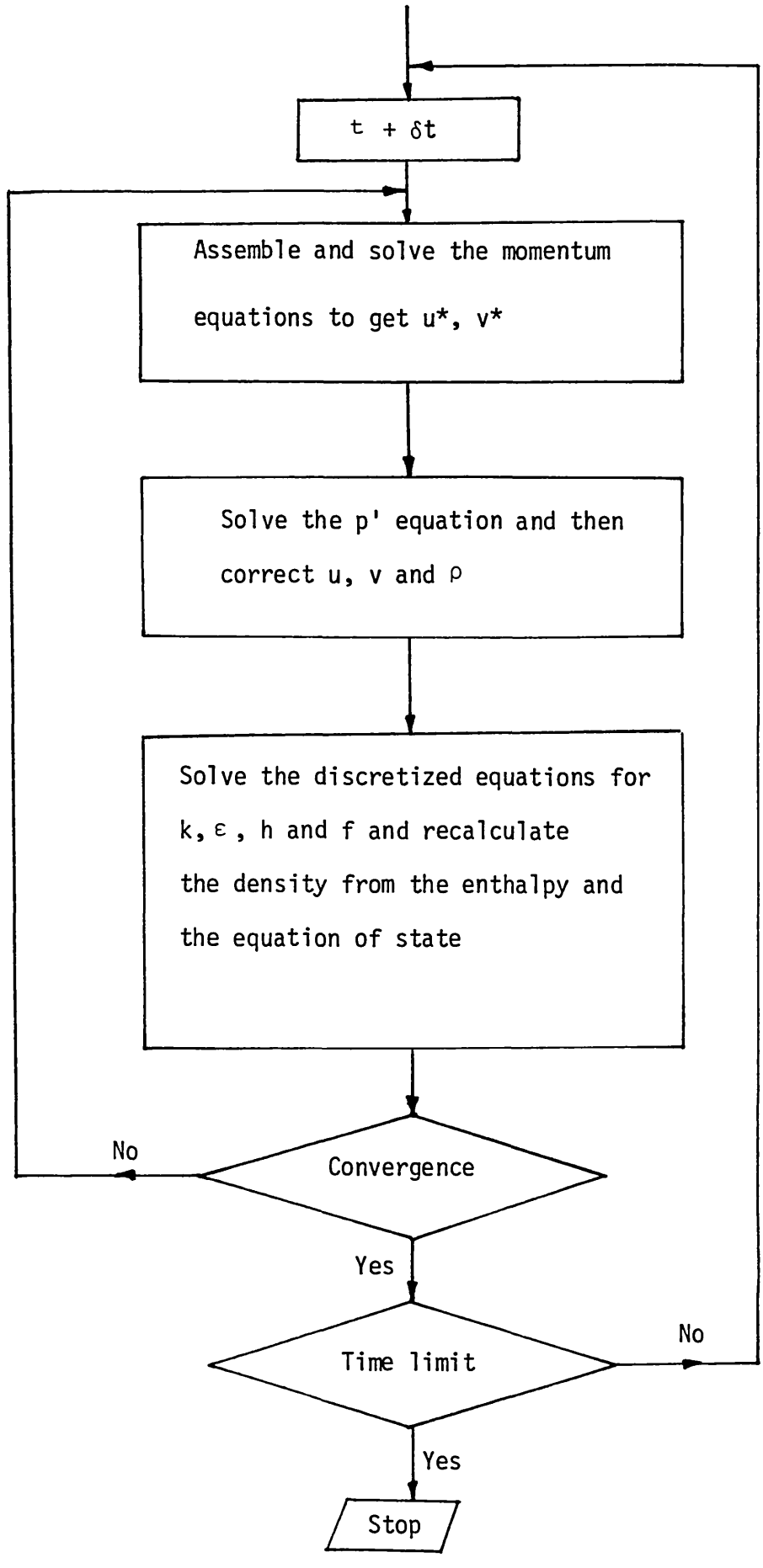


Fig. (4.5) Flow chart of the fully implicit scheme

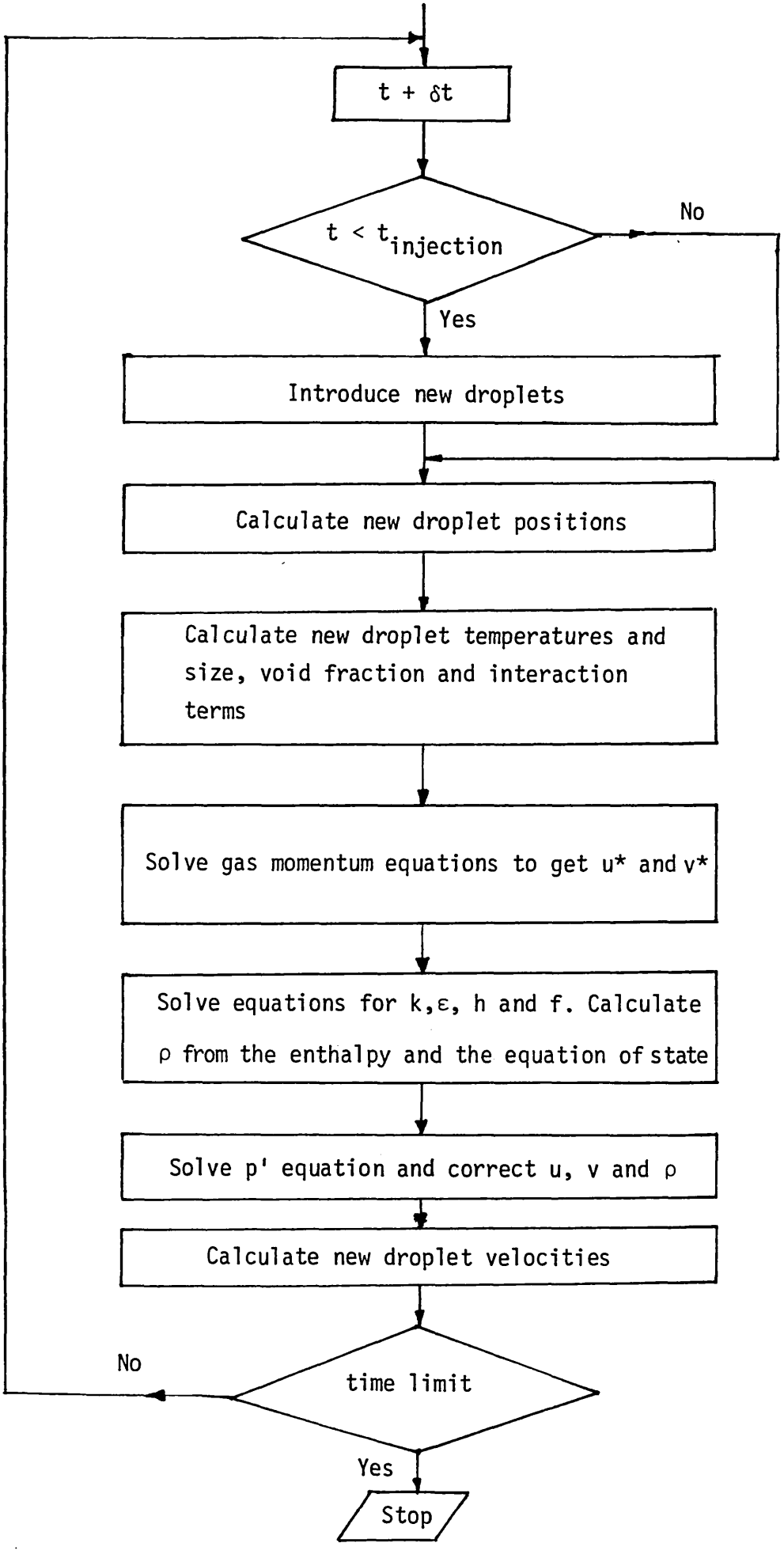


Fig. (4.6) Flow chart of the spray calculation procedure

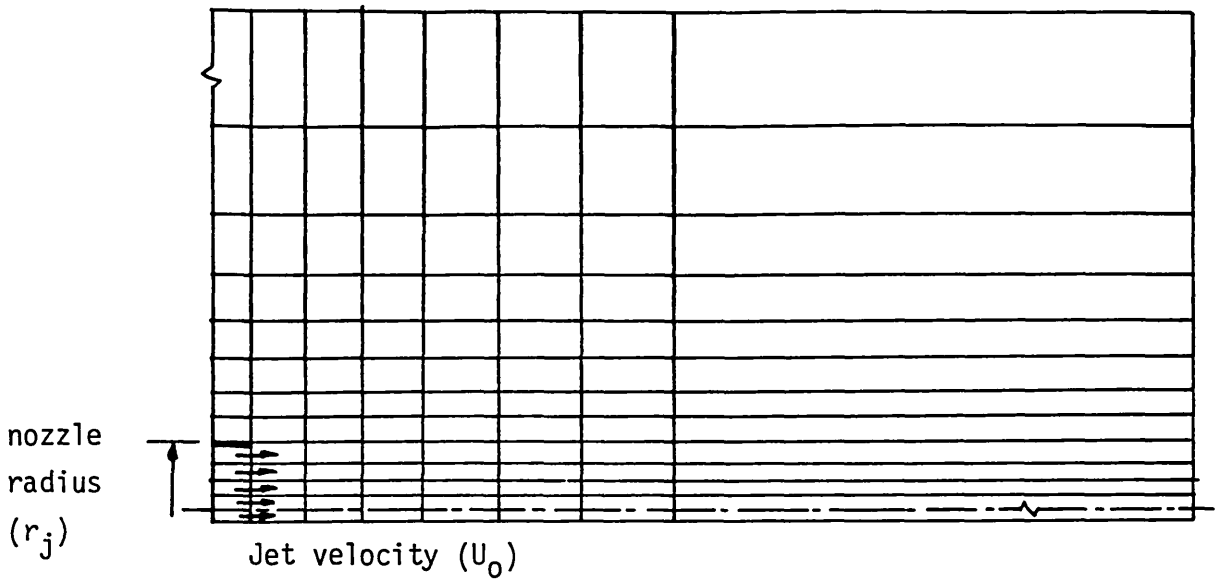


Fig. (4.7) Computational mesh for the gas jet studies

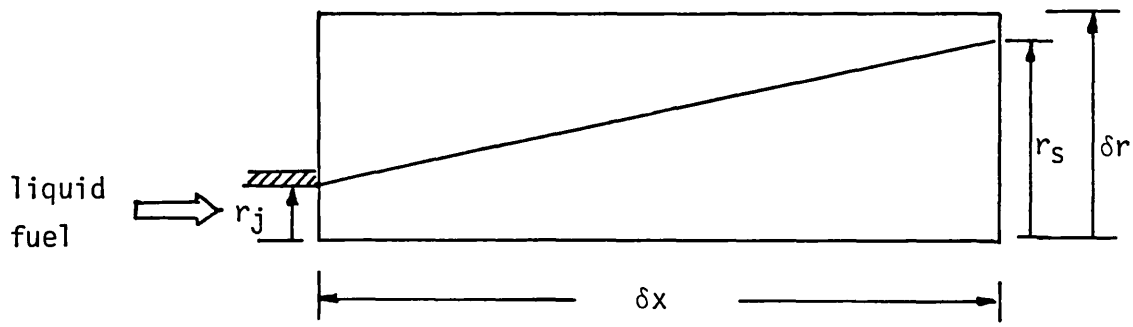


Fig. (4.8) Injection cell geometry

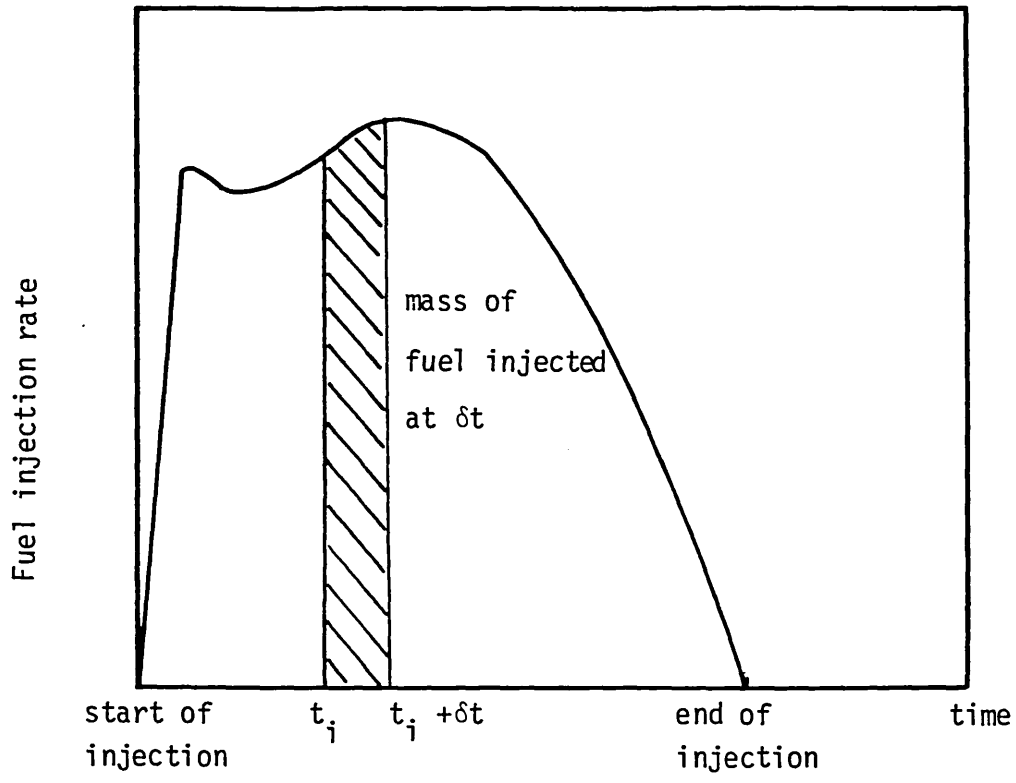


Fig. (4.9) Injection rate diagram discretization

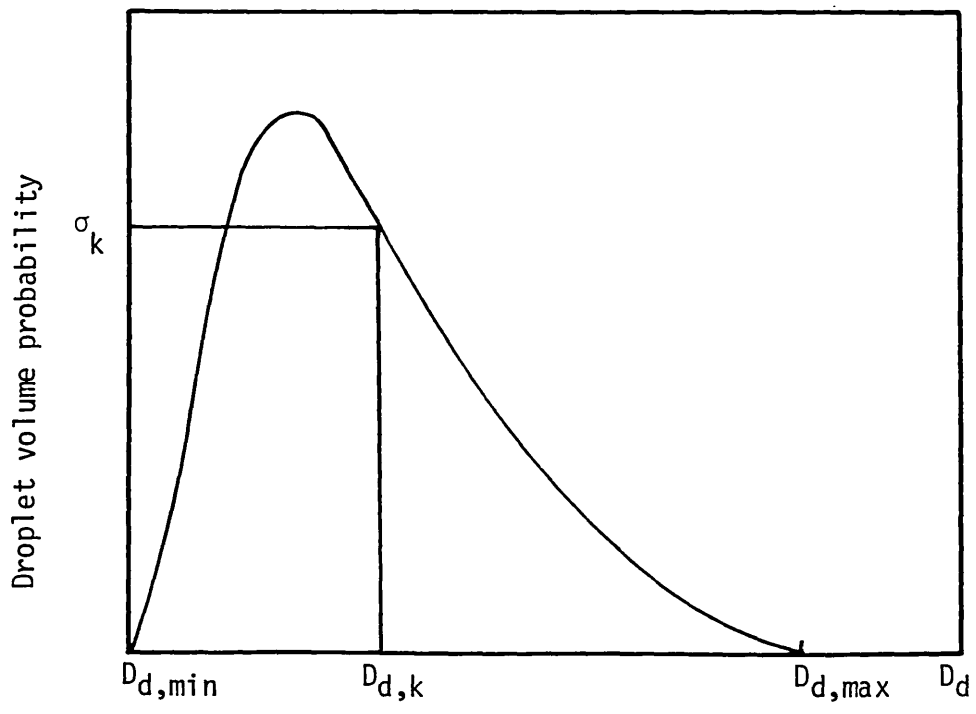


Fig. (4.10) Droplet size distribution function

CHAPTER 5

PRELIMINARY TESTING OF GAS JET AND SPRAY CALCULATION PROCEDURES

5.1 Introduction

This chapter is concerned with the numerical tests which were performed to assess the accuracy and reliability of the numerical methods assembled for the present study.

The effects of the number of grid nodes of the computational mesh and the size of time step on the performance of the fully implicit scheme, are dealt with in section (5.2). The predictions of the semi-implicit and fully implicit schemes are compared in section (5.3) for transient laminar and turbulent round free gas jet test cases.

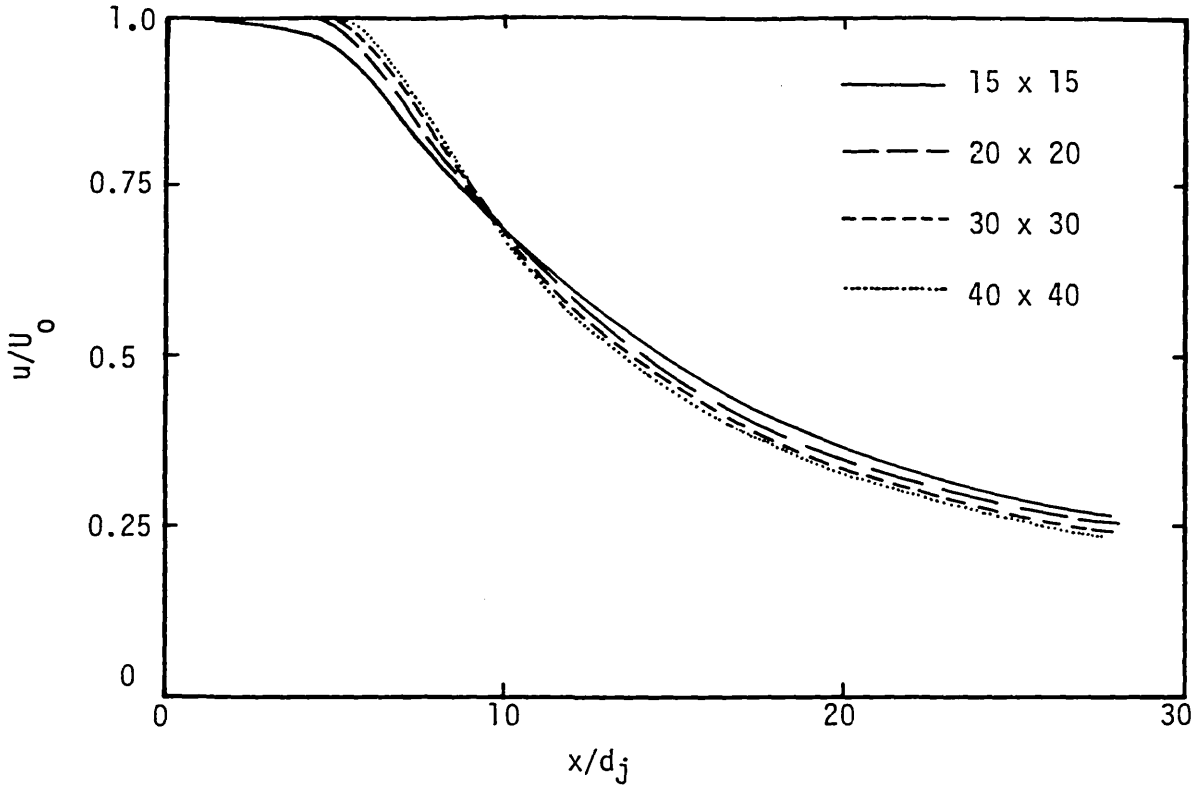
In section (5.4), the accuracy of the droplet trajectory calculation is examined by performing calculations for a simple case for which an analytical solution can be obtained. Also examined, is the effect of the integration time step on the trajectory calculation.

In the final section (5.5), tests are made of the full spray calculation method; including the effect of the grid size, time step, number of droplets injected per unit time and stochastic variations of penetration and gas phase properties.

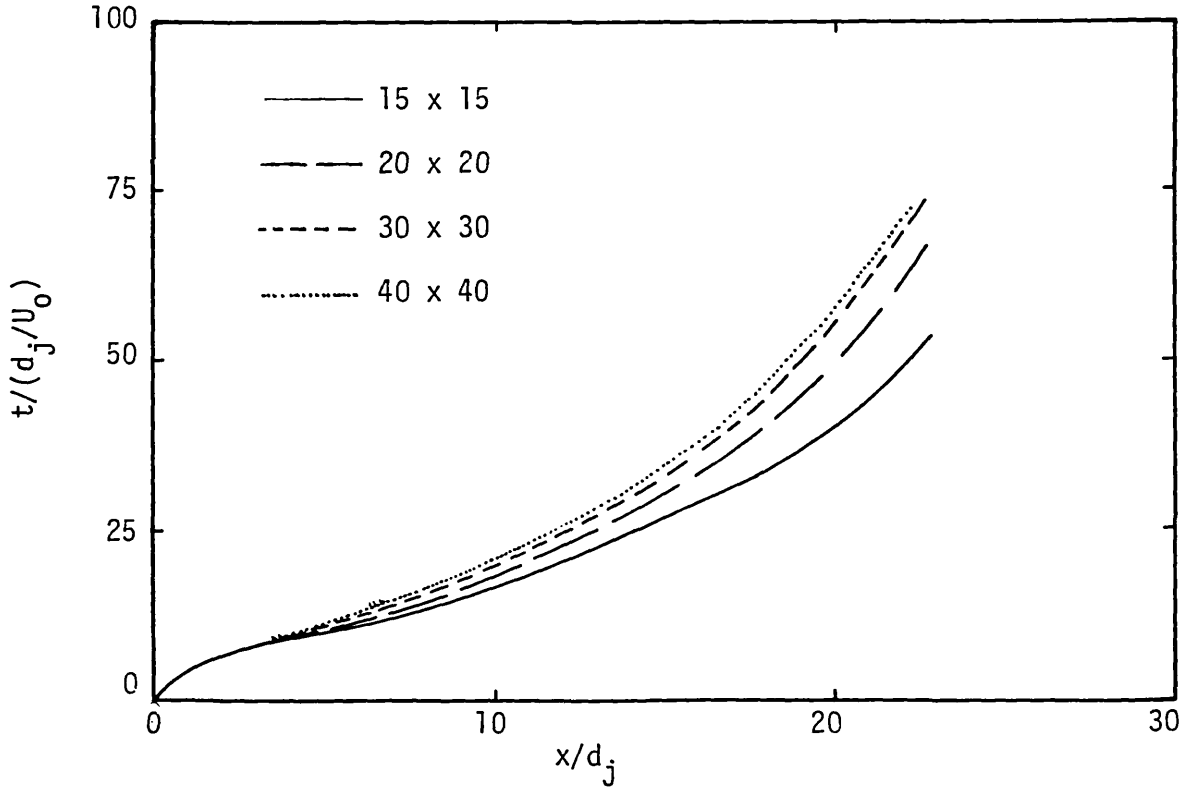
5.2 Assessment of Accuracy of Fully Implicit Scheme

The accuracy of the fully implicit scheme which is used in the present study for the gas jet calculations depends on the fineness of the grid spacing in the two spatial directions. The grid system used for these calculations was depicted earlier in Fig. (4.7). The size of the cells increases away from the nozzle exit with an axial expansion factor of 1.1. In the radial direction, the cell sizes are uniform within the nozzle radius, but outside this nozzle they expand by a factor of 1.1. The reason for this arrangement is to keep the number of nodes to a minimum while ensuring that the large velocity gradients in the mixing region near the nozzle are adequately resolved. In these calculations, the time step δt is initially held constant for 1 ms and then increased by 20% at each step until it reaches a maximum value equal to 4 times the starting value. An exception to this practice is the calculation of the hot jet case, for which a constant time step was used due to the time-varying injection rate (details of which are given in chapter 5).

The effects of the grid size on the steady-state centreline velocity decay and the jet tip arrival time (defined as the instant when the jet velocity reaches 70% of the steady state value at any axial location) of an impulsively started jet emanating at a velocity of 103 m/s from a nozzle of diameter d_j = 1.35 mm are depicted in Fig. (5.1). The initial time step is 0.05 ms. It can be seen from Fig. (5.1)(a) that the results obtained with 15 x 15 grid show a very short ($\simeq 1.5\ d_j$) potential core and slower rate of decay than those



(a) Steady-state centreline velocity decay



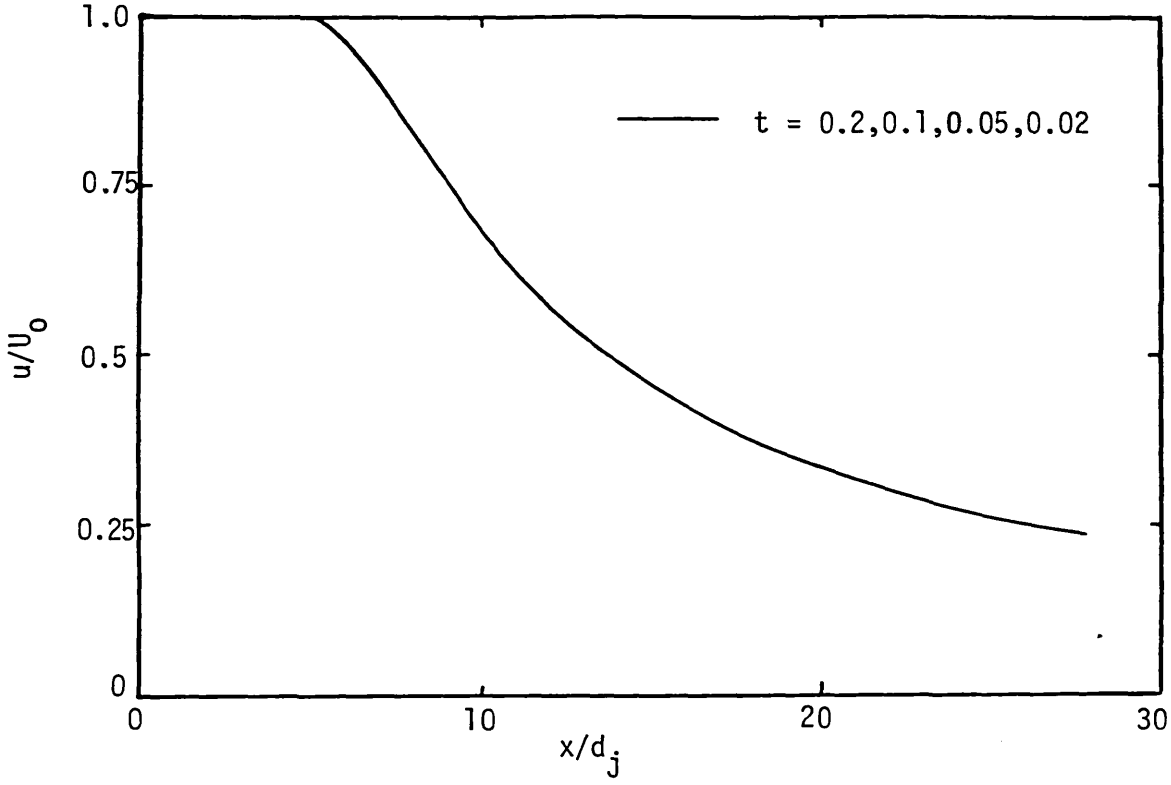
(b) Transient jet tip penetration

Fig. (5.1) Effect of grid size on the behaviour of transient turbulent gas jet

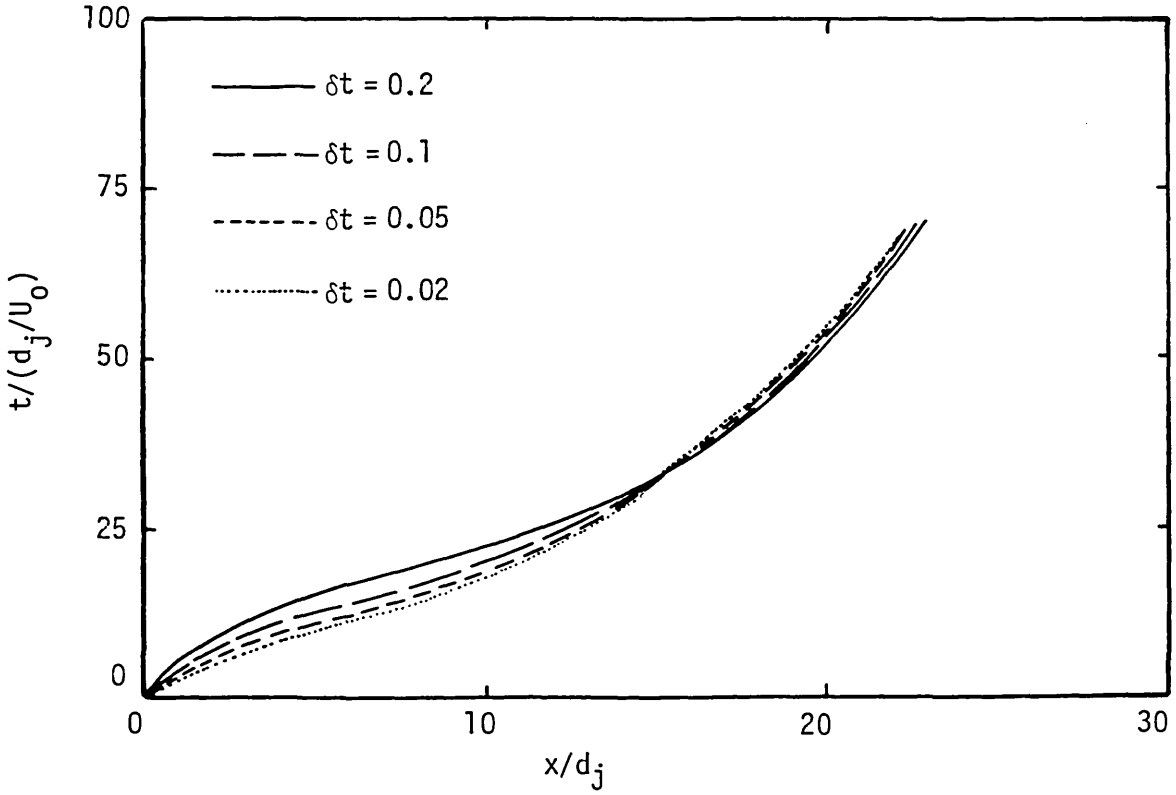
obtained with 20 x 20, 30 x 30 and 40 x 40 meshes (for the same size of the computational domain). The latter three give nearly equal potential core lengths of ~5 d_j. The centreline velocity decay shows also small signs of sensitivity to the grid, provided that it is 20 x 20 or greater.

The effect of the grid density on the tip arrival time (transient jet tip penetration) is more significant as shown in Fig. (5.1)b. In this figure t is defined as the instant when the jet velocity reaches 70% of the final plateau value at any x. It is clear that increasing the number of the grid lines decreases the differences between the results obtained using two successive grid sizes i.e. at $x/d_j = 20$ the difference in the jet arrival time between the 15 x 15 and 20 x 20 mesh results is 11%, while that between 20 x 20 and 30 x 30 is only 5%. A further increase in the grid density to 40 x 40 produces no appreciable change in the results as shown in Fig. (5.1)b. It should be mentioned that an increase of the mesh density from 30 x 30 to 40 x 40 increases the computer storage by about 78% and the computational time by about 90%.

The exploration of the effect of the time step size was performed using a 30 x 30 mesh and starting time steps (expressed as Courant number C_R, defined as $\frac{U_o \delta t}{\delta x}$ where δx is the minimum cell size) varies between 23 and 2.3. The outcome is given in Fig. (5.2). It is obvious from diagram (a) that, as expected, varying δt produces no effect on the steady-state centreline velocity decay. In the transient case (diagram (b)) a reduction in δt increases the penetration but only in the early stages of jetting (up to $\frac{t}{d_j/U_o} \simeq 30$).



(a) Steady-state centreline velocity decay



(b) Tansient jet tip penetration

Fig. (5.2) Effect of the time step on the behaviour of the transient turbulent jet

It should be noted that the reduction of δt from C_R = 5.75 to 2.3 has no appreciable change in the predict tip penetration, while it increases the computational time by about 40%.

The foregoing findings suggest that, considering both accuracy and economy of the computations, the grid and time step specifications are 30 x 30 and 0.05 ms (C_R = 5.75) respectively.

5.3 Assessment of the Semi-Implicit Scheme

The accuracy and reliability of the semi-implicit method used for the gas phase computations in the spray calculation procedure are assessed here by comparing its predictions with those obtained with the fully implicit scheme, for single phase laminar and turbulent starting gas jets. In these calculations, the same grid size (30 x 30) is used for both implicit and semi-implicit schemes. The computational time step of the semi-implicit scheme is automatically adjusted so as to obey the stability criteria mentioned earlier in chapter 4: in general the obtained values are much smaller than those used in the fully implicit calculations.

Figure (5.3) displays a comparison of the jet penetration obtained by the two schemes for a laminar starting jet having a Reynolds number $Re(\rho U_o d_j/\mu)$ of 254. It is clear from the figure that the difference between the predictions is negligibly small

and that both lie within the scatter of the experimental measurements of Abramovich and Solan (1973) for the Reynolds number range $80 < Re < 500$. It should be mentioned here that the time step of the semi-implicit scheme is reduced (below the stability limit) to obtain a time step-independent solution. In this case, the size of the time step used in the implicit scheme (equivalent to $C_R \simeq 5$) is 12 times greater than that of the semi-implicit one ($C_R \simeq 0.4$).

Similar trends to those of Fig. (5.3) are also observed in Fig. (5.4) which compares the turbulent round jet penetration predicted by the two schemes for a Reynolds number of 3750 and the experimental data of Witze (1980). Here, the size of the time step of the semi-implicit scheme is $\simeq 10$ times less than that of the fully implicit scheme in order to obtain the same (time step-independent) solution.

From the above findings, it can be concluded that the semi-implicit solution scheme is less economical than the fully implicit one for gas jet calculations, however it turns out to be the more efficient and economical for the small sizes of the time steps necessary for spray calculations.

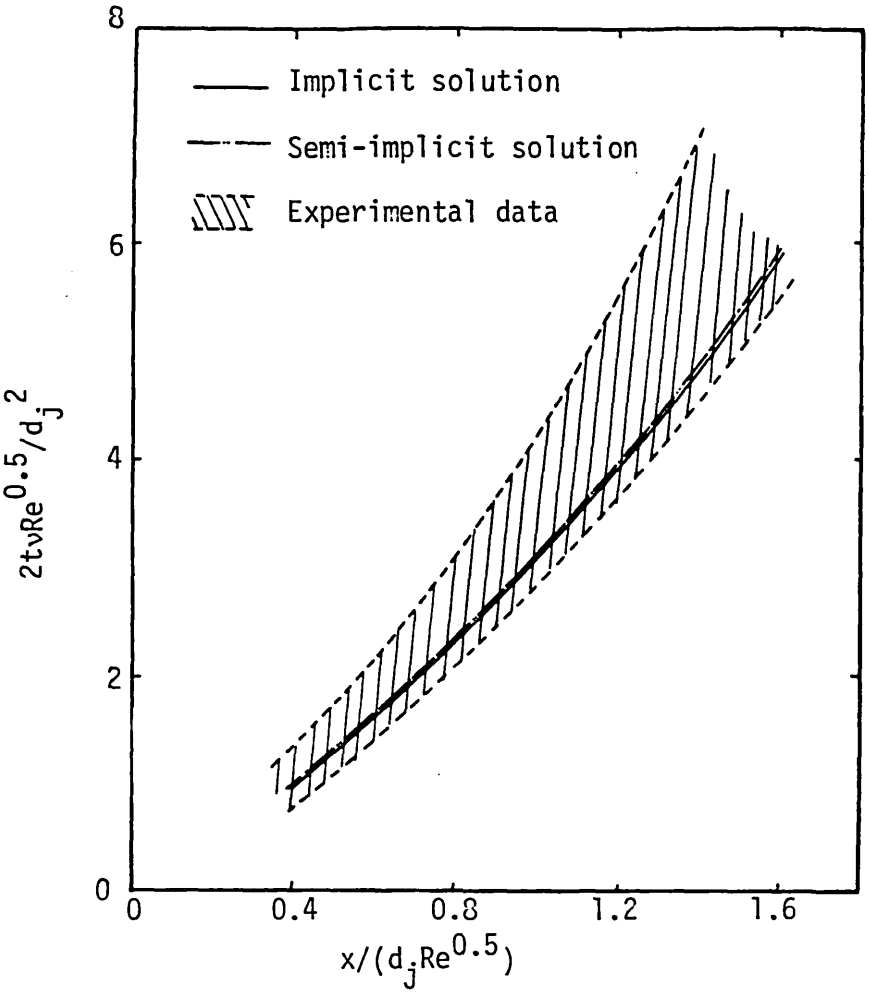


Fig. (5.3) Comparison of laminar jet tip penetration obtained by implicit and semi-implicit solution procedure

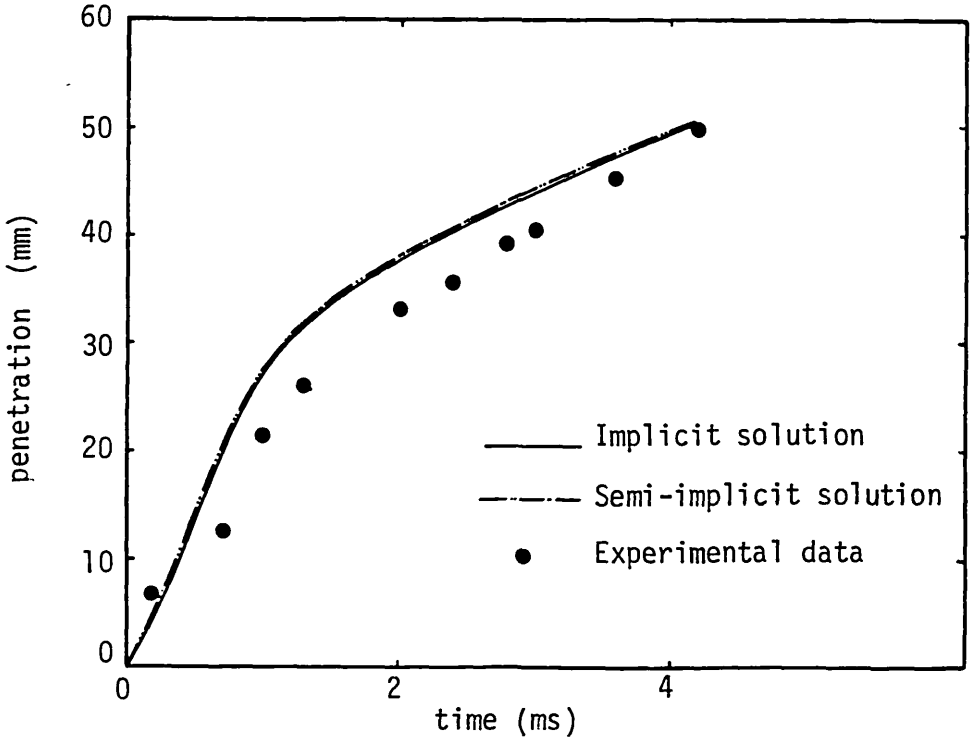


Fig. (5.4) Comparison of turbulent jet penetration obtained by implicit and semi-implicit solution procedures

5.4 Droplet Trajectory Calculations

As described in section (4.6) the droplet tracking is performed by numerically integrating, using Euler's method, the ordinary differential equations governing the motion, heat and mass transfer of each parcel. In this section the accuracy of this procedure is assessed by calculating the droplet trajectories in circumstances for which it is possible to obtain an exact solution to the differential equations.

For this purpose, droplets are injected into a quiescent gas which is deemed to be uninfluenced by their presence. Further, the droplet Reynolds number Re is supposed to be in the Stokes regime, for which according to equation (3.65) the drag coefficient $C_D = 24/Re$. Insertion of this into the axial momentum equation (3.63) gives

$$\frac{du_d}{dt} + u_d/\tau = 0 \tag{5.1}$$

where τ is the 'relaxation' time defined (for Stokes regime) as $\tau = \rho_d D_d^2/18\mu$. The solution of equation (5.1) is, for an initial droplet velocity U_{d_o} at time $t = 0$:

$$u_{exact} = U_{d_o} e^{-t/\tau} \tag{5.2}$$

Further, since the penetration x obeys $dx/dt = u_d$, it follows that

$$x_{exact} = U_{d_o}\tau(1 - e^{-t/\tau}) \tag{5.3}$$

A similar analysis for the vertical velocity v_{exact} and penetration y_{exact} gives:

$$v_{exact} = V_{d_o} e^{-t/\tau} \tag{5.4}$$

and

$$y_{exact} = V_{d_o} \tau (1 - e^{-t/\tau}) \tag{5.5}$$

Computations were performed to simulate the above case for droplets having relaxation time of 2.5, 15.6 and 62.5 ms (corresponding to droplets of 10, 25 and 50 μm diameter respectively). The numerical integration time steps $\delta t/\tau$ for those droplets were 1×10^{-3}, 1.6×10^{-4} and 4×10^{-5} respectively ($\delta t = 2.5$ μs). The results of the Euler's method are compared with the exact solution in Fig. (5.5) which displays the axial velocity and penetration histories of the droplets. It is clear from this figure that the smaller droplets loose their momentum faster than the larger one and hence penetrate less. This may be attributed to the inverse dependence of the drag force on the droplet diameter as seen in equation (3.63). It is also clear from the figure that both the numerical and analytical solutions produce the same results. However, a detailed inspection of the numerical results showed an error, as plotted (normalised by the exact solution) versus time for $\delta t/\tau = 1 \times 10^{-3}$, 2×10^{-3} and 4×10^{-3} in Fig. (5.6). As expected (Carnahan et al (1969)), the error resulting from the use of Euler's method increases linearly with time and is proportional to the size of the integration time step. For example, the error at $t = 0.9$ ms, for $\tau = 2.5 \times 10^{-3}$ ms droplet, decreases from 8.4% for $\delta t/\tau = 4 \times 10^{-3}$; to 4.2% for $\delta t/\tau = 2 \times 10^{-3}$ and 2.1% for $\delta t/\tau = 1 \times 10^{-3}$. These errors decrease for droplets having larger relaxation times.

Similar errors are also obtained by considering the radial behaviour of the droplets (not displayed) since equations (5.4)

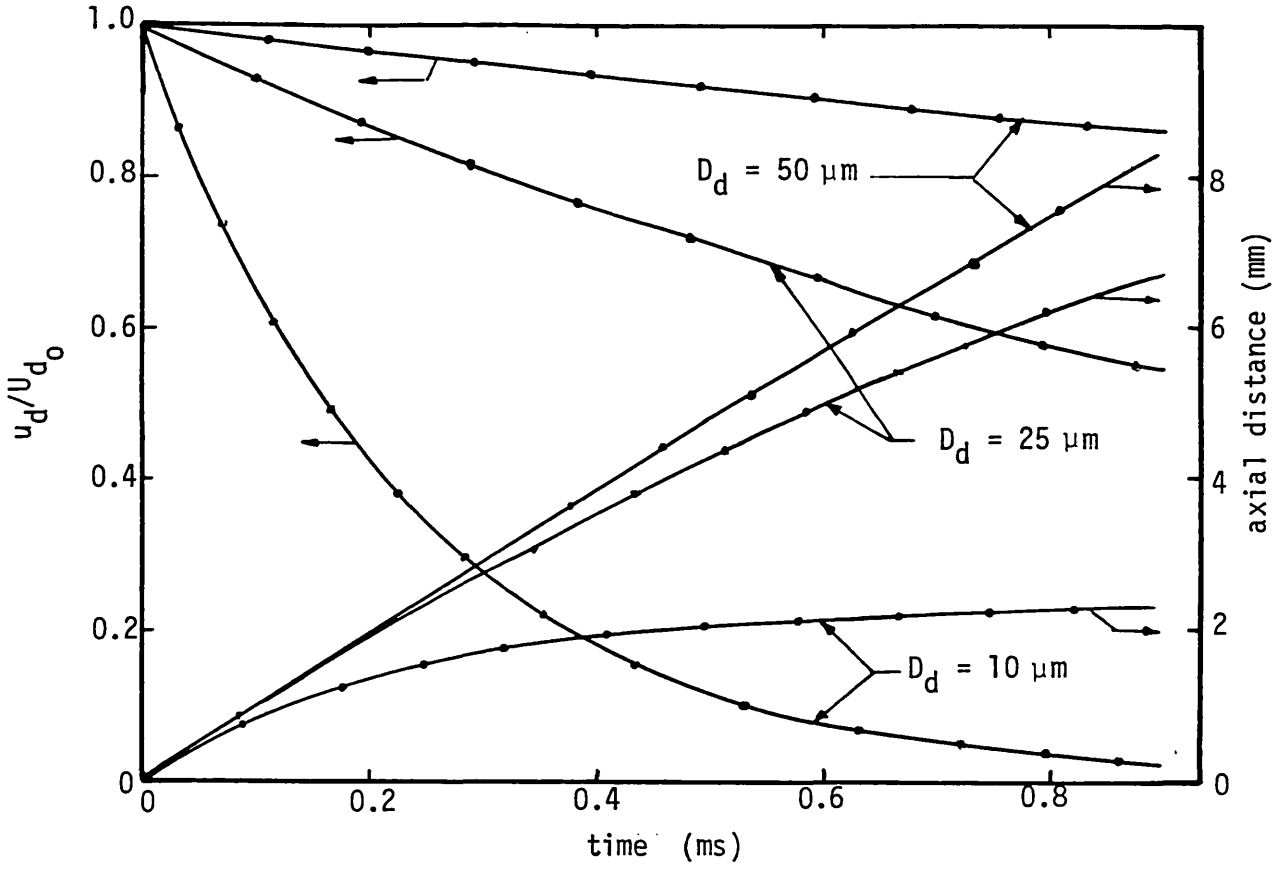


Fig. (5.5) Behaviour of droplets injected into a linear drag medium (— exact solution, ••• prediction)

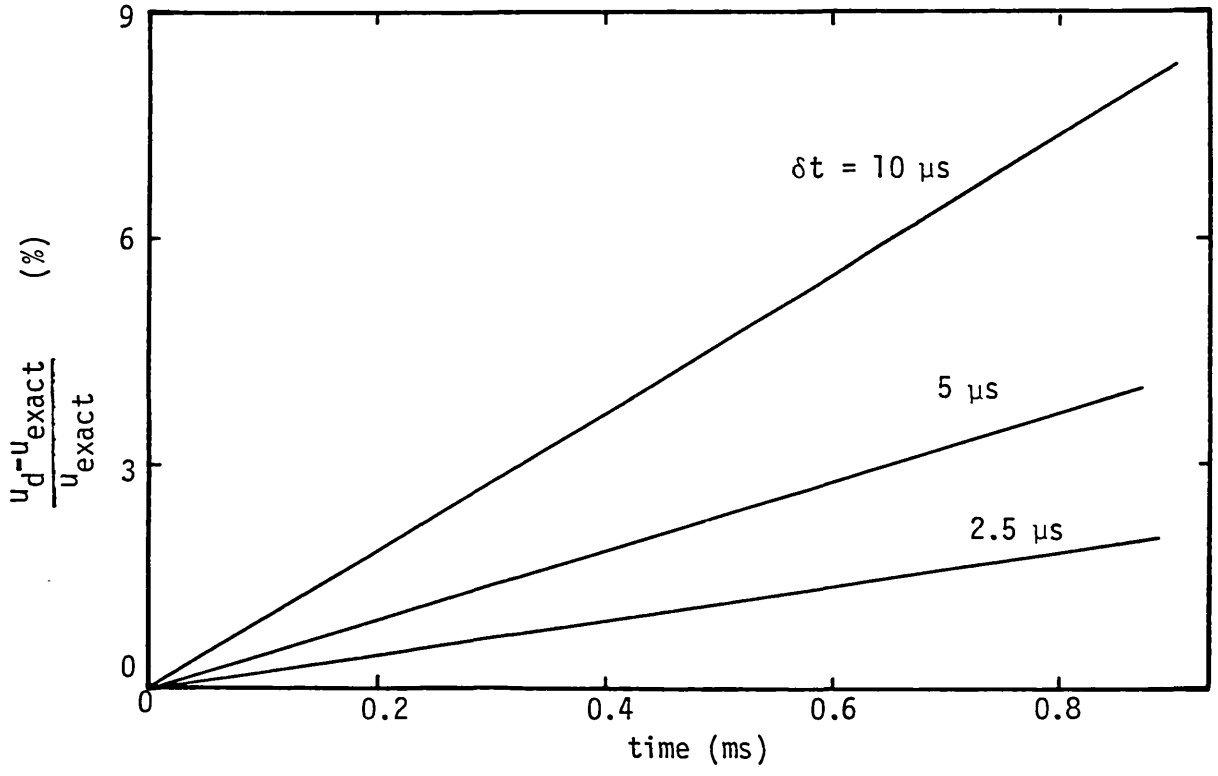


Fig. (5.6) Effect of the time step on the behaviour of the droplets injected into a linear drag medium (D_d = 10 μm)

and (5.5) are similar to equations (5.2) and (5.3), differing only by a factor of V_{d_o}/U_{d_o}. Therefore, it can be concluded that an accurate calculation of the droplet behaviour necessitate the use of small enough integration time step especially for small droplets. In the present study an average time step of 3 μs is used for droplet integration.

5.5 Spray Calculation

The full spray computation method was subjected to preliminary assessment tests reported here, which include the effects of the grid density, the computational time step and the number of droplet parcels introduced per unit time. Also examined was the degree of randomness introduced by the stochastic elements of the method.

a. Effect of the grid size

The grid system used for the spray computations uniformly expands in the axial and radial directions. The smallest cell is adjacent to the nozzle exit and the expansion factors are 1.1 and 1.15 in the axial and radial directions respectively.

The effect of the grid density on the spray tip penetration was investigated by decreasing the size of the injection cell, which has the effect of increasing the grid lines to cover the

same computational domain. The results are displayed in Fig. (5.7), from which it is clear that reducing only the axial spacing has very little effect, compared to that of reducing the radial spacing. Generally speaking, reducing the latter causes a systematic increase in tip penetration until the injection cell radius falls below 0.4 mm: then the calculation scheme fails because the void fraction near the injection cell becomes negative, which is non physical, since it implies that the droplets occupy more space than is available. This is a basic defect of the Lagrangian model as employed here and elsewhere, for it contains no provision for recognizing the proximity of the droplets and preventing overfilling. Similar problems are recorded by Dukowicz (1980), O'Rourke (1981) and Kuo and Bracco (1982a, b). This is an important drawback, because it effectively prevents grid independence solution from being achievable and thereby introduces errors into the calculations.

In the spray computation of the present study, the injection cell size is 1.5 x 0.5 mm and a total of 24 grid lines in the axial direction and 12 cells in the radial direction are used.

b. Effect of the time step

As discussed earlier in section (4.7) the computational time step is calculated from equation (4.108) which ensure that it remains below the level required to ensure numerical stability (In practice the limit is set by the magnitude of the velocities at the exit of the injection cell). It is also however necessary to ensure that δt is sufficiently small to ensure accuracy as well.

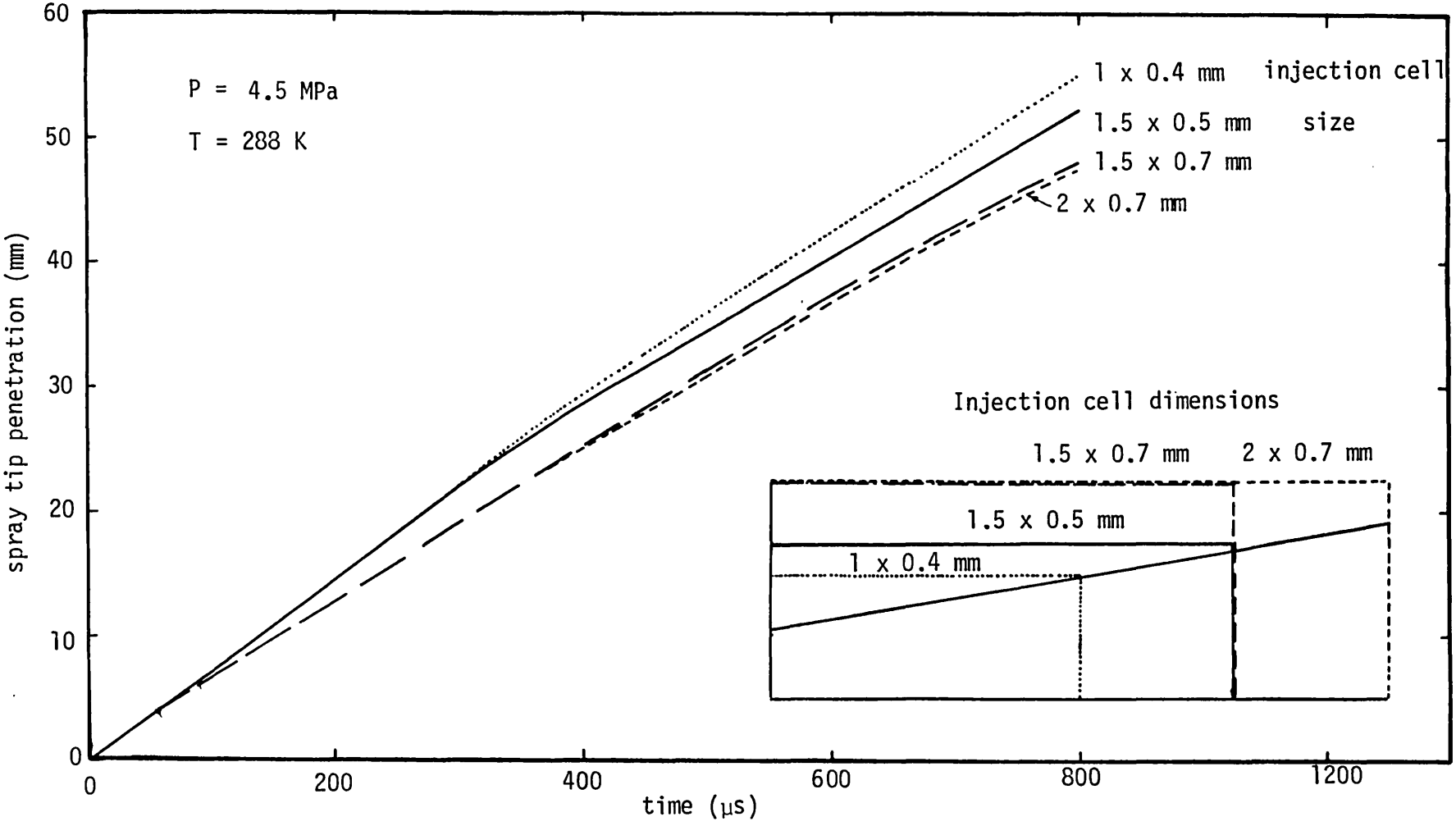


Fig. (5.7) Effect of grid size on computed spray tip penetration (C_R = 0.5)

Therefore, computations were performed to investigate the effect of the computational time step on the predicted spray tip penetration. In this investigation, the time step was reduced from 5 μs, corresponding to C_R = 0.5 to 2.5 μs, corresponding to C_R = 0.25 using the same computational mesh (24 x 12) and the same number of droplet parcels introduced per unit time (500).

Figure (5.8) shows the predictions for the conditions of the isothermal spray of Yule's (1985b) experiments (P = 4.5 MPa, T = 288 K). Each of the two curves is the average of three runs: this was done to minimise the effect of the stochastic elements of the calculation. It is clear from this figure that halving δt produces little change in the tip penetration, but of course increases the computational costs. Therefore, in all subsequent calculations presented in the present study a Courant number of 0.5 is used.

c. Effect of the droplet number

It is recalled that in the Lagrangian formulation of the spray used in the present work, a finite number of droplet parcels (sample) is used to represent the entire population. The total number of droplets in that sample influences the economy of the procedure since it determines the computational time and storage requirements. Therefore, calculations were performed to investigate the effect of the number of droplet parcels introduced per unit time on the tip penetration as well as on the spray structure.

Since the mass injected per unit time is fixed by the injection rate schedule, varying the number of droplet parcels implies a

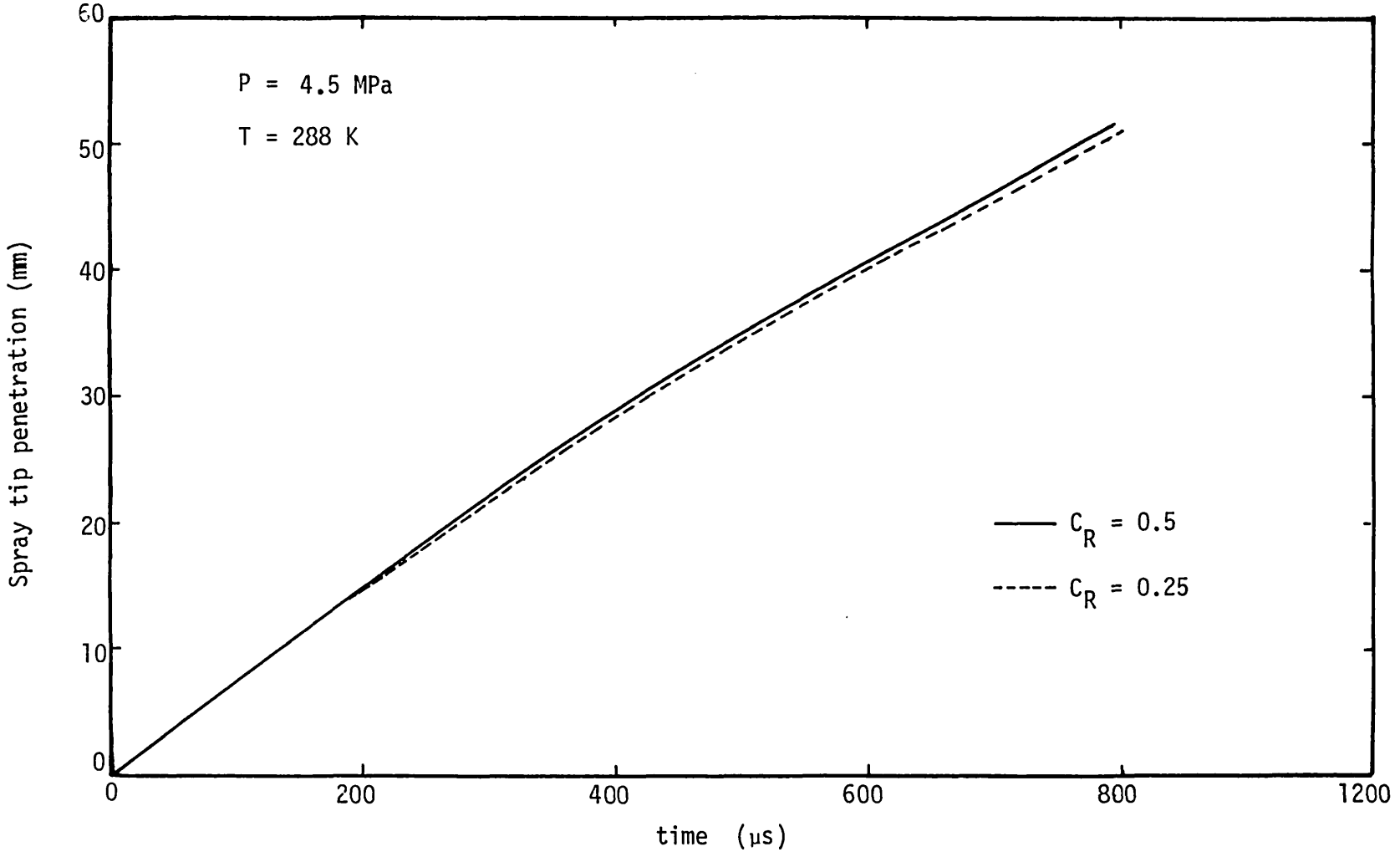


Fig. (5.8) Effect of the time step on the computed spray tip penetration (injection cell size 1.5 x 0.5 mm)

change in the number of droplets in each computational parcel. Increasing the number of droplet parcels improves the statistical accuracy of the calculation but as already noted, also increases the costs.

Figure (5.9) illustrates the effect on the spray tip penetration of increasing the introduction rate from 250 droplet/ms to 500 droplet/ms and Fig. (5.10) shows the corresponding spray structures at different times. It appears that the tip penetration is not sensitive to variations in this parameter within the range covered while the statistical accuracy of the 250 droplet/ms spray is less than that of the 500 droplet/ms one.

d. Stochastic variations

In the parcel injection technique described in chapter 4, both the droplet diameters and the radial injection velocities are chosen randomly from specified distributions of diameters and velocities respectively (see section (4.8) for details). Also the effect of gas turbulence on droplet behaviour is treated stochastically, as described in section (3.8). It is therefore of interest to assess how large are the stochastic variations in the spray predictions introduced by these features. Towards this end, several calculations were performed for the conditions of the isothermal spray of Yule et al (1985b) (P = 4.5 MPa and T = 288 K) with different random number sequences and the results are displayed in Fig. (5.11) and (5.12). Figure (5.11) shows that the stochastic variation in the spray tip penetration is 9%. The gas-phase centre-

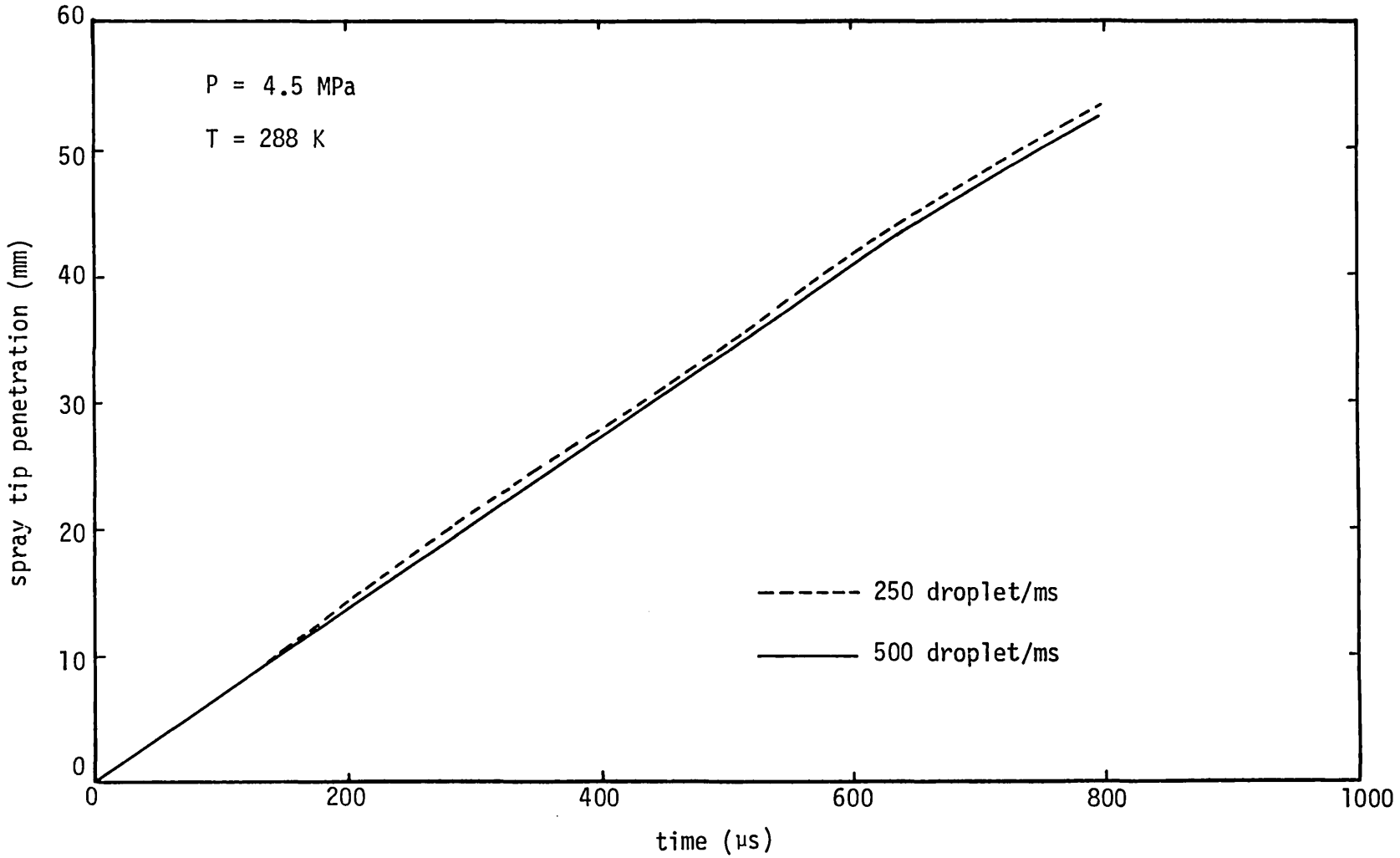


Fig. (5.9) Effect of the number of droplets introduced per unit time on the spray tip penetration

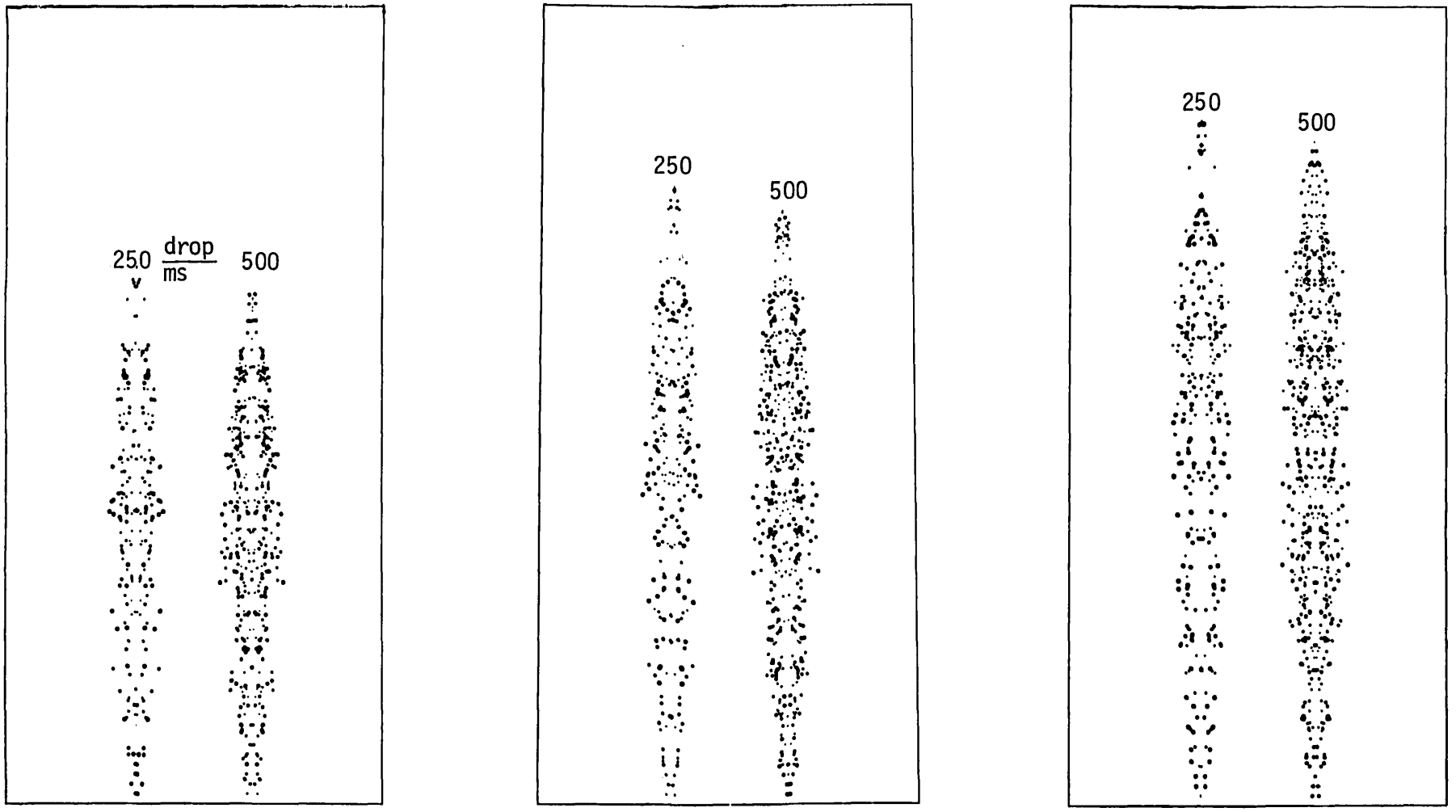


Fig. (5.10) Effect of the number of droplets introduced per unit time on the spray shape (P =4.5 MPa , T = 288 K)

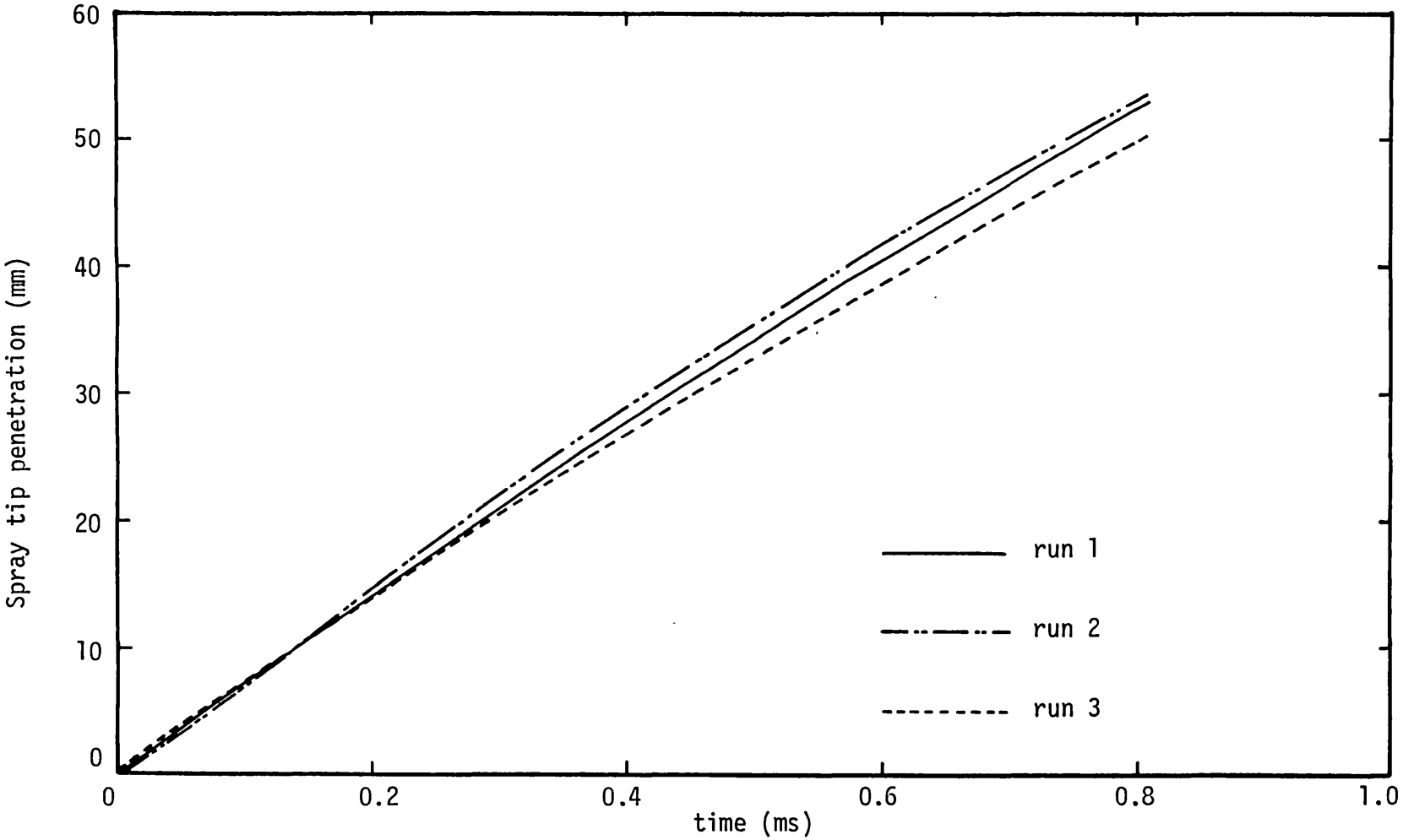
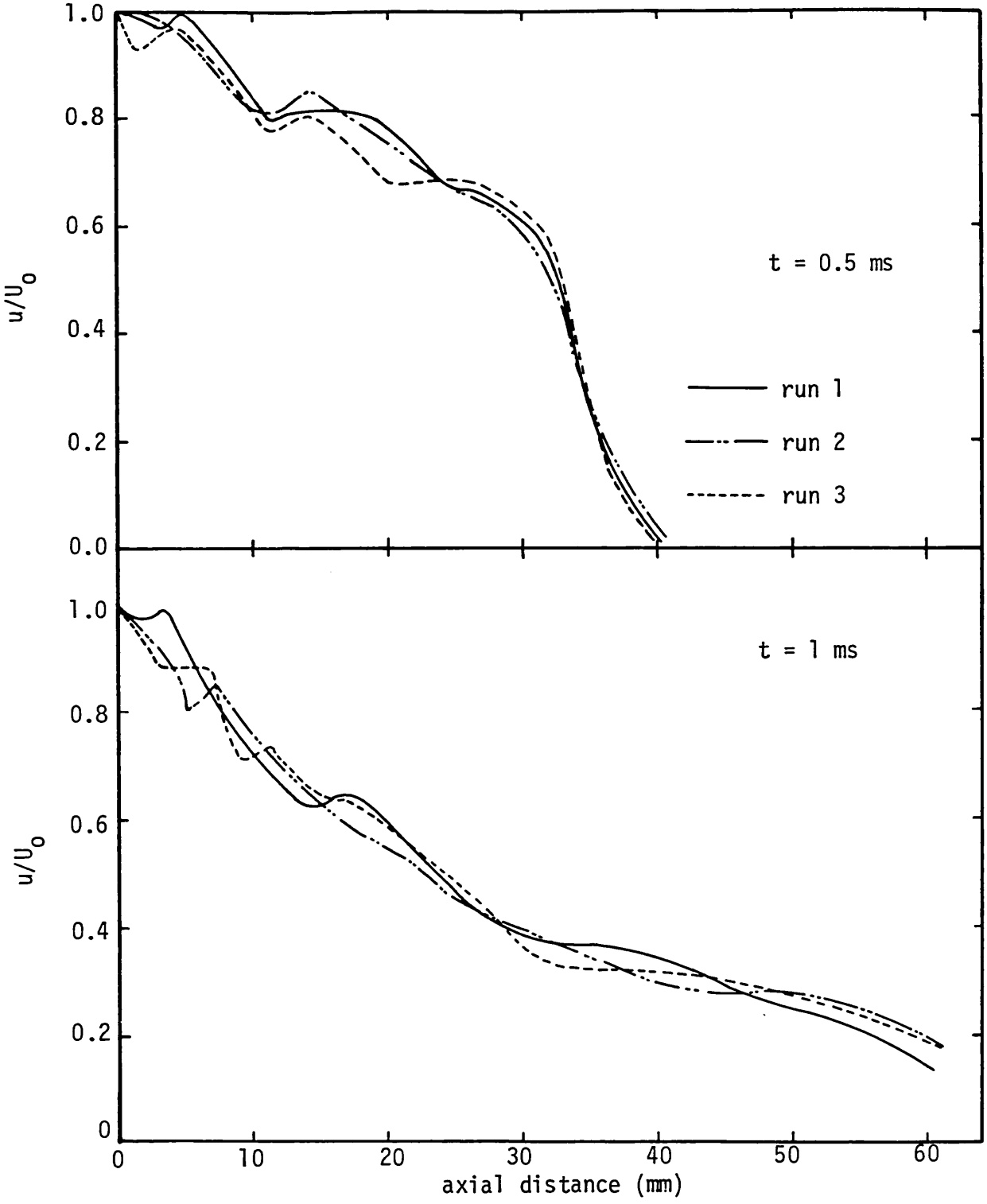


Fig. (5.11) Stochastic calculation effect on the spray penetration (P =4.5 MPa , T = 288 K)

line velocities illustrated in Fig. (5.12)(a) show larger differences, e.g. at t = 1 ms from the start of injection, the differences are 20% or less. The gas-phase turbulent intensity and viscosity displayed in Fig. (5.12)(b) and (c) show markedly larger differences, especially near the injector, since in this region the spray occupies at most two or three grid cells and a change in the centre-line velocity causes a drastic change in the velocity gradient.

Similar calculations were also performed for an evaporating spray for conditions corresponding to those of Kuniyoshi et al (1980) (P = 6.28 MPa and T = 800 K). Figure (5.13)(a)-(c) show the vaporization rate, equivalence ratio and temperature distributions and profiles resulting from three runs with different random number sequences. The differences in the total masses evaporated are always less than 10%, while larger differences are observed in the predicted equivalence ratio and ambient gas temperatures.

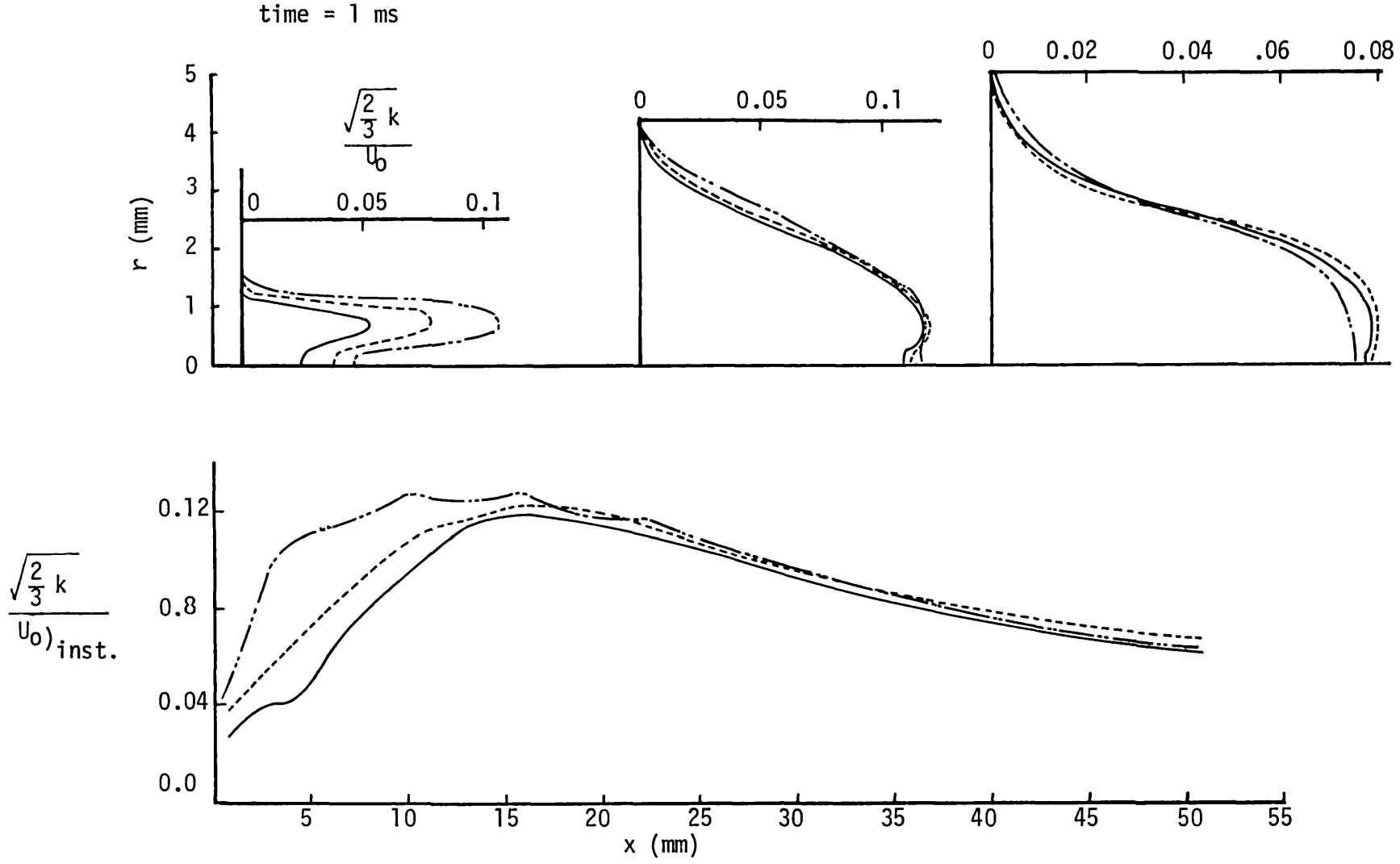
It can be concluded from the above that both spray tip penetration and vaporization rate are less sensitive to the stochastic calculation than the other gas-phase properties such as velocity, turbulence parameters, equivalence ratio and temperature. Therefore, a statistical averaging of results from many runs is needed if comparisons are made with similarly averaged measurements.



(a) Stochastic variation of the gas-phase centreline velocity

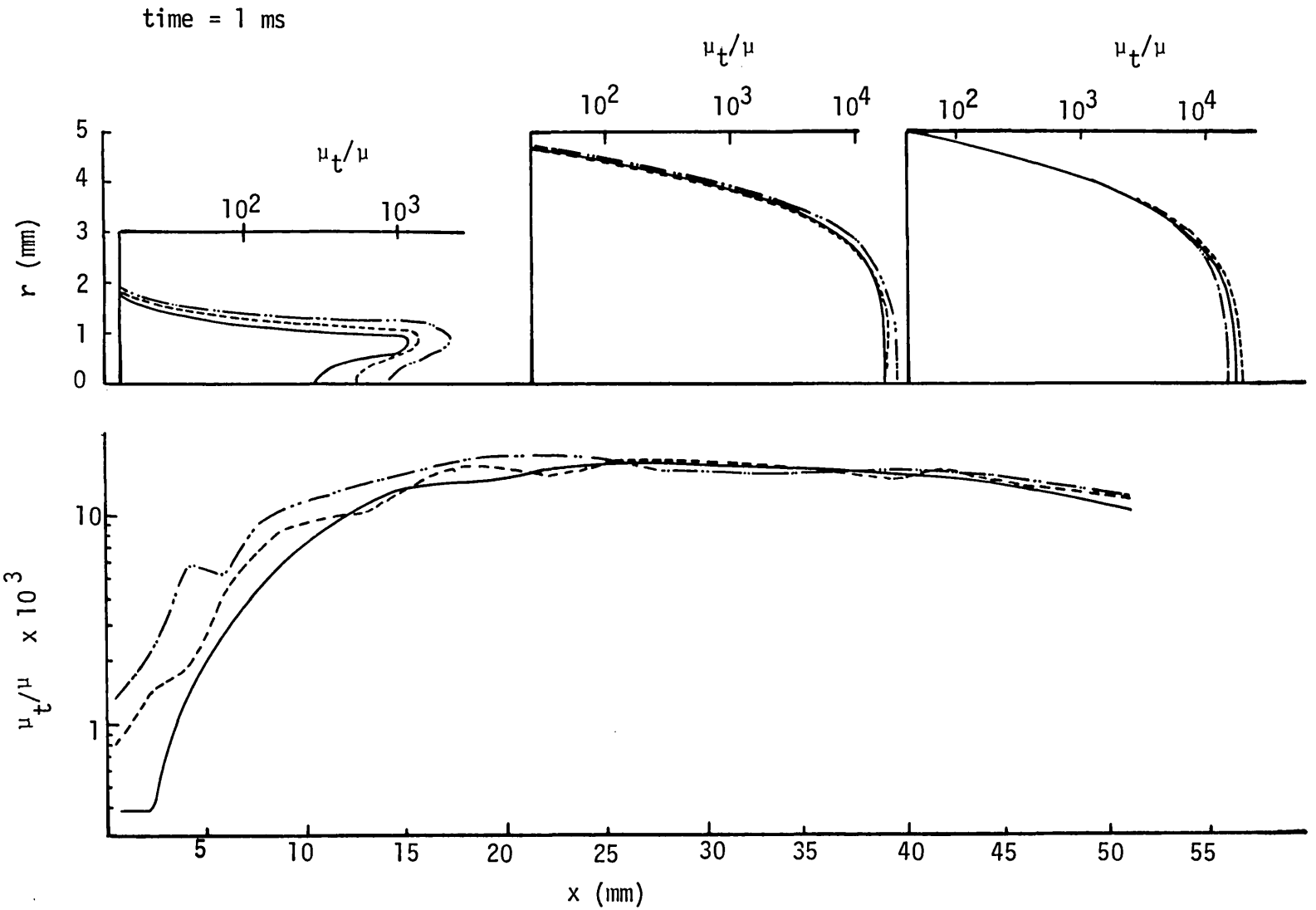
($P = 4.5$ MPa, $T = 288^{o}K$)

Fig. (5.12) Stochastic calculation effects



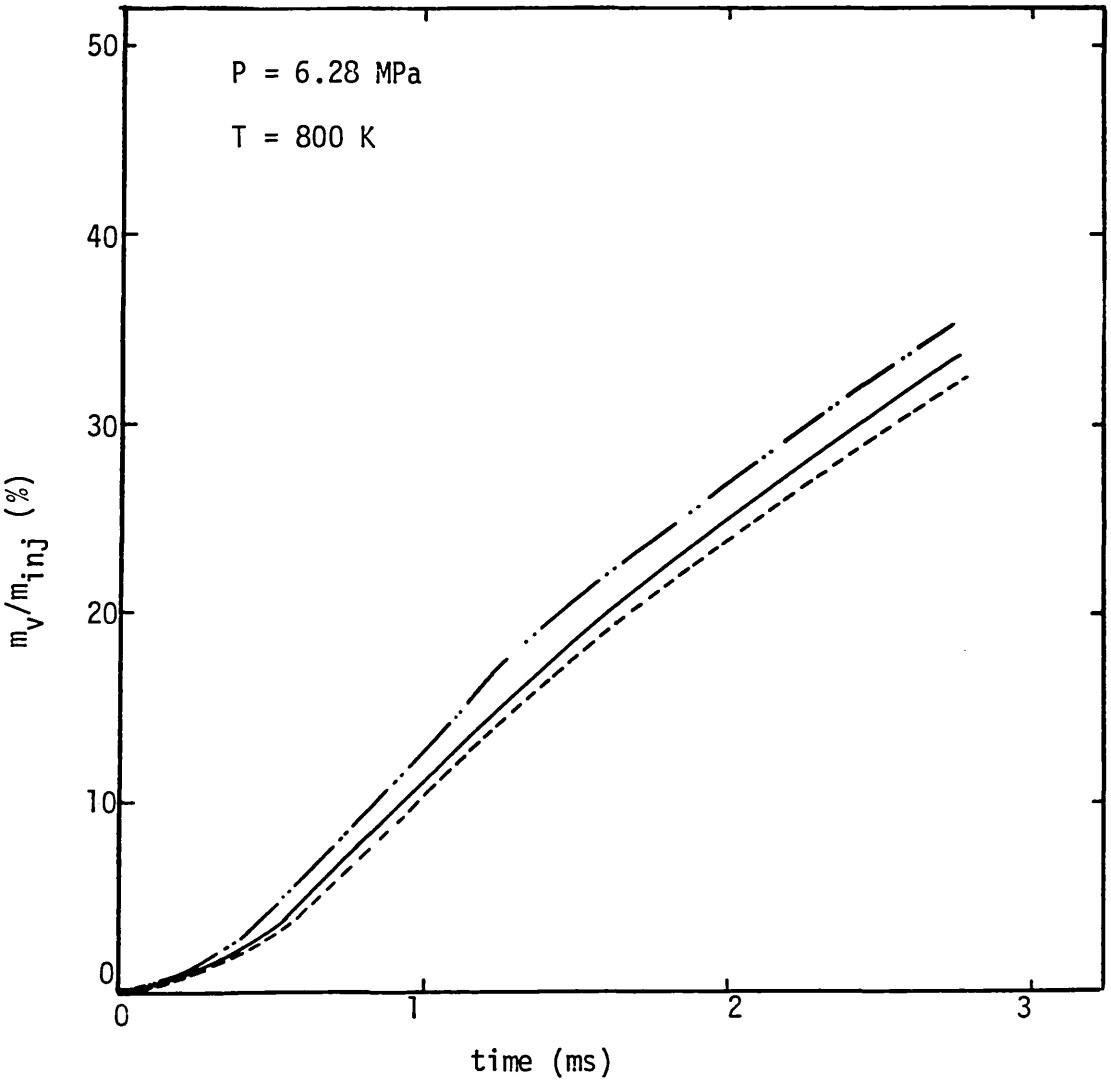
(b) Stochastic variation of the gas-phase turbulent intensity (P=4.5 MPa , T = 288^{o}K)

Fig. (5.12) Cont'd



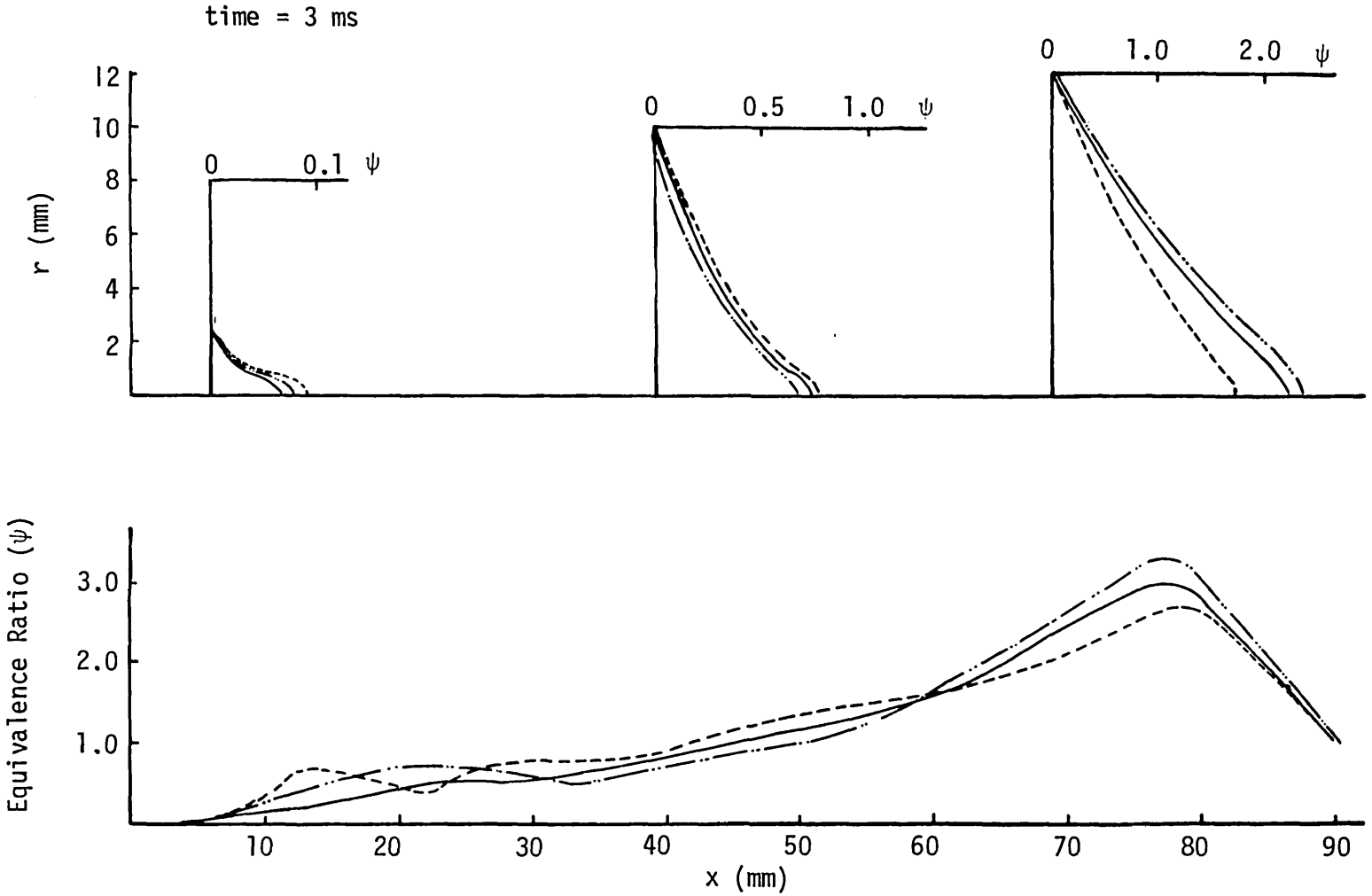
(c) Stochastic variation of the gas-phase turbulent viscosity (P=4.5 MPa., T = 288^{o}K)

Fig. (5.12) Cont'd



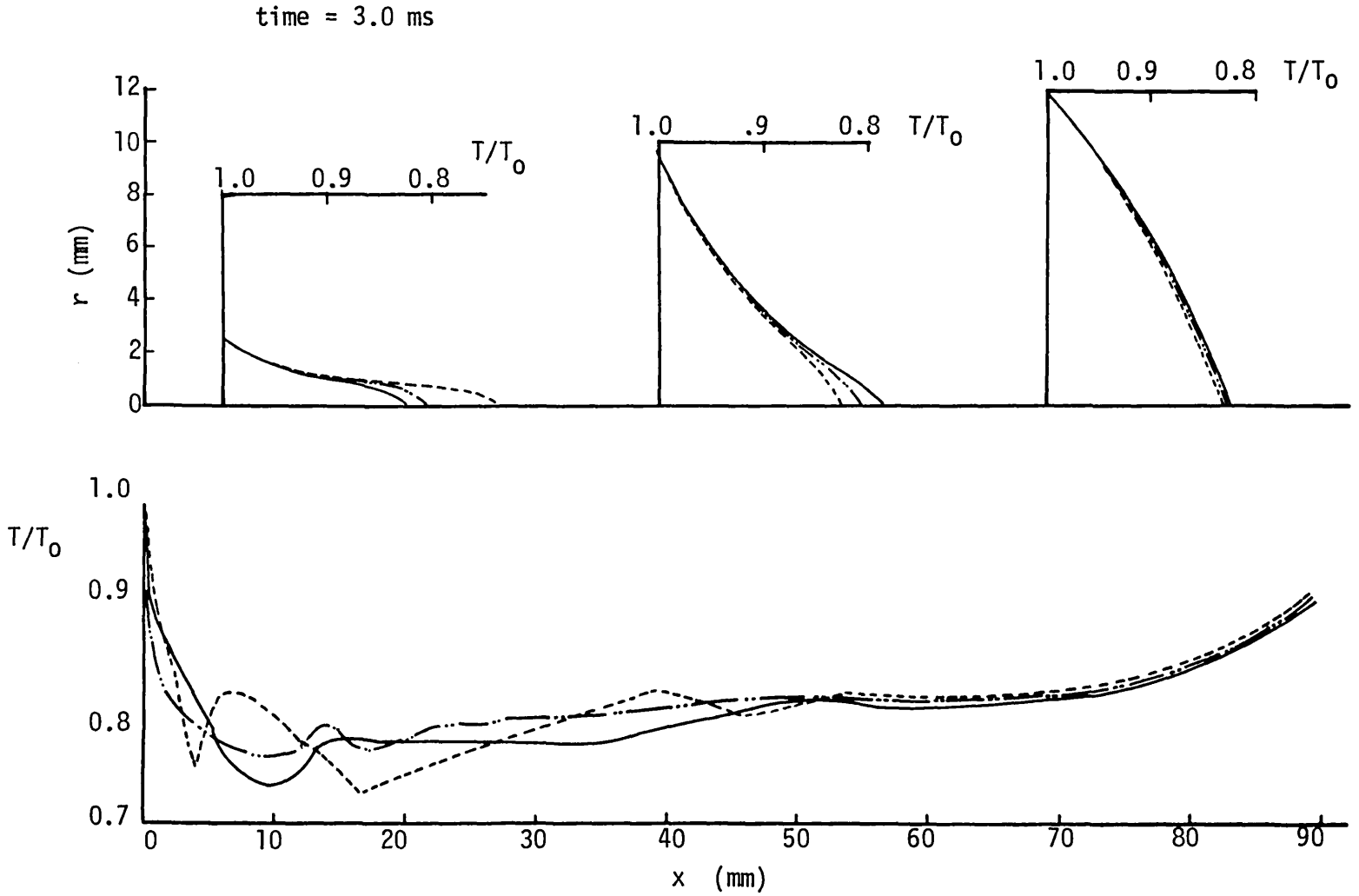
(a) Predicted vaporization rate

Fig. (5.13) Stochastic calculation effect on evaporating spray



(b) Stochastic calculation effect on the equivalence ratio (P = 6.28 MPa, T = 800 K)

Fig. (5.13) Cont'd



(c) Stochastic calculation effect on gas phase temperature (P = 628 MPa, T = 800 K)

Fig. (5.13) Cont'd

5.6 Concluding Remarks

In this chapter, the different numerical tests which were performed to assess the accuracy and reliability of both the fully implicit and the semi-implicit solution algorithms were presented.

In the fully implicit scheme, used for gas jet calculations, a grid and time step independent solution was obtained by increasing the number of grid points (for constant δt) and decreasing the time step (for the same mesh) until no further changes were obtained in the final solution. It was found that the optimum grid and time step specifications are 30 x 30 and 0.05 ms respectively.

The numerical technique employed for spray calculations becomes unstable and the procedure fails to give a solution under conditions when the droplets cluster locally giving negative void fraction. This effectively prevents grid independence solution from being achievable. A time step independent solution was obtained by decreasing C_R (below the level required to ensure numerical stability) to 0.5 and a further decrease to 0.25 produced a very little effect on the spray tip penetration.

As far as the effect of increasing the droplet introduction rate (from 250 to 500 droplet/ms) is concerned, it was found that the penetration is not very sensitive to this variation while the statistical accuracy of the spray increases.

Finally, further computations were performed to investigate the stochastic variation associated with the use of different random number sequences in the spray calculations. The stochastic variations of the spray tip penetration and the total vaporized

mass were always less than 10% while larger differences were observed in other gas phase properties such as velocity, turbulence parameters, equivalence ratio and temperature. Therefore, a statistical averaging of the results from many runs is necessary if comparisons are made with similarly averaged measurements.

CHAPTER 6

ASSESSMENT OF THE PROCEDURE
GAS PHASE

6.1 Introduction

The main objective of this chapter is to assess the ability of the theoretical model presented in chapter 3 to predict droplet-free steady and transient gas jets such as round jets. Assessment of the procedure is carried out here using five such test cases, all of which involve comparison with experiments.

Predictions of the steady laminar free jet and comparison with the experimental data of Abramovich and Solan (1973) are given first in section (6.2). Then section (6.3) deals with calculations of the starting laminar jet.

The steady turbulent round free jet serves as the third test case and is described in section (6.4), while predictions of impulsively started turbulent jets (isothermal and non-isothermal) are presented in section (6.5).

Finally, the scaling of the transient turbulent round free jet; including the effects of the Reynolds number, length scale and turbulent intensity, is given in section(6.6).

6.2 Steady Laminar Round Free Jet

Calculations were performed to predict the behaviour of an isothermal laminar free jet and the results are compared with the experimental data of Abramovich and Solan (1973). In their experiments, Abramovich et al measured the centreline velocity decay of air emanating from a 6 mm internal diameter pipe. The Reynolds number range was 80 - 500.

The computed result for the steady-state centreline velocity decay obtained from a parabolic starting profile of a Reynolds number of 254 is compared with that measured by Abramovich and Solan (1973) in Fig. (6.1). The dimensionless co-ordinates are those suggested by Abramovich and Solan, i.e. $u^* = U_m/U_{mo}$ and $x^* = x/d_j Re^{0.5}$ where U_m is the maximum velocity at any x from the nozzle, U_{mo} is the maximum velocity at the nozzle exit (here $U_{mo} = 2U_o$) and Re is the jet Reynolds number defined as $Re = \rho U_o d_j/\mu$. It is clear from the figure that the calculated result fits inside the experimental scatter. Kuo and Bracco (1982a) made similar calculations and found that the results obtained for different Reynolds numbers, do not coincide when the non-dimensional parameters of Abramovich and Solan are used. They concluded that the experimental scattering observed in Fig. (6.1) may not be due wholly to experimental error but also to improper account of the Reynolds number effect in the normalisation of x by $d_j Re^{0.5}$. They suggested that a more appropriate length scale is $d_j Re$. Figure (6.2) shows that Kuo's predictions for Re = 70, 100 and 500 as well as the present prediction for Re = 254 which is displayed in Fig. (6.1) all coalesce when

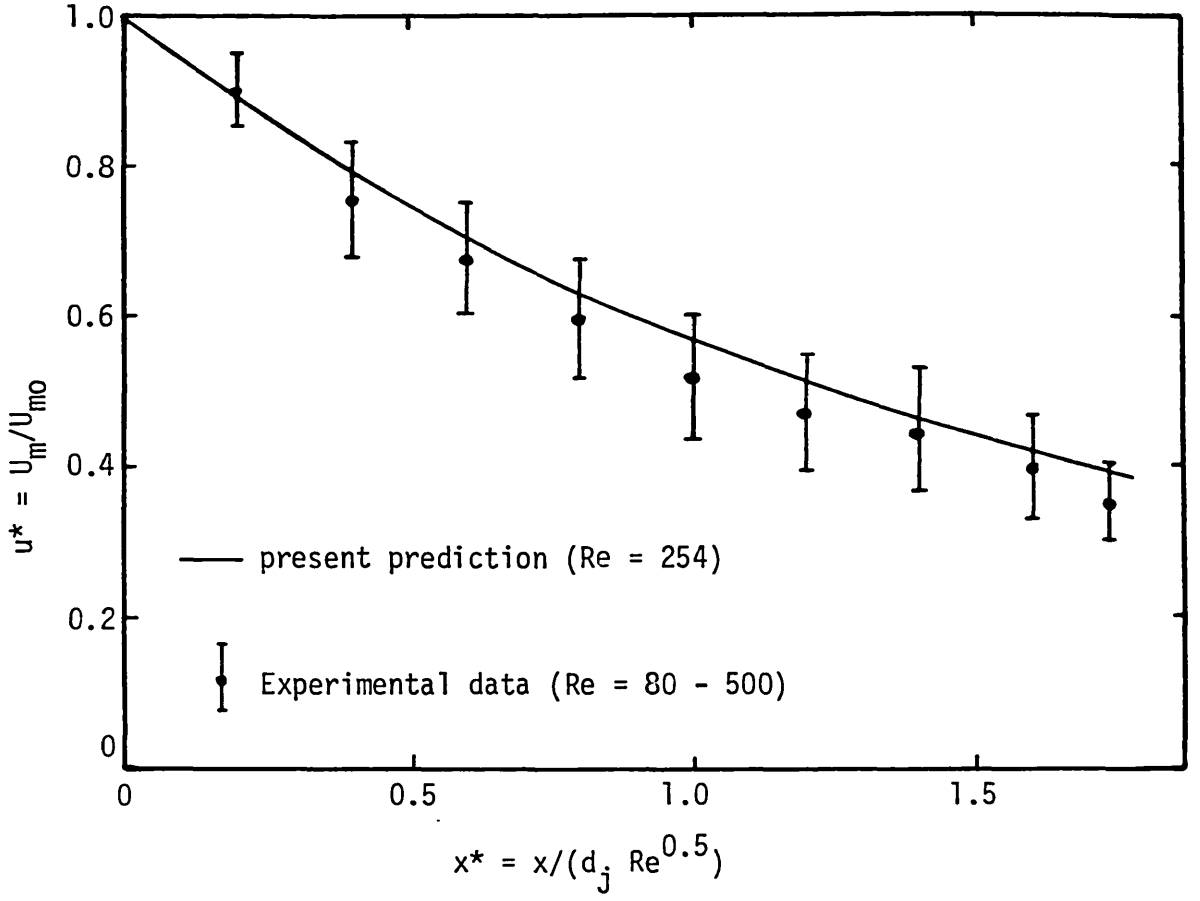


Fig. (6.1) Centreline velocity decay of laminar round free jet

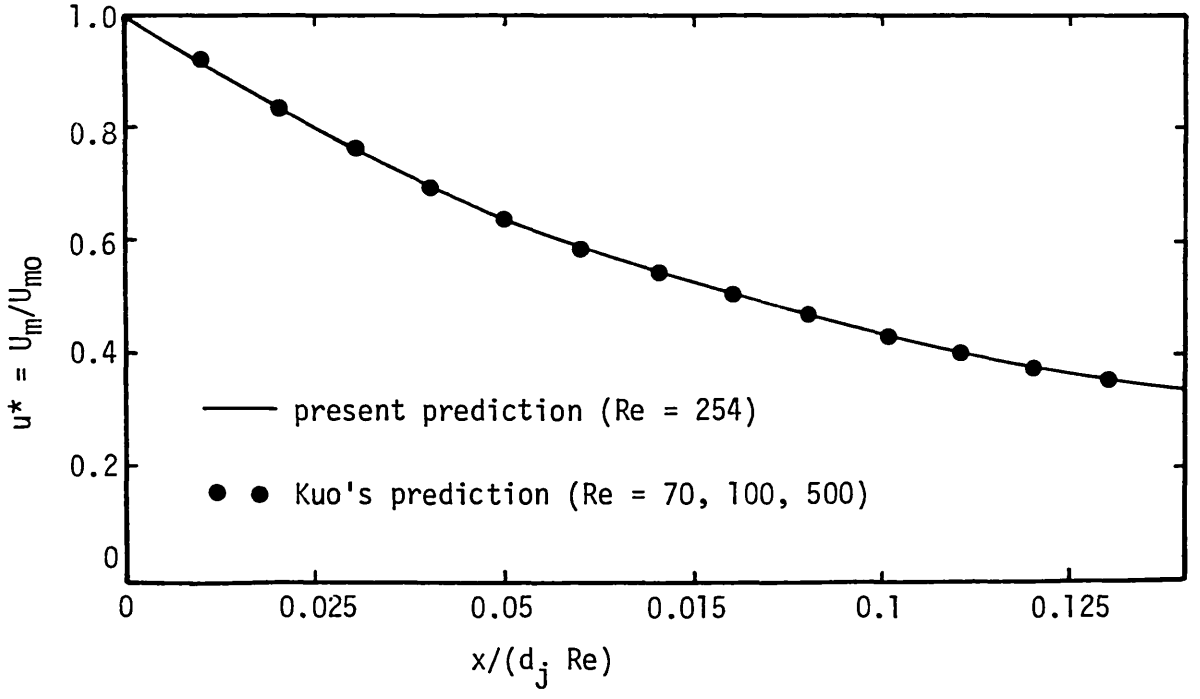


Fig. (6.2) Centreline velocity decay using Kuo's length scale

plotted in this way. Unfortunately the experimental data of Abramovich and Solan cannot be reported in the same figure because they did not identify the Reynolds numbers corresponding to each of their experimental points.

6.3 Transient Laminar Round Free Jet

The predicted transient behaviour of a starting laminar round free jet is assessed against the experimental data of Abramovich and Solan (1973). They measured the travel time of the spherical vortex at the front of a suddenly switched on, submerged, laminar jet in the Reynolds number range $80 < Re < 500$. The centreline velocity plateau was recorded from which the jet penetration was obtained.

A typical set of results for the predicted centreline velocities at several axial locations for an unsteady air jet with a parabolic starting velocity profile at Re = 254 is given in Fig. (6.3). At each location the velocity is seen to reach a steady-state plateau with the plateau level decreasing with distance from the nozzle exit. Following the somewhat arbitrary procedure introduced by Abramovich and Solan, the arrival time (t) of the jet tip at a point x on the centreline is defined as the instant when the jet velocity reaches 70 per cent of the final (steady) plateau value. When x and u are scaled as before and t is non-dimensionalised as $t^* = 2t\nu Re^{0.5}/d_j^2$ where ν is the dynamic viscosity,

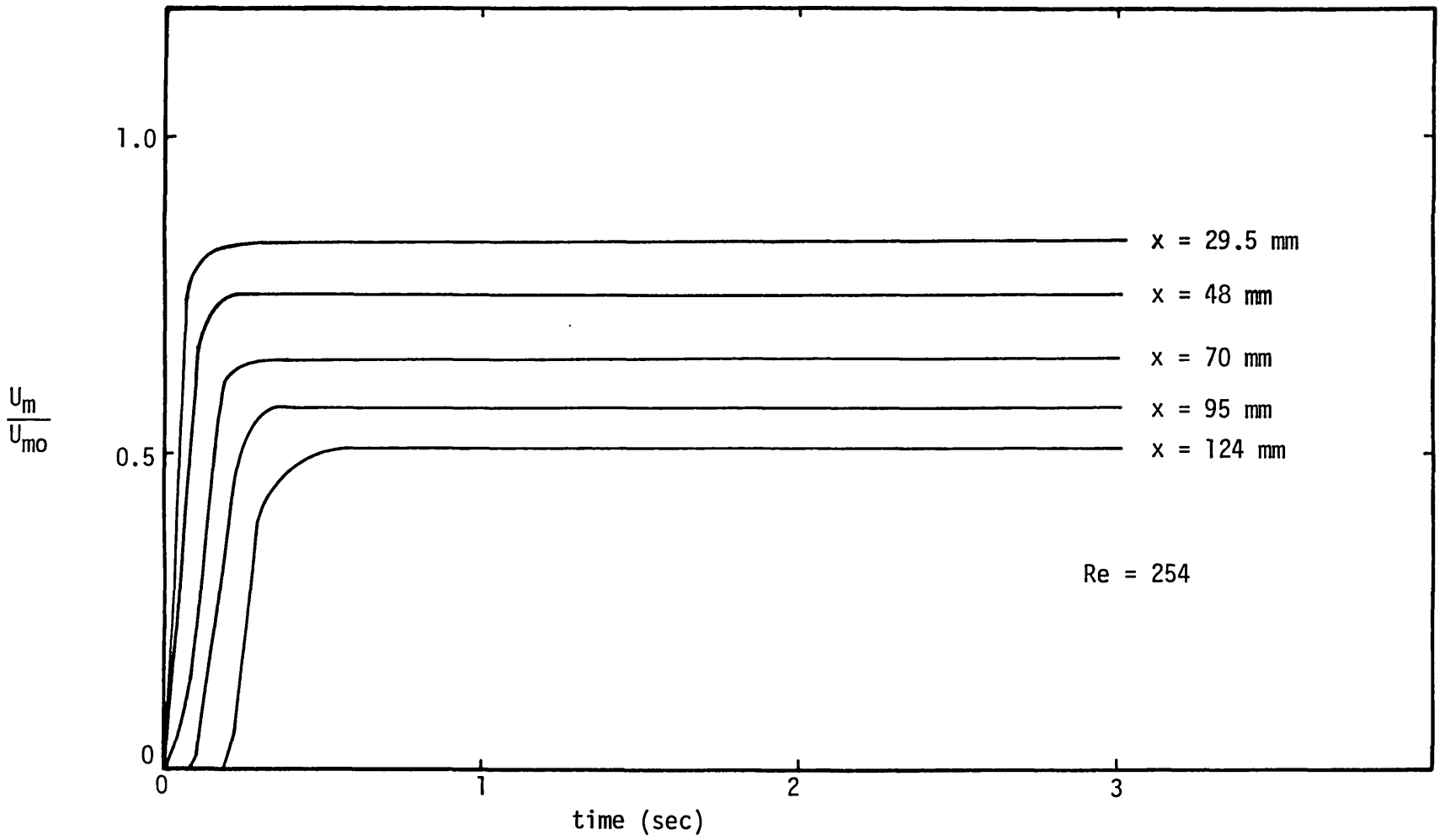


Fig. (6.3) Centreline velocity plateau of a starting laminar free jet

the computed results for the transient jet tip penetration histories for Re = 125 and 254 appear as in Fig. (6.4), where they are plotted with the experimental data for Reynolds number range $80 < Re < 500$. It is clear from the figure that the results for Re = 127 and 254 lie inside the experimental range but do not coincide, i.e. they show a Reynolds number dependence similar to the centreline velocity decay of the steady laminar jet presented in section (6.2). Once more Kuo and Bracco (1982a) concluded that the observed experimental scattering is partially due to the improper account of the Reynolds number effect in Abramovich's scaling parameters and they proposed new dimensionless parameters as $x^* = x/d_j Re$ and $t^* = t/(d_j^2/\nu)$. Figure (6.5) shows that Kuo's predictions for Re = 70, 100, 500 and the present predictions for Re = 127 and 254 coalesce when plotted in this way.

6.4 Steady-State Turbulent Free Jet

An isothermal axisymmetric turbulent free jet serves as the third test case, which is used to assess the applicability of the k-ε turbulence model in these circumstances. The ensemble-averaged form of the Navier-Stokes equations for steady state axisymmetric turbulent flow are solved in conjunction with the turbulent kinetic energy and its dissipation rate equations and the results are compared with the experimental data of Witze (1980) and Wygnanski and Fiedler (1969).

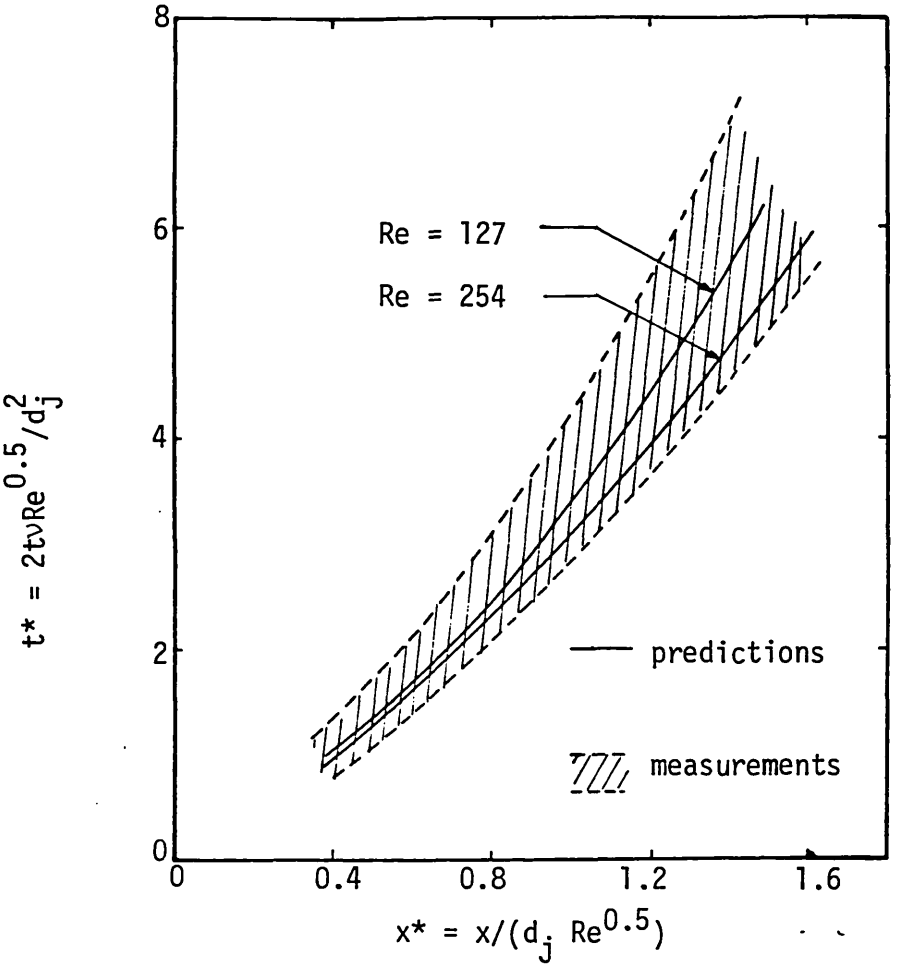


Fig. (6.4) Travel time of transient laminar jet

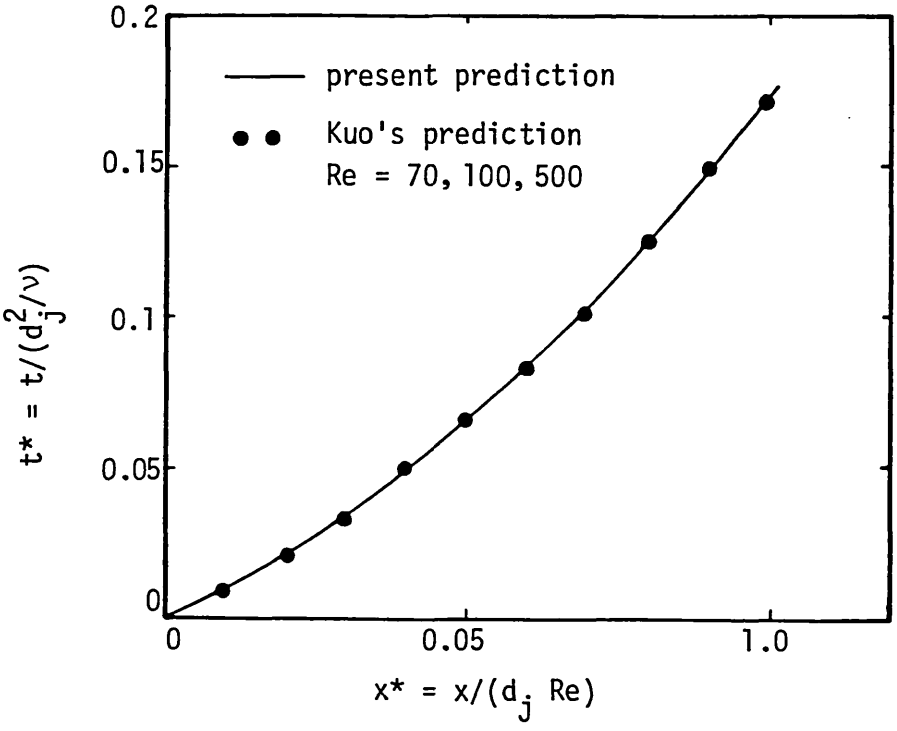


Fig. (6.5) Travel time of transient laminar jet using Kuo's length and time scales

Witze (1980) measured the mean and fluctuating components of the axial velocity at the centreline of air-into-air jets emerging from two different nozzle geometries using hot film anemometry. Calculations were performed to simulate Witze's experiment for his 'nozzle A' which has a diameter of 1.35 mm and uniform exit velocity of 103 m/s (Re = 8200). The value of the turbulent kinetic energy at nozzle exit k_{in} was specified as

$$k_{in} = iU_o^2 \tag{6.1}$$

where i is the turbulence intensity and the dissipation rate at nozzle exit ε_{in} was estimated through the expression

$$\varepsilon_{in} = k_{in}^{3/2}/\ell_o \tag{6.2}$$

where ℓ_o is the length scale, taken as a fraction of the nozzle radius. In the present computations, the value of i is specified as 0.03 guided by the experimental measurements while ℓ_o is evaluated, following Kuo and Bracco (1982a) as $0.09r_j$ where r_j is the nozzle radius. Except for the coefficient, c_1, in the dissipation rate equation, which is set equal to 1.5 (the reason for this will be discussed later), all the other constants of the k-ε model are those given in table (3.1). From Fig. (6.6) it can be seen that, as far as the steady state centreline velocity decay is concerned, the agreement with Witze's experimental correlation is quite good for $7.5 < x/d_j < 30$. It is also clear from the figure that the measured potential core length is much smaller than the generally accepted experimental value for free

jets of 4 to 6 orifice diameters (see e.g. Rajaratnam (1976)), while the predicted one lies inside that range. The discrepancy may be attributed to the uncertainty in the measurements near the nozzle exit.

Wygnanski and Fiedler (1969) carried out detailed measurement of axial and radial velocity and turbulence characteristics of the steady round free jet. The nozzle diameter was 2.64 cm and the air velocity at nozzle exit was 51 m/s ($Re \simeq 79000$). Calculations were performed using the above injection condition as well as the initial turbulence prescription mentioned earlier. Figure (6.7) shows the predicted mean velocity distribution acorss the jet at $x/d_j = 40$, compared with the experimental measurements of Wygnanski and Fiedler. The velocity scale in this figure is the maximum velocity at this section and the lateral distance from the axis of symmetry r is rendered dimensionless by dividing by the axial distance from the nozzle exit. It is obvious from the figure that the predicted axial velocity profile agrees well with the measured one in the inner region of the flow and overestimates it in the outer region. This discrepancy can be attributed to the deficiency of the k-ε turbulence model to deal with different types of flow with the same set of constants c_1, c_2. (Abbas et al (1980) showed that a change of c_1 to 1.57 improves the agreement in the outer region and underestimates the experiment in the inner region).

The predicted turbulent intensities across the jet at $x/d_j = 40$ are compared with the measured intensities in the self-preserving region ($x/d_j > 40$) in Fig. (6.8). It is interesting

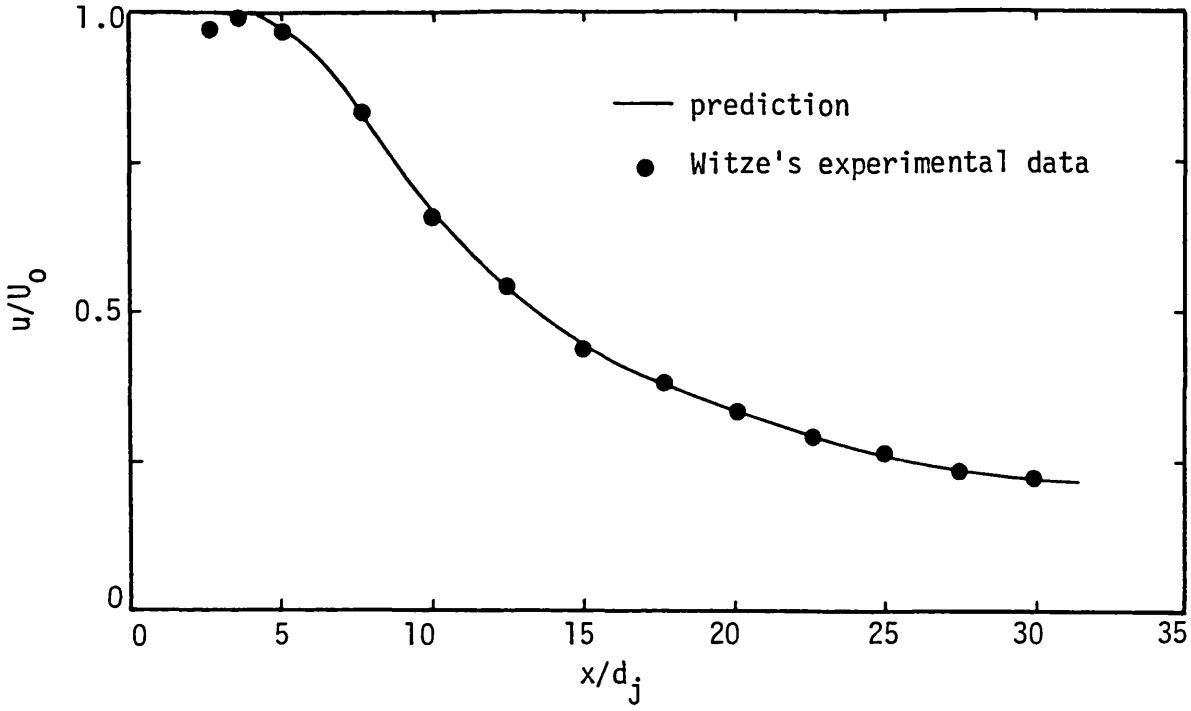


Fig.(6.6) Centreline velocity decay of steady turbulent jet.

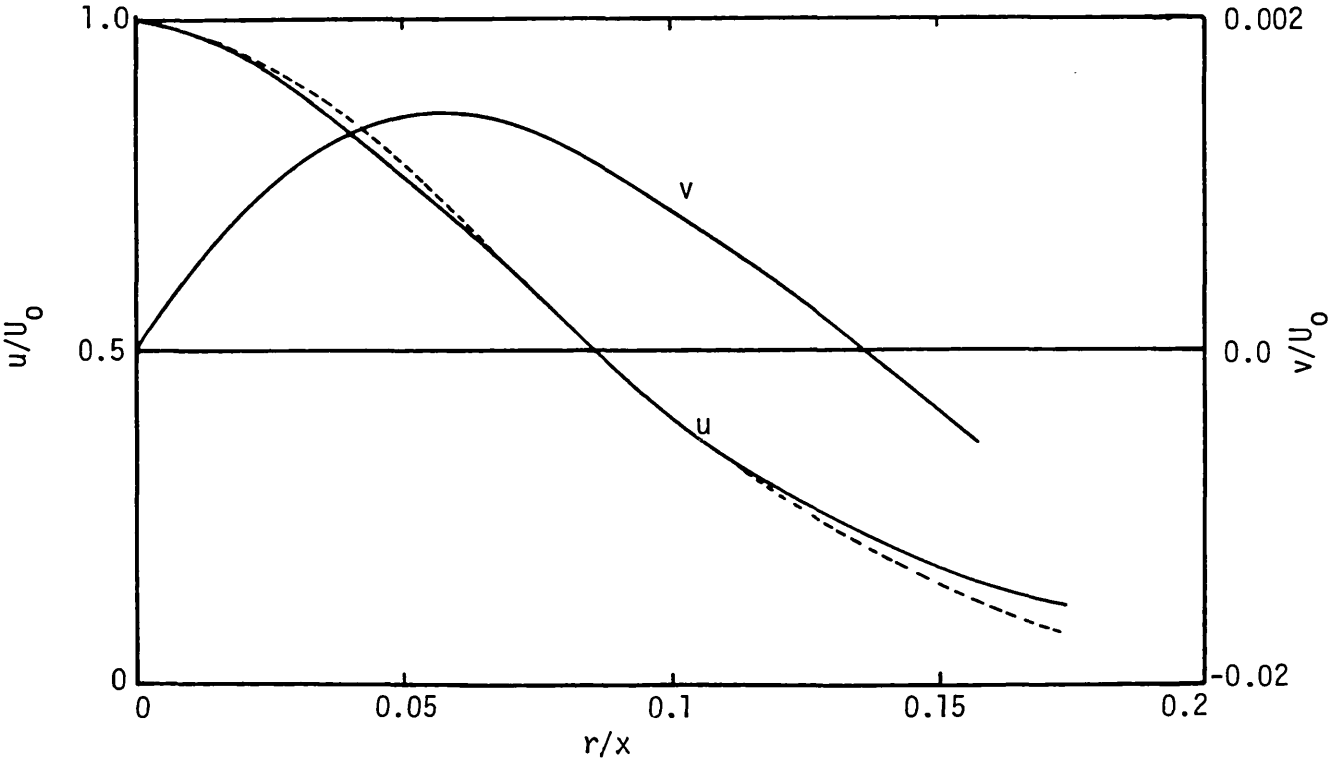


Fig.(6.7) Mean velocity of turbulent jet,---- Wygnanski et al (1969) data.

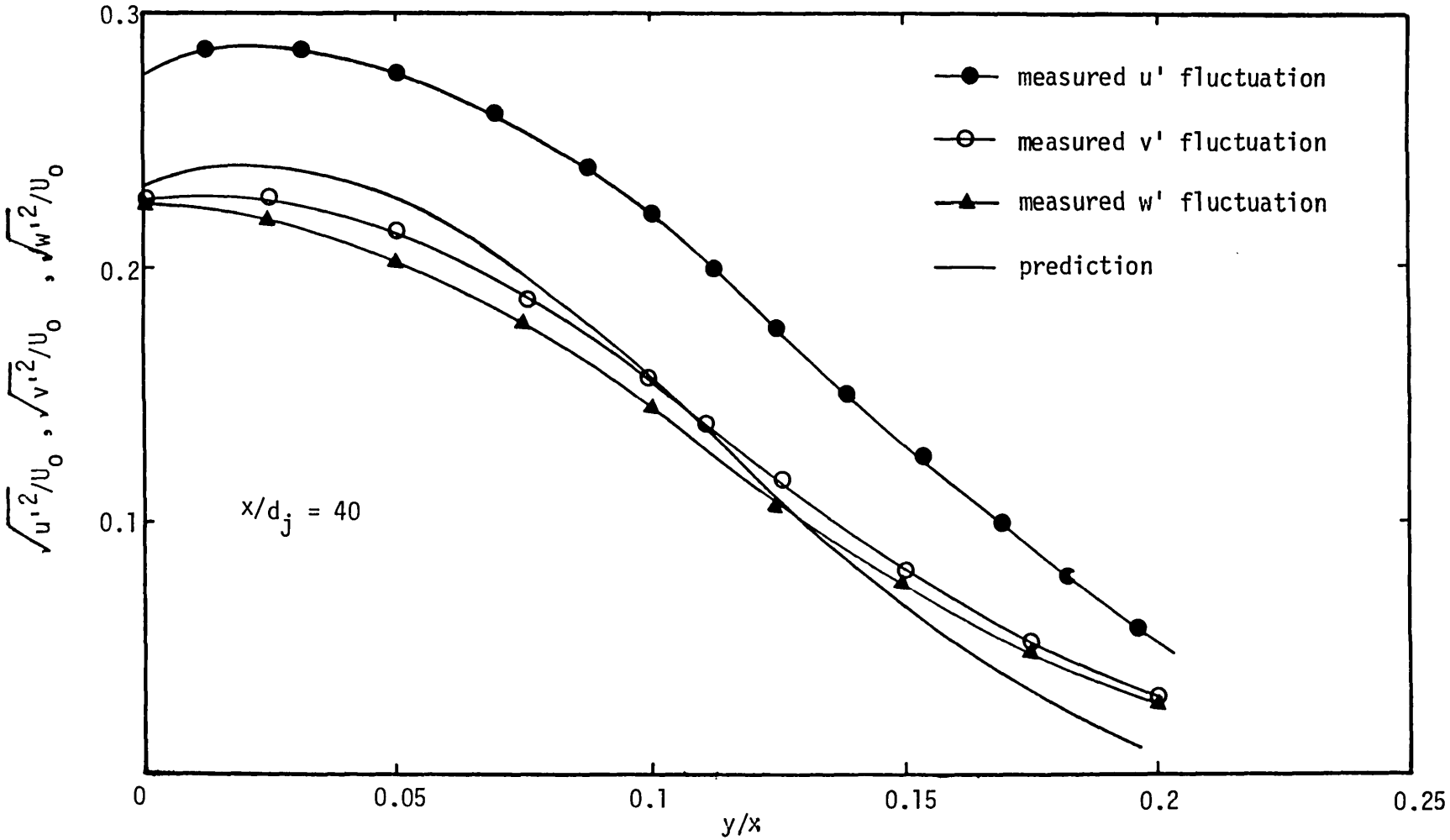


Fig. (6.8) Turbulent intensity across the jet

to note that the magnitude of the measured v' and w' in less than that of u' i.e. the turbulence of the jet is not isotropic, whereas isotropy is assumed in the calculation.

6.5 Impulsively Started Turbulent Round Jets

a. Isothermal jets

Despite its practical importance, the starting jet has received much less investigation in comparison to the steady jet. Earlier experimental work on impulsively started jets was mostly confined to the qualitative study of the flow patterns resulting from the mixing of isothermal homogeneous fluids. Rizk (1958) carried out flow visualization tests for the development of an axisymmetric starting water jet with particular reference to the scavenging process in two-stroke engines. Recently, Witze (1980) made detailed measurements in impulsively started isothermal air-into-air jets by hot-film anemometry. He measured both mean and fluctuating components of the axial velocity for both steady and transient cases, and presented four sets of experimental data using two nozzle exit configurations as shown in Fig. (6.9). He showed, as did the present calculation, that these jets exhibit an interesting feature: ahead of the advancing jet tip front, the surrounding fluid remains undisturbed and at a distance behind it steady state can be considered to have been reached (for a steady injection velocity). The transition between the undisturbed and the steady state occurs mostly in the jet tip vortex.

The different operating conditions for Witze's two nozzles A and B are given in table (6.1) below.

Table (6.1) Witze's operating conditions

case	nozzle	U_o m/s	d_j mm
1	A	53.0	1.152
2	A	103.5	1.35
3	B	22.0	1.68
4	B	54.4	1.818

For computational purposes, the set of constants used in the steady turbulent jet calculations given in section (6.4) is also used here. The results for the jet penetration are compared with those measured by Witze (1980).

A typical set of results for the velocity histories calculated at several axial locations for Case 2 of table (6.1) is given in Fig. (6.10). It can be seen from the figure that, as expected, at each location the velocity reaches a steady-state plateau, with both the rate of rise and the plateau level decreasing with distance from the nozzle exit.

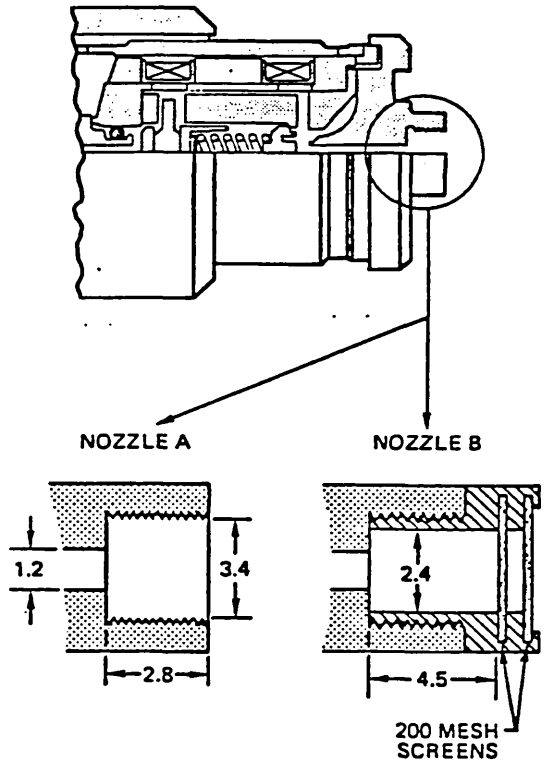


Fig. (6.9) Nozzle exit configurations of Witze's(1980) experiments

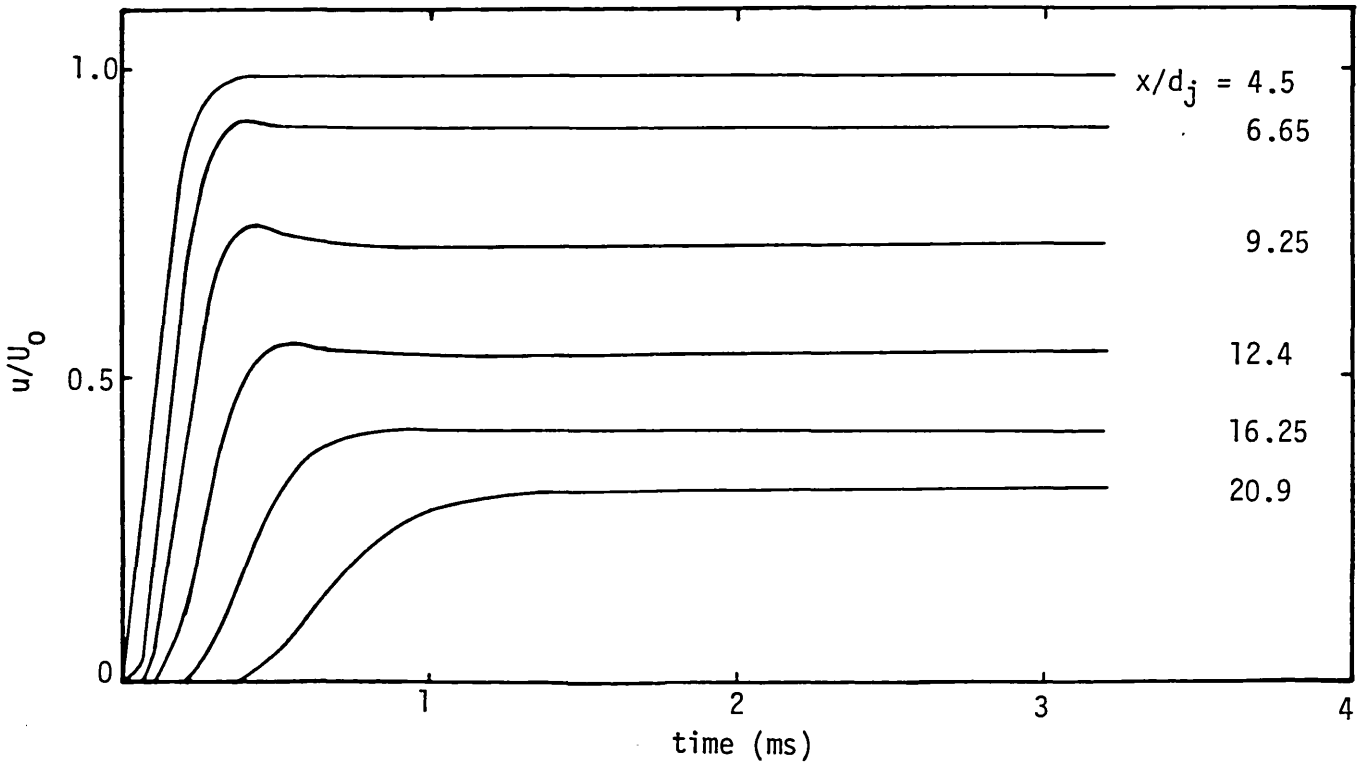
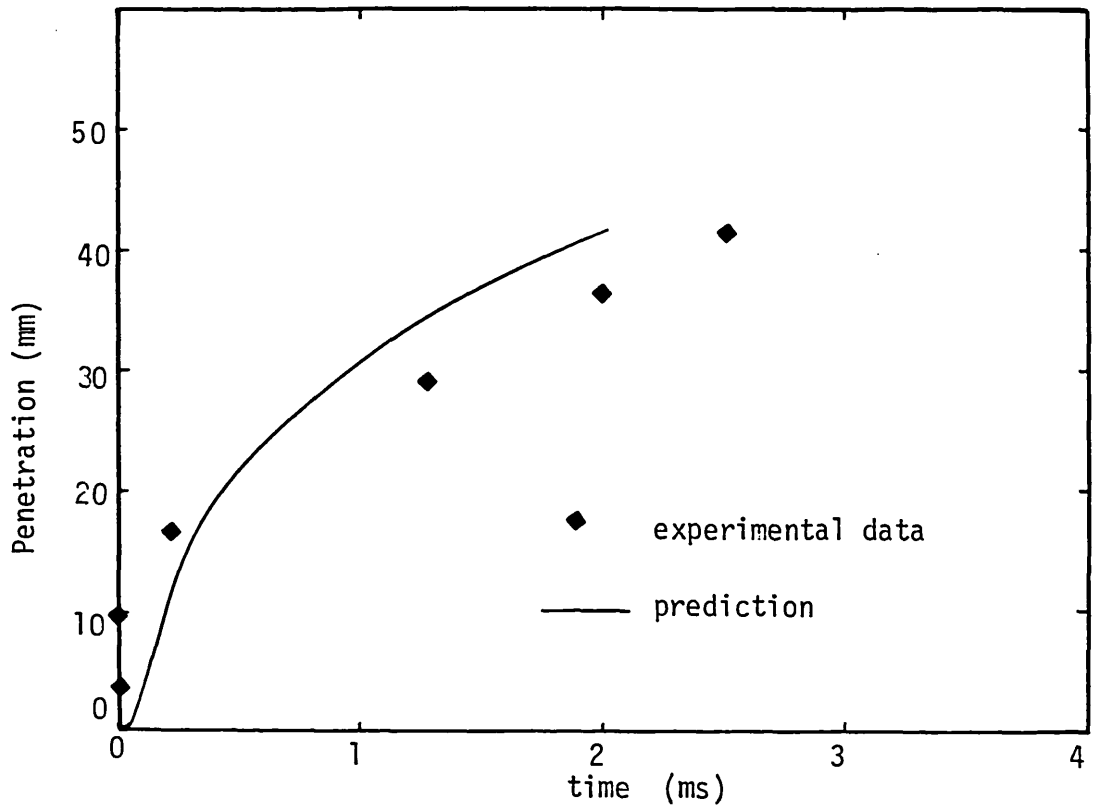


Fig. (6.10) Centreline mean velocity plateau of starting turbulent jet (U_o = 103 m/s; d_j = 1.35 mm; nozzle A)

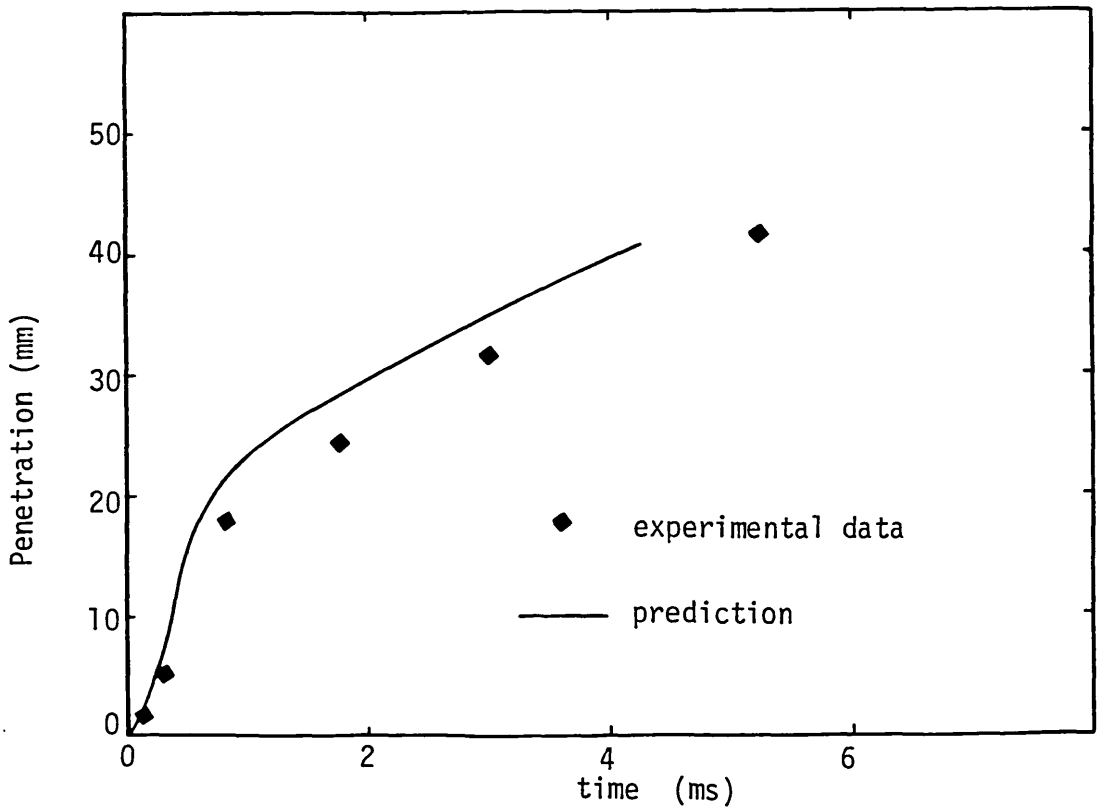
Following the procedure introduced by Abramovich and Solan (1973) the arrival time of the jet tip at a point in space is defined as the instant when the jet velocity reaches 70% of the final (steady-state) plateau value. The predicted jet penetrations are compared with the measured ones, for the four cases studied, in Figs. (6.11)(a)-(d). The overall agreement is fairly satisfactory in view of the uncertainties in both the measurements and the computations which are:

i. The computations were performed using the same turbulence constants as for the steady jet, thus assuming that the turbulence generating mechanism is the same for both steady and transient situations. However, Bermhorst et al (1977) observed in their experimental measurements of the characteristics of a pulsed jet that the turbulence at $x/d_j < 10$ is significantly higher than the steady state value.

ii. The experimental measurements of Witze were made by hot-film anemometry. As the orifice diameters were small (1.2 - 2 mm) and the hot film probe was of the same size this may have affected the flow near the orifice and presented spatial resolution limitations near the injector.

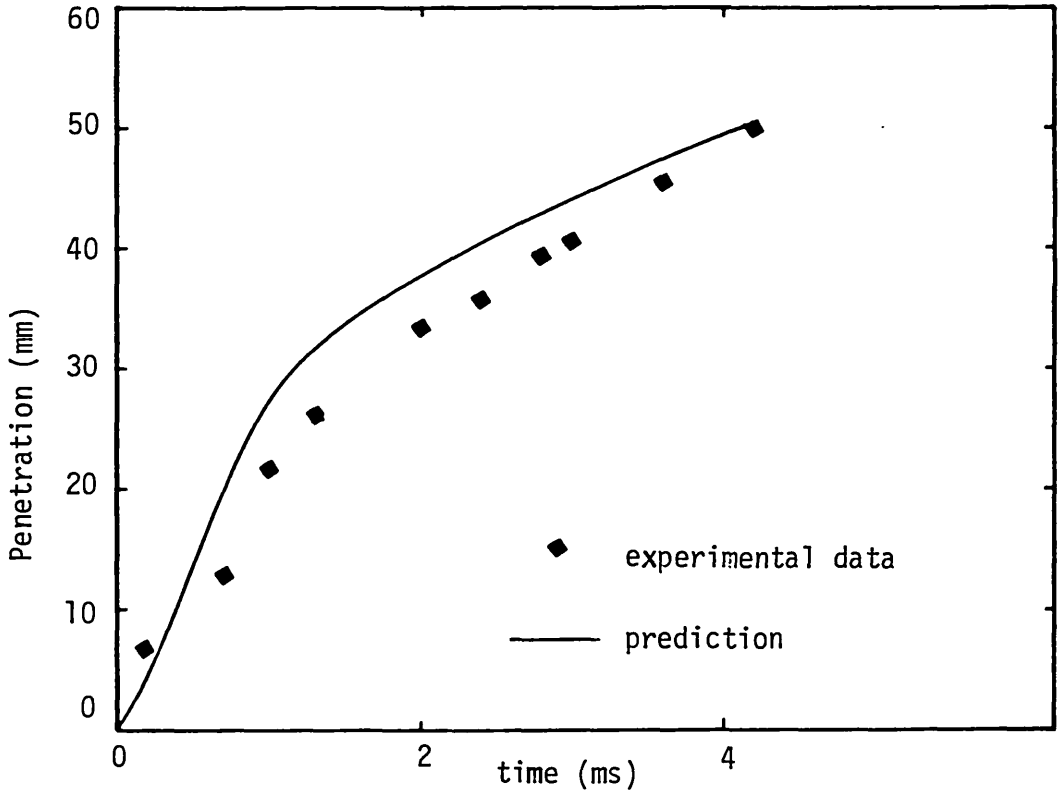


(a) Nozzle A; U_o=103 m/s; d_j=1.35 mm

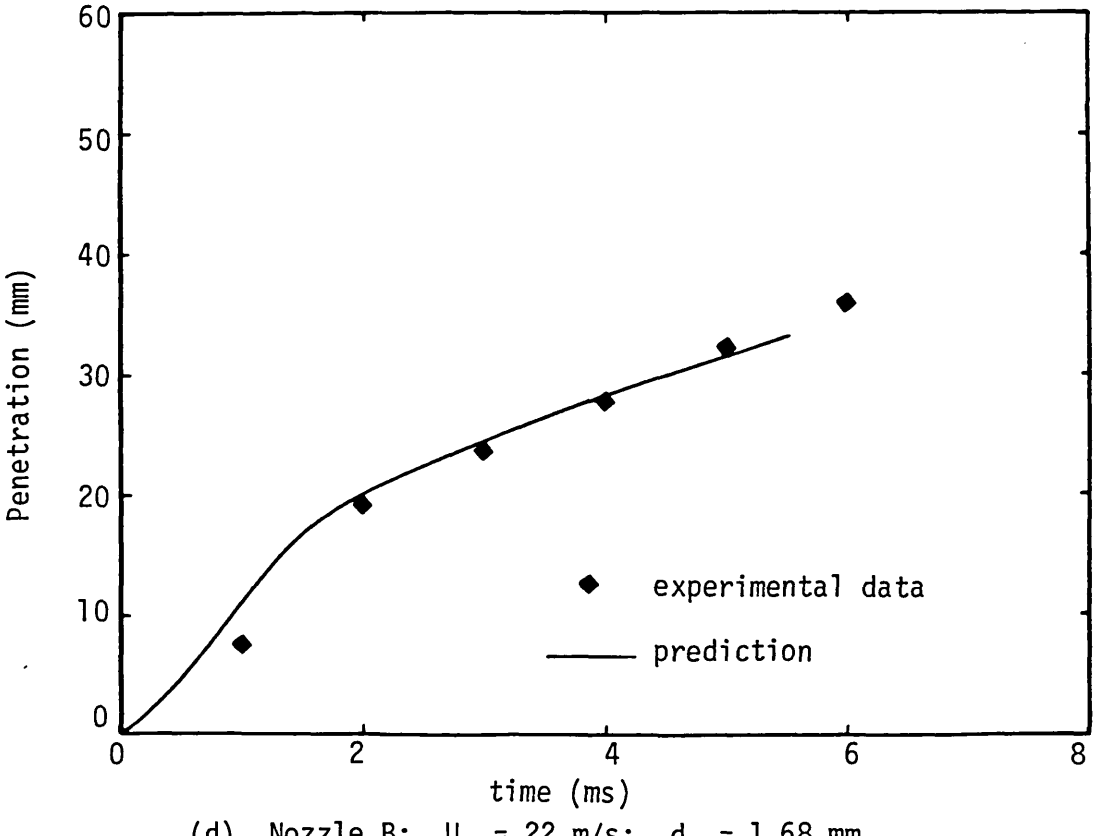


(b) Nozzle A; U_o = 53 m/s; d_j = 1.14 mm

Fig. (6.11) Comparison of predicted jet penetration with Witze's (1980) data



(c) Nozzle B; U_o = 54.4 m/s; d_j = 1.818 mm



(d) Nozzle B; U_o = 22 m/s; d_j = 1.68 mm

Fig. (6.11) Cont'd

b. Non-isothermal jets

The behaviour of the heated starting jets was investigated by Wolfhard and Bruszak (1960) and more recently by Phillips (1971). Phillips took Schlieren photographs of the development of a hot, subsonic jet emanating from a small nozzle (3 mm diameter) into cold surrounding and driven by the ignition of a combustible gas mixture. Hengrussamee (1975) conducted a similar experiment in which he only measured the velocity and temperature time histories of the gases at the nozzle outlet as shown in Figs. (6.12) and (6.13) respectively. Curve fitting to his data yields the following formulae for the variation of the gas velocity and temperature at the nozzle exit:

$$U_o = -1.637 \times 10^2 + 1.8 \times 10^5 t - 5.382 \times 10^7 t^2 + 6.7979 \times 10^9 t^3 - 3 \times 10^{11} t^4 \quad (6.3)$$

$$T_o = -2.7865 \times 10^3 + 3.796 \times 10^6 t - 1.5496 \times 10^9 t^2 + 3.027 \times 10^{11} t^3 - 2.78 \times 10^{13} t^4 + 9.7 \times 10^{14} t^5 \quad (6.4)$$

where t is the time from ignition in seconds and U_o and T_o are the gas velocity (m/s) and temperature (K) respectively. It should be noted that a time delay of about 2 ms was observed from the time of ignition to the start of the jet.

For the purpose of calculating the Phillips case and as he did not report the operating conditions of his experiments, the hot gases emerging from the nozzle are treated as air whose

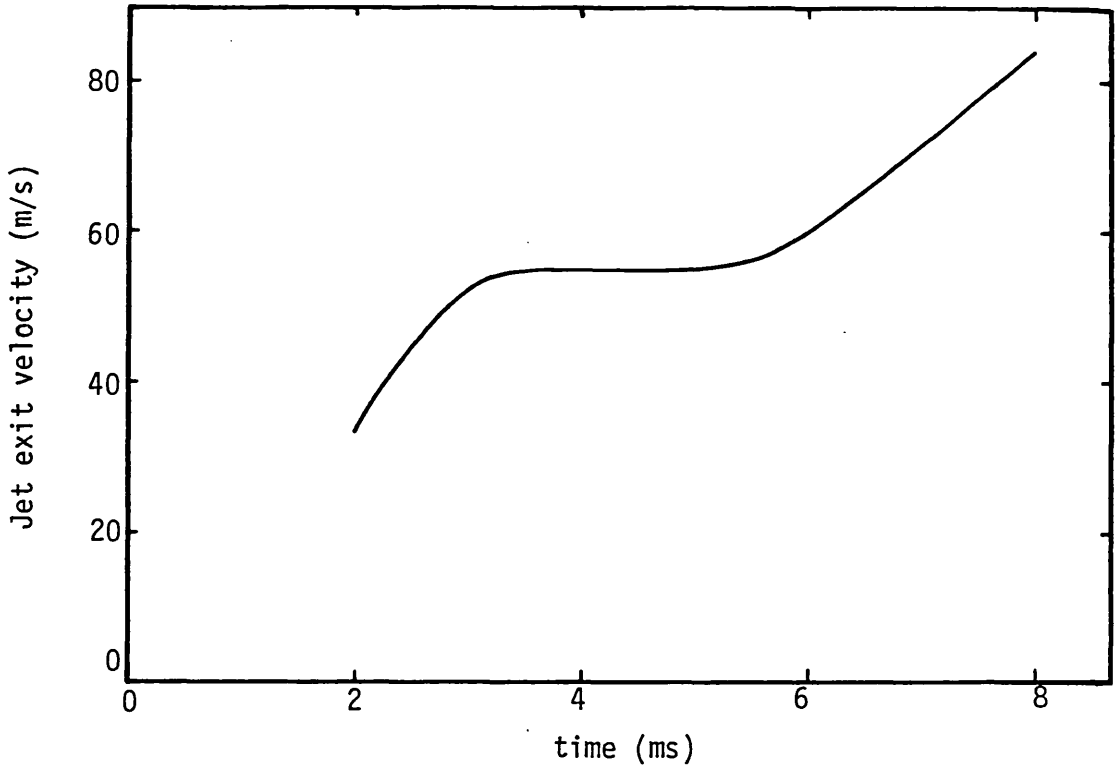


Fig. (6.12) Variation of axial velocity at the nozzle exit in the experiments of Phillips (1971)

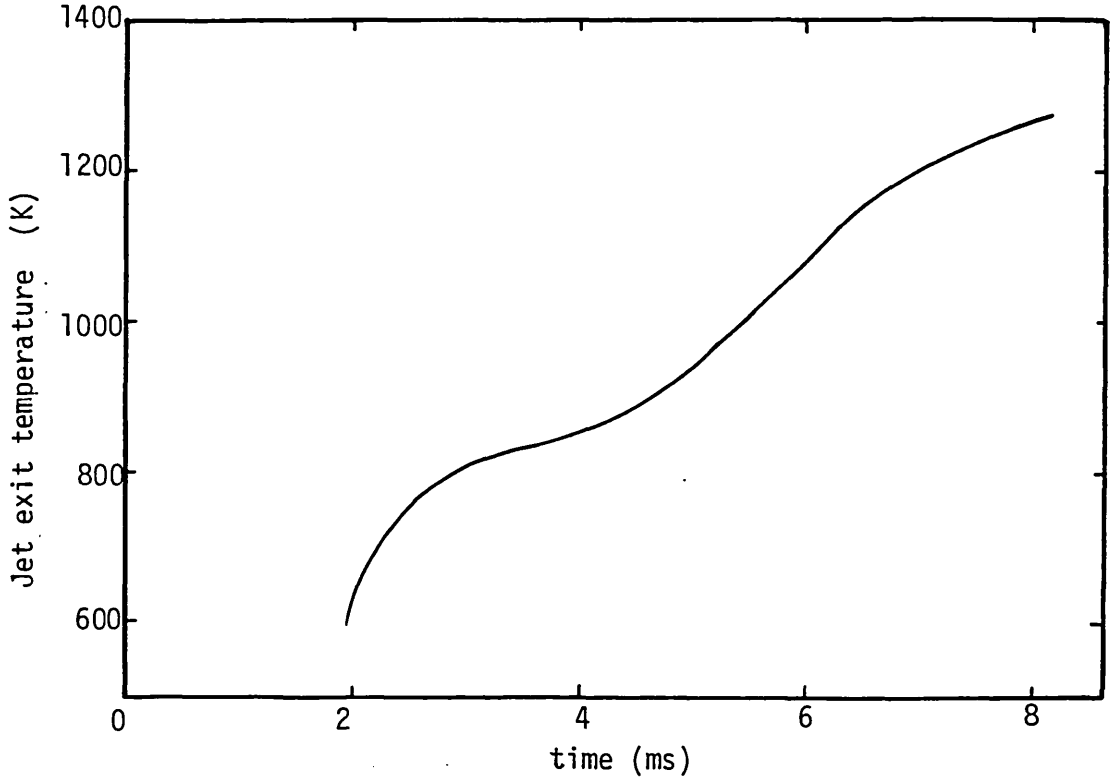


Fig. (6.13) Development of temperature at nozzle exit in the experiments of Phillips (1971)

velocity and temperature are obtained from equations (6.3) and (6.4) respectively. The initial level of the turbulent kinetic energy and dissipation rate at nozzle exit are evaluated as presented in section (6.4) i.e. in equations (6.1) and (6.2) $i = 0.03$ and $\ell_0 = 0.09\ r_j$ respectively.

The predicted development of the jet front, defined as the axial location at which the gas temperature (density) has a maximum gradient, is compared with the measured one taken from the Schlieren photographs in Fig. (6.14). The time is calculated from the instant the spark inside the enclosure is initiated. Despite the uncertainties about the turbulence level at the nozzle exit and the other exit conditions, the agreement is fairly satisfactory.

Figure (6.15) shows the comparison of the development of the jet radius (r_w) at $x/d_j = 14.3$ downstream of the nozzle outlet. The predicted radius is defined as the radial distance from the jet axis to the position where the gas temperature is 300 K (the ambient temperature). It is clear from the figure that fairly good agreement is obtained in view of the above uncertainties.

A further feature of interest which emerged from these calculations is that despite the unsteady nature of this process the predicted jet velocities at various axial positions tend to be self-similar after 8 ms from the start of ignition as shown in Fig. (6.16). The length used to render the radial distance r dimensionless is the local half-width of the profile, namely

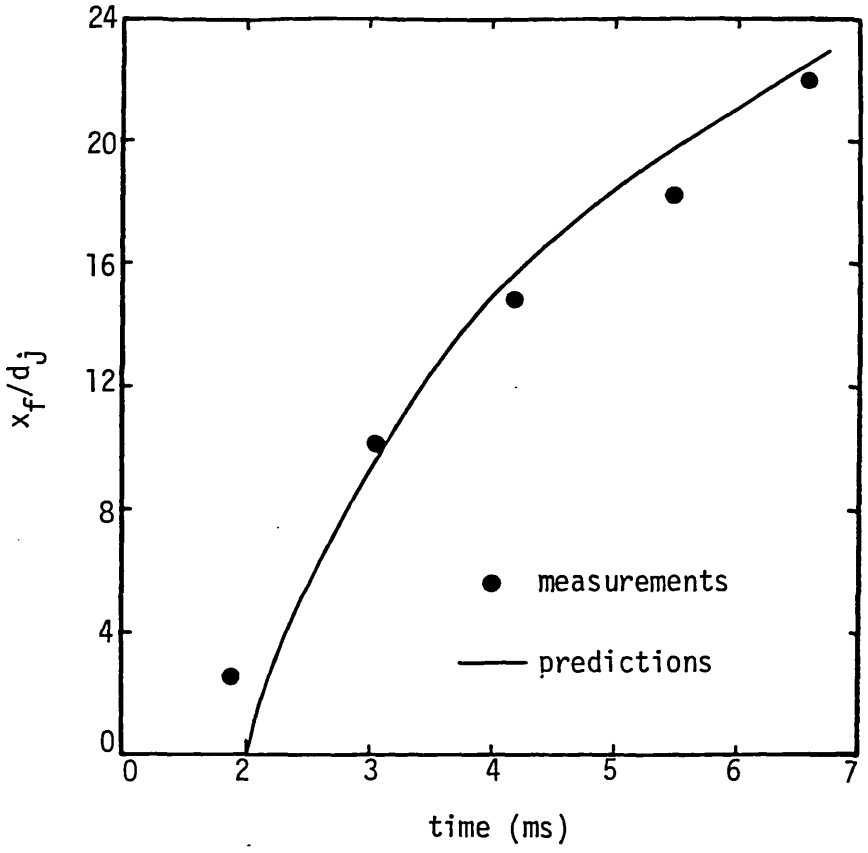


Fig. (6.14) Comparison of the predicted and experimental development of jet front

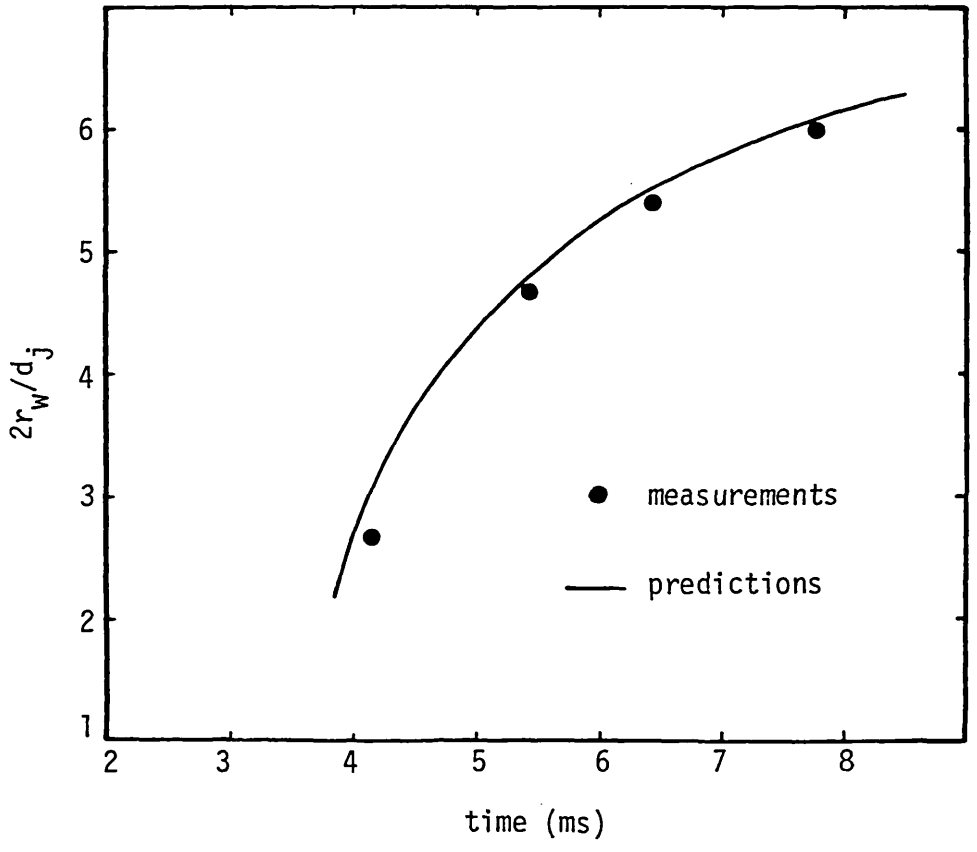


Fig. (6.15) Comparison of the predicted and experimental development of jet radius at x/d_j = 14.3

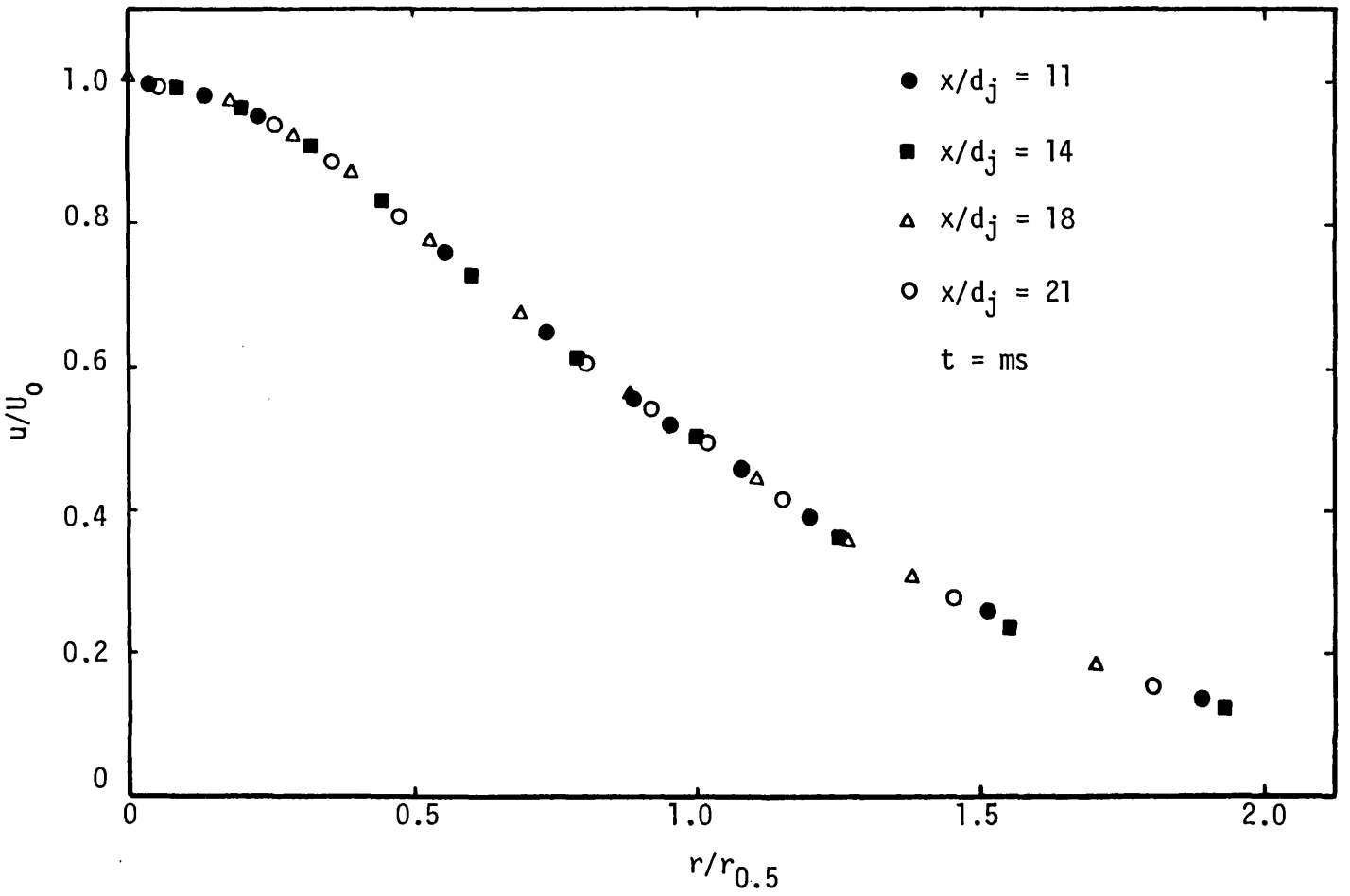


Fig. (6.16) Dimensionless velocity distribution of starting turbulent hot jet (Phillips simulation)

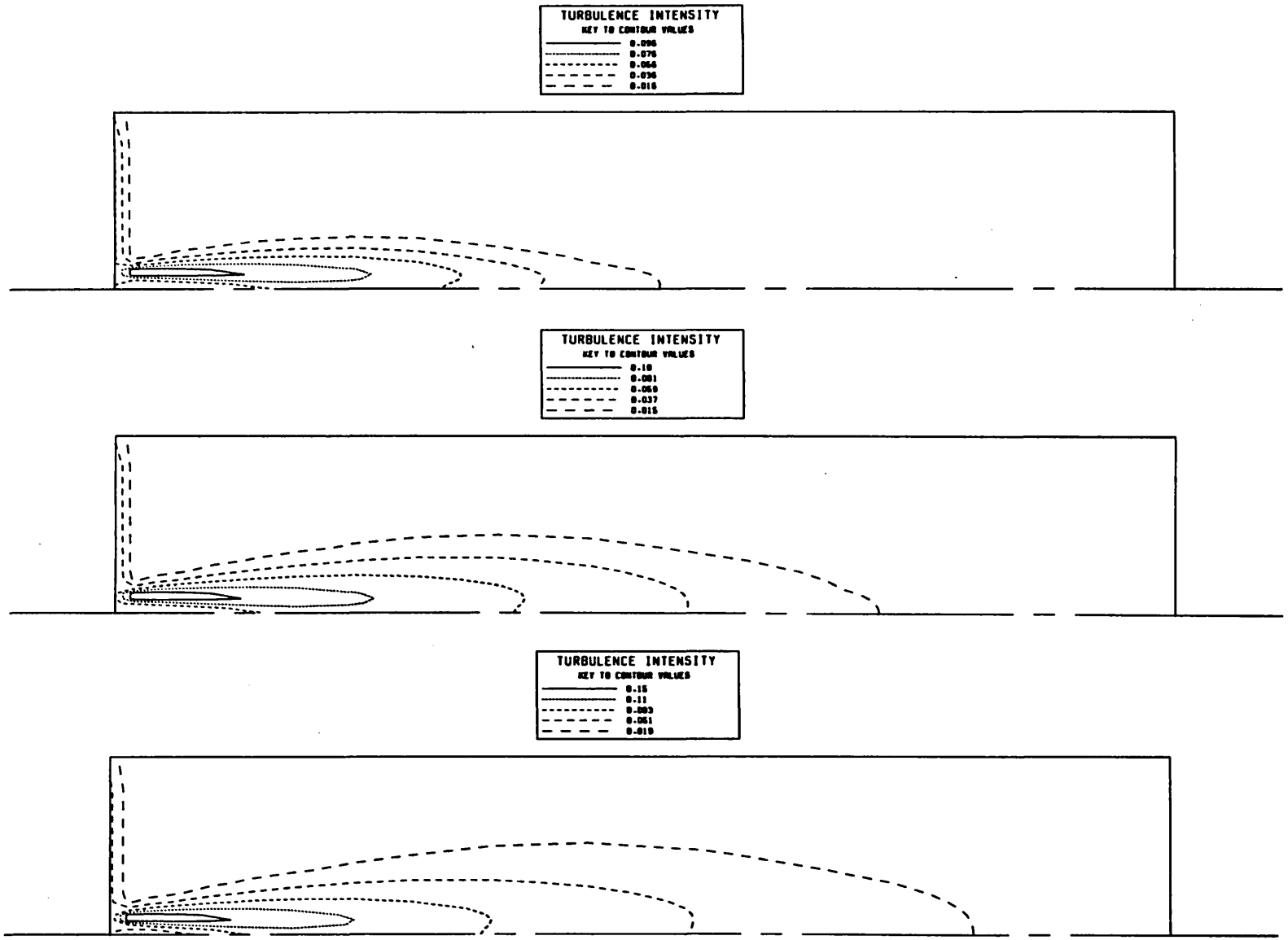
the width corresponding to the point where the mean velocity is equal to one-half of its value on the axis. It should be mentioned here that the self-similar profile of the hot starting jet is identical to that of a steady jet.

Figures (6.17)a-c show the predicted fields of turbulence intensity ($\sqrt{\frac{2}{3}k}/U_0$), turbulent viscosity and gas temperature (T/T_0) respectively. The values of U_0 and T_0 are chosen as the injection velocity and temperature at t = 8 ms. These figures display the characteristic feature of strong turbulent mixing near the nozzle. The turbulent viscosity levels vary between 10 and 200 times the molecular one, a range which is small compared with typical spray behaviour as will be shown later in Chapter 7. This is mainly due to the larger lateral spreading of the jet.

6.6 Parametric Study and Scaling Laws

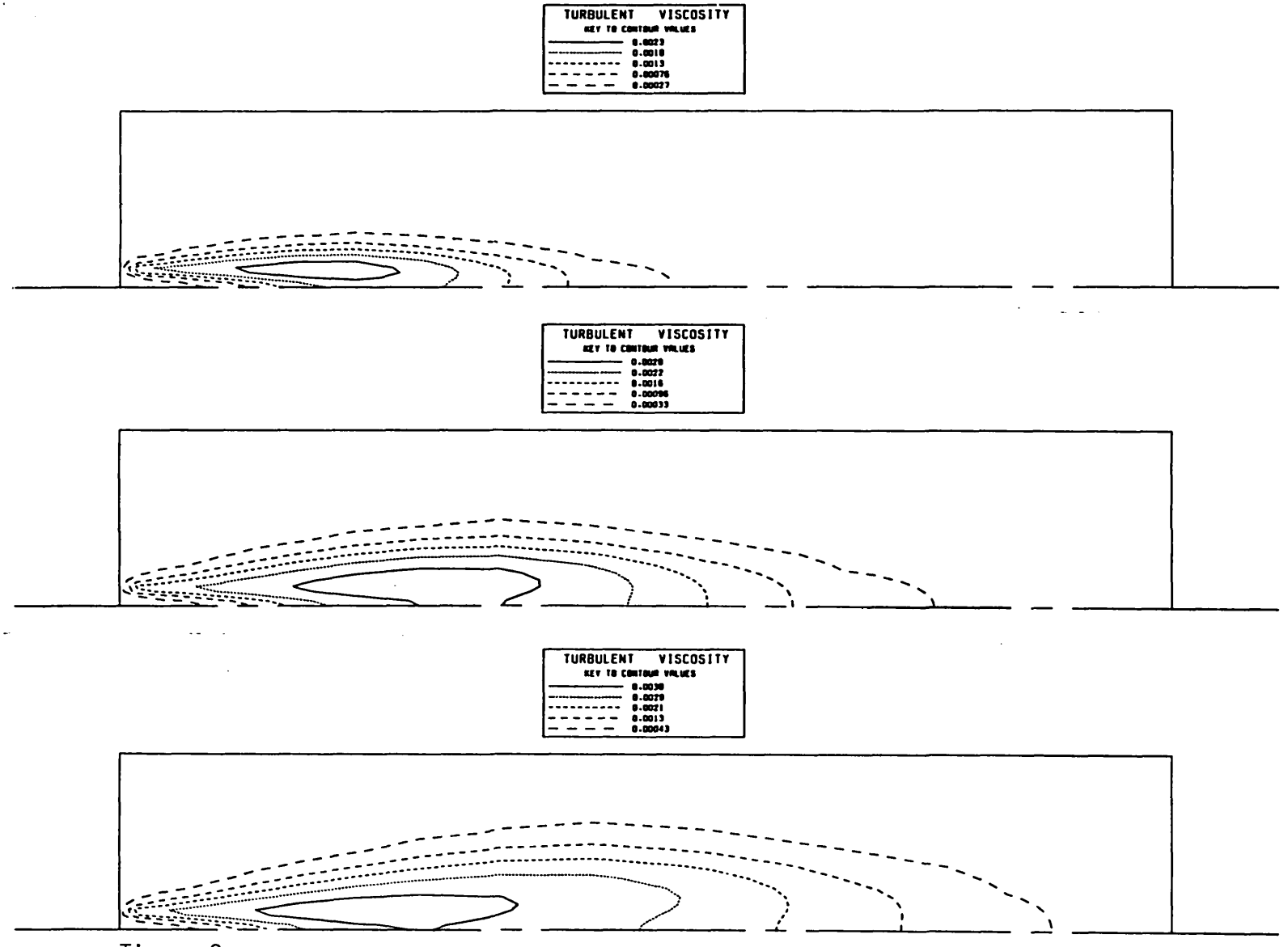
a. Parametric Study

Calculations were performed to quantify the effects of the different input parameters and physical factors on the behaviour of the steady state and transient turbulent isothermal round free jet. The values of the parameters used in the various calculations are given in table (6.2). The parameters varied are: the turbulence model c_1 coefficient, jet Reynolds number, initial



(a) Turbulence intensity contours ($\sqrt{\frac{2}{3}}\, k/U_o$)

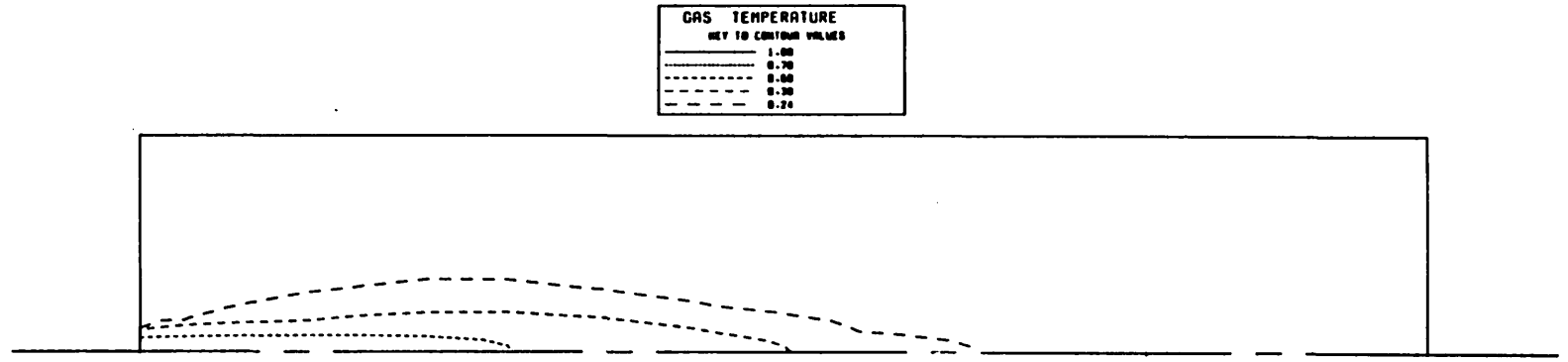
Fig. (6.17) Predicted field values of turbulence quantities and temperature of the starting non-isothermal jet



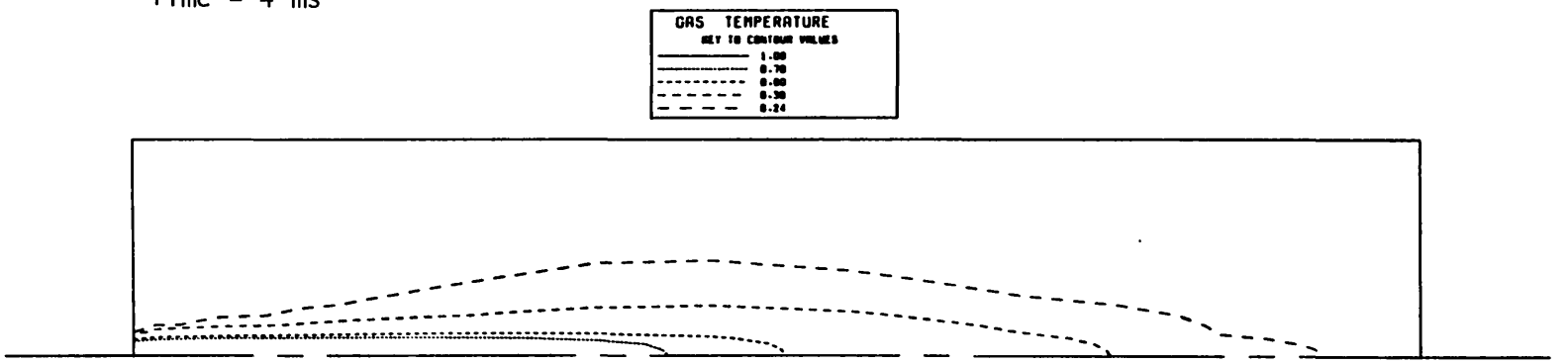
Time = 8 ms

(b) Turbulent viscosity contours (molecular viscosity = 1.9×10^{-5} kg/(m.s))

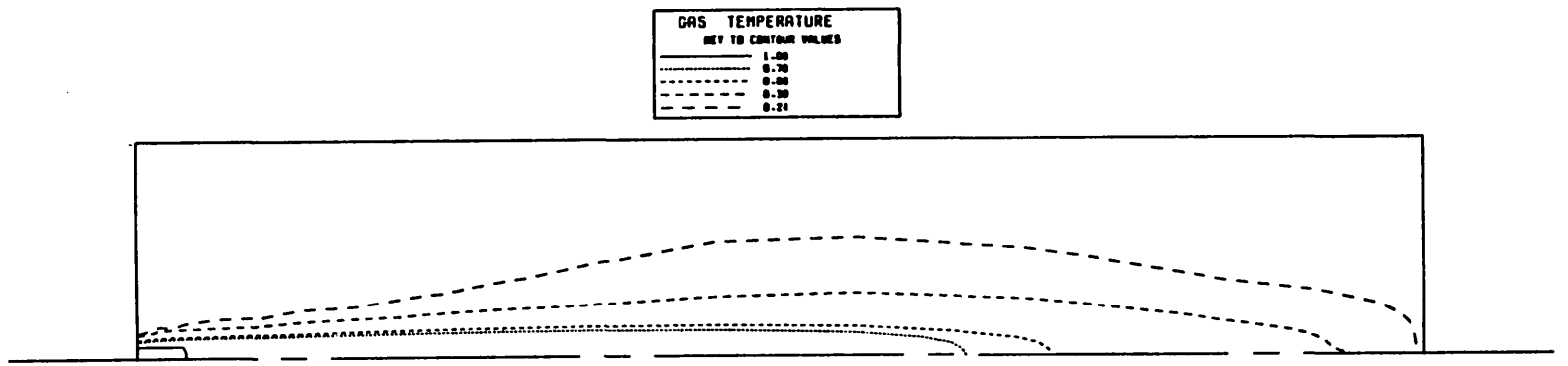
Fig. (6.17) Cont'd



Time = 4 ms



Time = 6 ms



Time = 8 ms

(c) Temperature contours (T/T_o)

Fig.(6.17) Cont'd

jet exit turbulence intensity and initial turbulent length scale.

Table (6.2) Input parameters of the parametric study

Case	$Re = \frac{U_o d_j}{\nu}$	U_o m/s	d_j (mm)	c_1	i	λ
1	8193	103	1.35	1.5	0.03	0.09
2	8193	103	1.35	1.44	0.03	0.09
3	81930	103	13.5	1.5	0.03	0.09
4	8193	103	1.35	1.5	0.003	0.09
5	8193	103	1.35	1.5	0.03	0.009

i. Effect of c_1

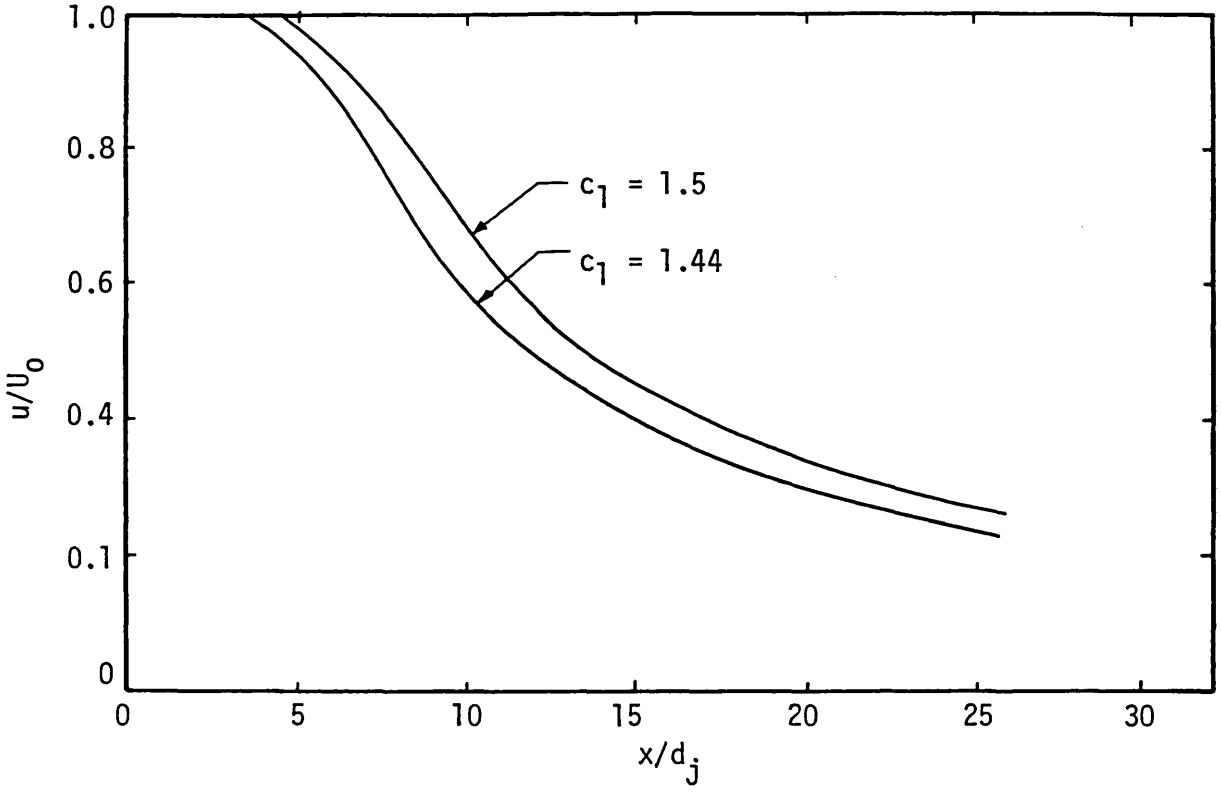
Calculations of the steady state round free jet over-estimate the spreading rate by about 40% when based on the k-ε turbulence model with coefficients optimised for plane flows (see for example Gosman et al (1976b)). A similar trend was also observed by Launder and Morse (1977) in computations based on a second-order closure for the Reynolds stress. The origin of the deficiency was shown by McGuirk et al (1977) to be the source term in the dissipation rate equation.

In the present study calculations were performed to investigate the effect of changing c_1 from 1.44 (the optimised value for planar flows) to 1.5, corresponding to cases 2 and 1 of table (6.2) respectively. This 4% variation of c_1 produces a marked change in the centreline velocity decay as shown in Fig. (6.18)a. It also affects the transient jet penetration but to a lesser extent (Fig. (6.18)b). As far as the jet spreading rate is concerned, it was found that a 15% decrease occurs. Kuo (1982) also reported that 10% increase of c_1 produced 45% decrease in the spreading rate and Launder et al (1977) pointed out that a 1% variation in either of the coefficients c_1 and c_2 can alter the rate of spread by about 4% (using the Reynolds stress closure model).

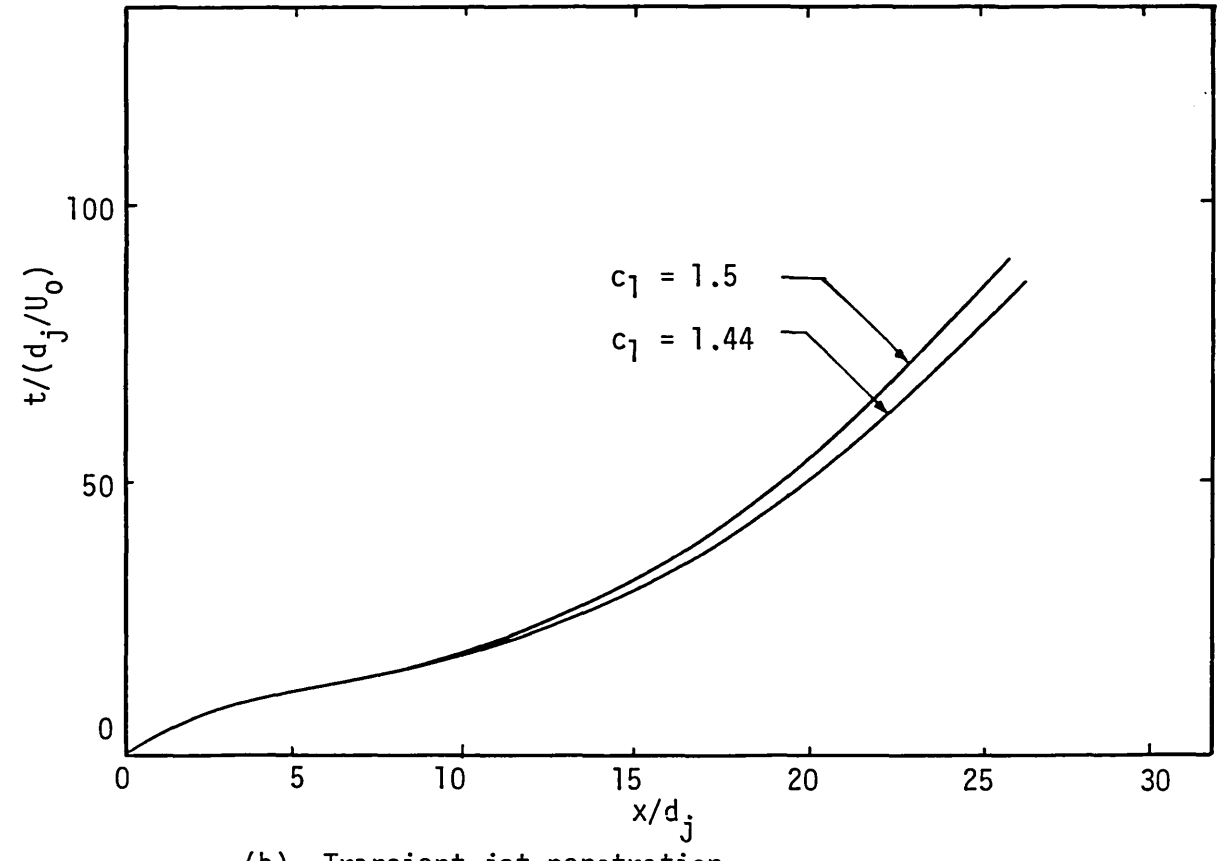
Thus it can be concluded that the computed flow field for both steady state and transient cases are very sensitive to the value of c_1; the 'best' value seems to be 1.5.

ii. The Effect of the Jet Reynolds Number

For fixed values of c_1 and levels of the turbulence intensity and length scale at the nozzle exit, computations were performed for Re = 8193 (case 1 of table (6.2)) and Re = 81930 (case 3). The results are displayed in Fig. (6.19) from which it is evident that increasing jet Reynolds number lengthens the potential core and thus delays the steady-state centreline velocity decay (diagram (a)). Also, the transient jet tip penetration



(a) Steady-state centreline velocity decay



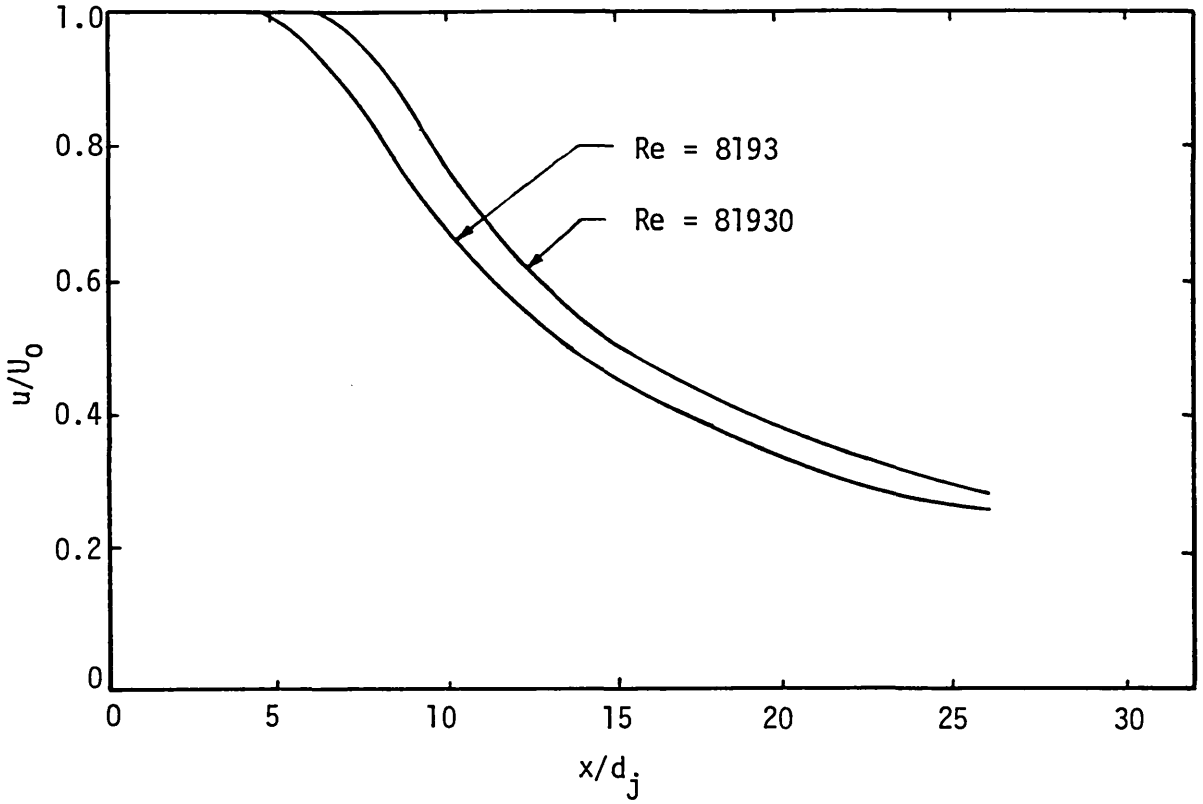
(b) Transient jet penetration

Fig. (6.18) Effect of the turbulence model c_1 coefficient

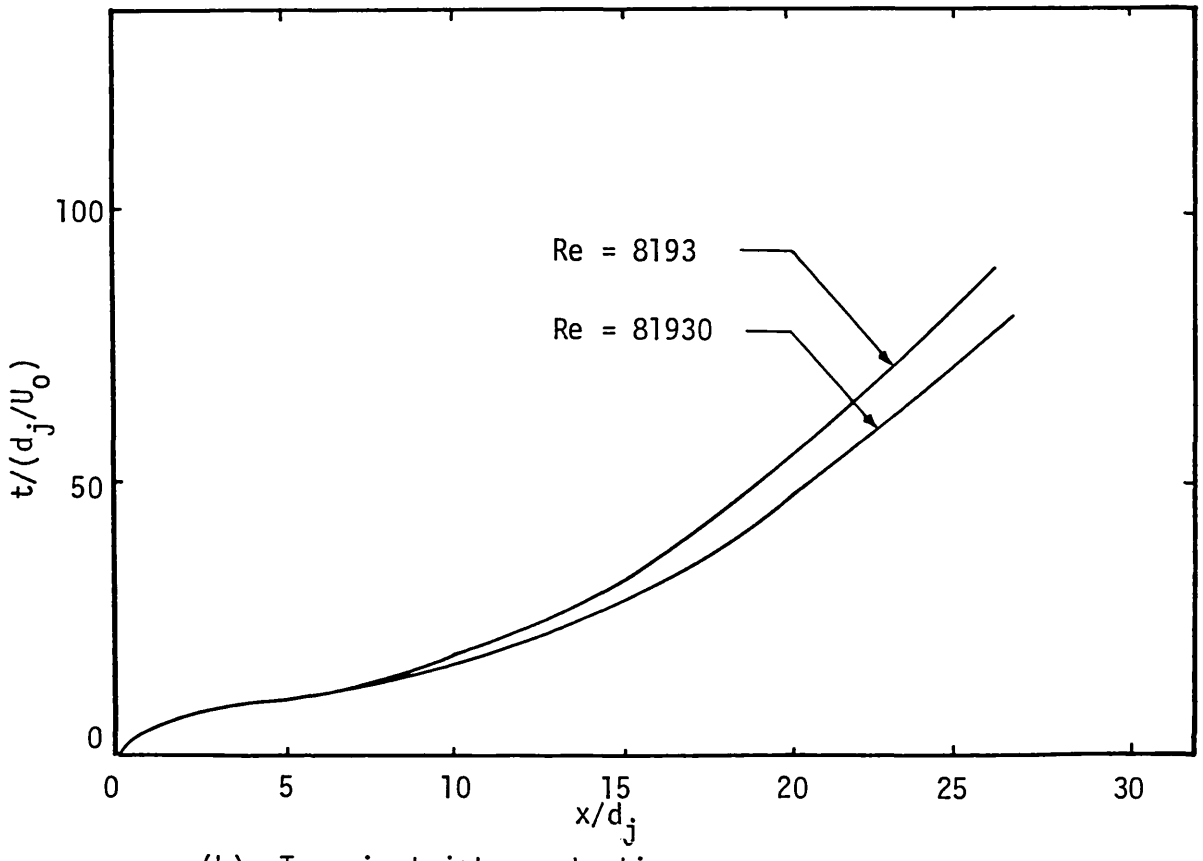
presented in Fig. (6.19)(b) shows a systematic Reynolds number dependence i.e. the higher the jet Reynolds number, the faster the penetration. Kuo (1982) observed the same tendency; he also noted that the Reynolds number dependence of both the steady-state centreline velocity decay and the transient jet penetration disappear for large values of Re ($Re > 10^5$).

iii. Effect of Initial Level of Turbulence Quantities

In the light of uncertainty about the initial level of the turbulence quantities at the nozzle exit, further predictions were performed to investigate the effect of both the turbulence intensity and the length scale on the jet behaviour. Figure (6.20) shows the effect of increasing the turbulence intensity i by a factor of 10 i.e. from 0.003 to 0.03. Although increasing i increases the turbulent kinetic energy k_{in} and hence the turbulent viscosity (for the same length scale), the results displayed in Fig. (6.20) show that increasing i yields a somewhat elongated potential core and a delayed centreline velocity decay. The transient calculations also showed a faster penetration with larger turbulence intensity. A similar trend was also observed by Kuo (1982) and Ideriah (1974). It seems that the reason for this behaviour lies in the dissipation rate ε_{in} since increasing i increases also ε_{in} according to the relation $\varepsilon_{in} = k_{in}^{3/2}/\ell_o$ and it was found that at $x/d_j > 3$ the viscosity decreases due to the higher values of ε.

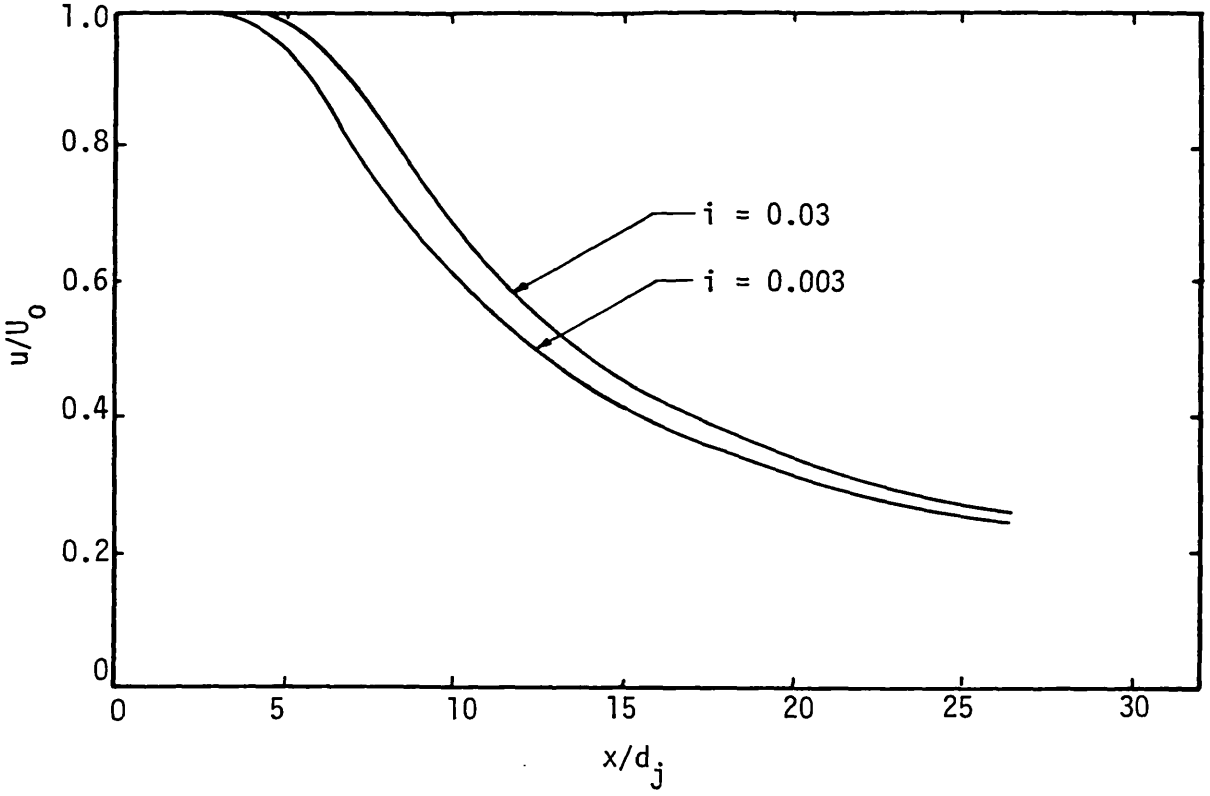


(a) Steady-state centreline velocity decay

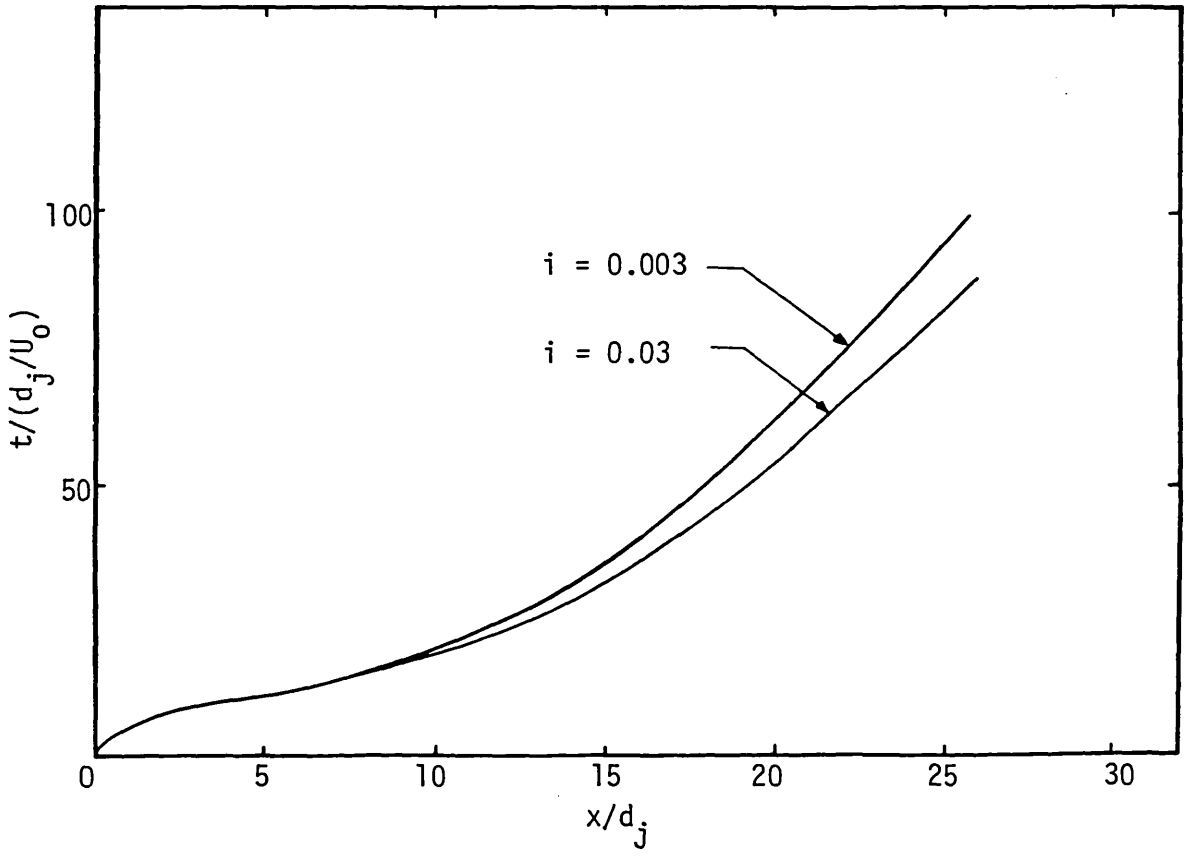


(b) Transient jet penetration

Fig. (6.19) Effect of the jet Reynolds number



(a) Steady-state centreline velocity decay



(b) Transient jet penetration

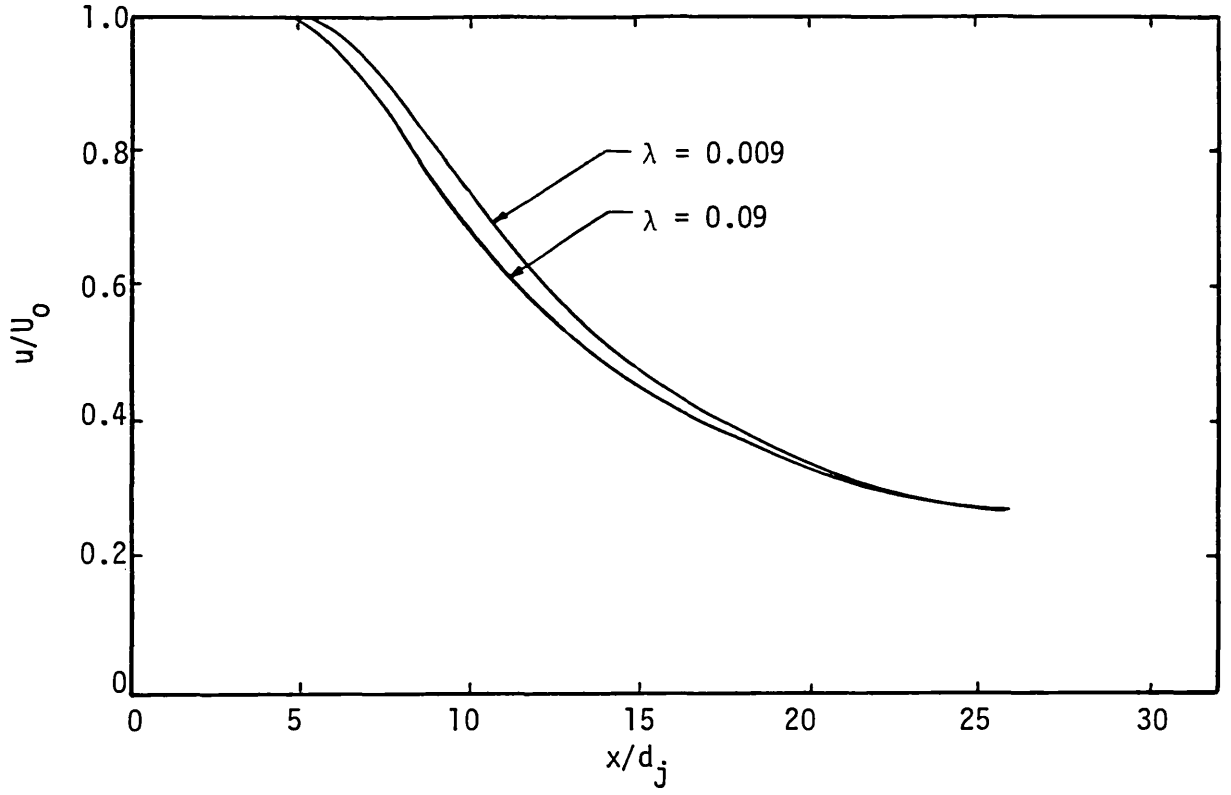
Fig. (6.20) Effect of the initial turbulence intensity

Figure (6.21) illustrates the effect of increasing the length scale by a factor of 10, i.e. from $\ell_o/r_j = 0.009$ to $\ell_o/r_j = 0.09$. As might have been expected, increasing the length scale, for the same turbulent kinetic energy, increases the turbulent viscosity and hence produces an earlier steady-state centreline velocity decay (Fig. (6.21)a) and a slower penetration as shown in Fig. (6.21)b.

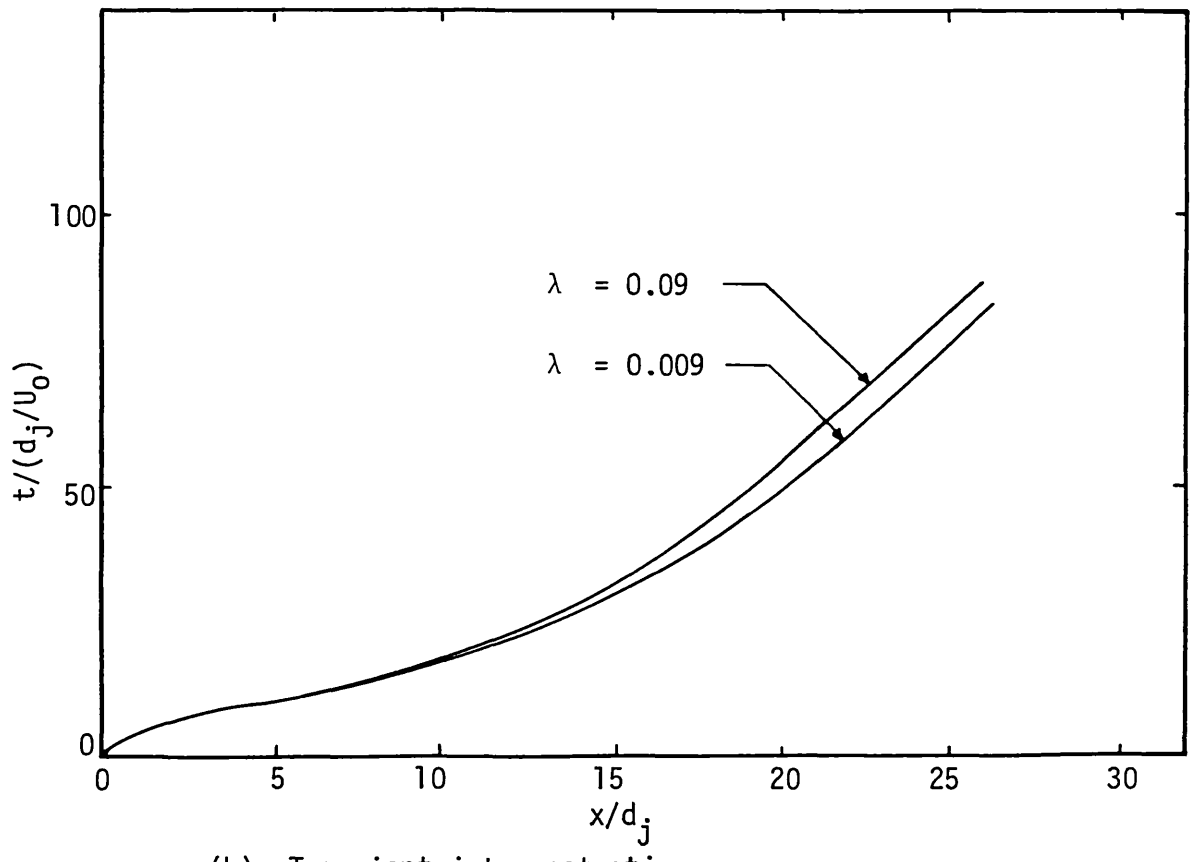
b. Scaling Laws

In sections (6.2) and (6.3), it has been shown that both the steady state centreline velocity decay and the transient jet tip penetration of the laminar round free jets exhibit a systematic Reynolds number dependence for the range $80 < Re < 500$. Also, it has been shown that the appropriate time and length scales to render all the predicted results with different Reynolds numbers lie on one line, are $t^* = t/(d_j^2/\nu)$ and $x^* = x/(d_j Re)$ respectively.

For transient turbulent round free jets, and similar to the laminar one, both the steady state centreline velocity decay and the transient jet tip penetration exhibit Reynolds number dependence (Fig. (6.19)). Following Kuo (1982) the dependence of the steady-state centreline velocity decay on the Reynolds number disappears when scaling the axial distance as $x^* = x/(d_j Re^{0.053})$ as shown in Fig. (6.22)(a). The penetration of the transient jet is scaled by $t^* = t/(d_j Re^{0.053}/U_o)$ to account for Re dependence as shown in Fig. (6.22)(b).

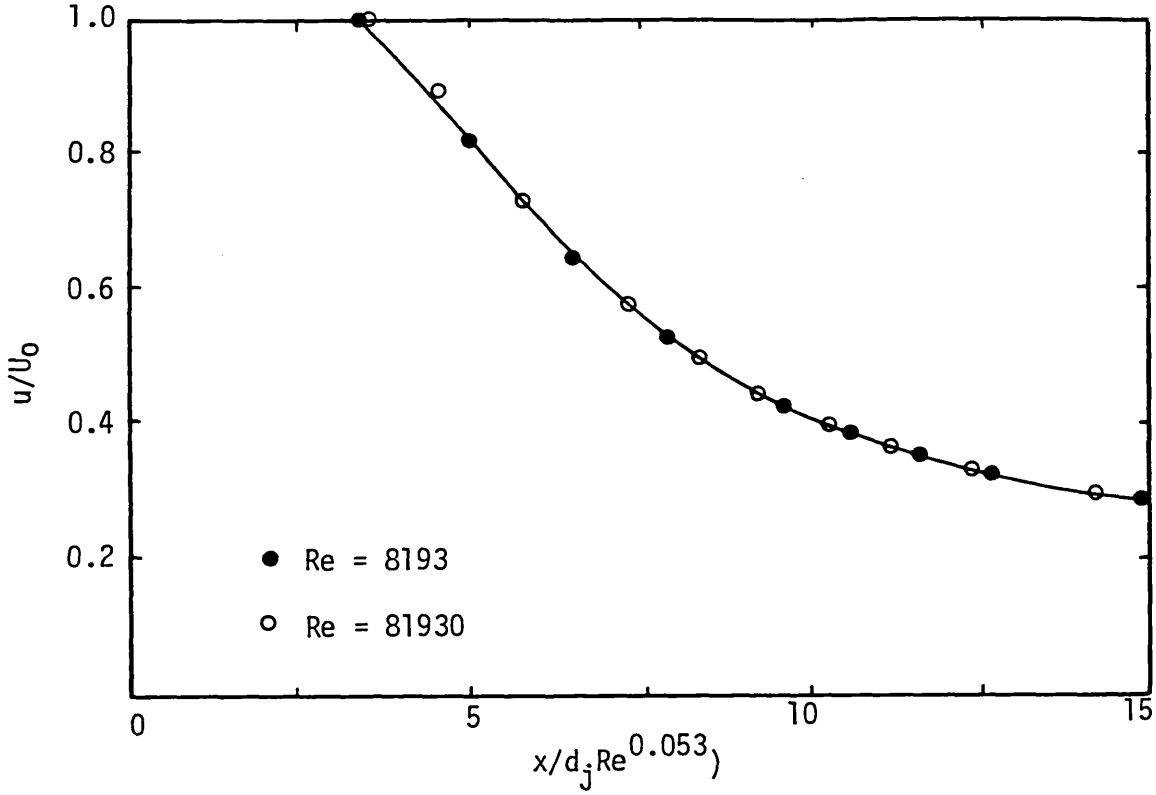


(a) Steady-state centreline velocity decay

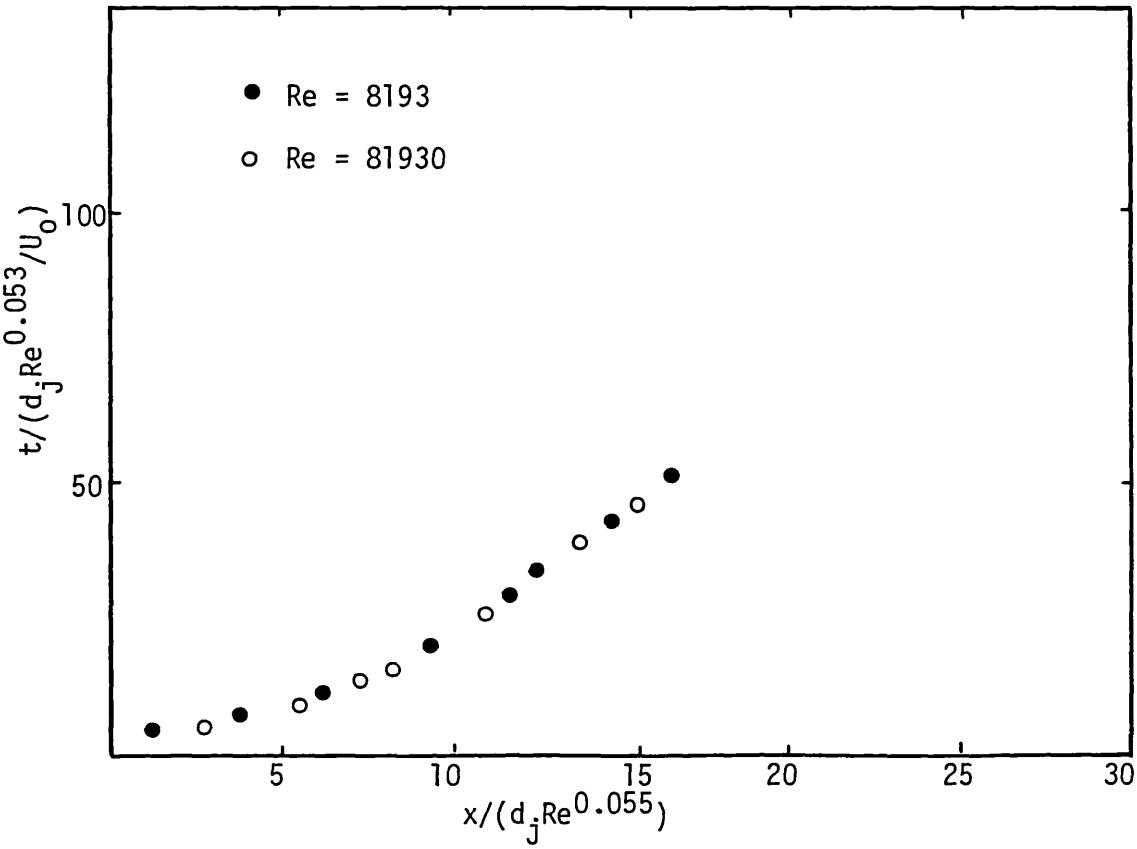


(b) Transient jet penetration

Fig. (6.21) Effect of the initial mixing length scale



(a) Steady-state centreline velocity decay



(b) Transient jet penetration

Fig. (6.22) Scaling of transient turbulent round free jets

6.7 Concluding Remarks

The present tests have demonstrated that it is possible to calculate the behaviour of laminar and turbulent gas jets to a tolerable degree of accuracy using the implicit method.

It has been shown in chapter 5 that also the semi-implicit method is capable of predicting the behaviour of laminar and turbulent gas jets provided that the time step satisfies the stability requirements.

The predicted steady-state centreline velocity decay and the transient jet tip penetration of incompressible laminar free jet agree well with the experimental measurements of Abramovich and Solan (1973) and it is found that the length and time scales are $x^* = x/(d_j Re)$ and $t^* = t/(d_j/\nu)$ respectively.

It is also found that isothermal turbulent jets can be well predicted provided that the coefficient c_1 in the dissipation rate equation is adjusted to the value 1.5.

The transient calculations of the turbulent hot jet have been shown to predict Phillips (1971) experimental data fairly well, despite the uncertainty about the turbulence level at nozzle exit.

The parametric study presented in section (6.6) revealed that increasing the turbulence intensity at nozzle exit lengthens the potential core and delays the steady-state centreline velocity decay while the transient behaviour shows a faster penetration. It is also found that increasing the length scale at nozzle exit, for the same turbulent kinetic energy, produces an earlier steady-state centreline velocity decay and a slower jet penetration.

Finally, the predicted steady-state centreline velocity decay and the transient behaviour of the turbulent jet showed a Reynolds number dependence for the range of Re studied. The spatial and temporal development of the turbulent jet are scaled as $d_j Re^{0.053}$ and $d_j Re^{0.053}/U_o$ respectively.

CHAPTER 7

ASSESSMENT OF THE SPRAY CALCULATION PROCEDURE

7.1 Introduction

As already noted, the main intended application of the procedure described in chapter 3 is to the modelling of diese-like fuel sprays. For the purpose of assessment of the procedure, which is the objective of this chapter, it is desirable to compute sprays for which experimental data are available. Unfortunately, experiments which provide sufficient data to fully specify the initial and boundary conditions of the spray do not appear to exist, due to the difficulty of conducting measurements near the injector. Thus, it has been necessary in the present study to estimate some of the required information, notably the initial droplet size and velocity distributions.

The prediction procedure is evaluated against four sets of experimental data which come closest to providing the necessary spray information: they are those of Yule (1984) and Yule et al (1985b) for isothermal and evaporating diesel sprays (which were conducted in parallel with the present study; Hiroyasu and Kadota (1974), for isothermal sprays; and finally, Kuniyoshi et al (1980) for evaporating sprays.

A second objective of this chapter is to test the sensitivity of the predictions to various features which it contains such as the initial level of turbulence quantities, initial velocity profile of the droplet, turbulent droplets dispersion, initial spray cone angle, initial droplet sizes, initial size distribution function, injection rate history and fuel introduction temperature.

7.2 Isothermal Sprays

7.2.1 Comparison With Measurements

i. The experiments of Yule et al (1985a,b)

As already shown in chapter 2, these experiments had the objective of measuring the structure and penetration of sprays injected from 0.46 mm diameter single hole Lucas nozzle into an inert quiescent gas. In addition, the fuel flow rate versus time characteristics were measured and a unique curve was found for all charge pressures and temperatures (Fig. (7.1)). The parcel masses and velocities are calculated from the injection rate diagram in the manner described earlier in section (4.8).

The droplet size distrubiton was measured at atmospheric pressure and at an axial distance of 64 mm downstream of the injector (see Boulderstone et al (1981)). The droplet size distribution was fitted by a Rosin-Rammler function as:

$$\frac{1}{V}\frac{dV}{dD_d} = n\,\frac{D_d^{n-1}}{\bar{D}}\,e^{-\{(D_d/\bar{D})^n\}} \qquad (7.1)$$

where dV is the volume of the droplets having diameter between D_d and $D_d + dD_d$ and n and $\bar{D}$ are the experimentally determined Rosin-Rammler exponent and mean diameter having the values of 2 and 25 μm respectively to yield droplets ranging from 0 to 60 μm approximately (Fig. (7.2)). In the present study this distribution was assumed to prevail in the vicinity of the injector and was used as the inlet conditions for the calculations, in the absence of any better information.

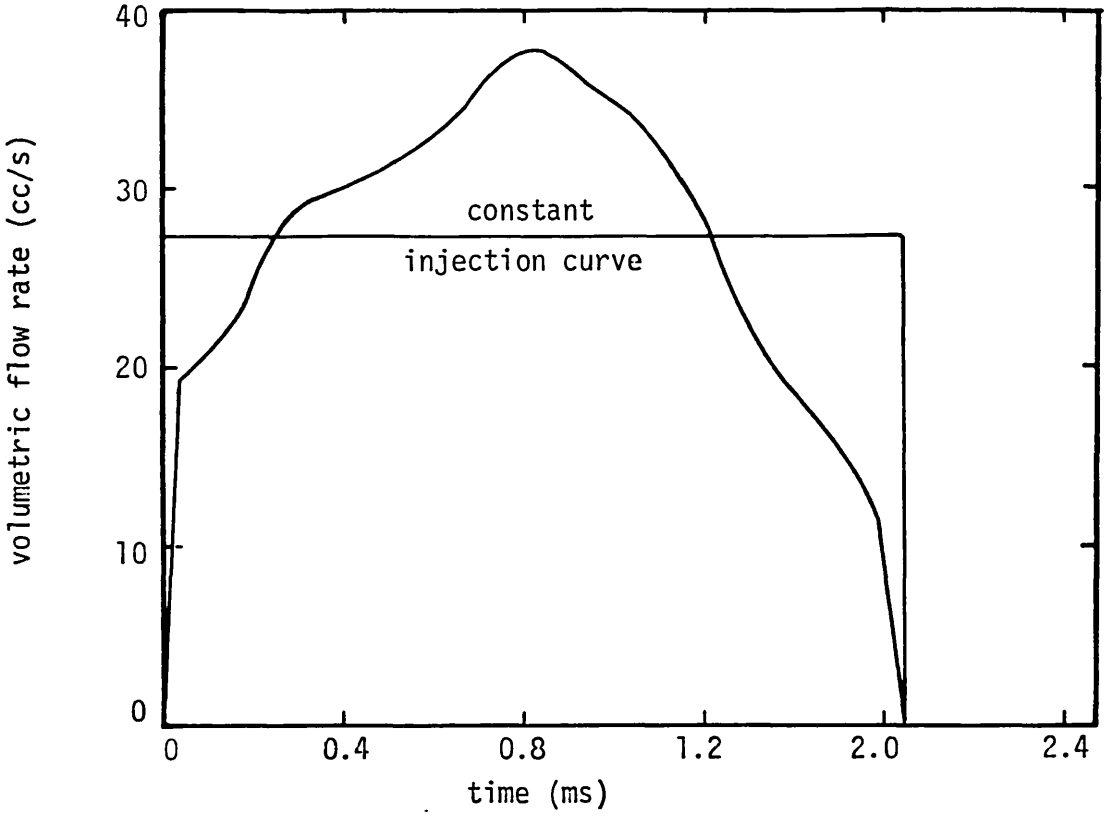


Fig. (7.1) Constant and measured injection rate diagrams from Yule et al (1985b)

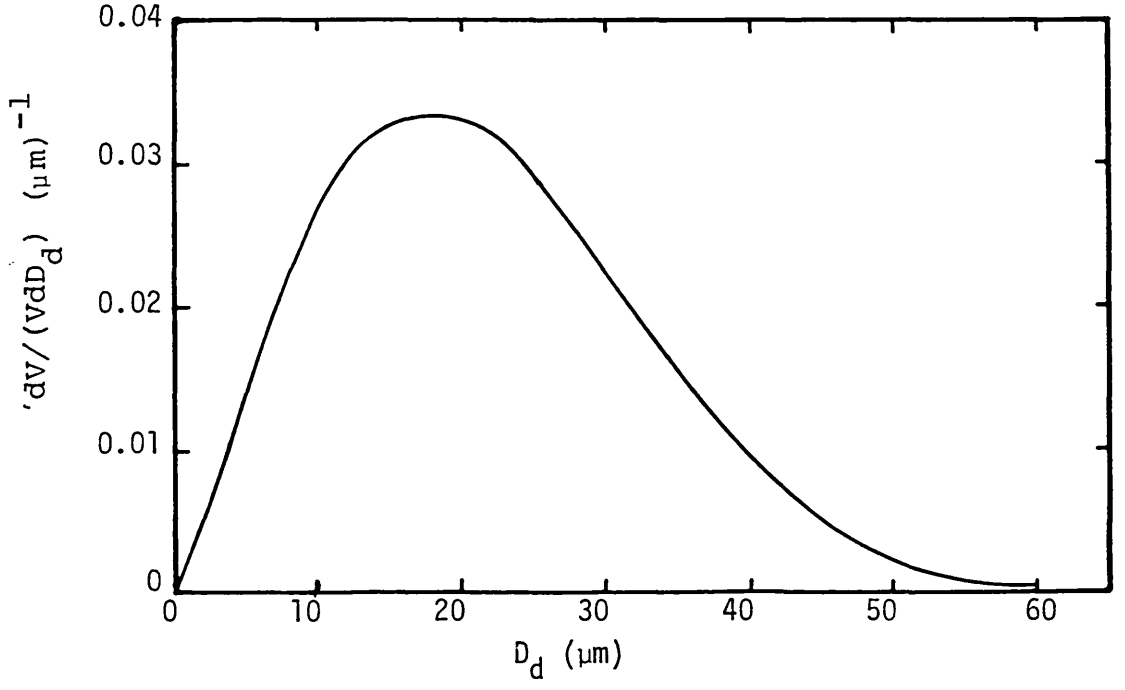


Fig. (7.2) Measured droplet size distribution, from Boulderstone et al (1981)

The measured spray cone angle versus time variation shown in Fig. (7.3) for different charge pressures (T = 288K) were used to calculate the inlet radial velocity of the droplets (see section (4.8)).

The different measurements of Yule et al (1985b) are summarized in table (7.1).

Table (7.1) Experimental measurements of Yule et al (1985b)

		P=0.5 MPa	1.5 MPa	2.5 MPa	3.5 MPa	4.5 MPa	5.0 MPa
T = 288K	penetration	✓	✓	✓	✓	✓	✓
	spray cone angle	✓	✓	✓	✓	✓	✓
	injection rate diagram	✓	✓	✓	✓	✓	✓
T = 373K	penetration	✓		✓		✓	
	spray cone angle	✓		✓		✓	
	injection rate diagram	✓	✓	✓	✓	✓	✓

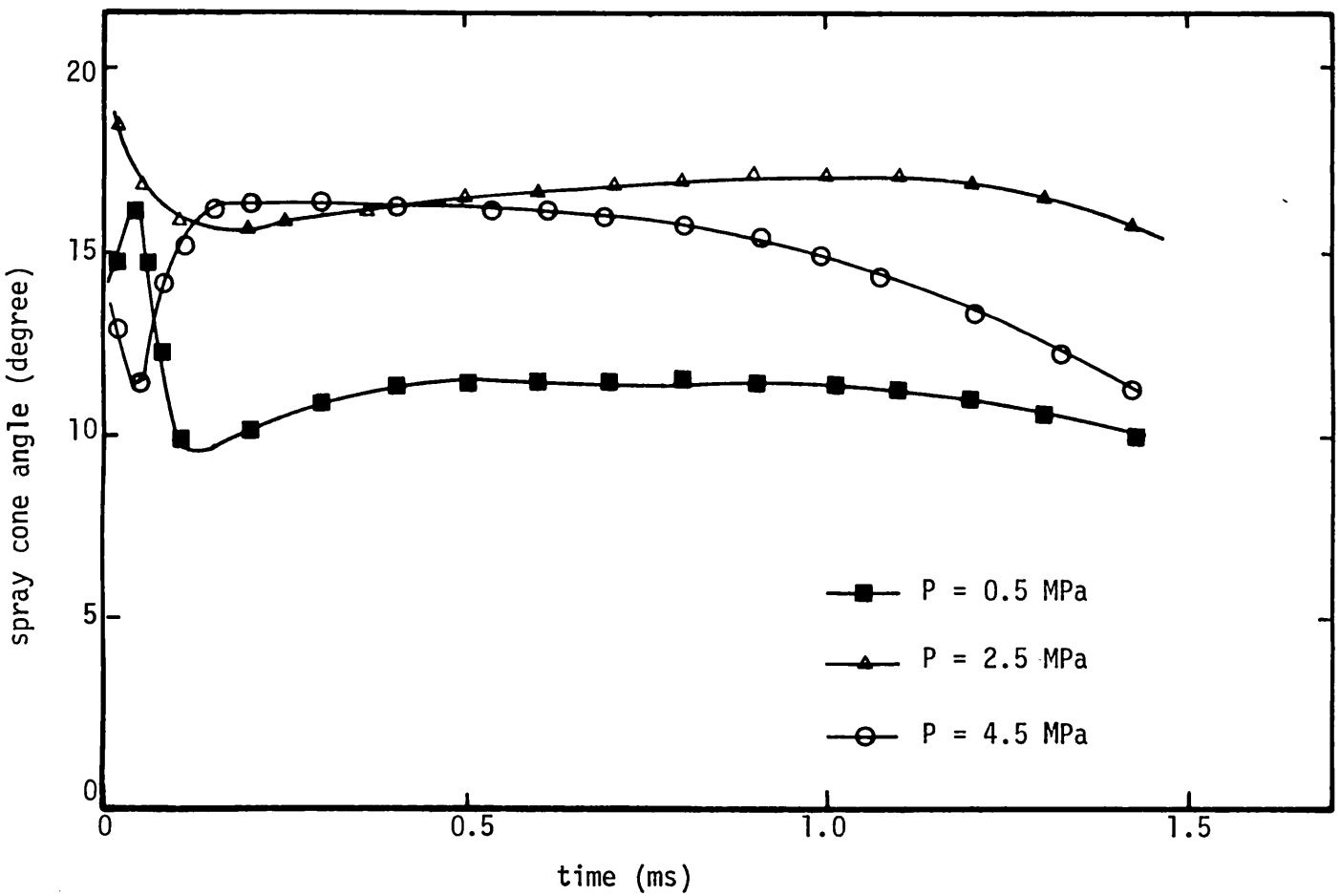


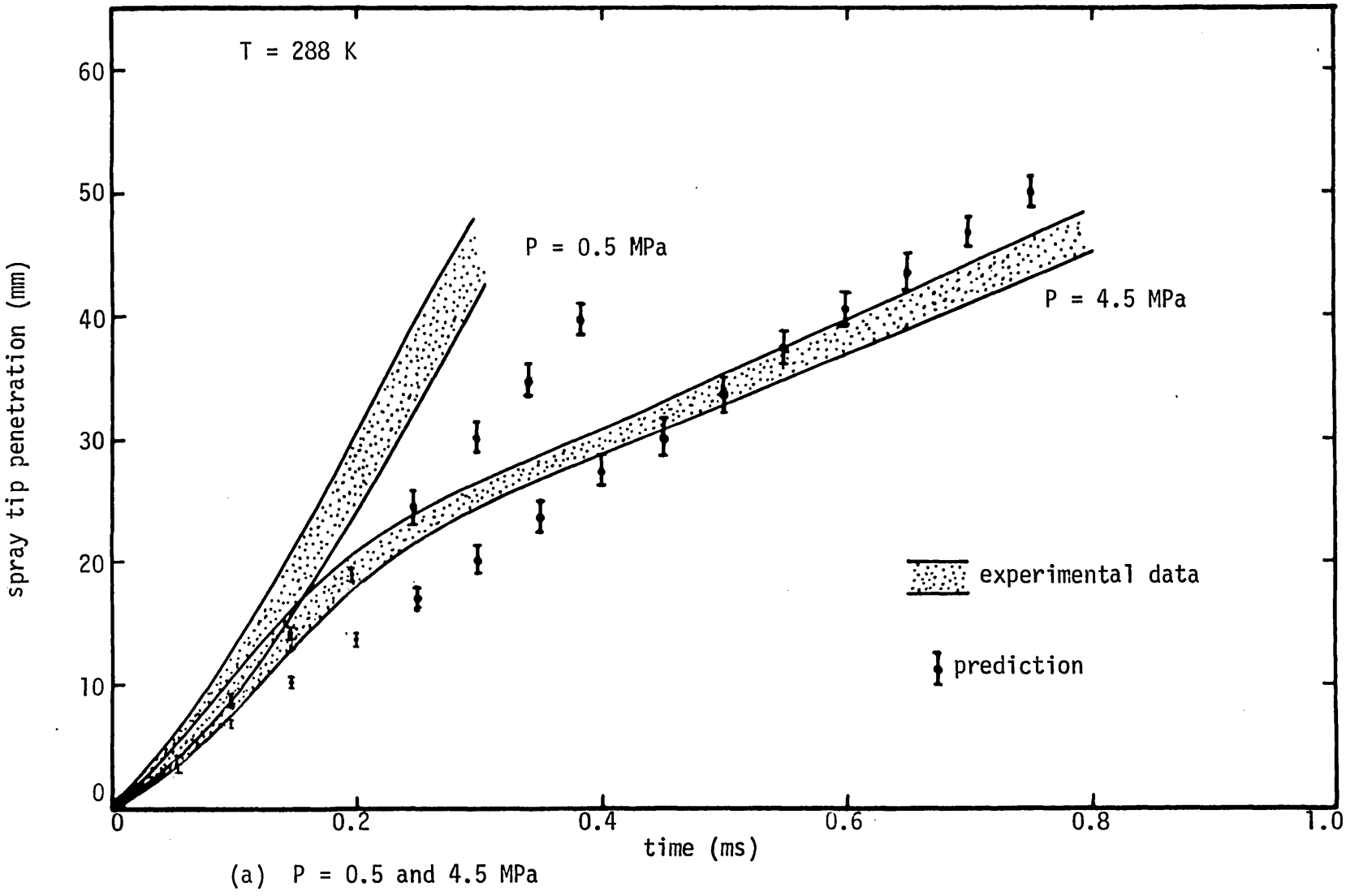
Fig. (7.3) Spray cone angle versus time at different charge pressures, from Yule et al (1985b)

Presentation of the results

The predicted penetration of the spray tip (defined as the axial position of the leading droplet) as a function of time from the start of injection is compared with Yule's (1985b) experimental data in Fig. (7.4)(a) and (b), for ambient pressures of 0.5, 2.5 and 4.5 MPa and an ambient temperature of 288 K. The measured curves show a scatter of about 15%, which Yule (1984) attributed to "jitter" from pulse to pulse and also, to irregularities in the spray leading edge. The predicted results are represented by the vertical bars in Fig. (7.4), showing the scatter resulting from four stochastic calculations with different random number sequences.

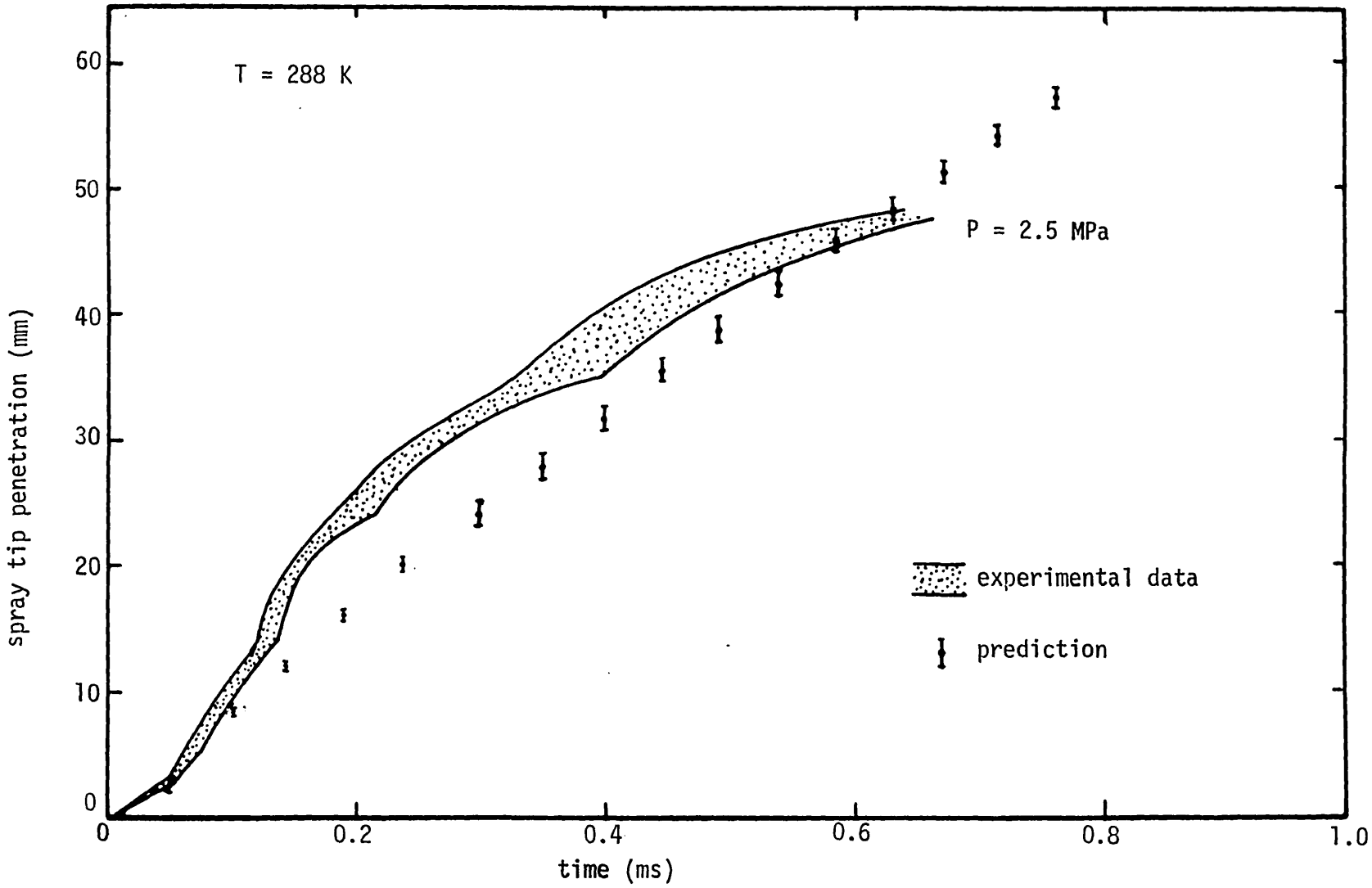
It is clear from the figure that the agreement is poor at the low pressure case (P = 0.5 MPa) and somewhat better at higher pressures, although even here the slope of the predictions are below the measurements in the early stages of injection (up to 0.3 ms from the start of injection).

The predicted spray structure for the P = 0.5 MPa case based on two alternative representations, one of which shows 'droplets' whose size is proportional to the local mass of the liquid, and the other which reflects the actual droplet diameters, are shown in Fig. (7.5)(a) and (b) respectively. Close inspection of the latter reveals a concentration of large droplets near the spray tip, as was also observed in the experiments. This was attributed to the observed tendency of such droplets to migrate to the front, aided by the fact that with practical systems droplets injected at later times enter at higher velocity than the very early



(a) P = 0.5 and 4.5 MPa

Fig. (7.4) Comparison of the predicted spray tip penetration with Yule's (1985b)data.



(b) P = 2.5 MPa

Fig. (7.4) Cont'd.

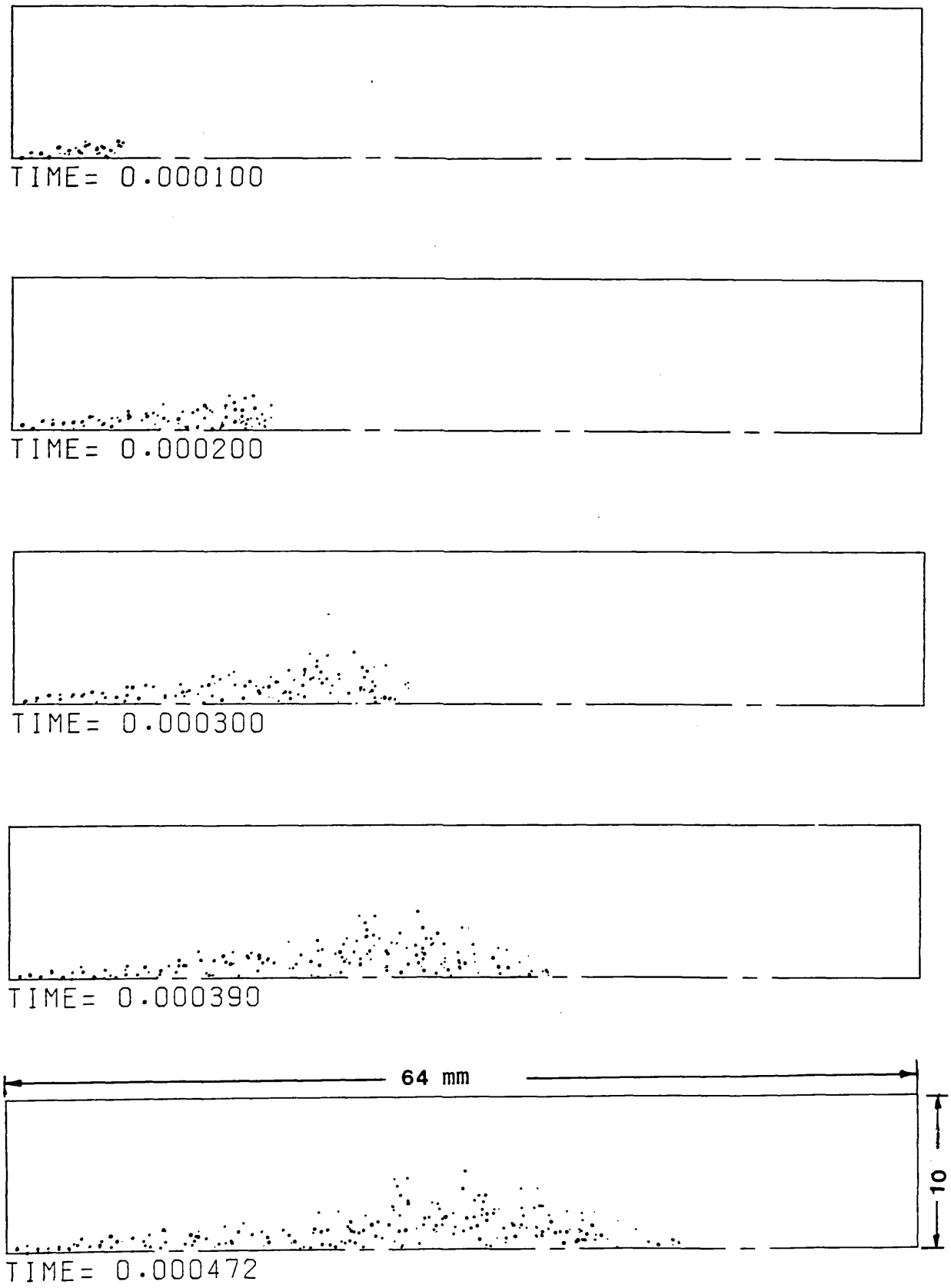


Fig. (7.5)(a) Spray representation according to parcel masses for P = 0.5 MPa and T = 288 K

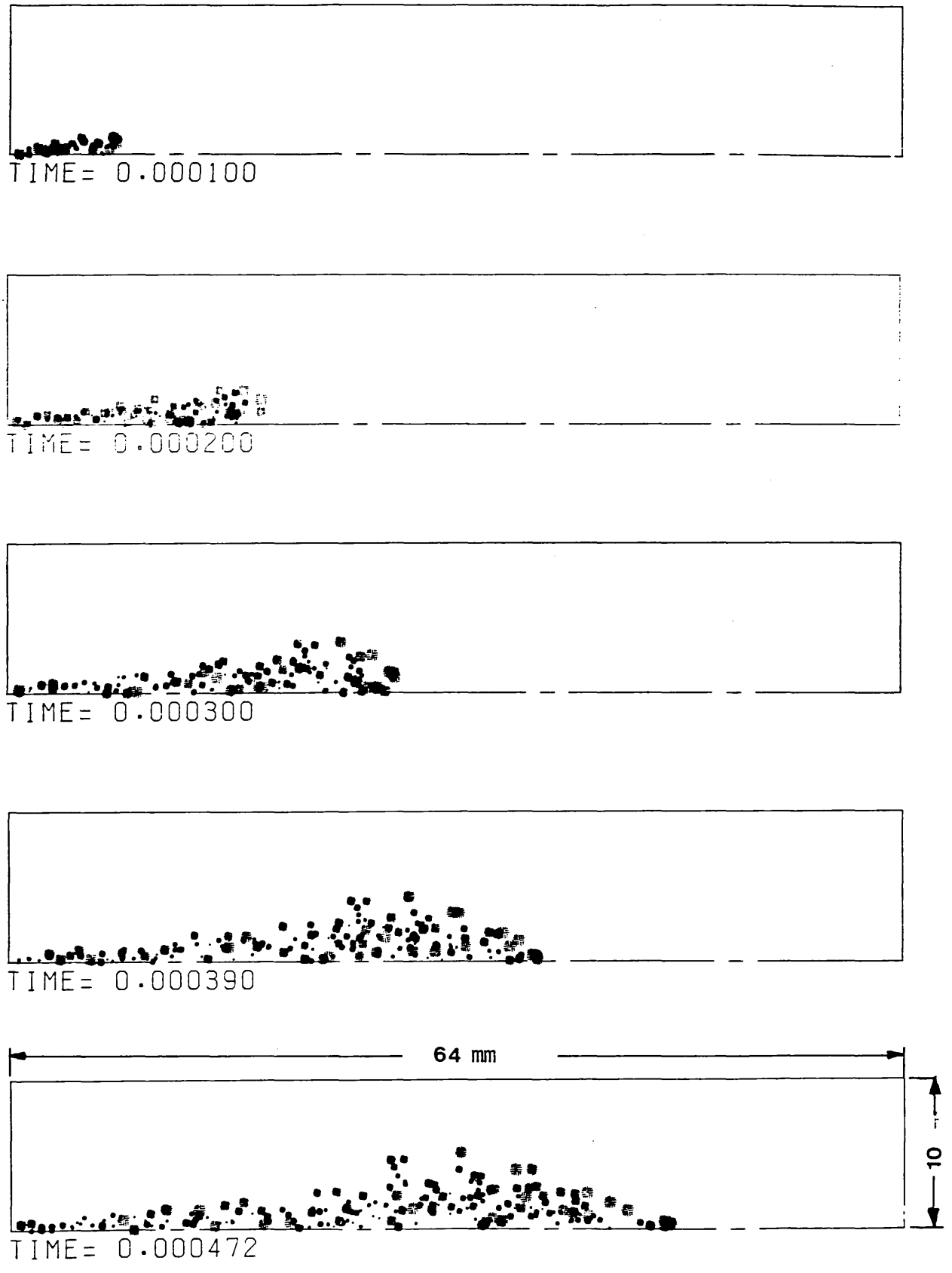
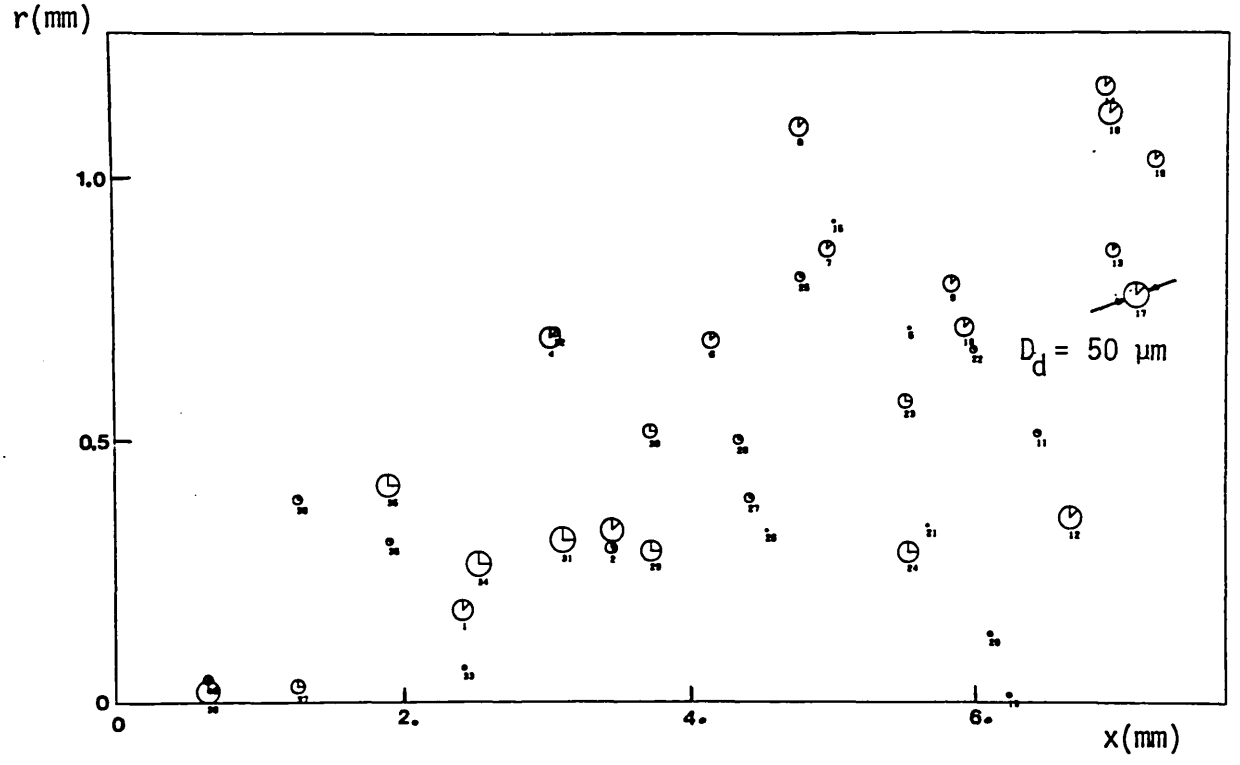


Fig. (7.5)(b) Spray representation according to droplet sizes for P = 0.5 MPa and T = 288 K

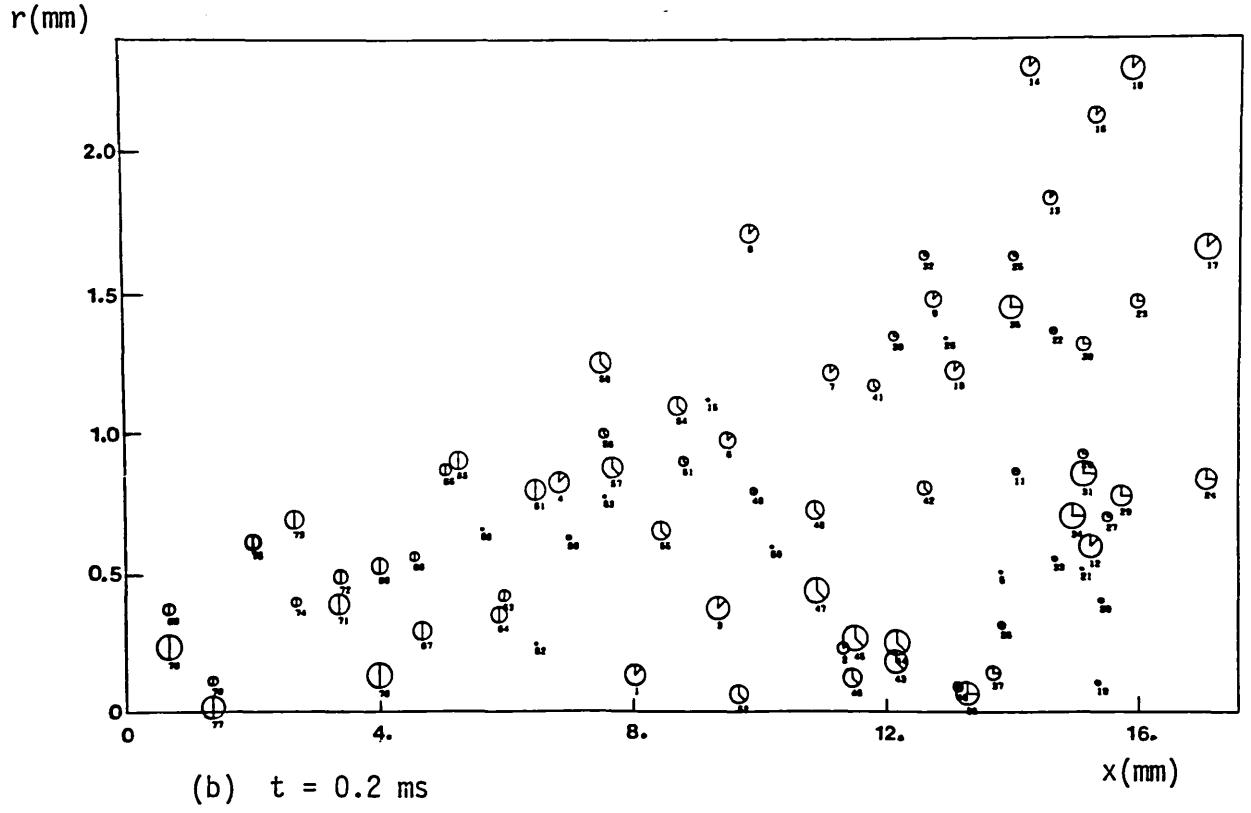
ones (c.f. Fig. (7.1)), at least until the peak injection rate is reached and passed. This phenomenon is readily apparent in the novel representation of, for example, the same (P = 0.5 MPa) spray in Fig. (7.6), where the cricles are proportional in diameter to droplet sizes and are numbered sequentially in order of introduction, i.e. droplet number 1 is the first introduced one. A further indicator of the timing of introduction is provided by the 'clock hands' appearing in each circle: these are advanced by an increment of 45^{o} at intervals of 50 μs, during each of which a number of droplets are introduced. (It should be noted that for clarity the radial scale of these plots is greatly enlarged since the spreading angle of the spray is usually small).

Typical predicted fields of gas velocity and turbulence characteristics are represented in Fig. (7.7) for the high pressure case (P = 4.5 MPa, T = 288 K). As shown in Fig. (7.7)(a), the injection process induces recirculation due to the fact that air is entrained into the jet close to the injector nozzle and flows radially away from the jet near the tip of the spray. Also, the large gas velocities are confined to the vicinity of the spray unlike the pure gas jet, where lateral spread is greater.

The main noteworthy points of the turbulence predictions of Fig. (7.7)(b)-(d) are the high turbulent viscosity (μ_t) levels, mainly due to the high turbulent intensities ($u' \equiv \sqrt{\frac{2}{3} k}$), which in turn result from the large velocity gradients near the spray axis. In this connection, it should be recalled that the version of the k-ε turbulence model employed here contains no provision

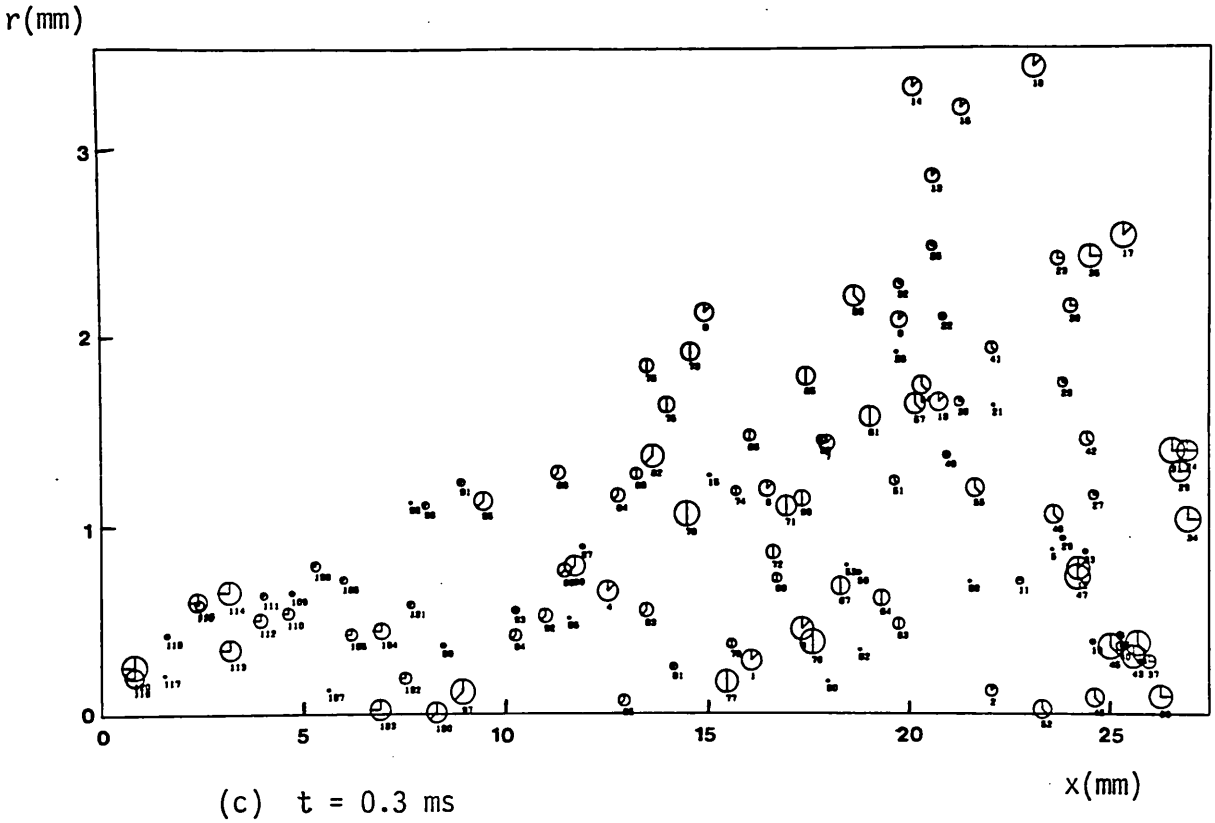


(a) t = 0.1 ms

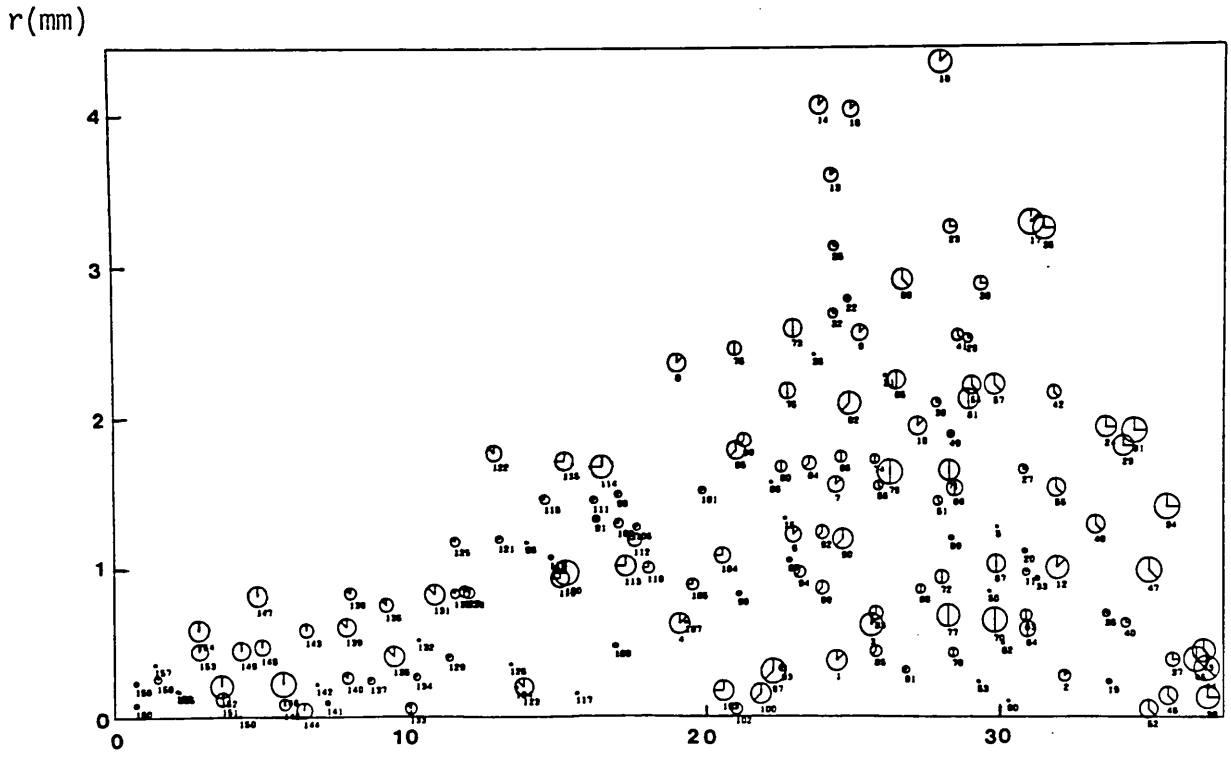


(b) t = 0.2 ms

Fig. (7.6) Predicted droplet histories for the P = 0.5 MPa, T = 288 K spray

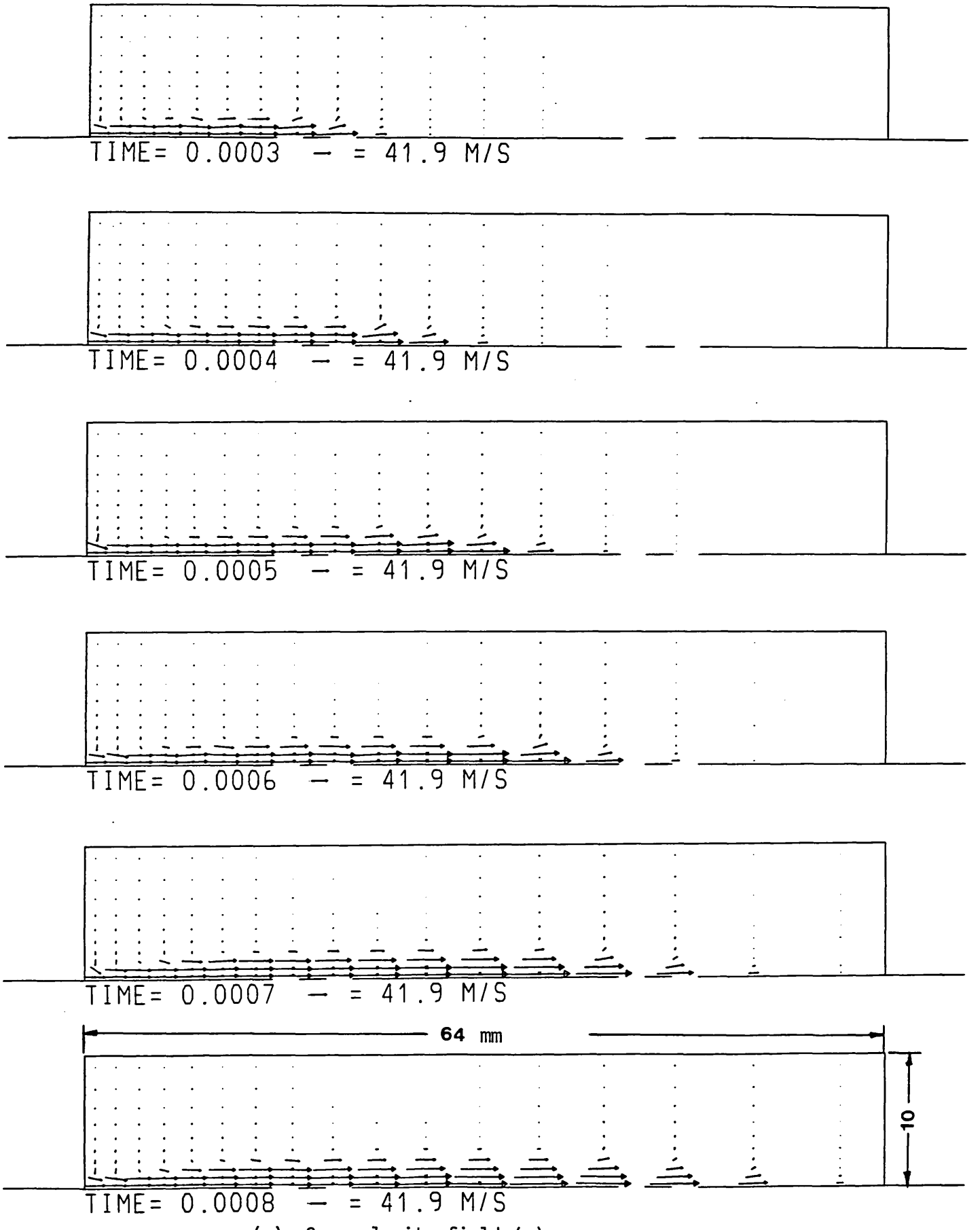


(c) t = 0.3 ms



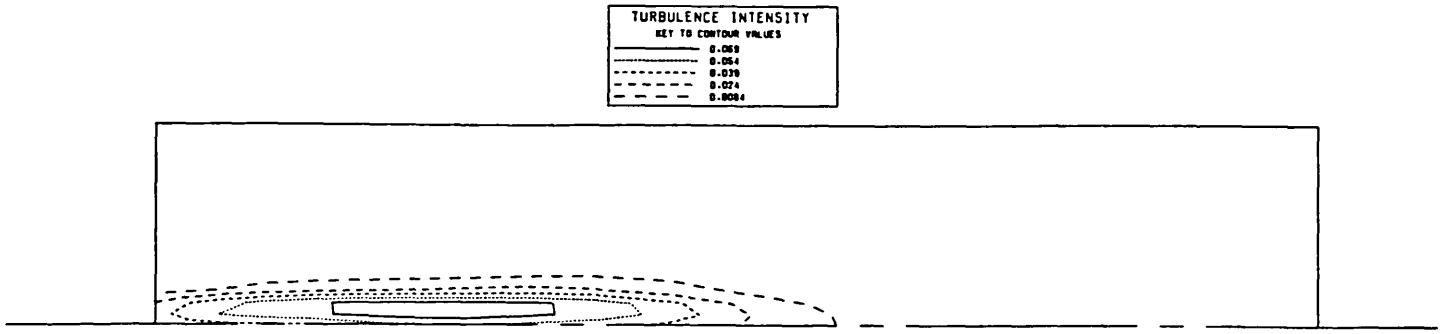
(d) t = 0.4 ms

Fig. (7.6) Cont'd.

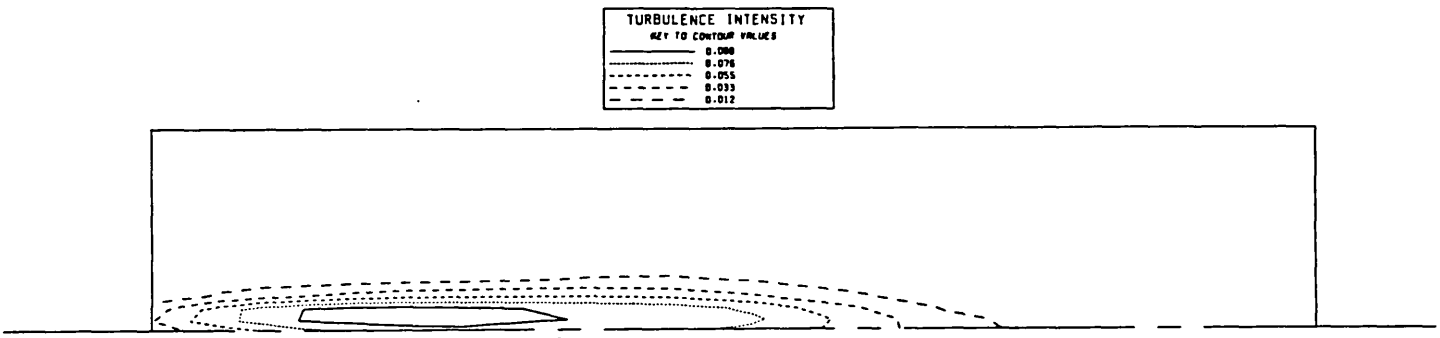


(a) Gas velocity field (u)

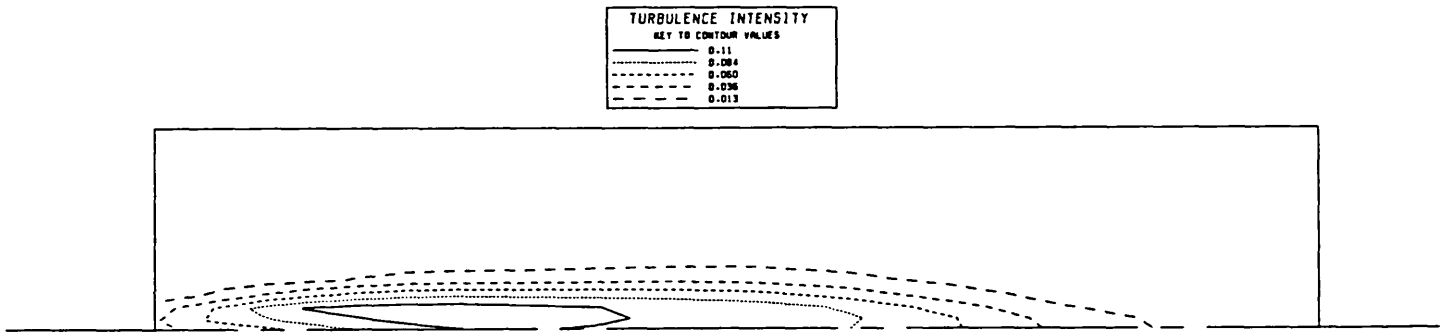
Fig. (7.7) Predicted gas phase characteristics for P = 4.5 MPa, T = 288 K case



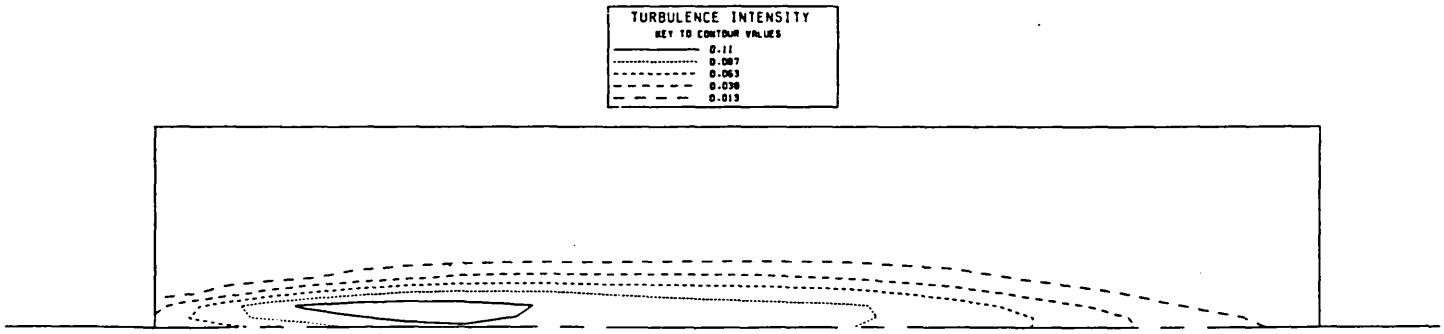
Time = 0.0005 s



Time = 0.00597 s



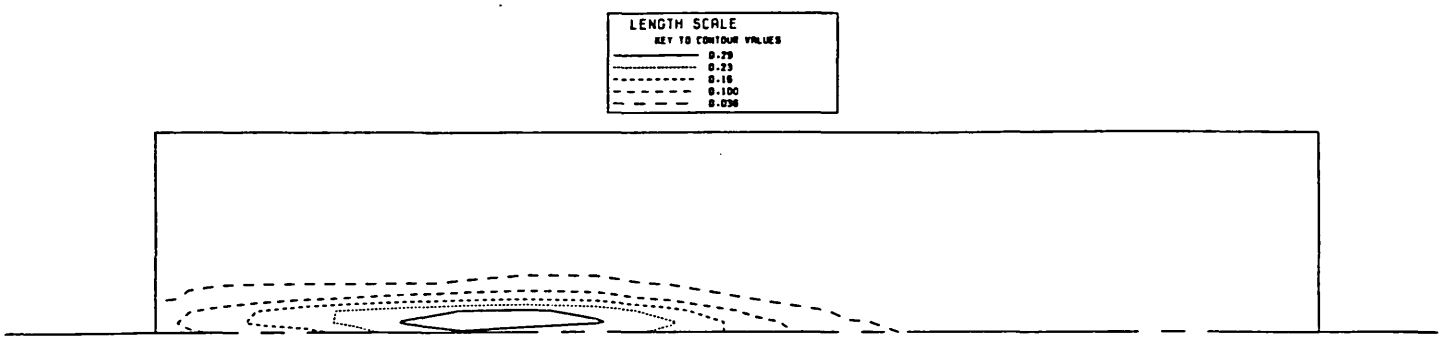
Time = 0.00691 s



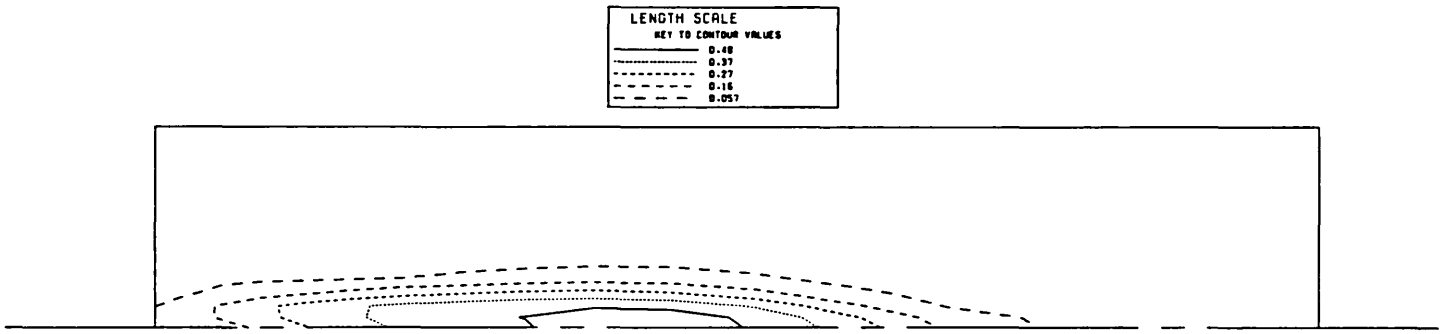
Time = 0.000782 s

(b) Ratio of turbulence intensity to introduction velocity, u'/U_o

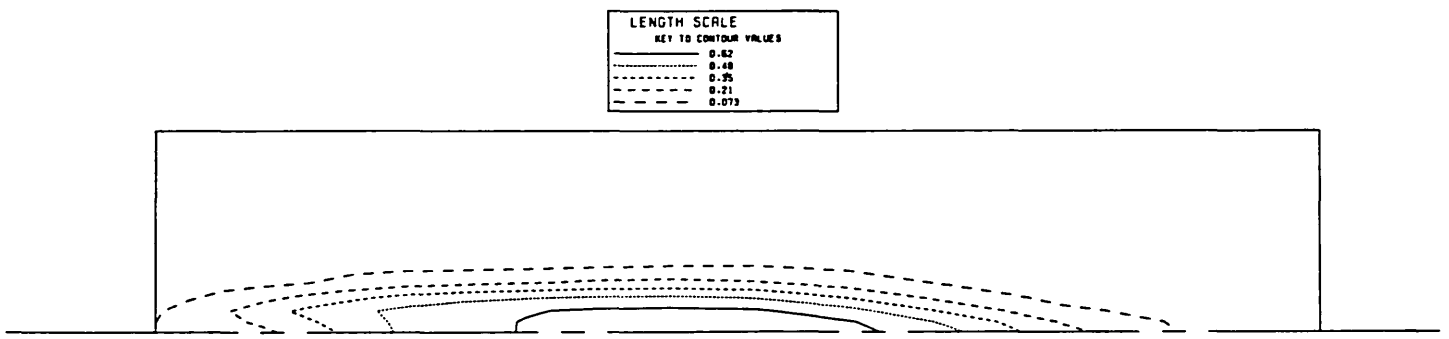
Fig. (7.7) Cont'd.



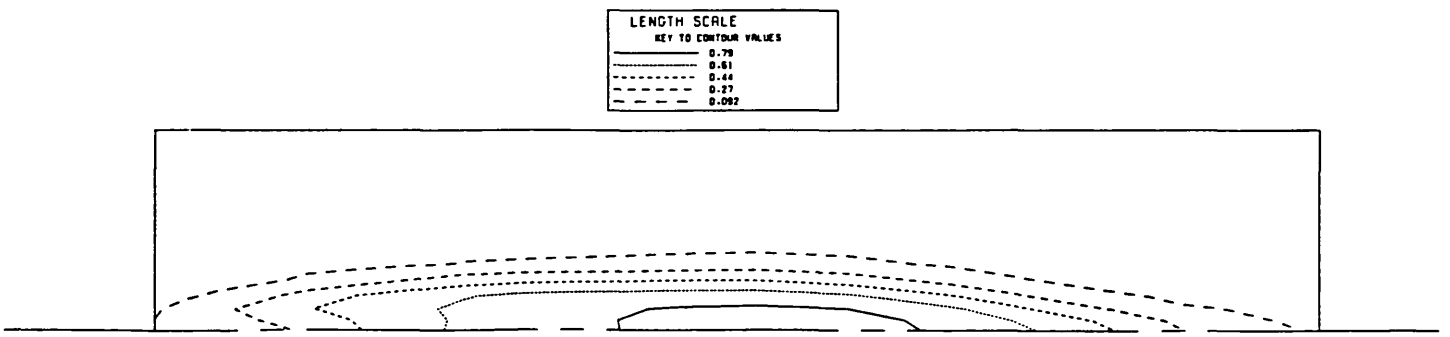
Time = 0.0005 s



Time = 0.000597 s



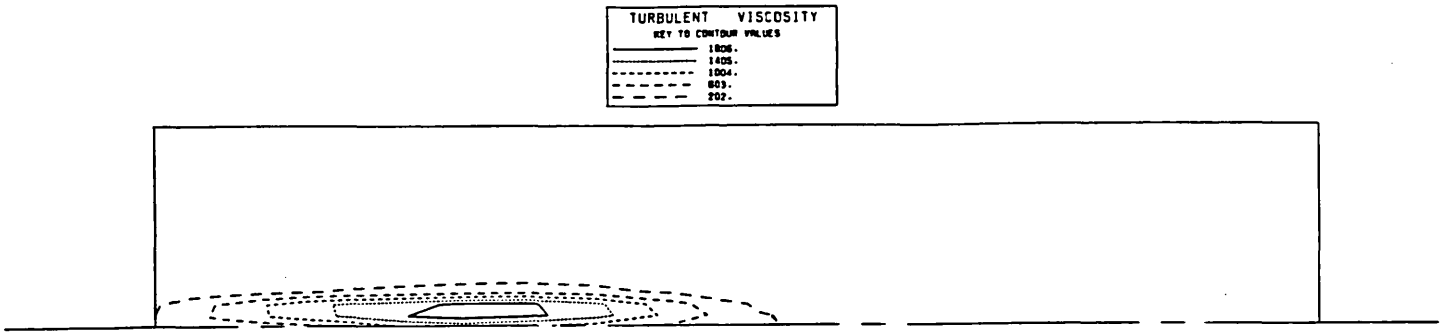
Time = 0.000691 s



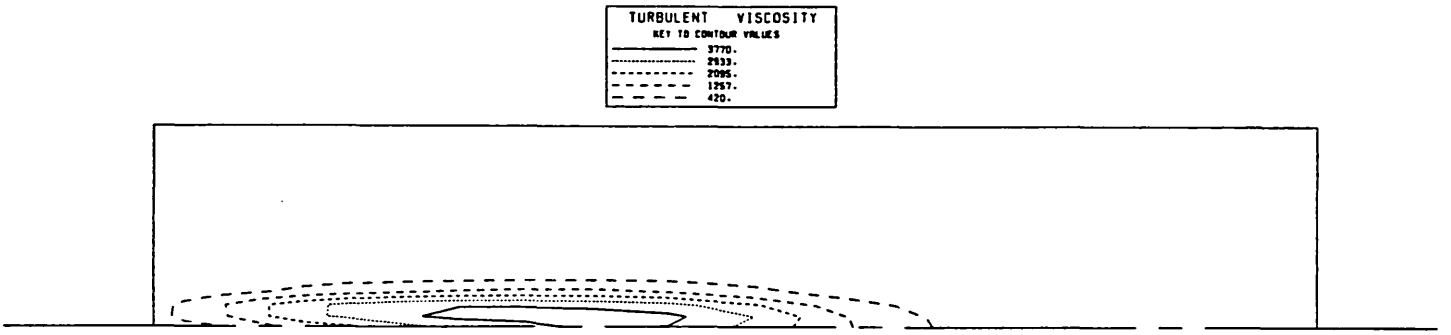
Time = 0.000782 s

(c) Ratio of dissipation length scale to nozzle diameter, ℓ/d_j

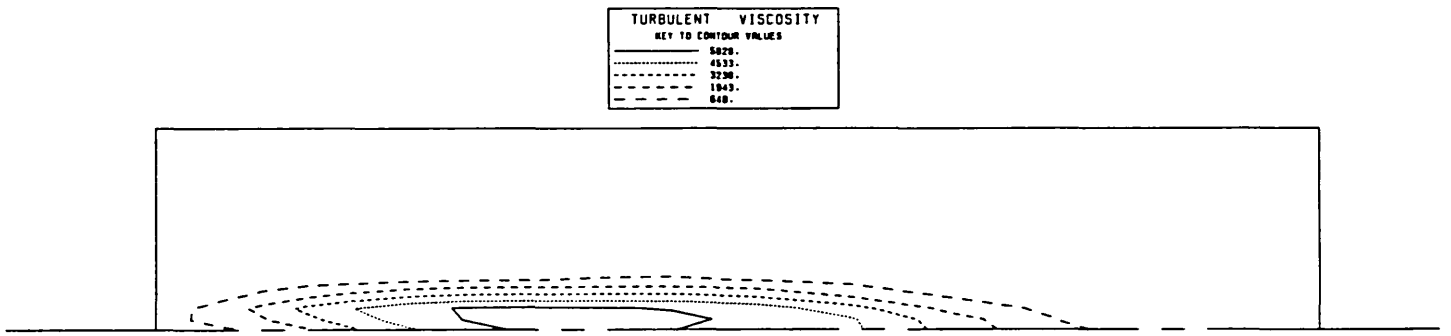
Fig. (7.7) Cont'd.



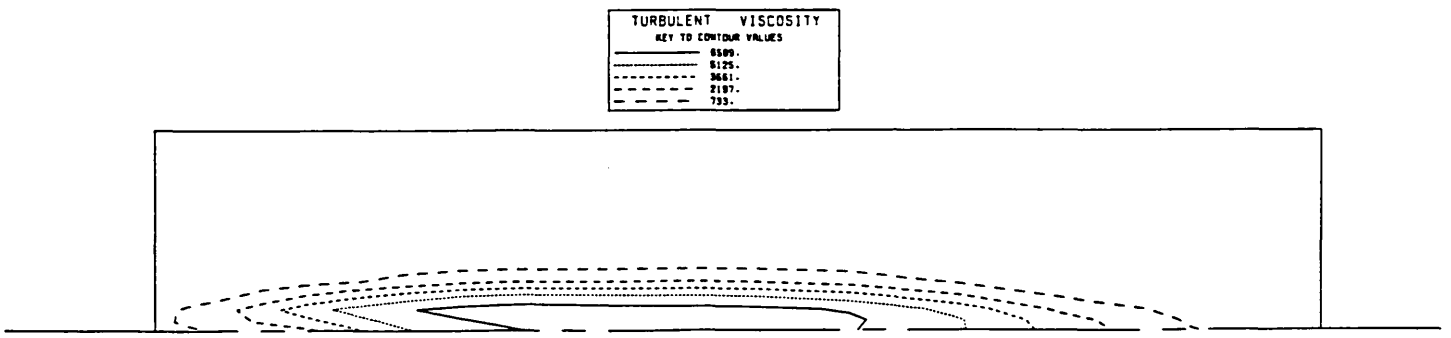
Time 0.0005 s



Time = 0.000597 s



Time = 0.000691 s



Time = 0.00782 s

(a) Ratio μ_t/μ

Fig. (7.7) Cont'd.

for the presence of the droplet (as discussed in Chapter 3), which have the effect of damping the turbulent motion, primarily due to inertial effects (see Buckingham and Siekhaus (1981)): so the present predictions are likely to be an overestimate.

In order to understand the reasons for the poor agreement in Fig. (7.4) between the predicted and measured spray tip penetrations at the low pressure case (P = 0.5 MPa), further investigations were made. In the first instance, a hypothetical situation where no atomization takes place was examined. It was assumed that the liquid exits the nozzle as an intact jet and travels through the gas (without exchanging mass, momentum or energy) at either the instantaneous mean exit velocity from the nozzle (i.e. the ratio of the volumetric flow rate to the nozzle area) or at the peak value of an assumed radial velocity distribution. The latter was taken to be either parabolic, which is appropriate to laminar flow (which is the case at times less than 0.1 ms from the start of injection, for which the nozzle Reynolds number, defined as $Re = \rho_d U_o d_j / \mu_d$ is less than 500); or a one seventh power law, corresponding to turbulent flow. The penetration histories for these two cases are plotted in Fig. (7.8) where it is seen than the result of the laminar exit velocity profile case agrees well with the experimental data at the early stages of injection (up to t = 0.18 ms). At later times, the measurements become bracketed by the non-uniform exit profile cases, suggesting that the initial fast penetration in the real case is due to incomplete atomization. In support of this, Yule et al (1985b) indicated that the photographs of the 0.5 MPa spray suggested that it has a continuous central bulk

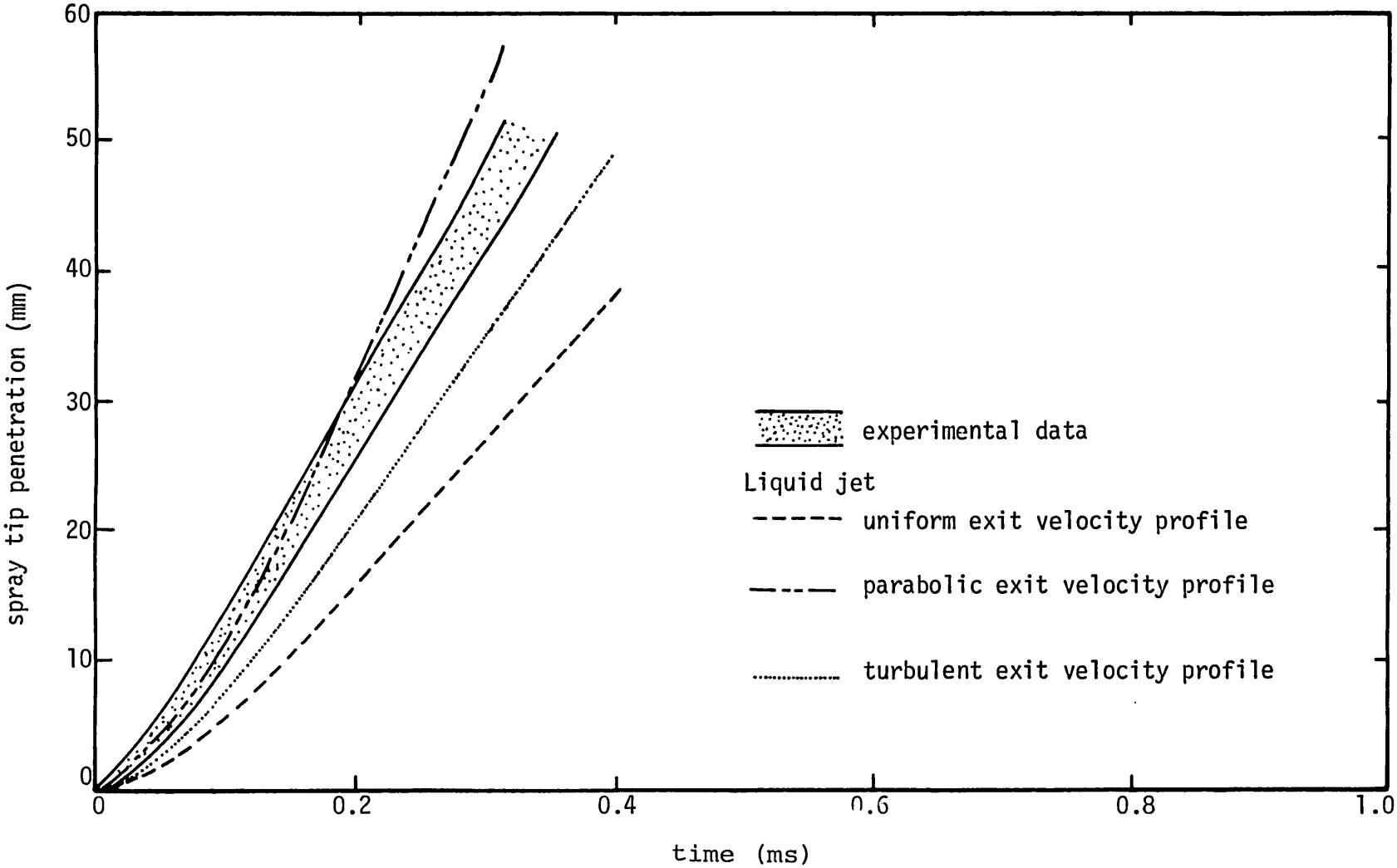


Fig. (7.8) Tip penetrations of P = 0.5 MPa, T = 288 K case based on the 'Liquid jet' model

liquid core extending over the first 40 mm from the nozzle exit while the higher pressure sprays have a dense and very poorly atomized core. Thus, these observations necessitate the need in the future to include 'ligament' and 'column break-up' regimes in the theoretical model, at least for low charge pressures.

A second possible cause for the discrepancies between the predicted and measured tip penetrations is the uncertainty in the initial part (up to 0.1 ms) of the fuel injection rate diagram (Fig. (7.1)). Firstly, Yule(1985b)could not measure the fuel flow rate reliably in the first 40 μs, so a straight line was drawn from the origin as shown in Fig. (7.1). Secondly, in view of the fact that the opening pressure is 12.0 MPa and the charge pressures vary from 0.5 to 5 MPa the injection rate would expect to show some variation between these, rather than the reported unique curve for all pressures. In this connection, it will be shown later that, as might have been expected, the penetration is sensitive to the initial injection schedule.

ii. The experiment of Hiroyasu and Kadota (1974)

The objective of the experiment of Hiroyasu and Kadota (1974) was to measure the penetration, initial cone angle and droplet size distributions of sprays injected into a high pressure and room temperature nitrogen environment (description of the experiment is detailed in chapter 2).

The droplet size distribution was measured about 650 mm downstream of the injector and it was found that the data for different charge

pressures, could be fitted by the size distribution function of the Chi form:

$$\frac{1}{V}\frac{dV}{dD_d} = 13.5\left(\frac{D_d^3}{D_{32}^4}\right) \exp\{-3\left(\frac{D_d}{D_{32}}\right)\} \qquad (7.2)$$

where D_{32} is the experimentally determined Sauter mean diameter. Unfortunately these data are unlikely to characterize the droplet sizes in the vicinity of the injector, due to the possibility of droplet coalescence causing a shift from the initially-generated distribution. For example, for the spray injected into a charge pressure of 5 MPa, droplet stability considerations based on the Weber number criterion (equation (3.57)) suggest a stable Sauter mean diameter of 25 μm compared to the measured value of 50 μm. For computational purposes, the measured size distribution was retained and the measured Sauter mean diameter was reduced by a constant factor of 2 to represent the distribution near the injector.

Since the injection mass flow rate was not measured, for the purposes of the simulation, it was estimated using equation (4.127), with the discharge coefficient, C_Q taken to be 0.7 (from the experimental data of Bergwerk (1959)) and assuming that the injection pressure was equal to the valve opening pressure of 9.9 MPa. The valve opening was assumed to be instantaneous, thus giving a steady injection rate. This is not entirely realistic since the measured injection pressure and needle lift signals showed a time-dependent nature and because there was no quantitative information concerning these signals, an accurate

calculation of the mass flow rate was unavailable. The input parameters for the different cases are given in table (7.2).

The outcomes of the predictions are compared with the experimental data in Fig. (7.9). It is clear that the agreement is fairly good for the low pressure case (0.1 MPa), but the predictions over-estimate the penetration for the higher pressures. As already noted, in the simulation of Yule's (1985b) low pressure cases, under-prediction occurred while here good agreement is obtained. The reason for this is that in the present simulation a constant injection rate is employed, in the absence of measurements of same. It will be seen later that using a constant injection rate in the Yule simulation improves the agreement for the low pressure case but leads to over-prediction for the high-pressure cases in a similar fashion to the behaviour exhibited in Fig. (7.9).

In spite of the uncertainties in injection velocity and initial droplet sizes, Dukowicz (1980), O'Rourke and Bracco (1980), and Kuo and Bracco (1982b)reported fairly good agreement with the same experimental data. Since Dukowicz's approach was similar to that of the present study, the present calculations were restructured so as to make them correspond, in principle. The results are compared with Dukowicz's for the P = 5 MPa case in Fig. (7.10) where it can be seen that the present predictions lie above his and the experimental data. The cause of the discrepancy is due, it is believed, to an erroneous treatment by Dukowicz of droplets which attempt to stray across the axis of the spray. He apparently allows them to escape, thereby causing a loss of mass and momentum (and

Table (7.2) Input parameters for the Hiroyasu and Kadota simulation

Case	Injection pressure P_{inj} (MPa)	Charge pressure P (MPa)	Discharge coefficient C_Q	Injection velocity U_{inj}(m/s)	Introduction velocity U_o (m/s)	Spray cone angle β (deg.)	Sauter mean diameter D_{32} (μm)	Charge temperature T (K)	Gas density ρ (kg/m^3)	Droplet temperature T_d (K)	Droplet density ρ_d (Kg/m^3)
1	9.9	0.1	0.7	122.2	112.9	3.6	15	293	1.123	288	840
2	9.9	2	0.7	96.2	82.5	5.5	22	293	22.47	288	840
3	9.9	5	0.7	86.41	58.9	7	25	293	56.17	288	840

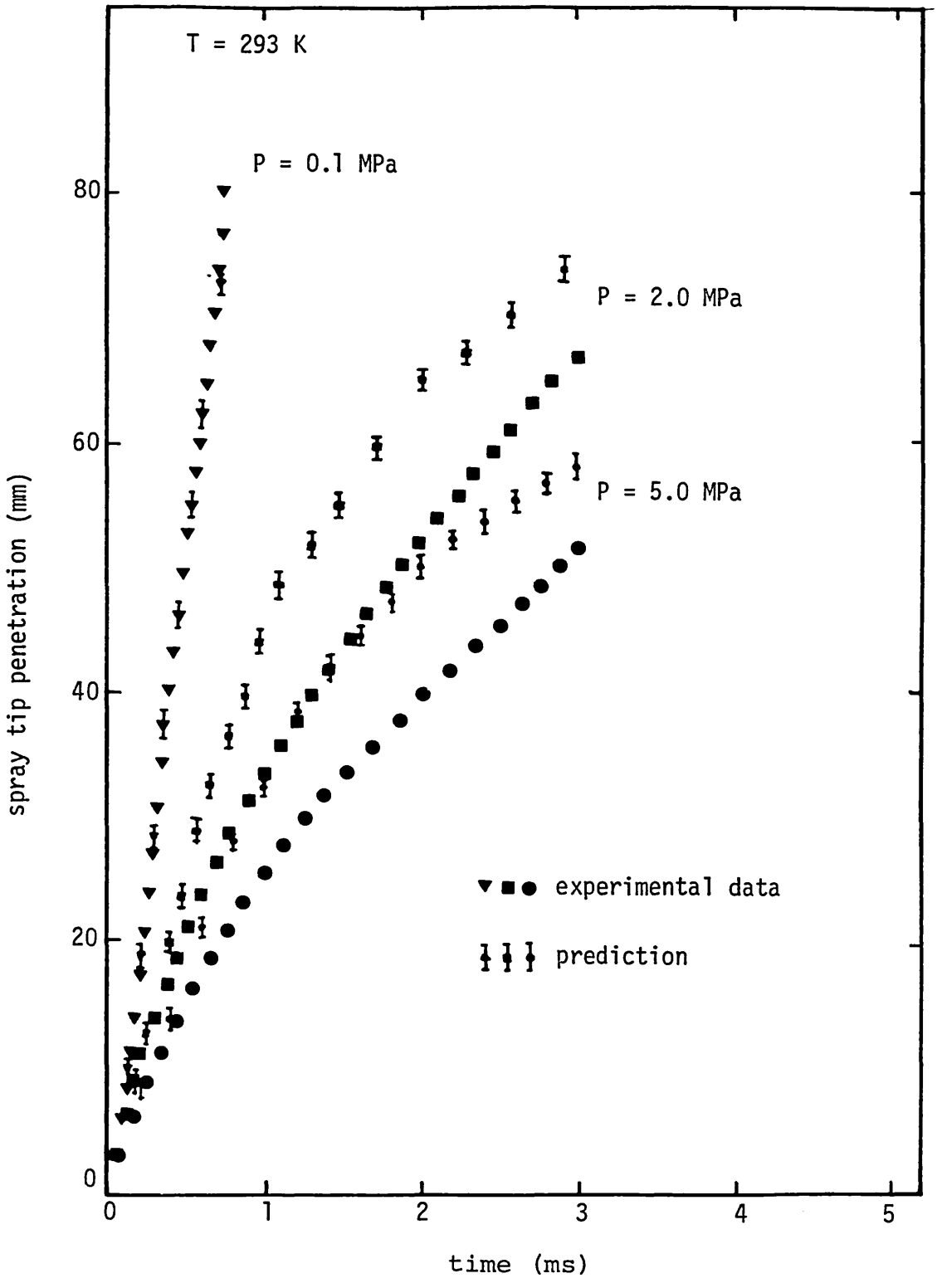


Fig. (7.9) Comparison of the predicted spray tip penetration with the experimental data of Hiroyasu and Kadota (1974)

hence reduced penetration), while a more realistic reflective boundary condition is used in the present study (as discussed in section (4.8)). To illustrate this, the present calculations were repeated using Dukowicz's treatment and as shown in Fig. (7.10) the erroneous one brings the predictions into line with his.

As far as the work of O'Rourke and Bracco (1980) and Kuo and Bracco (1982b)is concerned, they used an extension of Dukowicz's methodology, the most important addition being the calculation of droplet collision and coalescence. The fairly good agreement with the experimental data which they obtained was attributed to the dense spray treatment i.e. to collision effects.

7.2.2 Sensitivity Analysis

Although there are a great deal of experimental spray investigations reported in the literature, none of them report any detailed and complete measurements. Thus it is important to know the sensitivity of the predicted spray behaviour to the uncertainties in the various input parameters used in the calculations, whether they are taken from the measurements or approximated.

In this section, computational sensitivity such as the initial level of the turbulence quantities, initial velocity profile of the droplets and the residual effects in pulsed spray as well as the

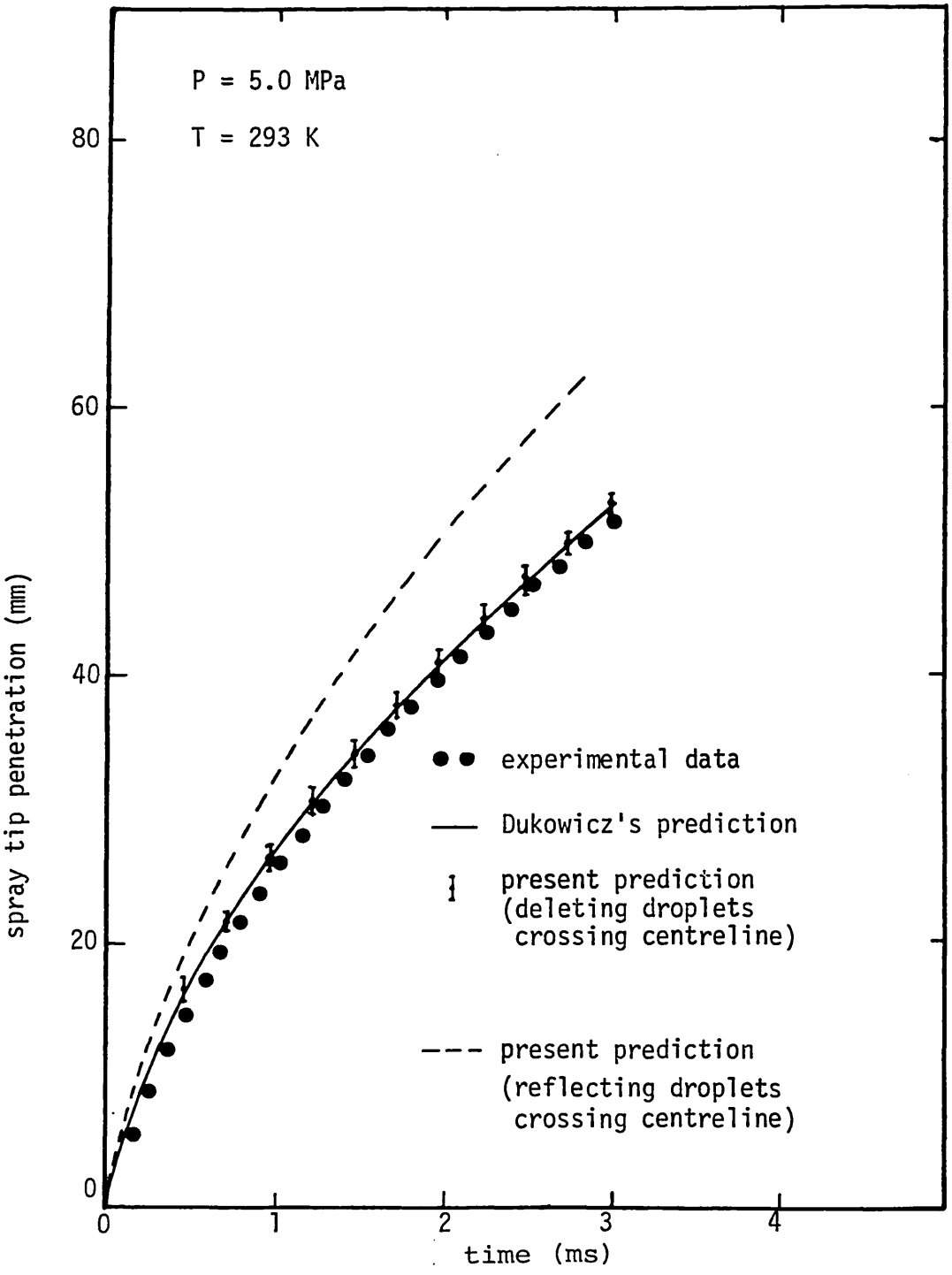


Fig. (7.10) Effect of deleting the droplets crossing the centreline on the spray tip penetration. (Hiroyasu and Kadota experimental data)

modelling sensitivity such as the turbulent droplet dispersion and the spray cone angle are presented for conditions corresponding to the P = 4.5 MPa case of Yule et al(1985b) since this pressure is close to that in a diesel engine at the start of injection (recall however that T = 288 K, which is well below diesel conditions: the effect of elevated temperatures will be examined later).

7.2.2.1 Computational Sensitivity

i. Initial levels of turbulence quantities

The response of the predicted penetration to the initial ambient levels of the turbulence quantities k and ε are displayed in Fig. (7.11). The lowest pair of values yield a turbulent viscosity equal to the molecular value i.e. the charge is essentially turbulent-free, as would occur, for example, in experiments where the spray is injected into a container of quiescent gas. Also shown are results for two ambient levels more representative to engine conditions (conditions 2 and 3). For these conditions, the turbulence intensity (normalised by mean piston speed) at the start of injection is taken to be $\simeq 0.6$, from the computer simulation of Jahanbakhsh (1984). For a typical diesel engine running at 1400 rpm and having a stroke of 0.129 m, the mean piston speed is 5.6 m/s and hence, k = 20 m^2/s^2. The dissipation rate ε is

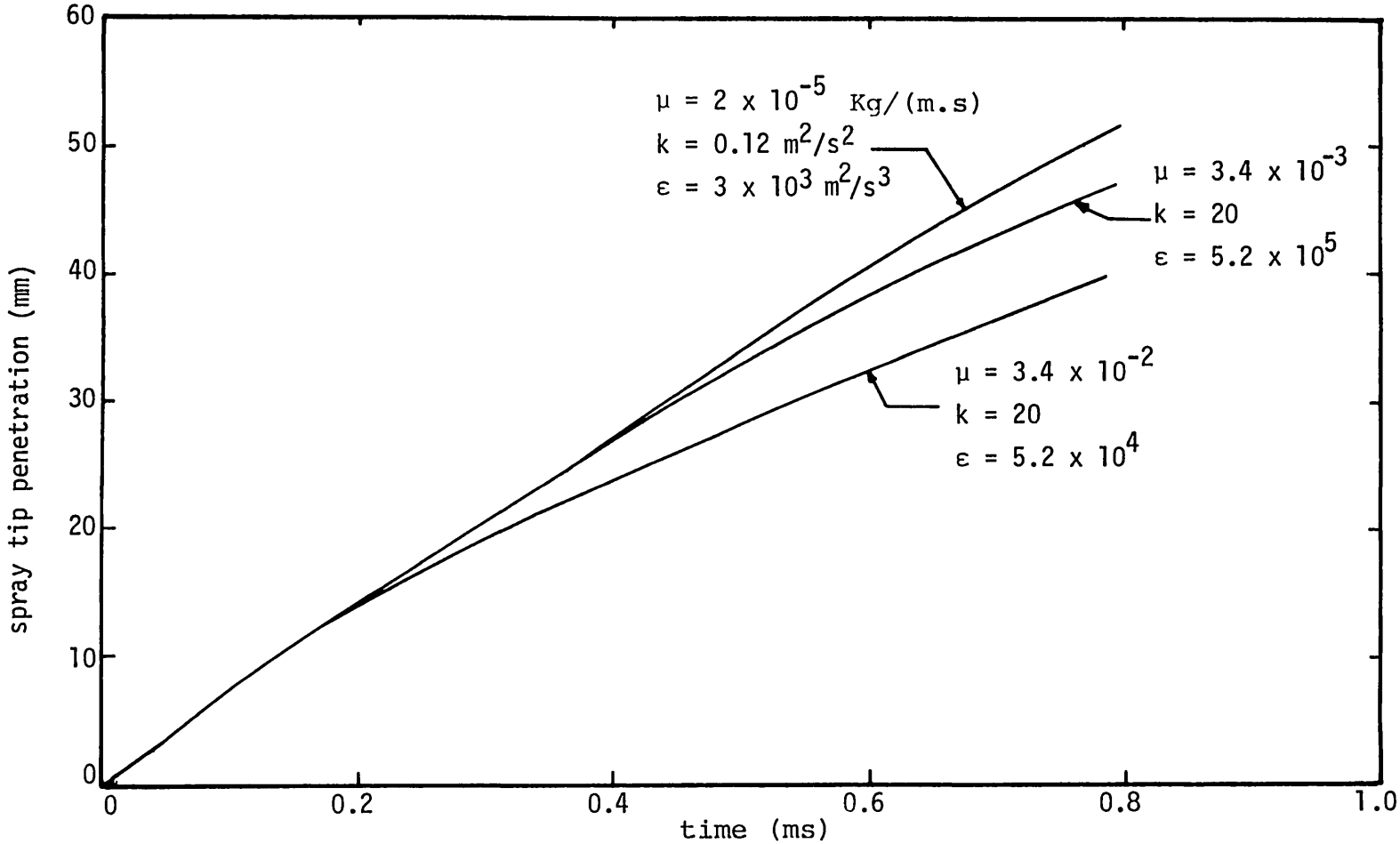


Fig. (7.11) Effect of the initial level of the turbulence quantities on the spray tip penetration (P = 4.5 MPa, T = 288 K)

specified so as to give turbulent to molecular viscosity ratios of the order of 10^2 and 10^3 respectively.

It is clear from the figure that an increase of μ_t from 2×10^{-5} to 3.4×10^{-3} yields no effect on the predicted penetration for the first quarter of the experimental injection duration (up to t = 0.5 ms): after this, the penetration decreases. Then further increase in μ_t to 3.4×10^{-2} produces an earlier and larger effect. The decrease in penetration with increased charge viscosity can be attributed mainly to the increased amount of momentum diffused to the gas surrounding the spray by means of the Reynolds stresses, hence decreasing the gas velocities and thus reducing penetration. Another possible reason for the reduction of the penetration (but to a lesser extent) is that due to the turbulent dispersion of the droplets. Higher turbulent viscosities generate larger values of turbulent kinetic energy which produce more widely dispersed spray, thus decreasing the penetration as will be discussed in section 7.2.2.2.

In the early stage of injections (up to $t \simeq 0.3$ ms) which is termed the 'initial' spray period (Hiroyasu et al (1980)), the penetration is determined by the behaviour of the droplets injected during the first 100 μs, as pointed out earlier in section (7.2.1) in connection with the history of the individual droplets. Since the momentum of the droplets is higher than that of the gas in this initial period (because the droplet masses are larger than the gas mass), only a small fraction of droplet momentum

is needed to equalise the velocities of the two phases. Thus during the initial spray period, the droplets move at their initial velocities without slip. Figure (7.12) displays the development of the average* droplet velocities at the injection cell exit and the gas and the average droplet velocities at the computational cell centred on the symmetry axis at x = 5 mm. It can be seen from the figure that, at the time the droplets enter the cell, their average velocity is higher than that of the gas, but shortly thereafter they equalise and increase with time (because droplets which enter the cell at later times have larger velocities). It can also be seen that the average droplet velocities at x = 5 mm are less than those at the injection cell exit, because the droplets give some of their momentum to accelerate the entrained gas.

Furthermore, the initial slopes of the penetration curves displayed in e.g. Fig. (7.27) reveal that the spray moves with a constant velocity equal to the forementioned average droplet velocity for those injected in the first 100 μs.

Hiroyasu and Kadota (1980) also concluded that the spray travels in the initial period with a constant velocity. Therefore it can be concluded that the spray penetration in this period is determined by its dominant momentum, which explains why initial turbulence characteristics of the gas phase have no effect during this period. Later it will be shown that other parameters, such as the initial spray cone angle and droplet diameters also have no effect on the initial penetration, for the same reason.

---

*Here defined as the mass-weighted average of the velocities of the droplets occupying the cell in question.

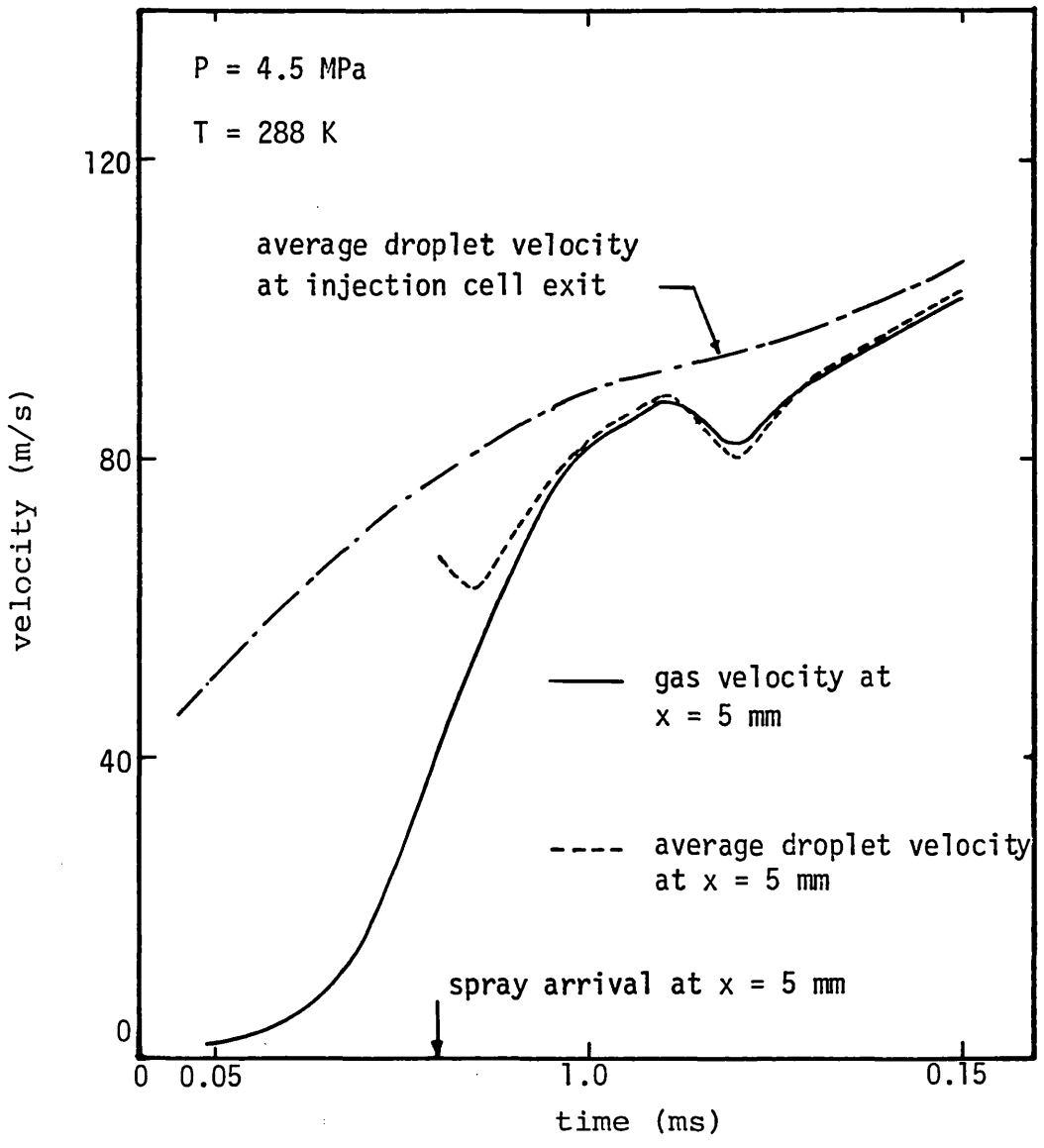


Fig. (7.12) Development of the average droplet velocities at the injection cell exit and at x = 5 mm

ii. Initial velocity profile of the droplets

In the light of the uncertainties about the initial velocities of the injected droplets, and prompted from the findings of the liquid jet study presented in Fig. (7.8), a prediction was performed assuming a one-seventh power law for the distribution of the fuel velocity at the exit of the nozzle as illustrated in Fig. (7.13)(a). Since the droplet introduction velocities are arrived at by sampling this distribution (Fig. (7.13)(b)), those injected near the centre-line have the largest axial velocities while ones injected near the edge of the nozzle have the lowest values. The overall effect is, for a given mass flow rate, to increase the total momentum of the injected liquid over that which would result from a uniform exit profile.

The predicted penetrations for the two exit profiles are compared with the experimental data in Fig. (7.14). It is clear from the figure that, as would be expected, the non-uniform exit profile improves the agreement with the measured penetration in the early stages of injection (i.e. the 'initial spray period'), but exacerbates the overprediction in the later stages. It also appears that towards the middle of the experimental injection period (t = 1.0 ms) the two predictions are converging. This is believed to be a coincidental consequence of the timing of the transitions from linear penetration to the situation where the penetration varies as $\sqrt{t}$.

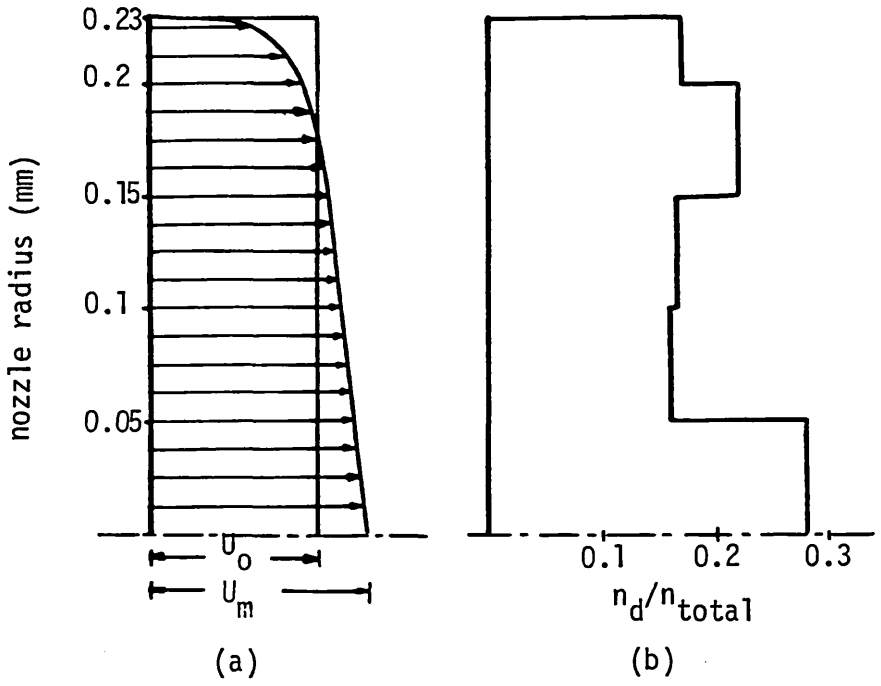


Fig. (7.13) Inlet velocity profiles and number density of the injected droplets (P = 4.5 MPa, T = 288 K)

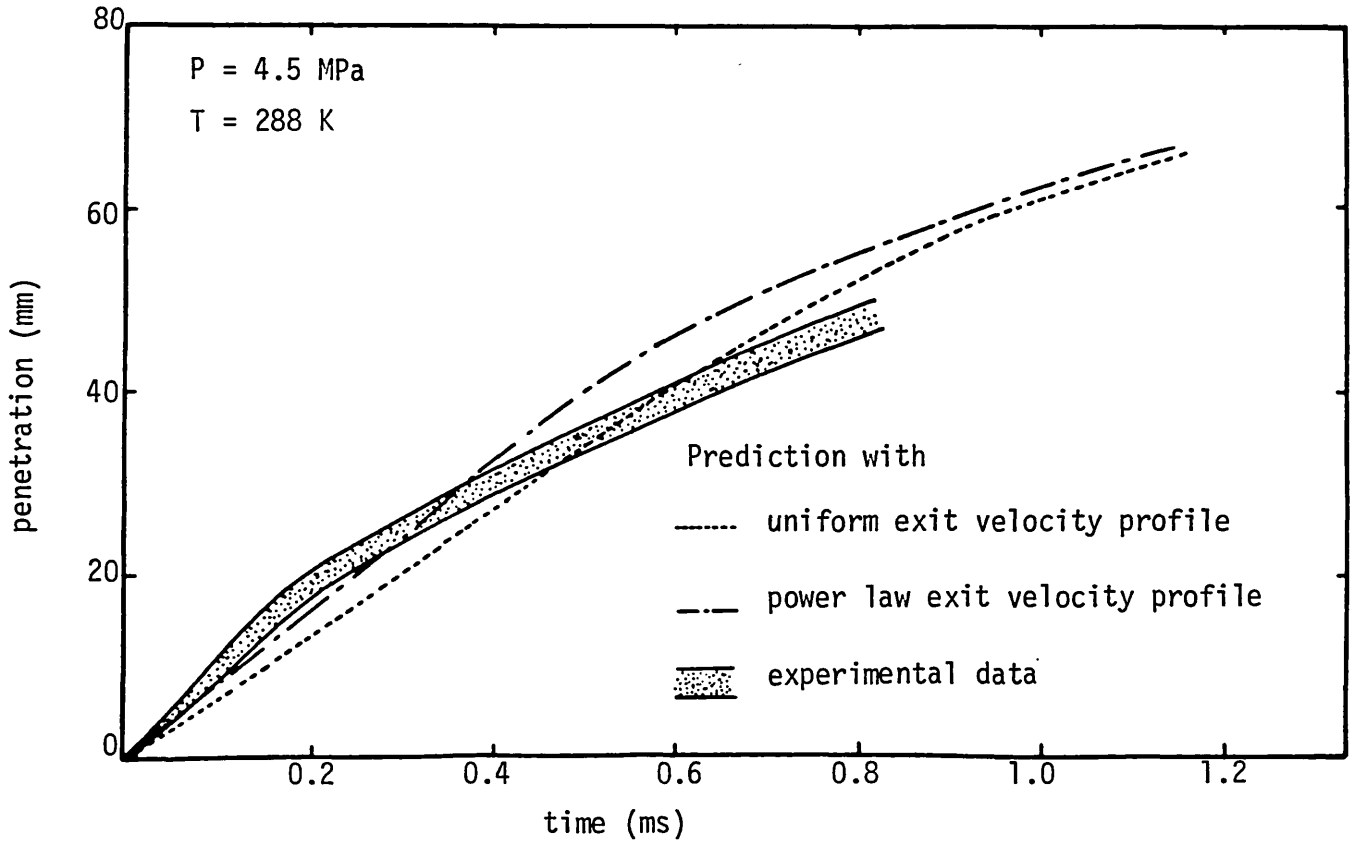


Fig. (7.14) Effect of initial velocity profile of the injected droplets on the spray tip penetration

iii. Residual effects in pulsed spray experiments

In order to ensure that the practice of simulating the behaviour of the pulsed spray by calculating just one pulse is justifiable, a calculation was performed to determine whether a given pulse is influenced by the previous one. In the experiments of Yule (1984), the spray pulses are of 2.05 ms duration and are separated by a period of 38 ms. Calculations were therefore performed up to 20 ms after the end of injection and the predicted centreline gas velocity and turbulent viscosity histories were examined. The gas velocities, which are plotted in Fig. (7.15), rapidly decrease with time, such that by t = 11 ms their maximum level is only 1% of the mean injection velocity (100 m/s). The same trend is observed for the turbulent viscosity whose temperol variation at x = 10 mm is plotted in Fig. (7.16): this shows that μ_t becomes of the same order as the molecular viscosity after about 20 ms. On the basis of those findings it can be concluded that there is negligible interaction between successive pulses.

7.2.2.2 Modelling Sensitivity

i. Turbulent droplets dispersion

The sensitivity of the calculations to the modelling of the turbulent dispersion of the droplets (described earlier in section (3.8)) was investigated by performing calculations:

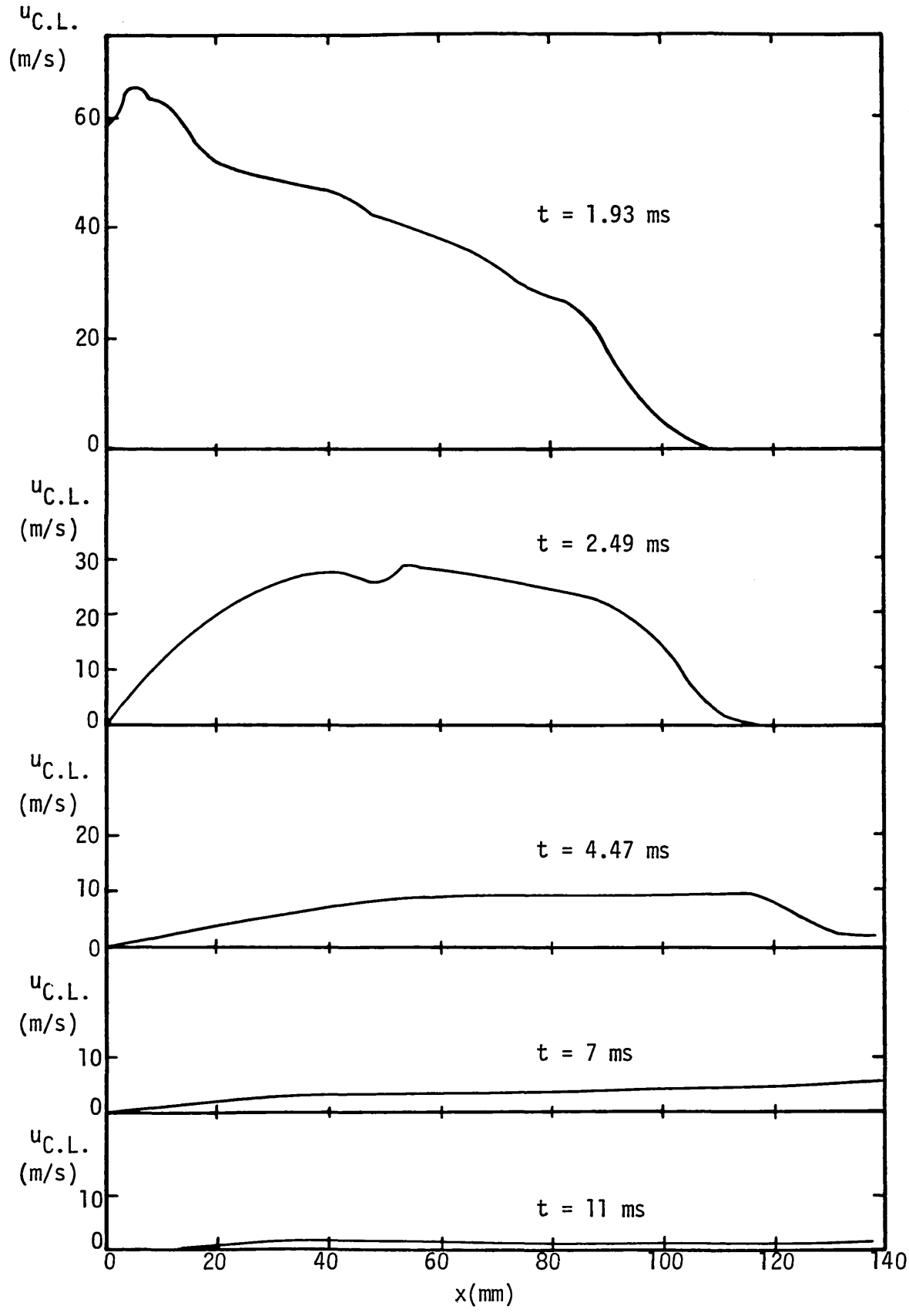


Fig. (7.15) Predicted centreline velocity variations before and after the end of injection (P = 4.5 MPa, T = 288 K)

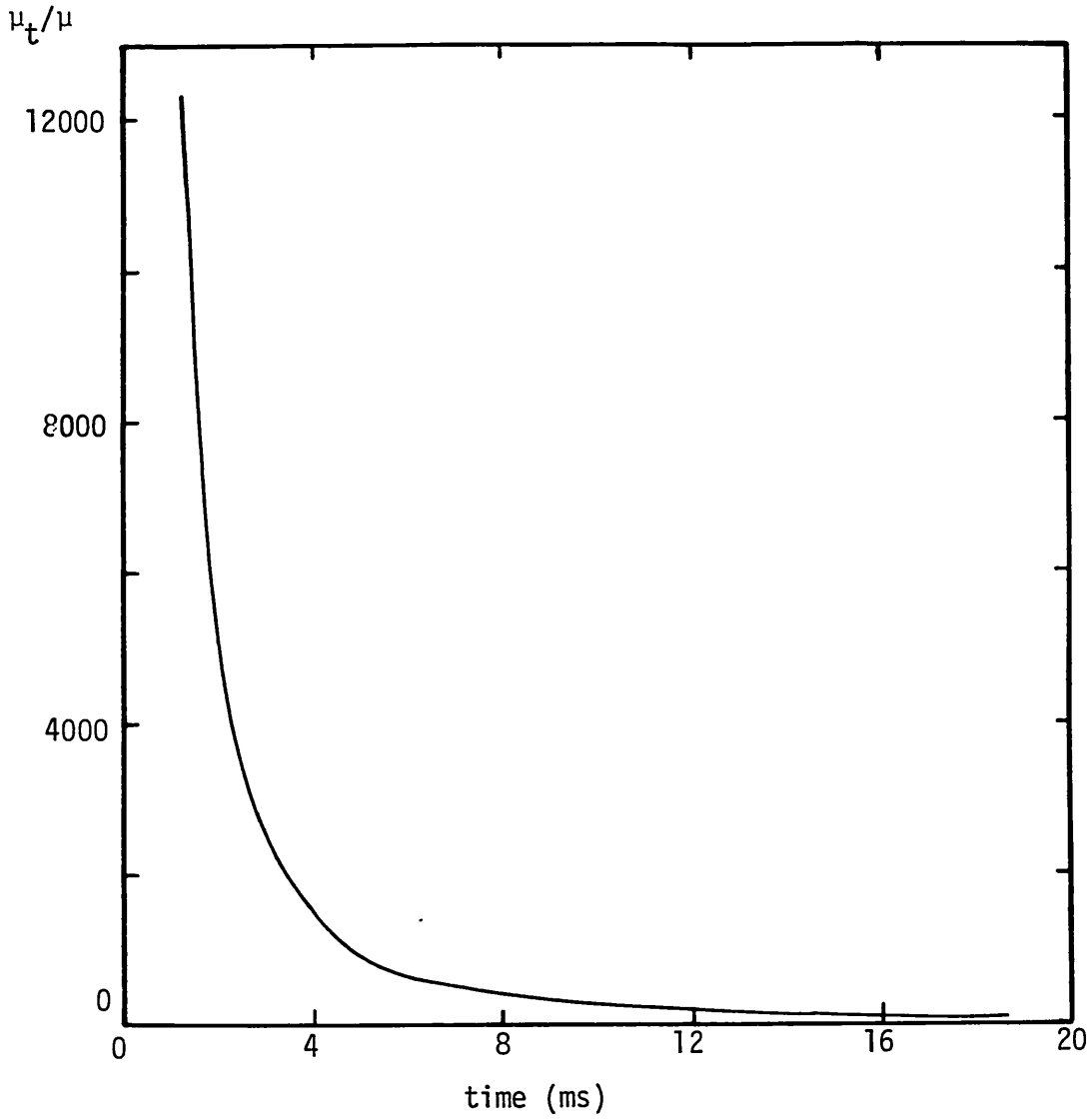


Fig. (7.16) Centreline turbulent viscosity decay at x = 10 mm for the case of Fig. (7.15)

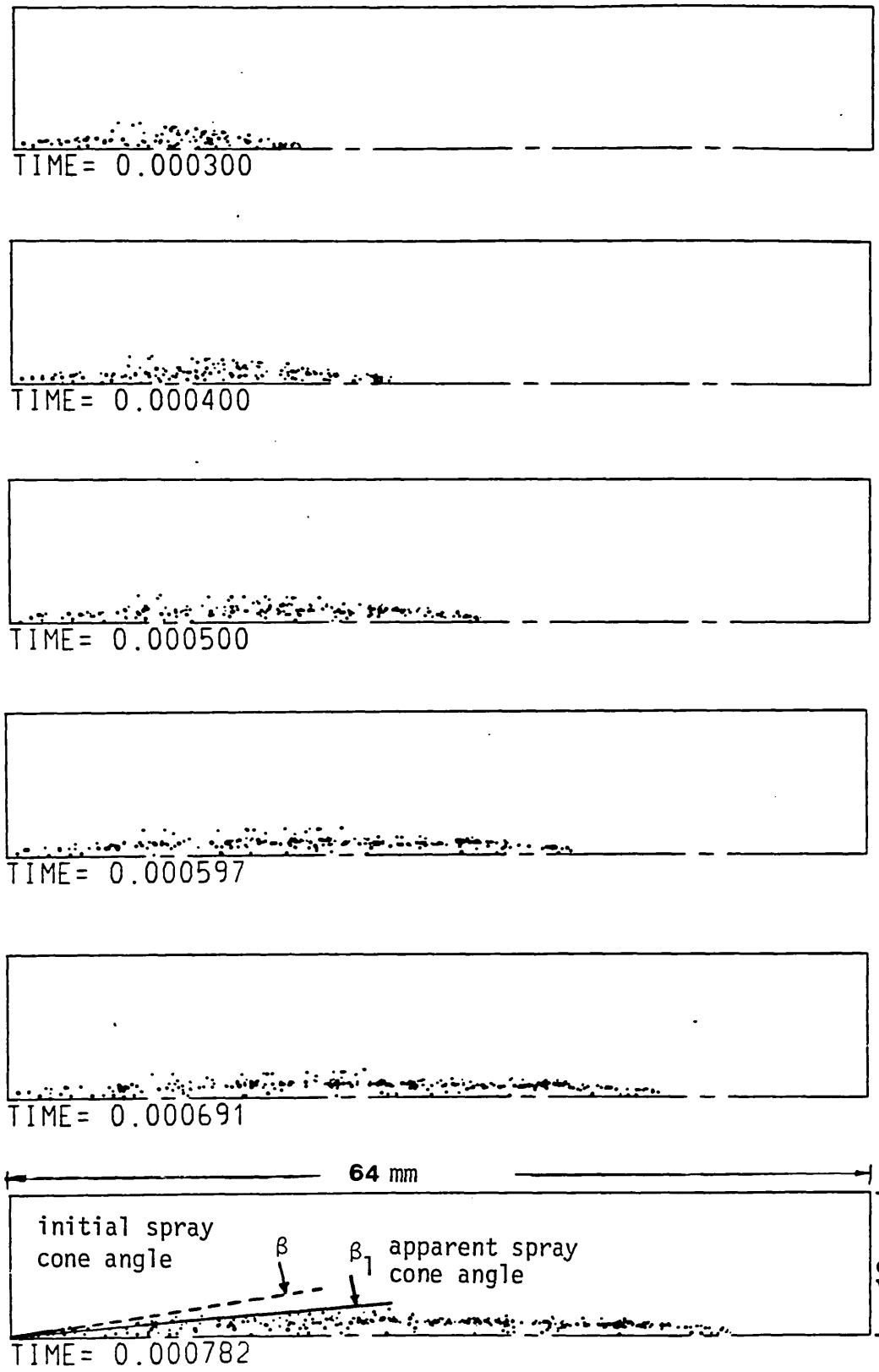
(a) ignoring droplets dispersion; (b) calculating it, and assuming the interaction time τ to be the same as the integration time step (as in the treatment of Dukowicz (1980)); and (c) using the present method (taken from Gosman and Ioannides (1981)).

The droplet fields displayed in Fig. (7.17) show that the spray produced by ignoring dispersion (diagrams (a)) has a smaller cone angle than those of (b) and (c). It is also clear that the 'apparent' spray cone angles (β_1) of (a) and (b) are smaller than the initial ones (β), while the spray of (c) has an equal apparent and initial cone angles since, generally, droplet dispersion increases the lateral spread of the spray. Also, the spread of spray (c) obtained by assuming that the turbulence acting time is the minimum of the eddy life time and the transit time (as given in chapter 3), is larger than that of (b).

The resulting penetration histories are shown in Fig. (7.18), from which it can be clearly seen that the dispersion slightly reduces the penetration of the spray, presumably because the more widely dispersed spray is able to transfer its momentum to more of the gas, reducing gas velocity (near the axis) and therefore increasing the drag on the spray.

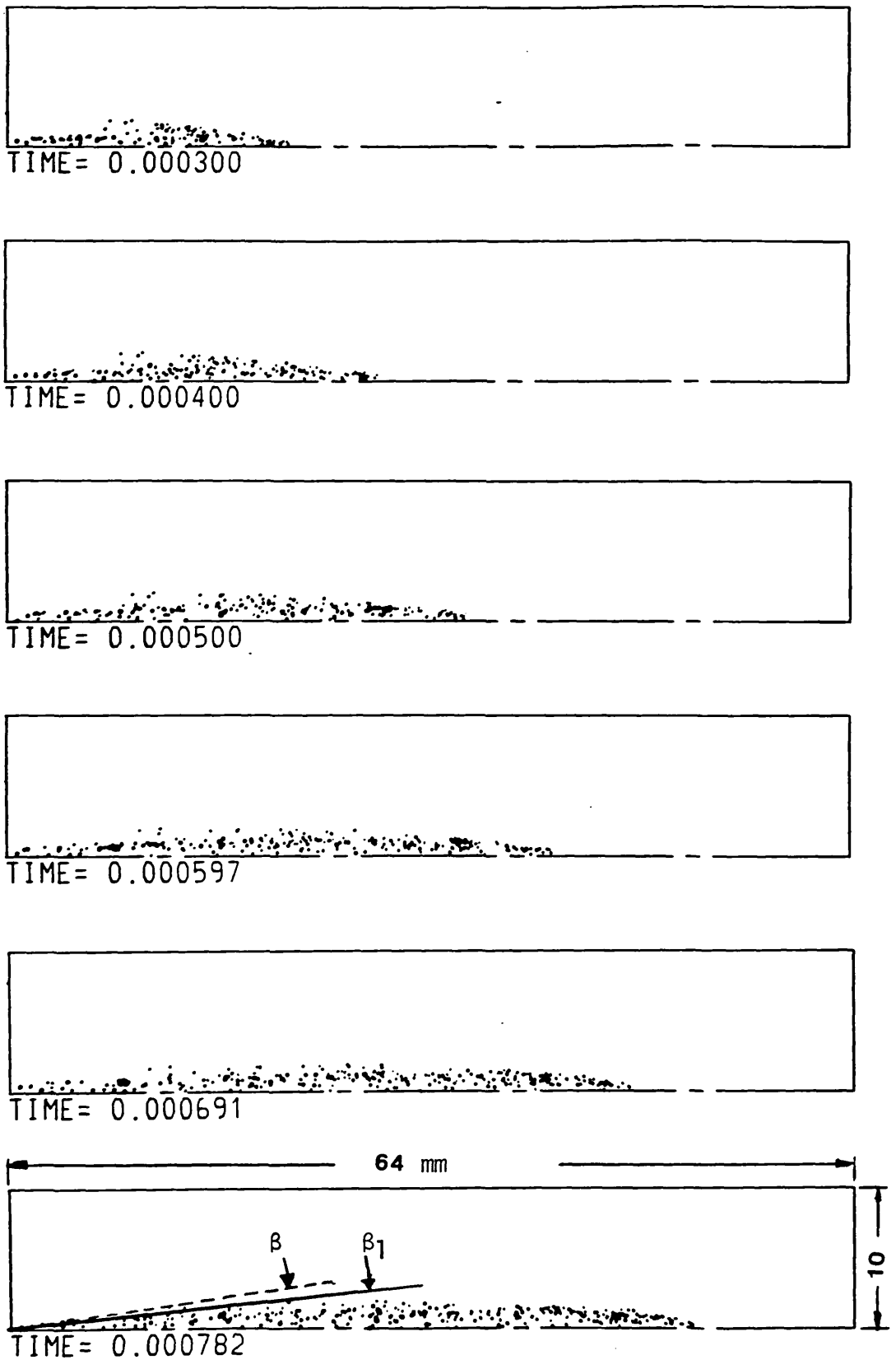
ii. Initial spray cone angle

An exploration has been performed of the sensitivity of the calculations to the value of the initial spray cone angle (β) since its value determines the initial radial velocity imparted to the injected droplets (see section (4.8)). For this purpose, two cases have been studied: (a) using the measured spray cone



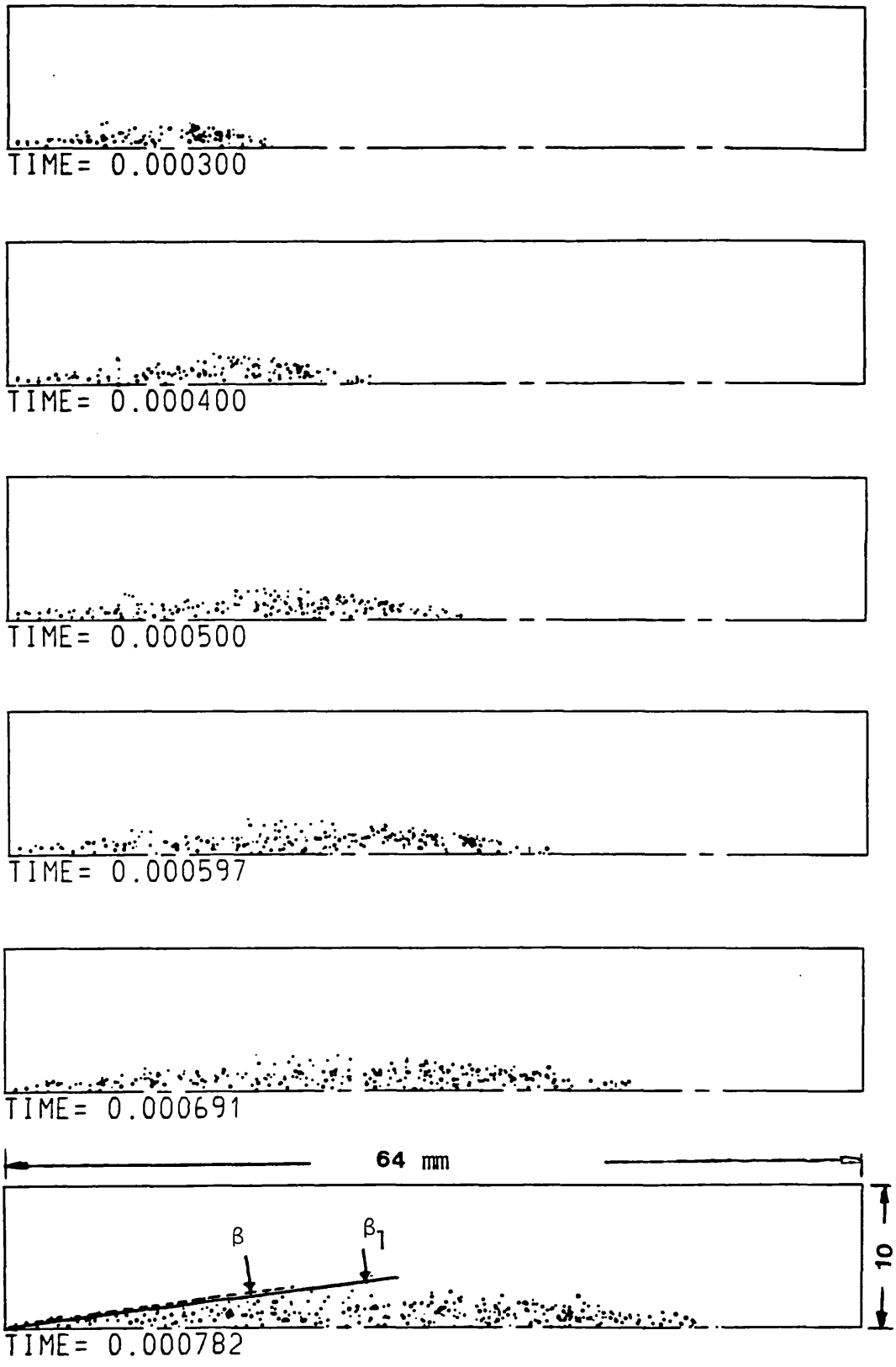
(a) ignoring dispersion

Fig (7.17) Effect of the turbulent dispersion treatment on the predicted droplet field



(b) Dukowicz treatment

Fig. (7.17) Cont'd.



(c) Gosman and Ioannides treatment

Fig. (7.17) Cont'd.

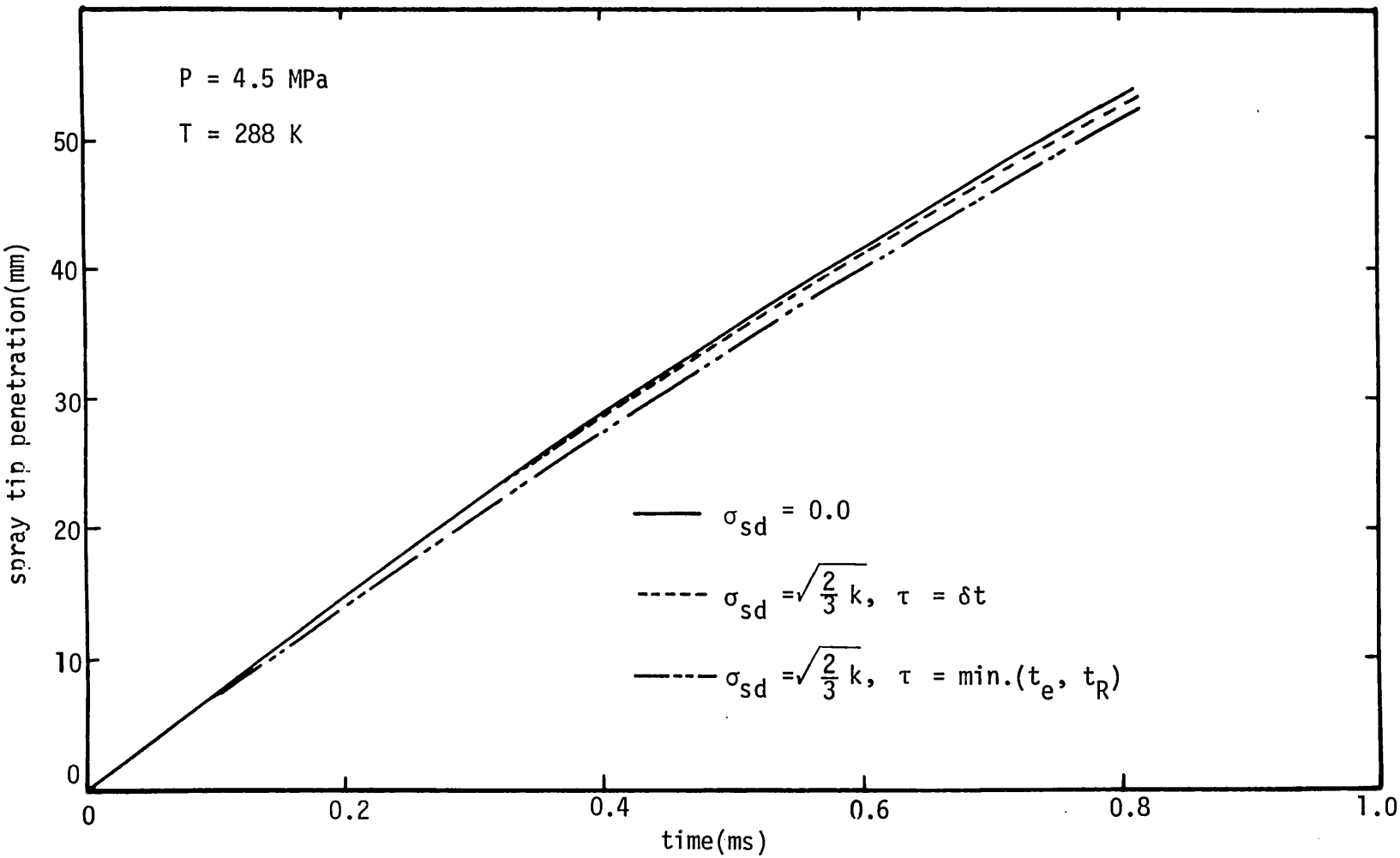


Fig. (7.18) Effect of the turbulent dispersion treatment on the predicted penetration

angle and (b) using half the measured one. The predicted spray shapes corresponding to those two cases are presented in Fig. (7.19) (plotted as whole sprays for the sake of clarity and comparison). It can be observed that although case (b) spray is initially narrower than that of (a), the apparent cone angle of spray (b) increases with time and by t = 0.782 ms, both sprays have more or less the same apparent angle. This can be explained with reference to Fig. (7.20) which displays the centreline variations of the turbulent kinetic energy of the gas phase at different times for both cases. The narrow spray of case (b) generates higher axial gas velocities in the spray region and also generates higher turbulence energies which in turn give rise to larger spreading of the droplets especially near the injector. The latter effect thus offsets the diminished initial angle.

The corresponding predicted spray tip penetrations are displayed in Fig. (7.21). As expected, the spray penetrates further for case (b) but the maximum difference between the two cases is only 6%. This may be attributed to the fact that because the initial spray width of case (b) is smaller than case (a) and less air is entrained, momentum is imparted to a smaller volume of gas, which results in a larger gas velocity. It should be noted that however, up to 0.25 ms, there is no effect, because the spray penetrates according to its axial momentum which does not change with the spray cone angle, as discussed earlier in section (7.2.2.1).

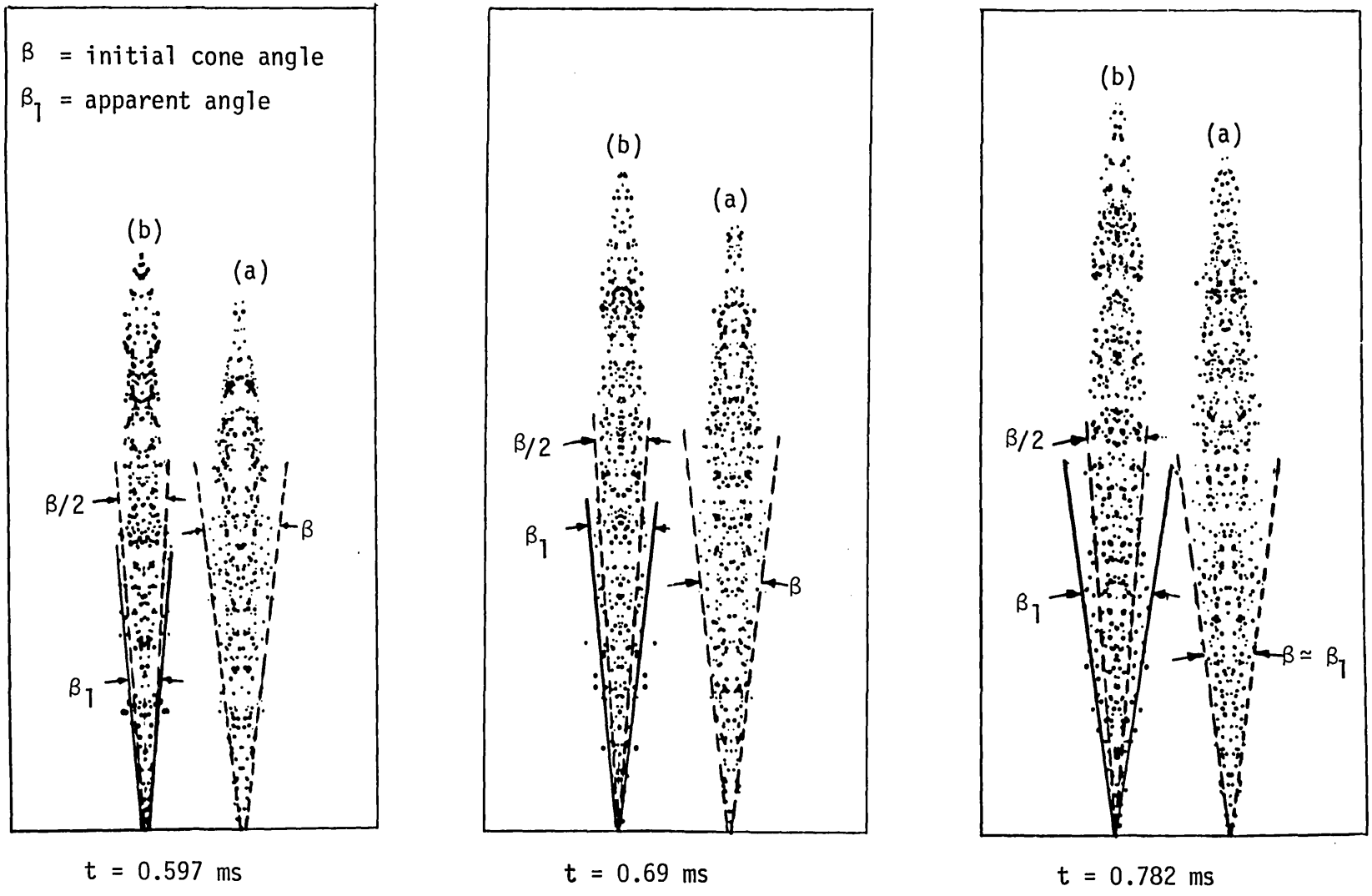


Fig. (7.19) Effect of the initial spray cone angle on the spray shape at different times (P = 4.5 MPa, T = 288 K)

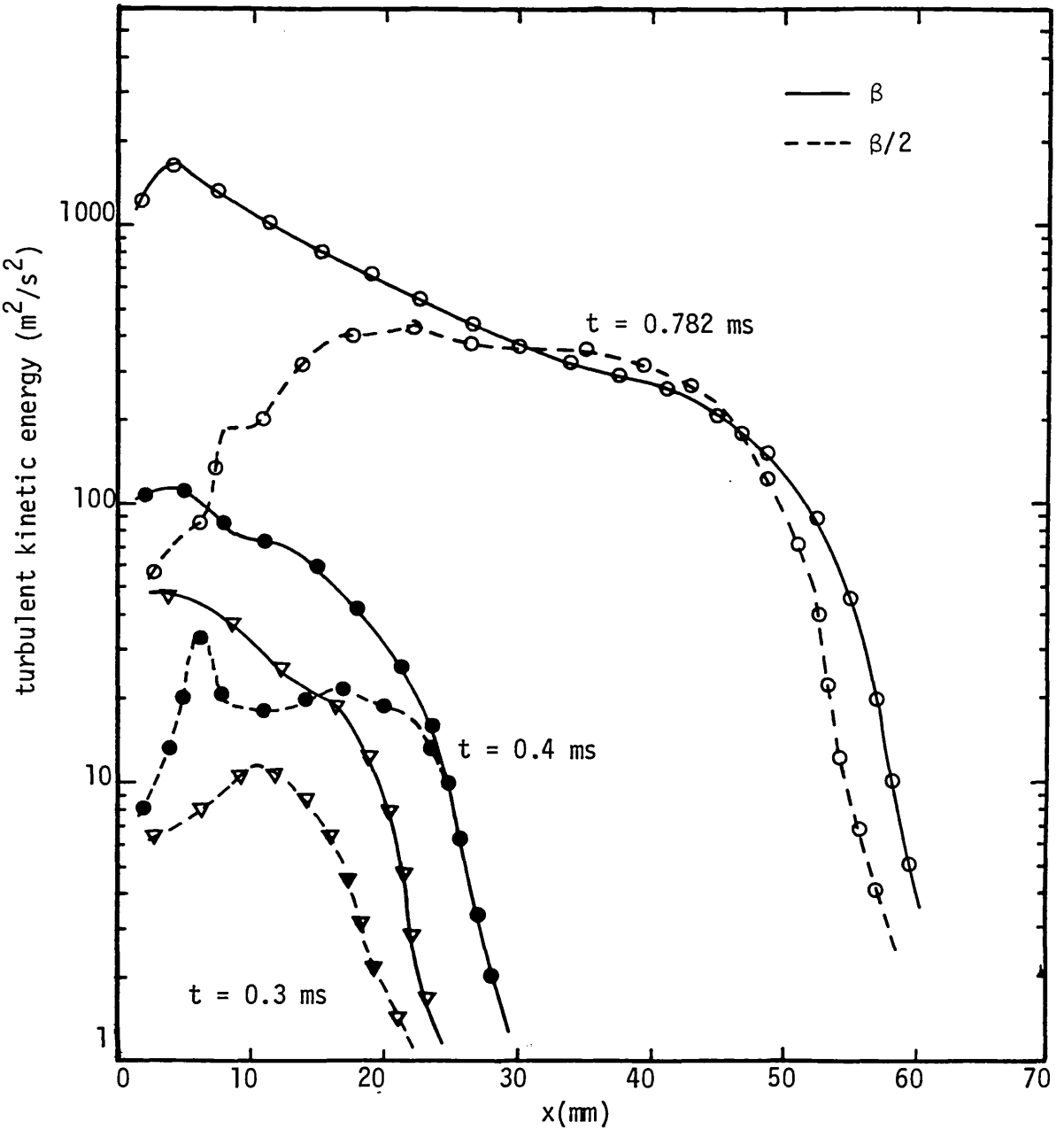


Fig. (7.20) Effect of the initial spray cone angle on the axial gas-phase variation of the turbulent kinetic energy (P = 4.5 MPa, T = 288 K)

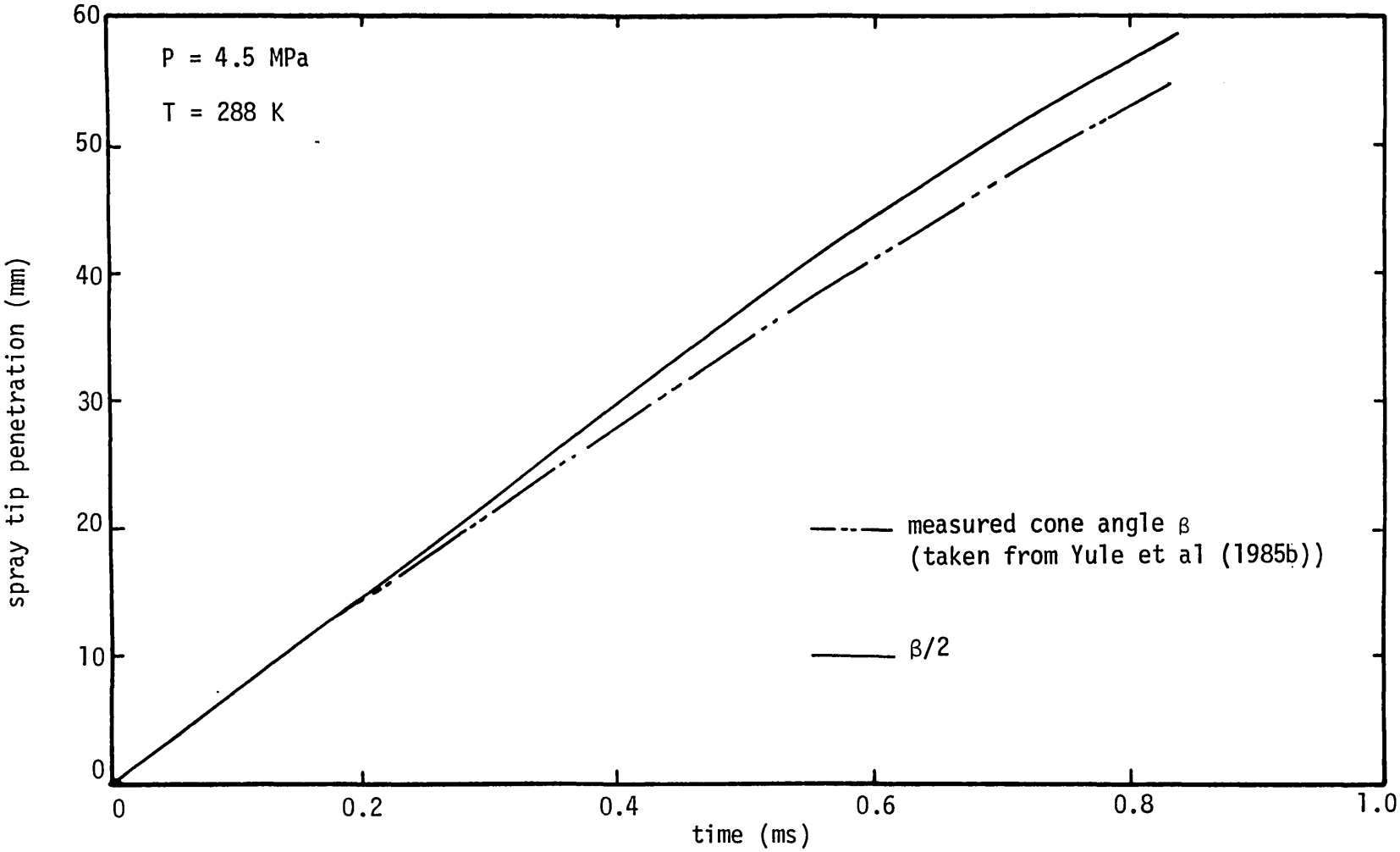


Fig. (7.21) Sensitivity of the predicted spray tip penetration to the initial spray cone angle

7.2.3 Parametric Study

a. Effect of droplet sizes

It is well known that because droplet sizes are invariably measured far downstream of the injector, they may not represent the distribution in its immediate vicinity, i.e. droplet coalescence may occur (Dukowicz (1980)). This possibility has motivated the first parametric study reported here, which is to investigate the effect of the initial droplet sizes on the calculated spray tip penetration. The procedure was to perform three runs with different initial distributions, all possessing the same shape (Rosin-Rammler distribution function) but covering different ranges. The three size ranges used are (i) D_d = 0 - 22 μm, with a mean diameter ($\bar{D}$) of 10 μm; (ii) D_d = 0 - 55 μm, with $\bar{D}$ = 25 μm; and (iii) D_d = 0 - 120 μm, with $\bar{D}$ = 50 μm. The results given in Fig. (7.22) show the expected trend of enhanced penetration with increasing droplet sizes. This occurs because, the drag force varies inversely with the droplet diameter (equations (3.63)) i.e. the larger droplets experience less drag than the smaller ones and thus the transition from the linear behaviour is delayed. In the early period, the effect is very small since the droplets move without slip (as discussed in section (7.2.2.1)) and hence experience no drag.

An interesting point evident in Fig. (7.22) is that the change in spray tip penetration is not directly proportional to changes in the droplet sizes, e.g. the maximum difference between the curves for $\bar{D}$ = 10 μm and $\bar{D}$ = 50 μm is only 7%.

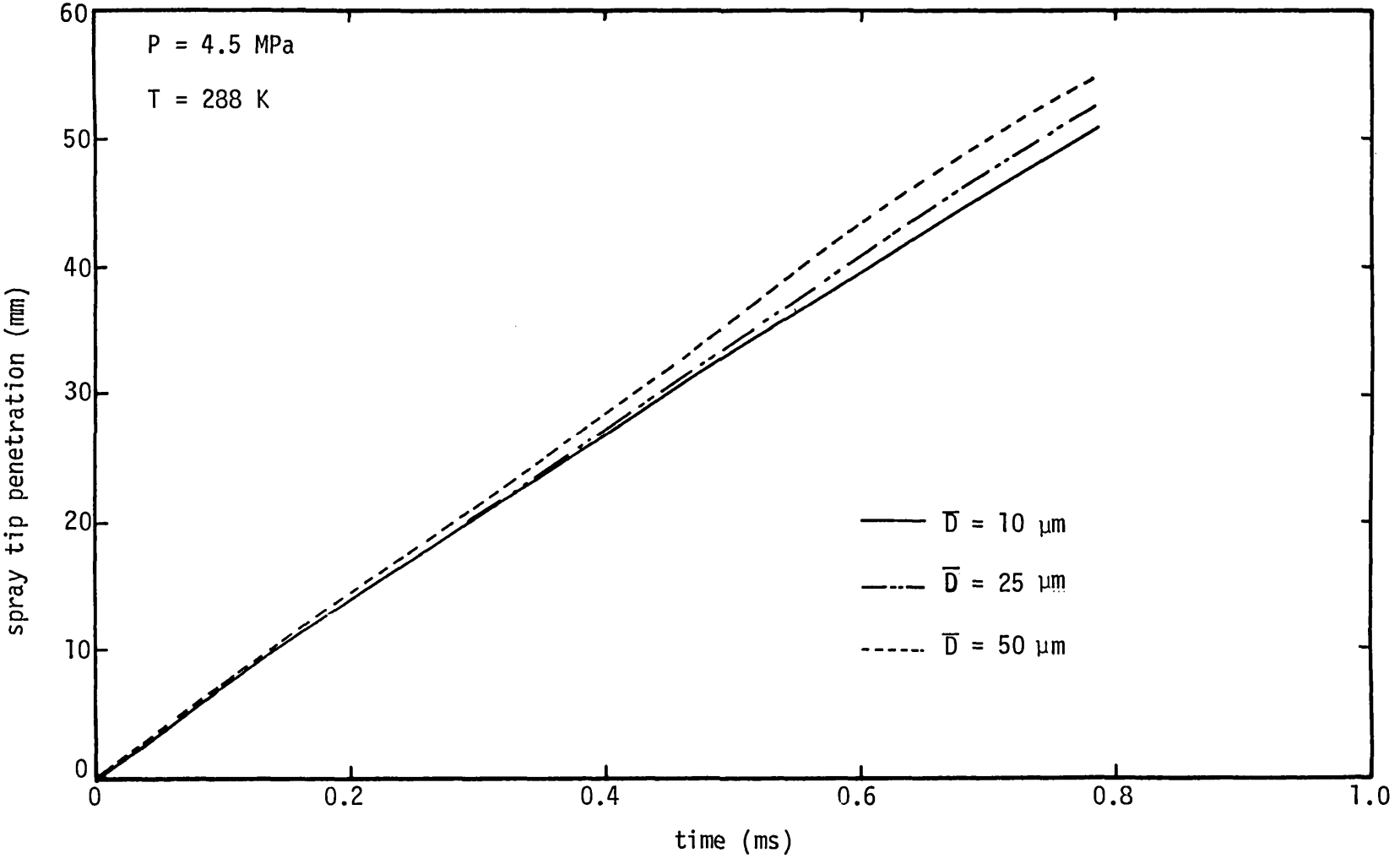


Fig. (7.22) Effect of the initial droplet sizes on the spray tip penetration

b. Effect of initial size distribution function

In the light of the large number of size distribution functions used to characterise measured droplet data such as Rosin-Rammler, Chi, Tanasawa-Tesima, log-probability etc. (see section 2.2.3)), calculations were performed to assess the effect of the different distributions possessing the same mean on the spray tip penetration. The Rosin-Rammler (equation (7.1)) and the Chi (equation (7.2)) functions were chosen for this purpose and are compared in Fig. (7.23) for a Sauter mean diameter (D_{32}) of 25 μm. It is clear that of the two, the Rosin-Rammler distribution gives a larger probability of finding finer droplets in the spray.

Figure (7.24) shows the predicted spray tip penetration corresponding to the two distributions. The results indicate that the Chi distribution gives slightly (≃ 3%) longer penetrations due to its predominance of coarser droplets, as would be expected.

c. Effect of injection rate history

In the light of the uncertainties about the initial part of the injection curve in the experiments of Yule (1984) (i.e. up to 100 μs) and of the entire history in most other experiments, sensitivity explorations were performed for the Yule case using a hypothetical constant injection rate throughout. It produces the same total injected mass over the 2.05 ms interval as the measured diagram as shown in Fig. (7.1). It should be noted that the constant injection rate diagram produces a higher rate than the 'measured' one during the first 0.3 ms of the injection pulse.

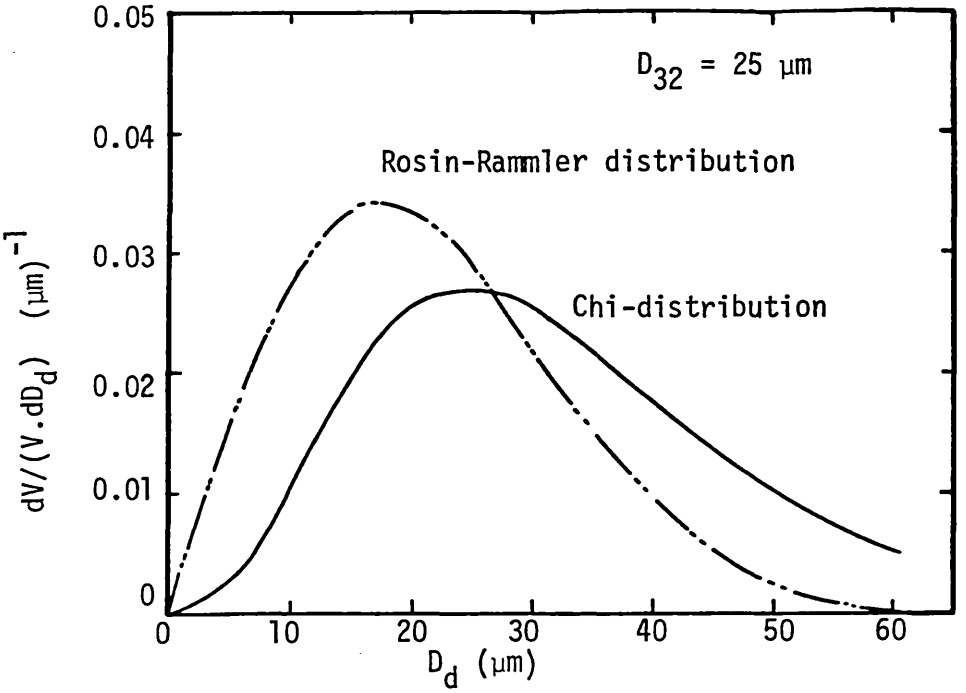


Fig. (7.23) Comparisons of the Chi and the Rosin-Rammler distributions with the same mean diameter

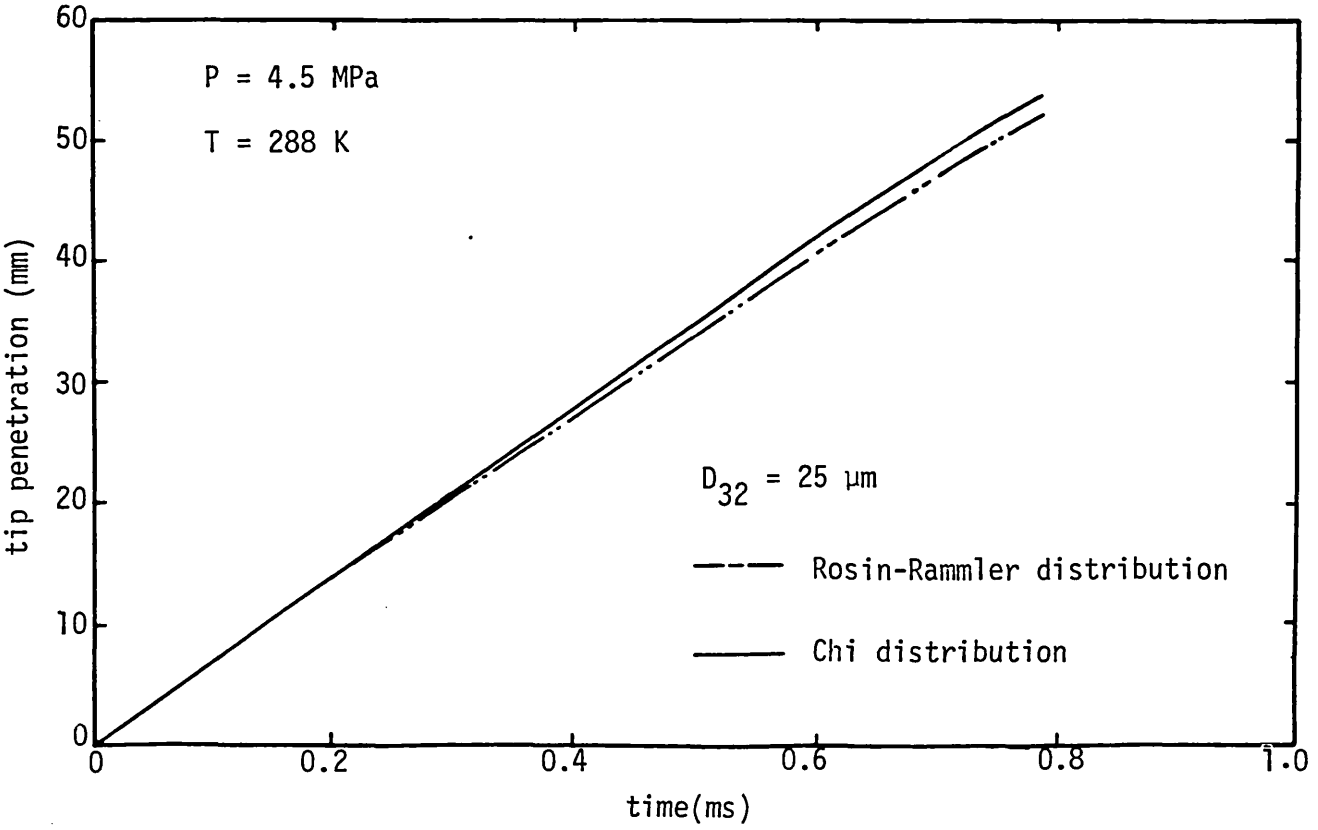


Fig. (7.24) Effect of the droplet size distribution function in the spray tip penetration

The results of these tests are shown in the form of plots of the calculated and measured spray tip penetrations in Figs. (7.25) and (7.26) for the 'low' and 'high' pressure cases respectively. These show clearly that, as might have been expected, the results are sensitive to the initial injection schedule and an enhanced penetration is obtained for a constant injection rate. This occurs because as already shown,the constant injection rate diagrams gives higher rates up to t = 0.3 ms which produces, for the same nozzle diameter, higher injection velocities, resulting in a higher momentum spray. Therefore, somewhat better agreement with the experimental data is obtained for the low-pressure case. For the high-pressure case, the agreement with the constant-rate predictions is fairly good up to t ≃ 0.3 ms, after which it deteriorates. This trend is now consistent with that of the Hiroyasu and Kadota simulation in which a constant injection rate was used (see section (7.2.1)). Of course, the use of a constant injection rate throughout cannot be justified, since the measurements show that the nozzle inlet pressure and needle lift are time dependent, so the improvement obtained especially for the low pressure case might be partly fortuitous.

d. Effect of injection velocity for a given injection mass schedule

Finally, the effect of injection velocity on the spray tip penetration was investigated. For this purpose, the injector diameter was reduced from 0.46 mm to 0.36 mm while the mass flow rate was kept constant, thus resulting in an increase in the injection velocity of 47%.

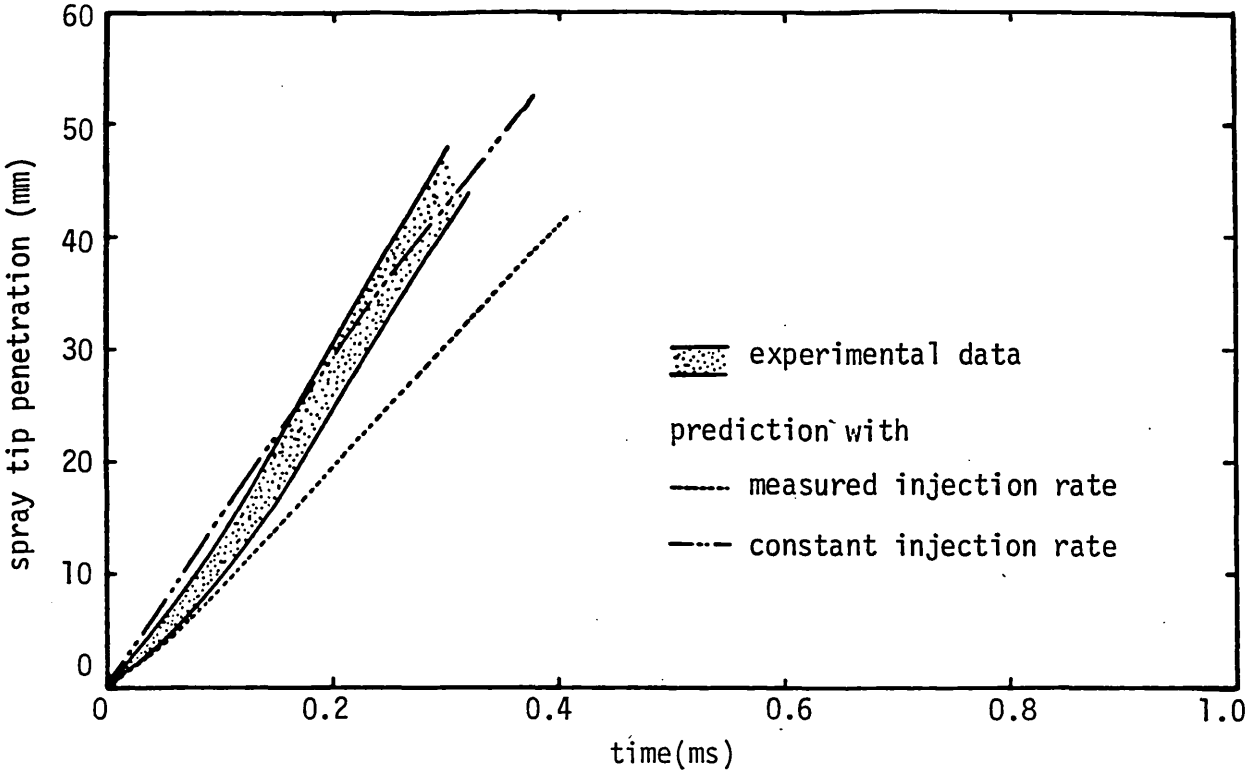


Fig. (7.25) Effect of the shape of the injection rate diagram on the spray tip penetration (P = 0.5 MPa, T = 288 K)

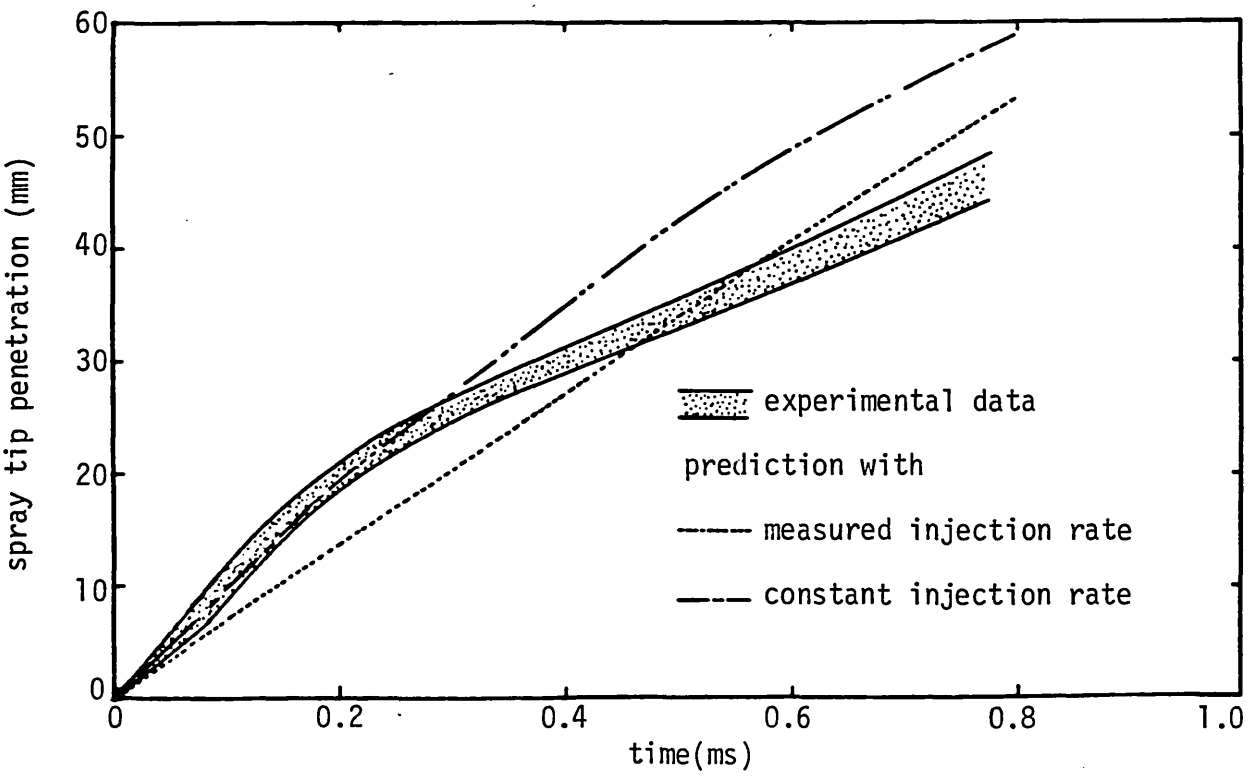


Fig. (7.26) Effect of the shape of the injection rate diagram on the spray tip penetration (P = 4.5 MPa, T = 288 K)

It will be recalled that experiments show that increasing the injection velocity decreases the Sauter mean diameter and the initial spray cone angle. The effect of those two on the spray tip penetration is small and of opposite direction, as was shown earlier. Thus it was decided not to take into consideration these two effects in this investigation, i.e. the initial spray angle and size distribution were left unchanged.

The predicted spray tip penetration for the two injector diameters studied are presented in Fig. (7.27), which shows clearly that appreciably enhanced penetration is obtained for higher injection velocity (and hence higher droplet momentum).

It is interesting to note that when comparing Figs. (7.22) and (7.27) it appears that the penetration is much more sensitive to an increase in droplet momentum resulting from higher initial velocity than to that corresponding to larger initial droplet sizes.

Summary

From the sensitivity and the parametric study presented earlier, one can establish the order of importance of the factors influencing the spray penetration under isothermal conditions. Droplet injection velocity, injection rate history and initial gas-phase turbulence characteristics are the most influential factors. The other parameters have a secondary effect on the

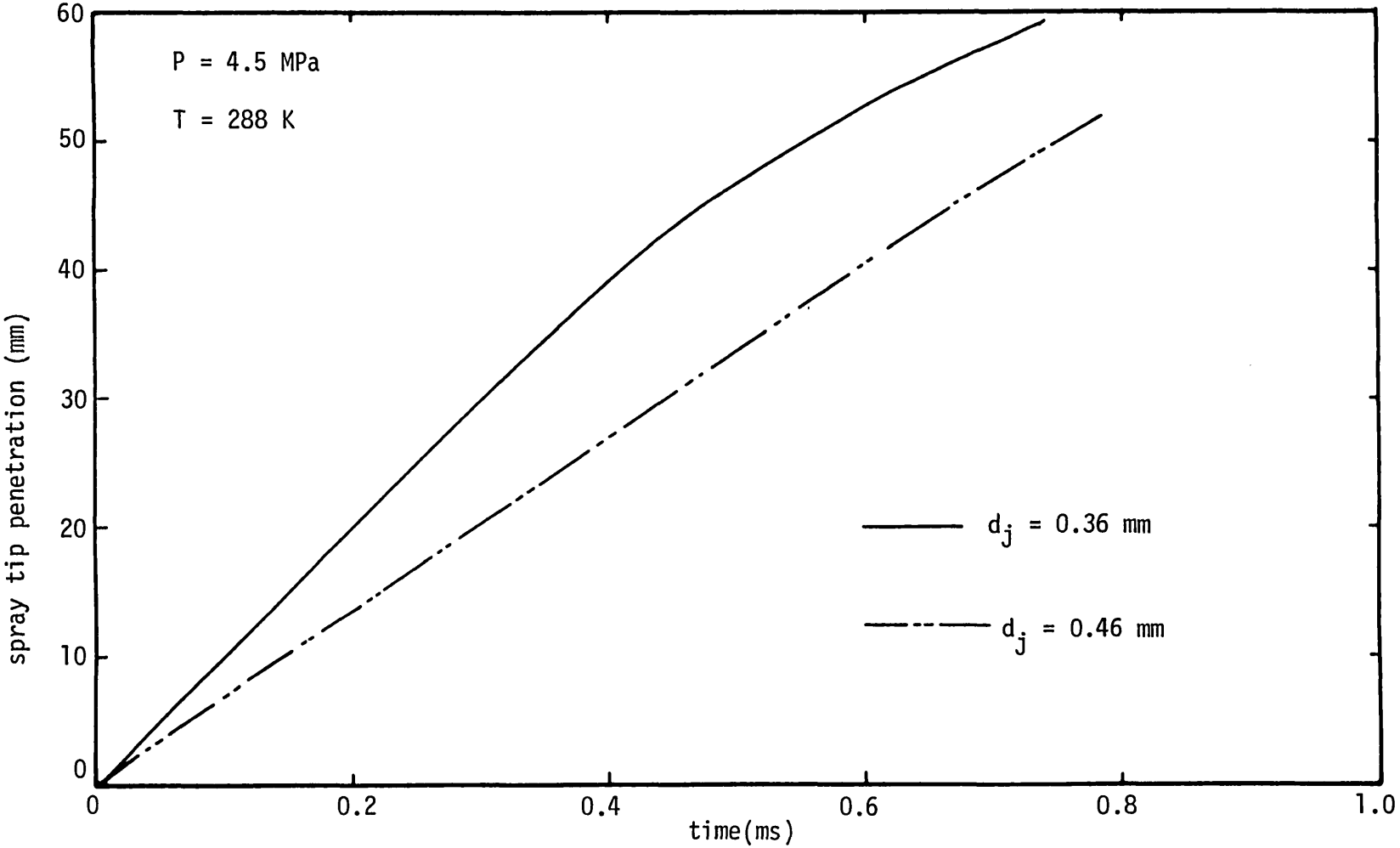


Fig. (7.27) Effect of the injection nozzle diameter on the spray tip penetration for the same mass flow rate

penetration. These are in descending order of importance: initial velocity profile of the liquid, spray cone angle, initial droplet sizes, initial droplet size distribution and finally turbulent dispersion of the droplets. The last named factor has the least effect on penetration but the highest effect on the spray shape. The effects of some of these factors on the evaporating spray behaviour will be discussed in the next section.

7.3 Evaporating Spray

7.3.1 Comparison With Measurements

i. The experiment of Yule et al (1985a,b)

Computations were performed to simulate the evaporating spray experiments of Yule et al (1985b) using the measured injection rate diagram and the spray cone angle to obtain the inlet masses and velocities of the introduced droplet as shown in section (4.8). In the absence of any other information, the size distribution of the injected droplets was approximated in the same way as in the isothermal spray calculations i.e. by a Rosin-Rammler distribution function (equation (7.1)) with mean diameter of 25 μm and exponent of 2, to yield droplets ranging from 0 to 60 μm in diameter.

The predicted spray tip penetration (defined as the furthest axial distance travelled by droplets) are compared with the measured

ones for P = 0.5 and 4.5 MPa in Fig. (7.28)(a) and for P = 2.5 MPa in Fig. (7.28)(b).

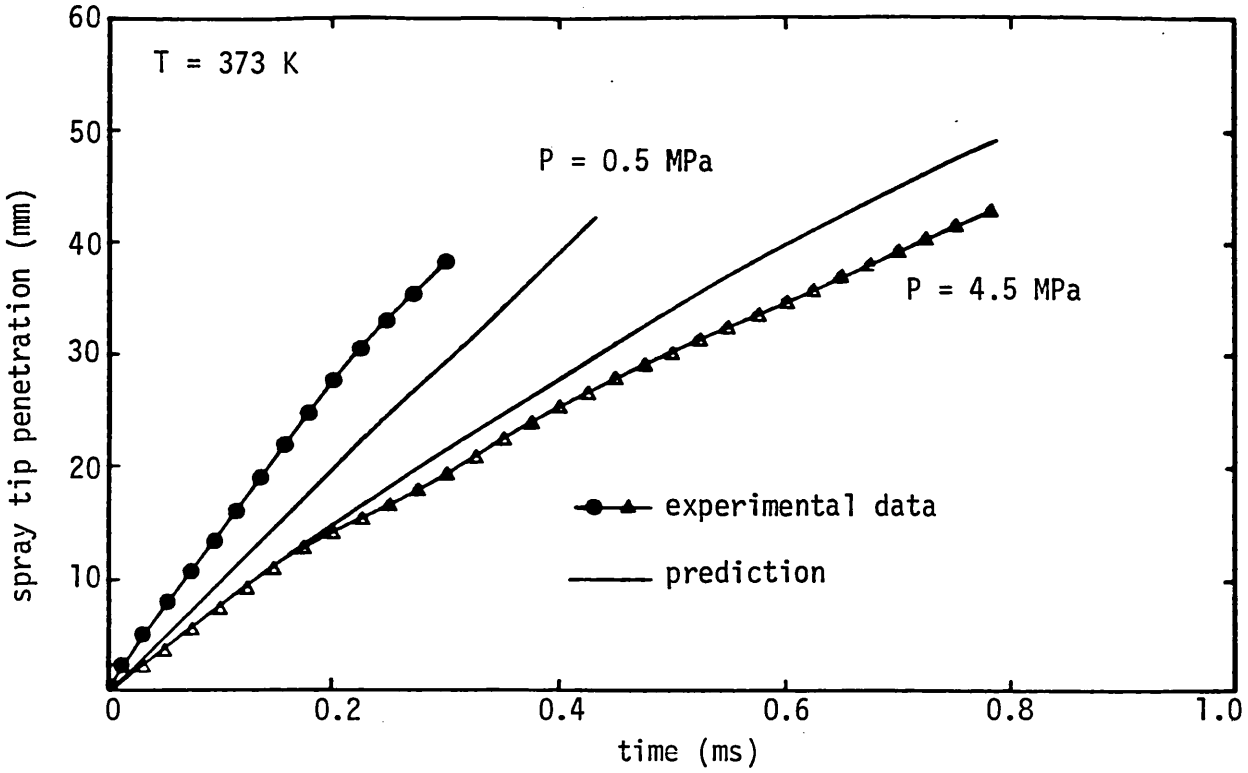
The increase of temperature it should be noted, has two effects: one is to reduce the gas density, which tends to increase penetration (see section (2.5.5)); and the other is to cause droplet evaporation, which will have the opposite tendency. The measurements show the nett effect to be considerably reduced penetration as discussed earlier in section (2.5.5). The predictions also, show a reduction in penetration, but to a considerably lesser extent. This could be due to underestimation of the vaporization rate, as can be seen from Fig. (7.29) which displays the cumulative evaporated mass (m_v) for the above mentioned cases and shows that by t = 0.9 ms the maximum value is only 0.11% of the injected mass (m_{inj}).

It should be pointed out that evaporating spray measurements were taken for single spray pulse. If the measurements were taken over many spray pulses, as in the isothermal spray experiments, the measured penetration will yield a band and hence, the agreement of the penetration with the measurements may vary quantitatively and probably, qualitatively.

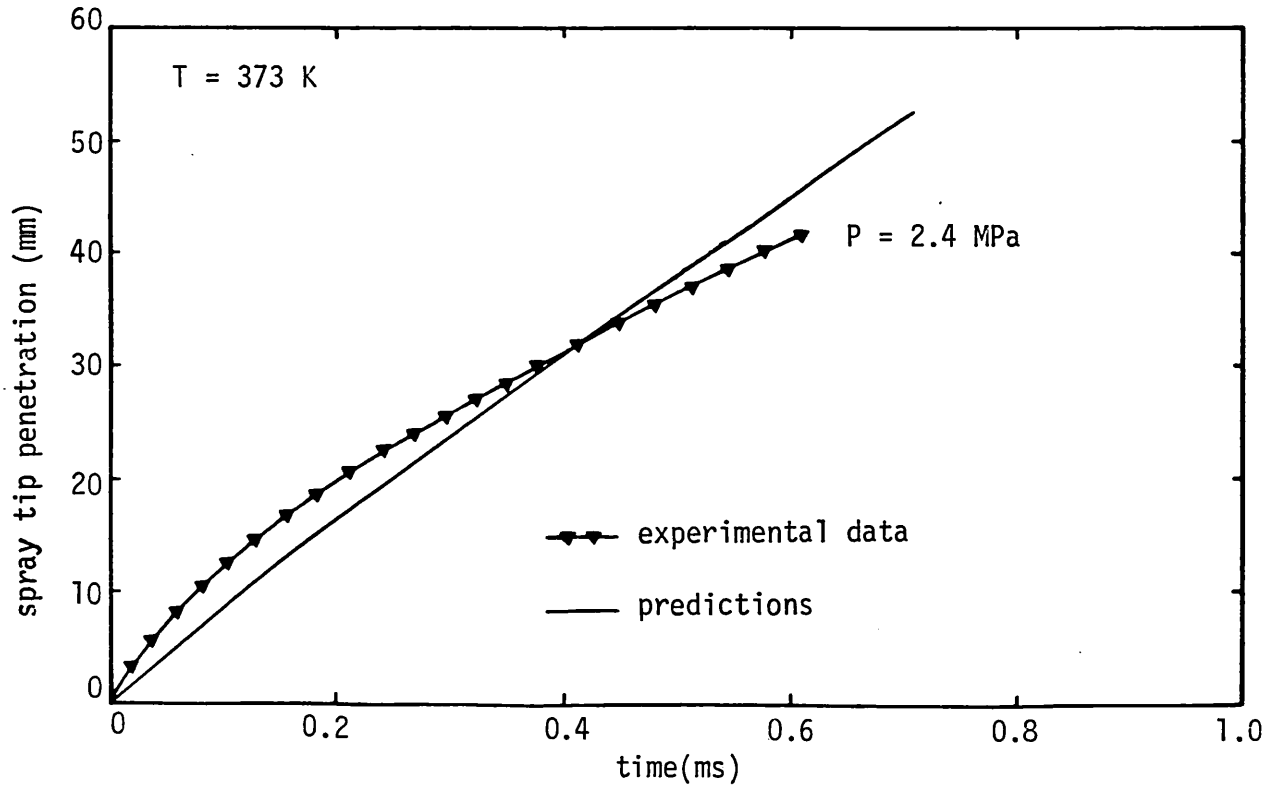
ii. Simulation of Kuniyoshi et al (1980) experiments

Inlet conditions

In the experiments the total amount of fuel injected per pulse as determined by collecting and averaging over many pulses was 0.12 g, and the pulse duration was 9 ms. Also reported was the fuel flow rate versus time history but this is inconsistent



(a)



(b)

Fig. (7.28) Comparison of the predicted spray tip penetration with the experimental data of Yule et al (1985b)

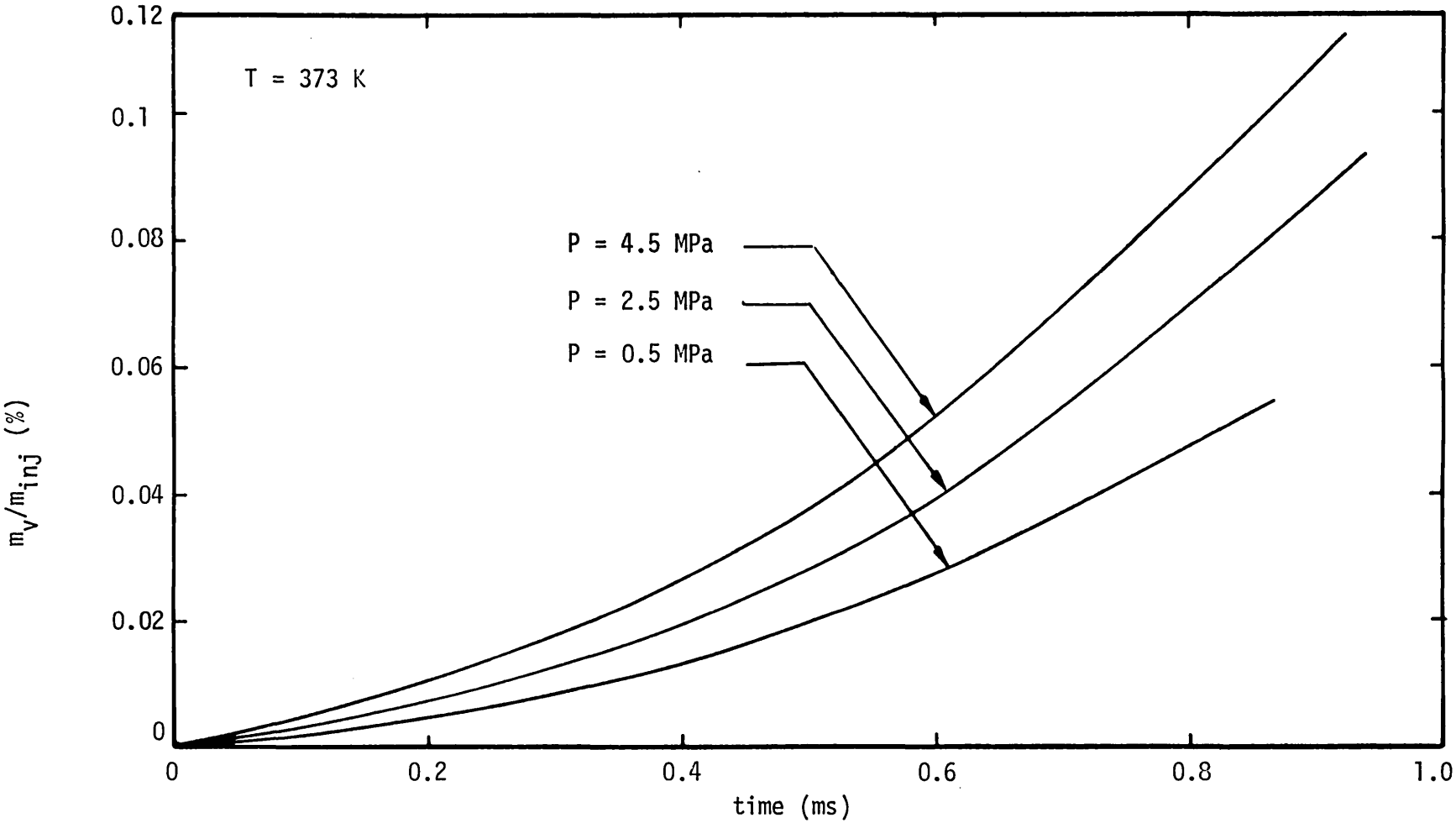


Fig. (7.29) Time history of the total evaporated mass for the evaporating spray of yule et al(1985b).

with the above information, for the total mass of fuel injected per pulse obtained from integration of this history is around 20% larger. Therefore, the computations were performed using a steady injection rate.

As noted in section (2.2.3), the droplet sizes were measured in the spray periphery at various sections downstream of the nozzle and they ranged from 5 to 50 μm. For computational purposes, a Chi size distribution function with D_{32} = 25 μm is used to represent the distribution in the vicinity of the injector in the absence of any better information (because it is characterised only by the Sauter mean diameter, unlike the Rosin-Rammler function which requires specification of $\bar{D}$ and n). Finally, the measured spray cone angles were employed.

Definitions of the spray tip penetration

There is some ambiguity in these experiments about the definition of the droplet-based spray tip penetration, which was obtained in the conventional way by deducing the leading droplet positions from photographs. The ambiguity arises at ambient temperatures greater than 750 K where, according to the experimentors, the density of the spray was less than the intensity of the transmitted light of the measuring technique due to the extensive vaporization of the spray. In these circumstances it is possible that the leading droplets in the sparse region were obscured resulting in under-estimation of the droplet-based penetration.

The flame-based 'vapour penetration' was defined as the axial position of the flame front just after ignition and was correlated by the empirical expression:

$$\ell_f = 418\ t^{0.375}(\rho g)^{0.092}\ \log t - 0.409 d_j^{0.538} \tag{7.3}$$

where ℓ_f is the 'vapour penetration', t is the time from the start of injection and g is the gravitational acceleration.

Accordingly the following two definitions of the spray tip penetration are used for comparison with these data

a. The distance travelled by the leading droplets, ℓ_d.

b. The location 'ℓ_f' on the axis where the equivalence ratio has a prescribed value ψ given by

$$\psi = f/(1 - f)/f_{stoich} \tag{7.4}$$

where f is a prescribed level of fuel vapour mass fraction and f_{stoich} is the stoichiometric ratio (0.0668).

The predicted penetrations according to the above definitions are displayed in Fig. (7.30) together with the measurements and the flame-based experimental correlation (equation (7.3)), for the case where P = 6.28 MPa and T = 800 K. In this figure, the droplet penetration is compared with the measured one while the vapour penetration for ψ = 0.15 (the lean limit of combustion) is compared with the flame-based empirical formula.

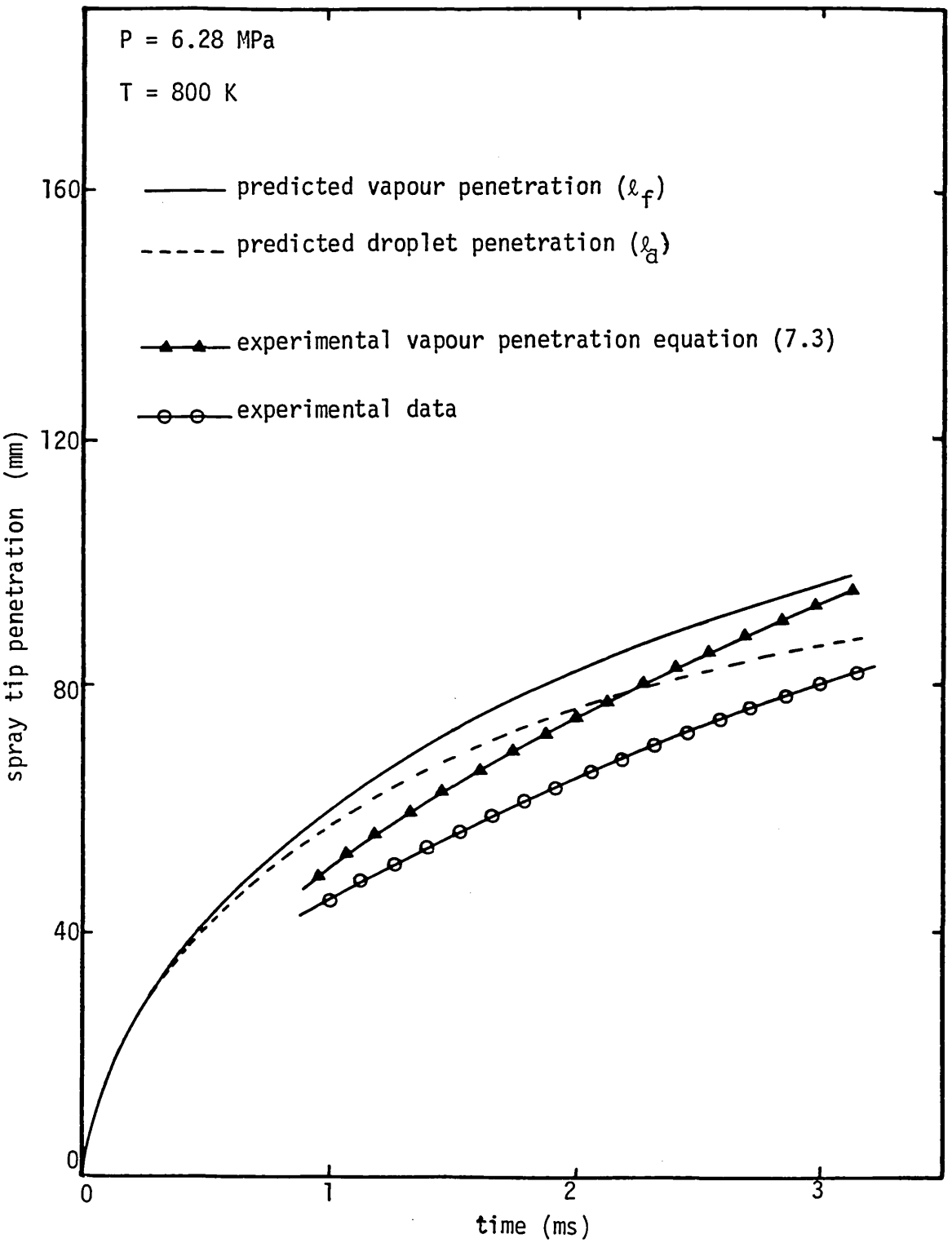


Fig. (7.30) Spray tip penetration definitions

Presentation of the results

The predicted vapour-based penetration (for ψ = 0.15) is compared in Fig. (7.31) with the experimental correlation over the full range of charge temperatures covered in the experiments. Evidently the calculations reproduce the trend of increasing penetration with increasing temperature, which is due, as explained earlier to the reduction in the charge density; however the levels are over-estimated during the early stages of injection, where the discrepancies reach a maximum value of 20% at t = 1 ms. At later times the sets of curves approach each other, reducing the maximum discrepancy to about 5% at t = 3 ms.

The discrepancies noted above may be attributed to two main factors. The first is the uncertainty about the injection rate history. A steady injection rate is used in this simulation, while the measured one shows a time varying rate although there is a very steep rise at the beginning of injection. The finite time required for the initial build-up would have the effect of slowing down the droplets injected in the early phases of injection and hence decrease penetration (see the isothermal tests in section (7.2.3)). The second source of uncertainty concerns the injection condition, such as the droplet sizes, size distribution and droplet velocity distribution.

Figure (7.32) displays the predicted integrated evaporation rates as a percentage of the integrated injected mass corresponding to the cases of Fig. (7.31). As might be expected, the evaporation rate increases with increasing charge temperature. This is because increasing the gas temperature increases the droplet temperature

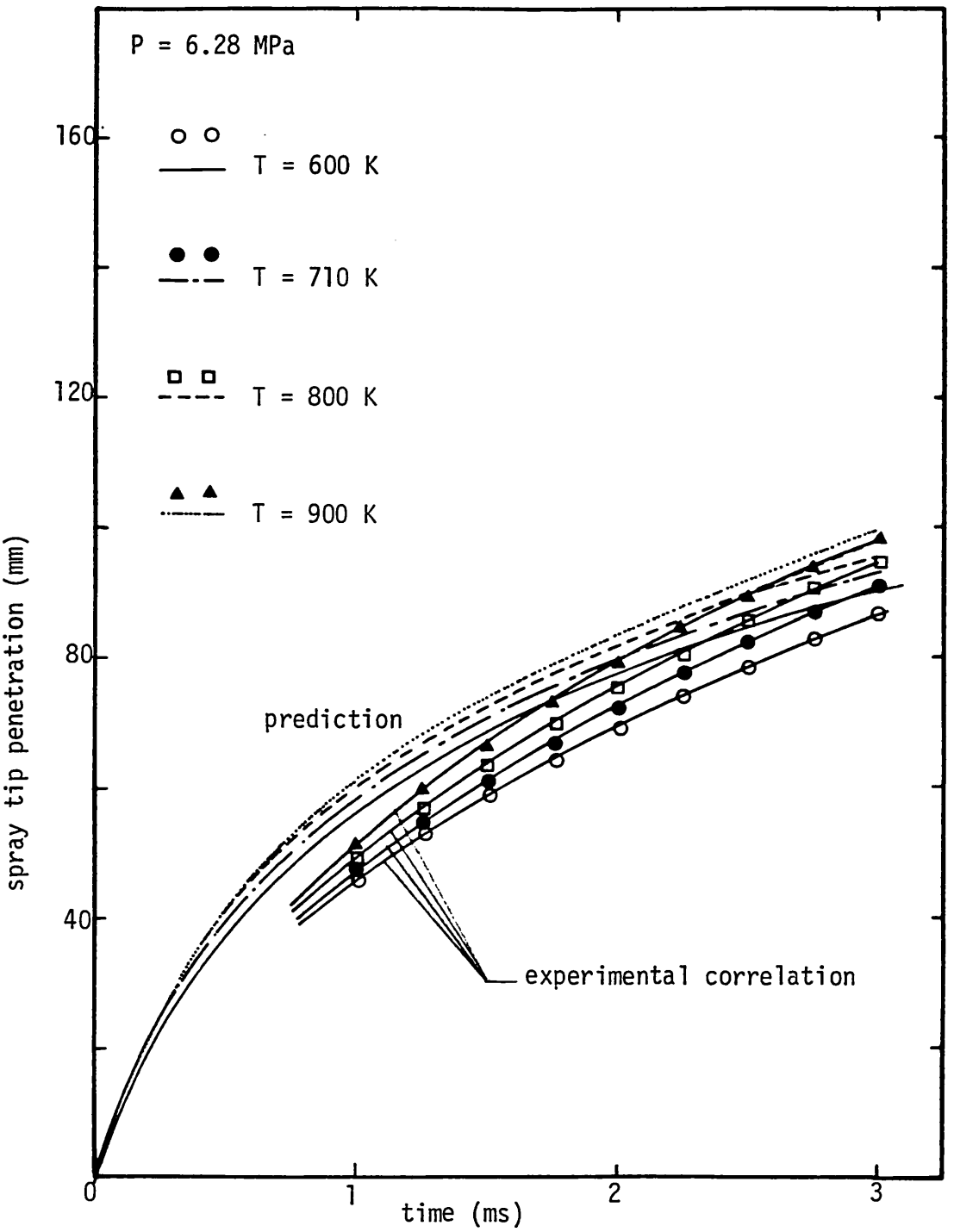


Fig. (7.31) Comparison of the spray tip penetration (vapour penetration) with the experimental correlation at different temperatures

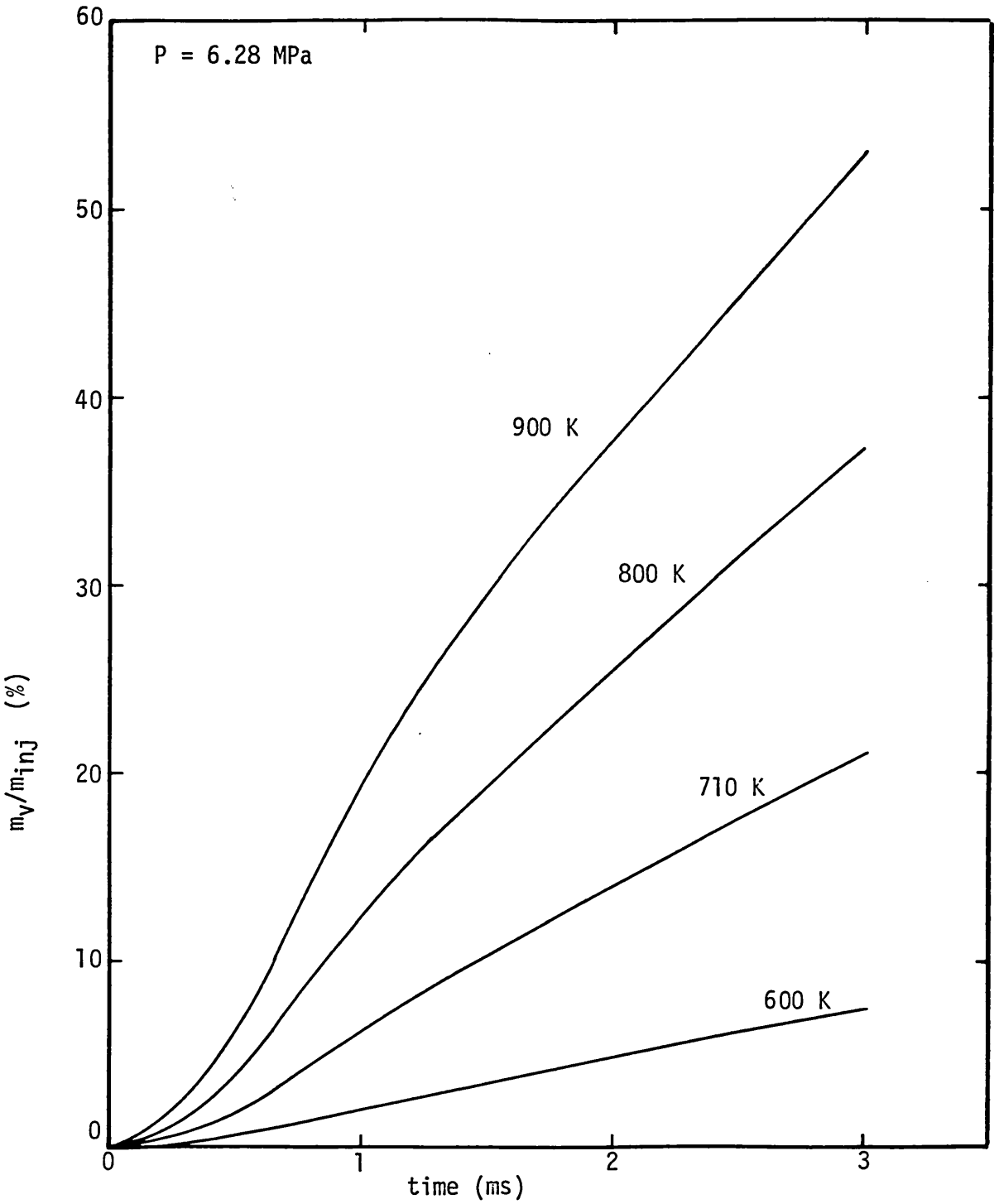
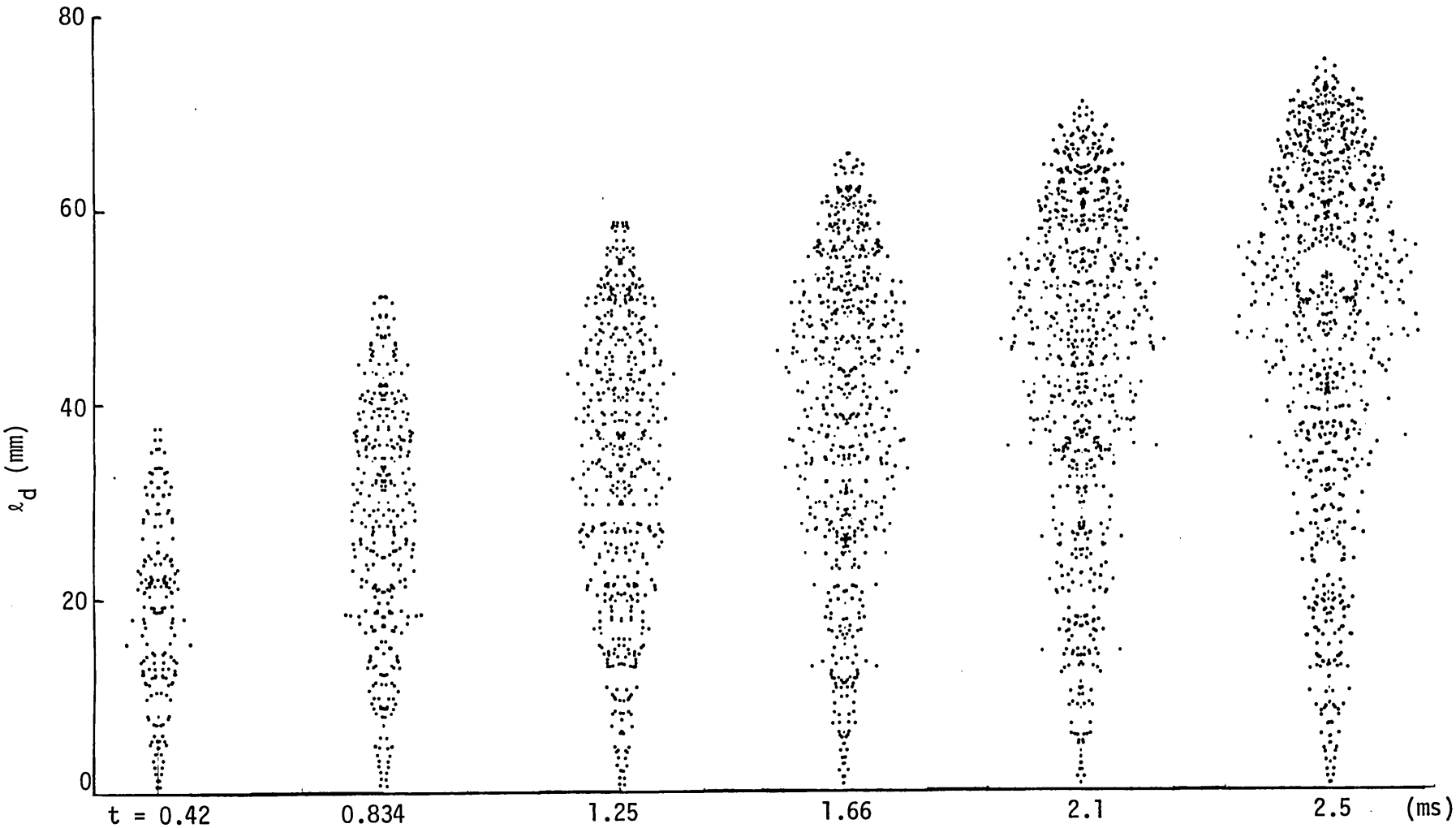


Fig. (7.32) Effect of the initial charge temperature on the predicted vaporization rate

(c.f. equation (3.73)) and hence exponentially increases the partial pressure of the fuel vapour (i.e. the concentration) at the droplet surface (c.f. equation (3.82)), thus in turn augmenting the driving force for diffusion. There is an opposite effect due to the decrease in mean density in the vapour film, but this is overshadowed by the increased driving force. It should be noted that the initial evaporation rate up to $t \simeq 0.5$ ms is lower than that at later times. This is because the droplets are heating up during this period. No data is available for the assessment of these predictions.

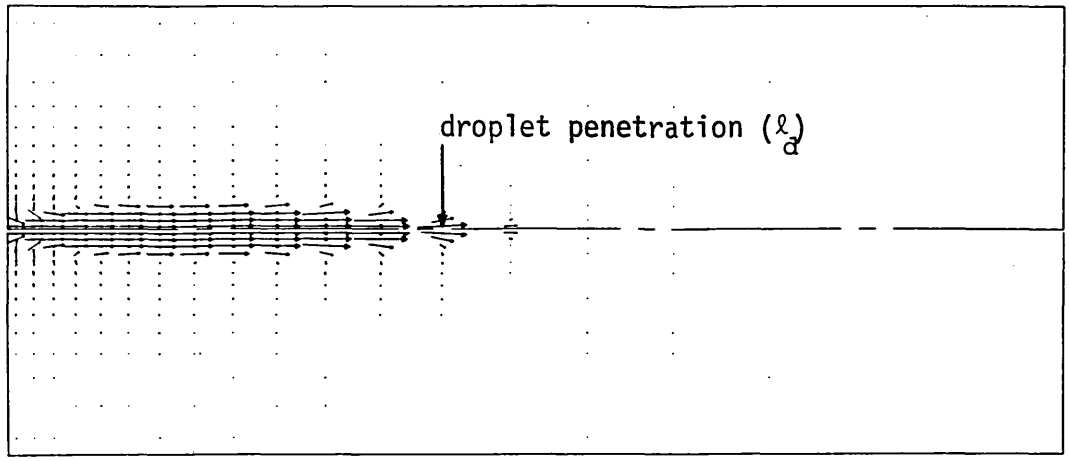
The predicted droplet pattern and fields of gas velocity, turbulence intensity, length scale, turbulent viscosity, equivalence ratio and temperature are shown in Figs. (7.33)(a) through (g) for the case where P = 6.28 MPa and T = 800 K. It is of interest to notice in Fig. (7.33)(b) that, at any time, air entrainment occurs near the nozzle in the same way as in the non-evaporating spray (note that the lower halves of the velocity field plots are the mirror images of the upper ones and they are presented in this way for the sake of clarity). The turbulent characteristics displayed in Figs. (7.33)(c) - (e) show, as in isothermal spray predictions, high values of turbulence intensities and high levels of turbulent viscosities.

The main noteworthy points in Figs. (7.33)(f) and (7.33)(g) are the evidence in the equivalence ratio contours of high evaporation rates near the tip of the spray and low rates near the nozzle. This is also clear from the close inspection of the droplet fields (Fig. (7.33)(a)) which reveals that, at later times,

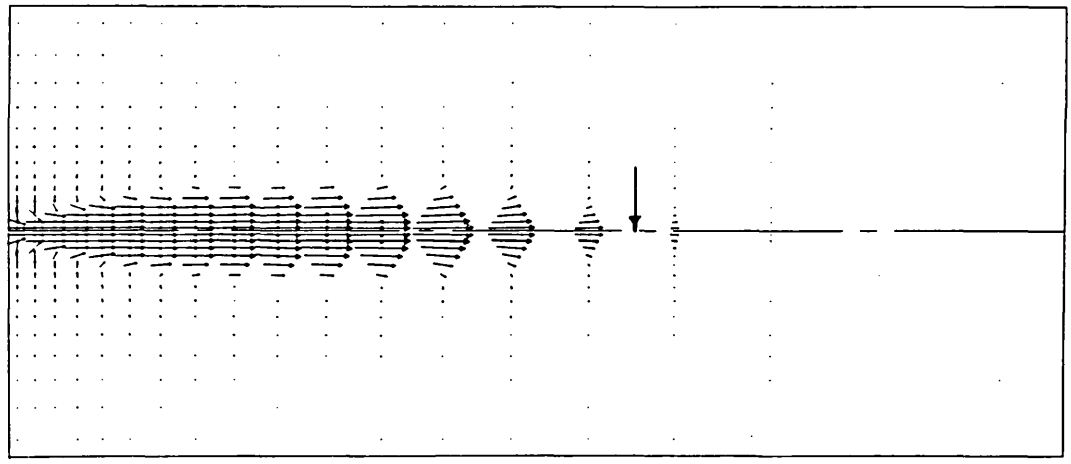


(a) Spray development

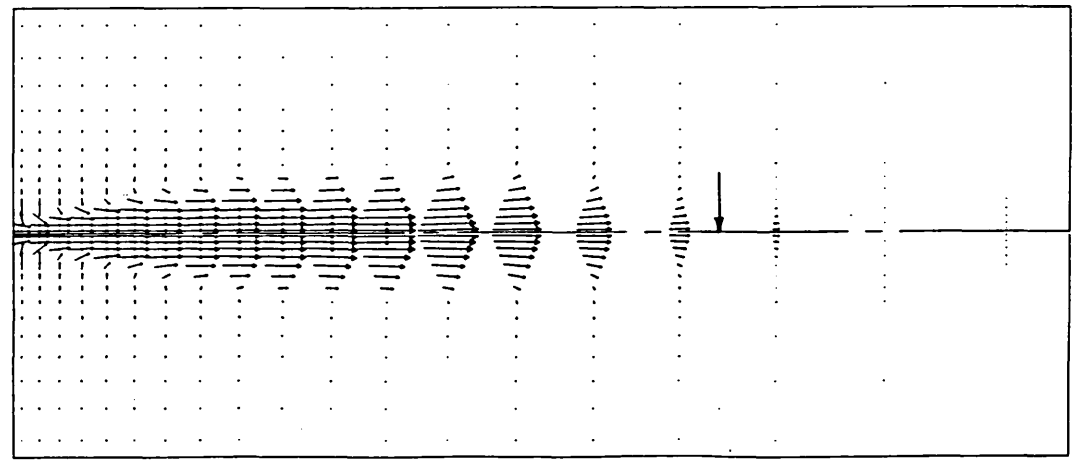
Fig. (7.33) Predicted field of droplets and gas characteristics (P = 6.28 MPa, T = 800 K)



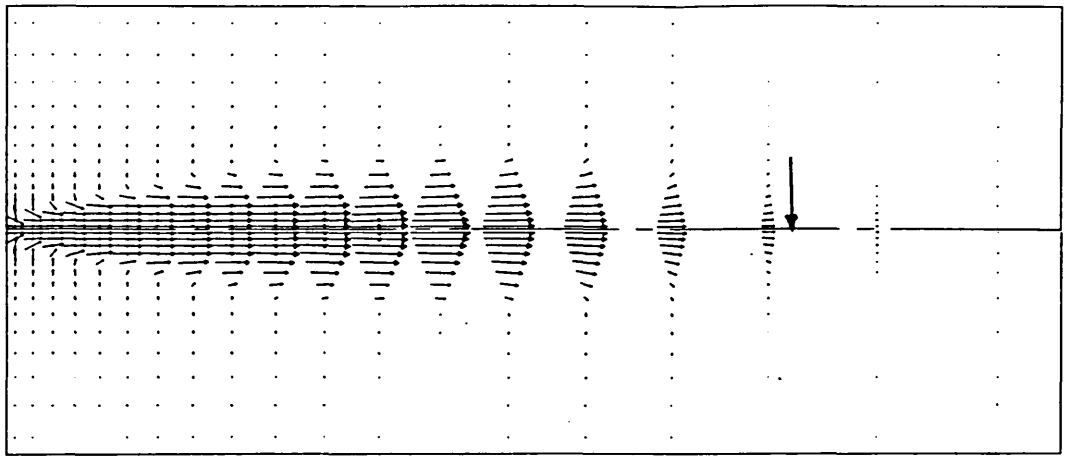
Time = 0.4 ms



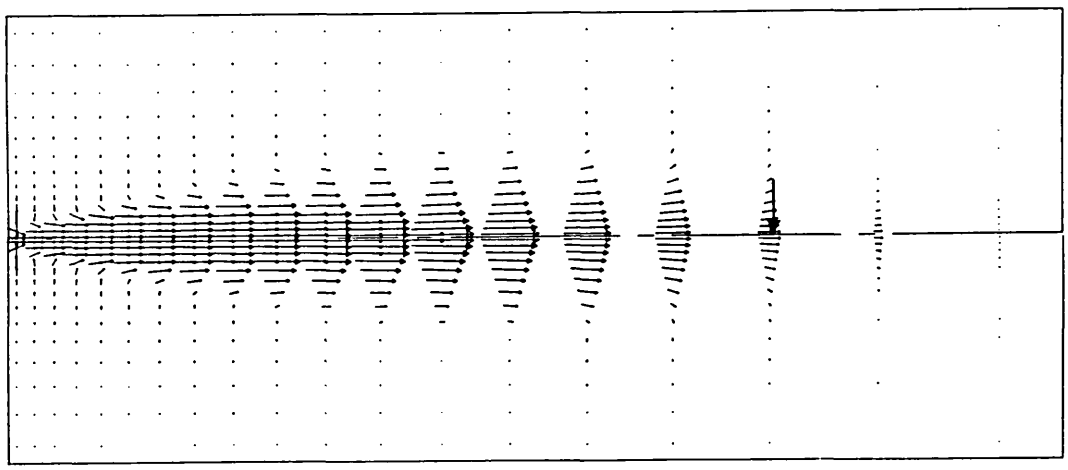
Time = 0.83 ms



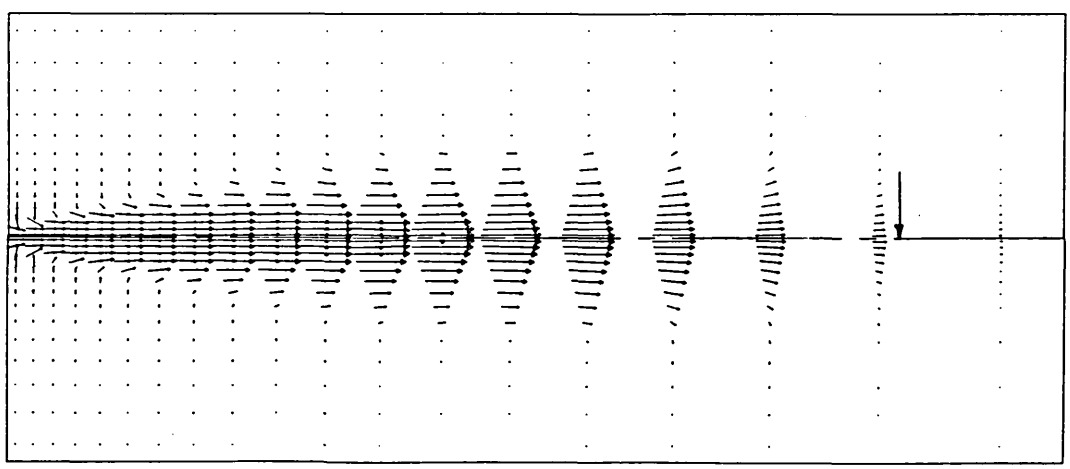
Time = 1.25 ms



Time = 1.66 ms



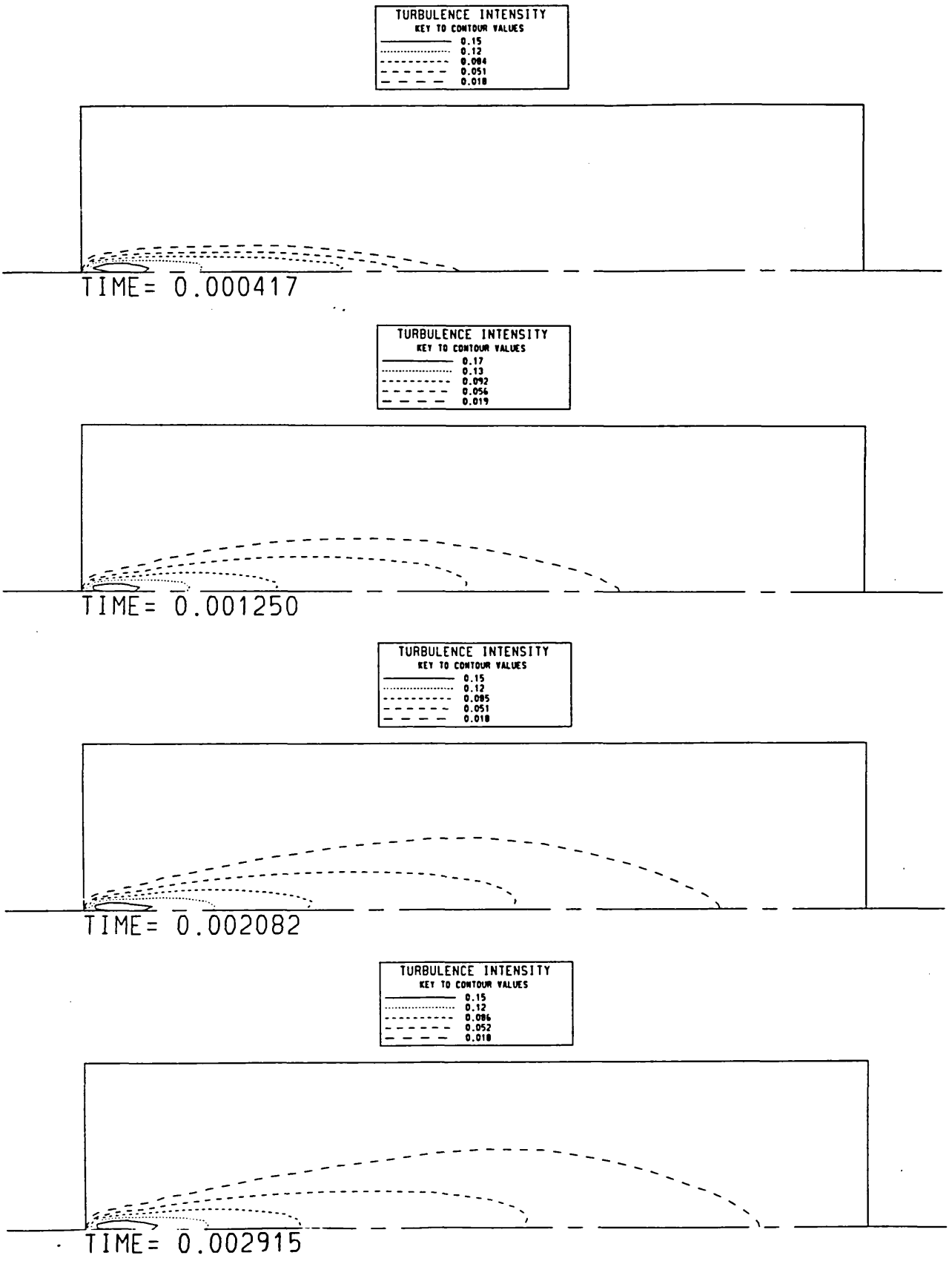
Time = 2.1 ms



Time = 2.5 ms

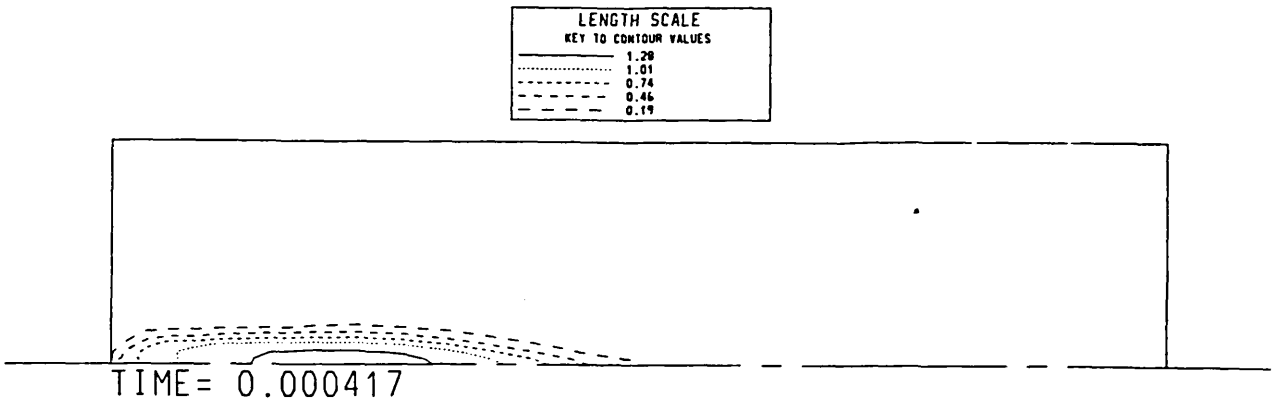
(b) Gas velocity field

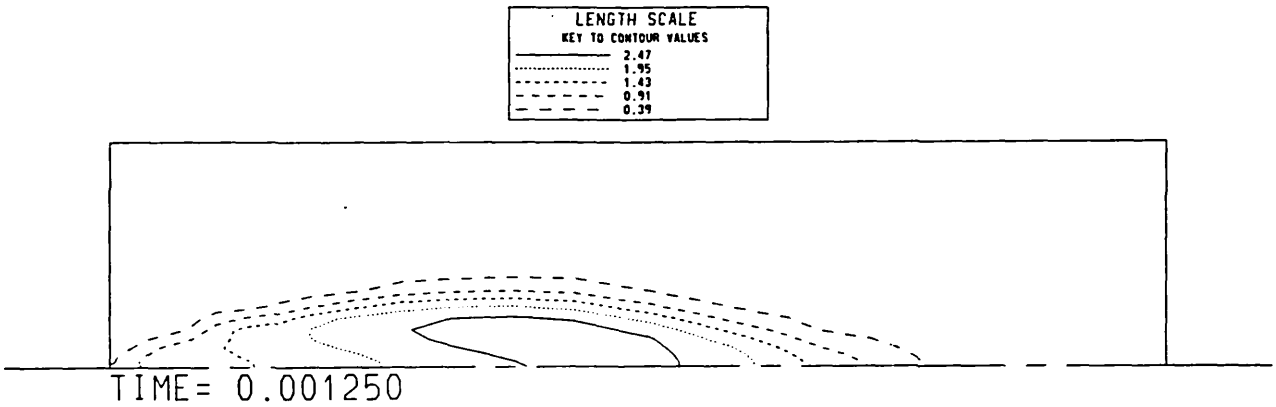
Fig. (7.33) Cont'd.

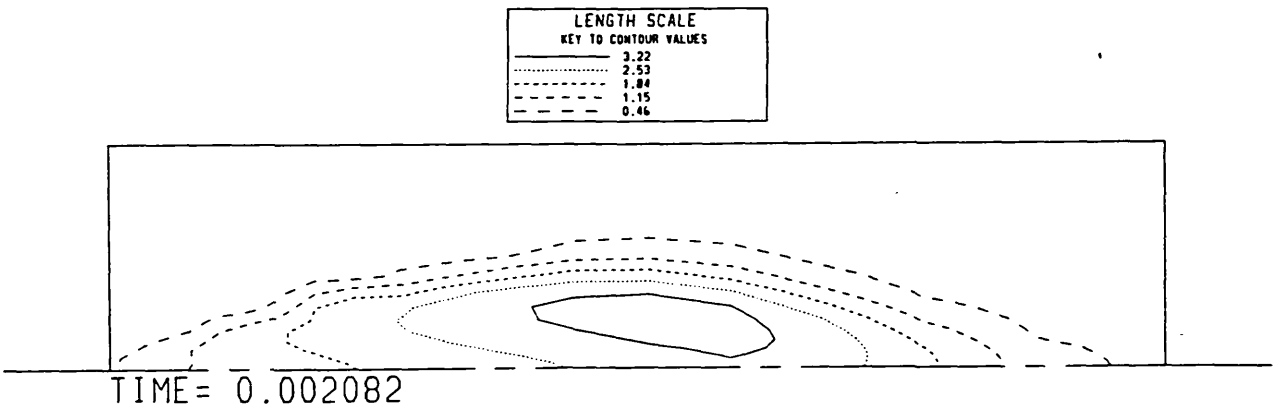


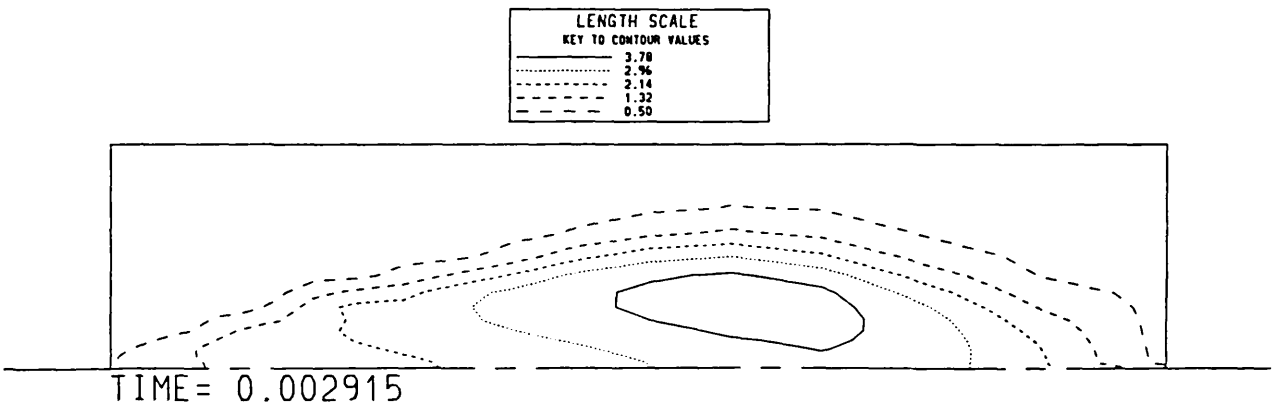
(c) Ratio of $\sqrt{\frac{2}{3}}\,k$ to introduction velocity (≡ 178 m/s)

Fig. (7.33) Cont'd.



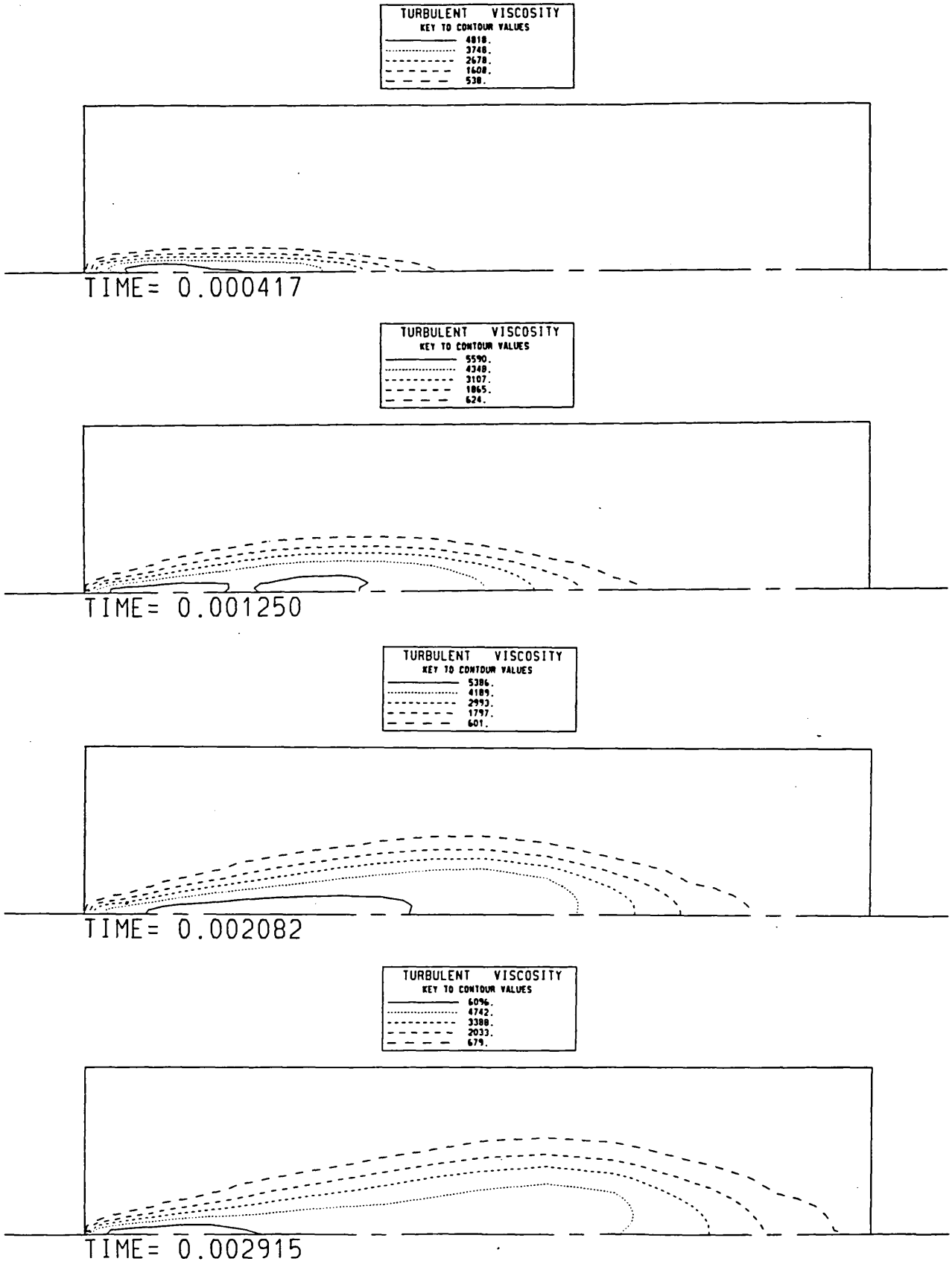






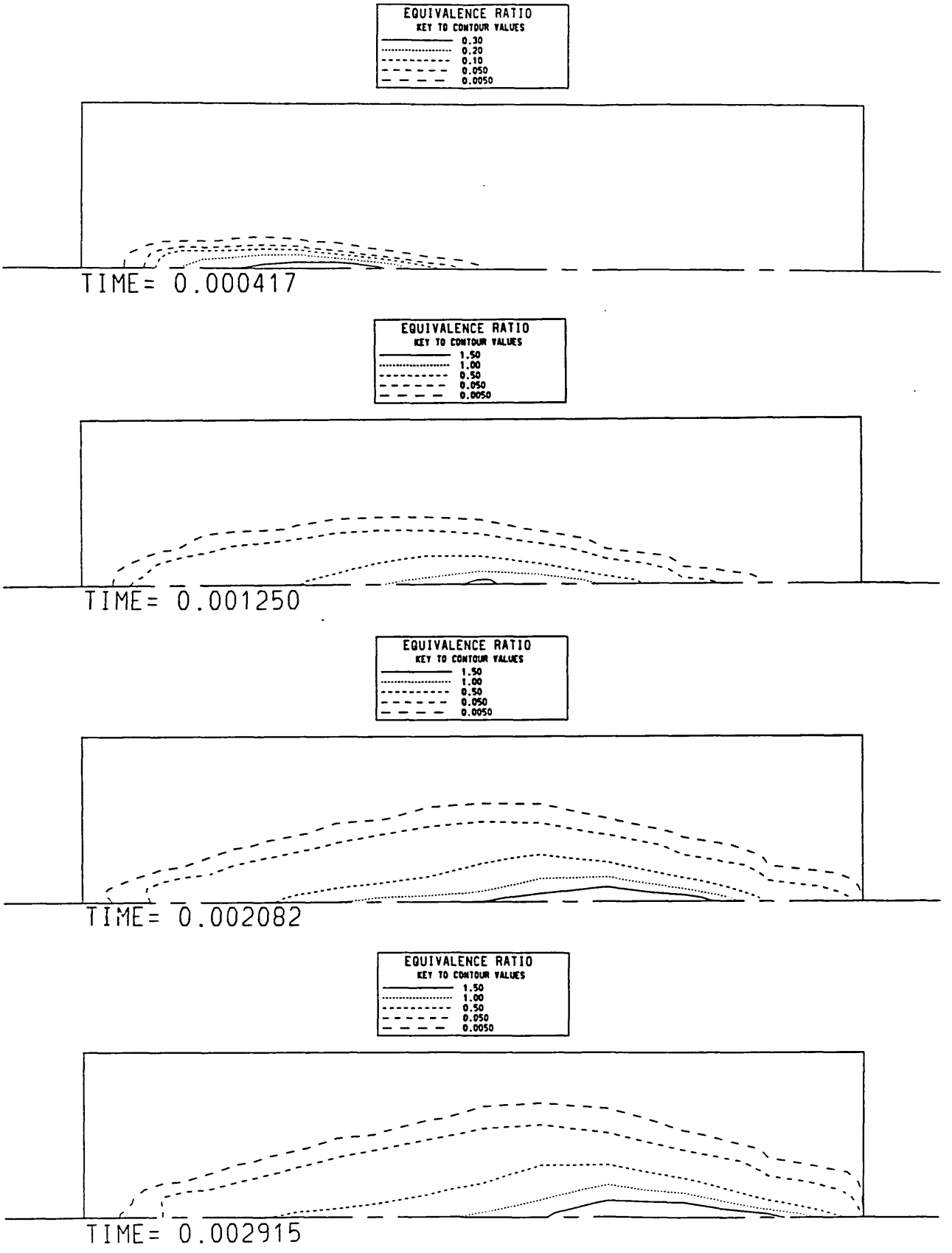
(d) Ratio of length scale to injector diameter

Fig. (7.33) Cont'd.



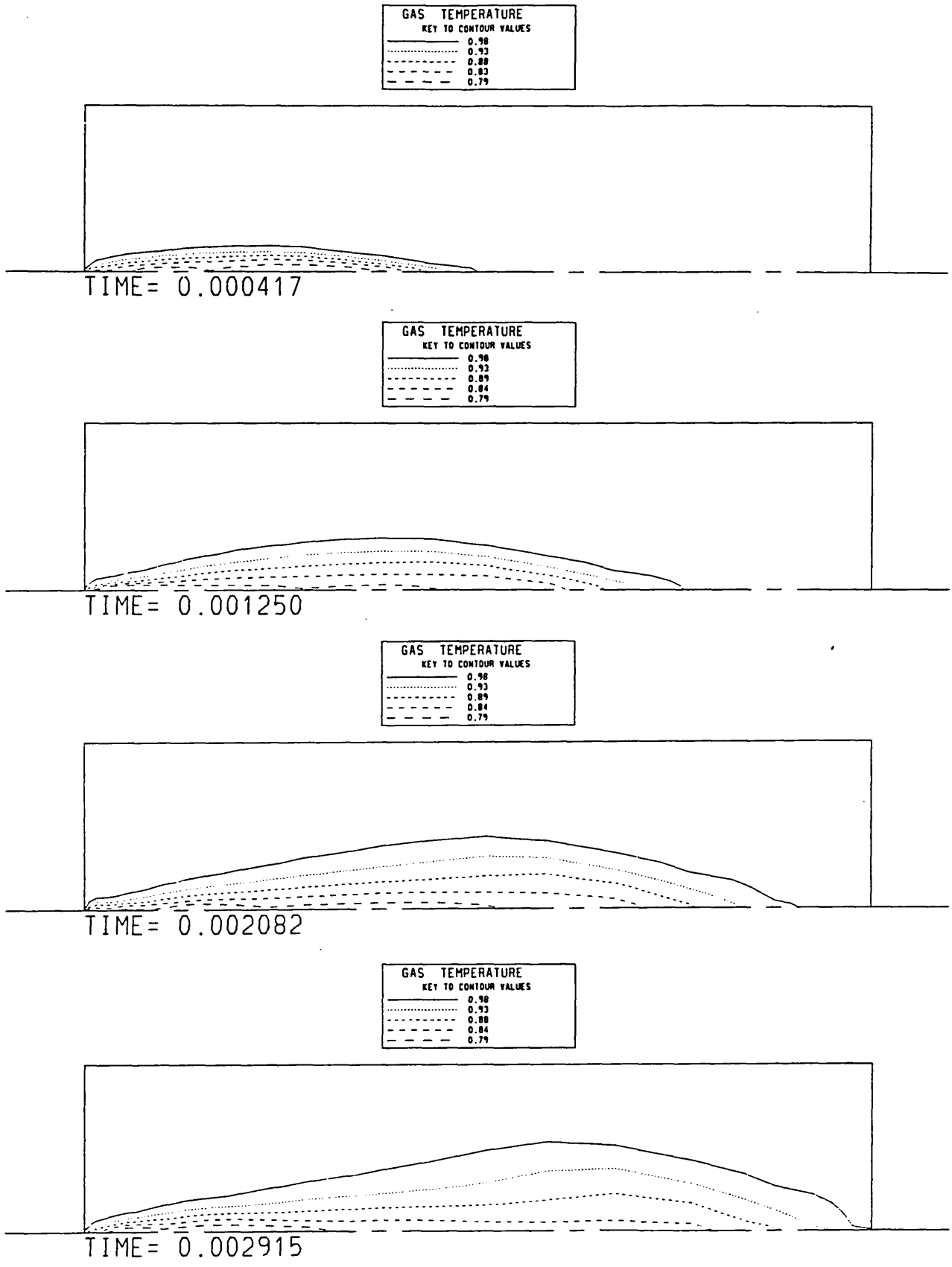
(e) Ratio of turbulent to molecular viscosity

Fig. (7.33) Cont'd.



(f) Ratio of the fuel vapour mass fraction to the stoichiometric ratio

Fig. (7.33) Cont'd.



(g) Ratio of the gas temperature to the ambient temperature (= 800 K)

Fig. (7.33) Cont'd.

there is a concentration of small droplet parcels (whose masses have been decreased due to evaporation) near the spray tip. This can be attributed to the fact that the droplets spend part of their flight time heating up from the low introduction temperature (288 K) where evaporation rate is very small. This explanation is supported by Fig. (7.33)(g); which displays the gas temperature contours normalized by the initial temperature (800 K) and indicates the cooling of the internal region of the spray by droplet heating and vaporization.

7.3.2 Parametric Study

Calculations were made to quantify the effects of the various inputs to the model on the spray tip penetration and vaporization rate histories. These include the fuel introduction temperature, the initial droplet sizes, the initial size distribution, the injection rate history and the injection velocity. For the purpose of comparisons, the case of the Kuniyoshi et al (1980) experiments where P = 6.28 MPa and T = 800 K is chosen, since it closely represents the actual engine conditions at the time of fuel injection. The various input parameters used in this parametric study is given in table (7.3).

Table (7.3) Input parameters of parametric study of evaporating spray

Run numbers	P MPa	T K	T_{d_o} K	d_j mm	D_{32} μm	Size distribution function	Injection rate diagram	Comments
1	6.28	800	288	0.3	25	Chi	Uniform	Base line
2	6.28	800	500	0.3	25	Chi	Uniform	Fuel introduction temperature effect
3	6.28	800	288	0.3	12	Chi	Uniform	Initial droplet sizes effect
4	6.28	800	288	0.3	25	R-R	Uniform	Size distribution effect
5	6.28	800	288	0.3	25	Chi	Trapezoidal	Injection rate history effect
6	6.28	800	288	0.24	25	Chi	Uniform	Injection velocity (injector diameter) effect

1. Fuel introduction temperature T_{d_o}

In all calculations reported earlier the fuel was assumed to enter at atmospheric temperature, taken to be 288 K. Here the effect of preheating, which may occur in practice, is assessed by increasing T_{d_o} to 500 K. The results are shown in Fig. (7.34)(a) and (b) displaying the droplet and vapour penetrations respectively and Fig. (7.35) showing the integrated evaporation rates. It should be noted that the temperature increase has two opposing effects:

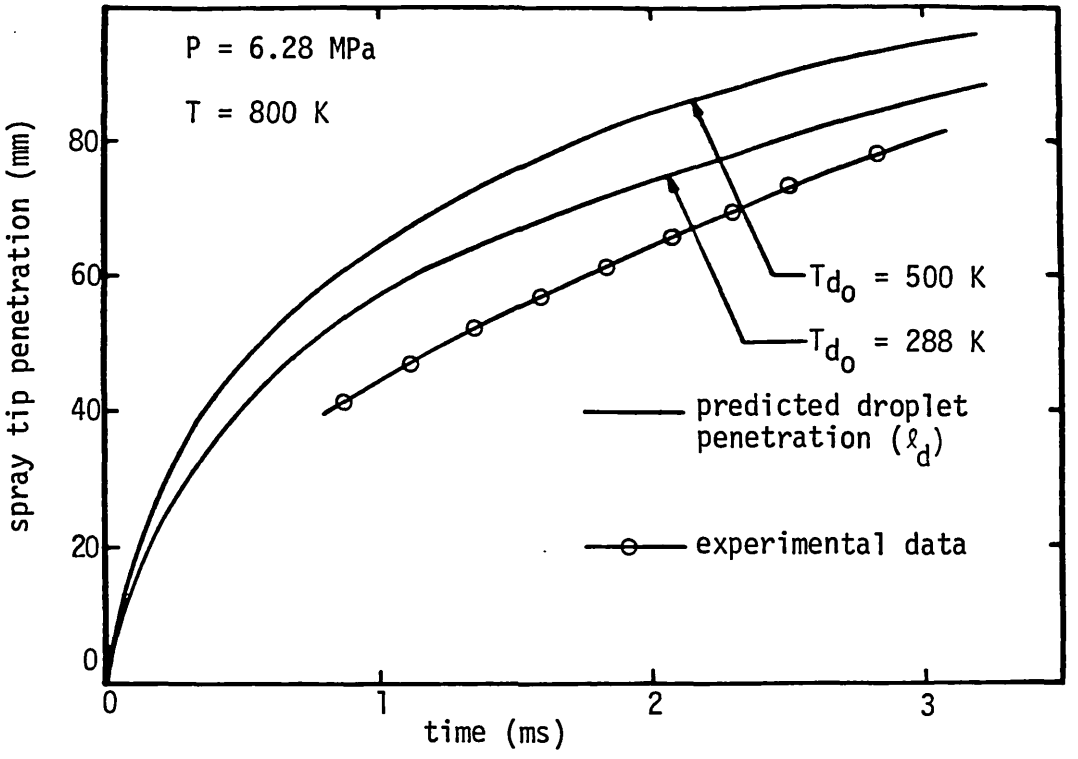
a. it reduces the heating up period; giving more time for the droplet to evaporate at high temperature, and thereby reducing droplet penetration.

b. It reduces the fuel density causing, for a given injection mass flow rate, higher injection velocities, which enhance spray penetration (c.f. section (7.2.3)). This in turn causes a further increase in the vaporization rate.

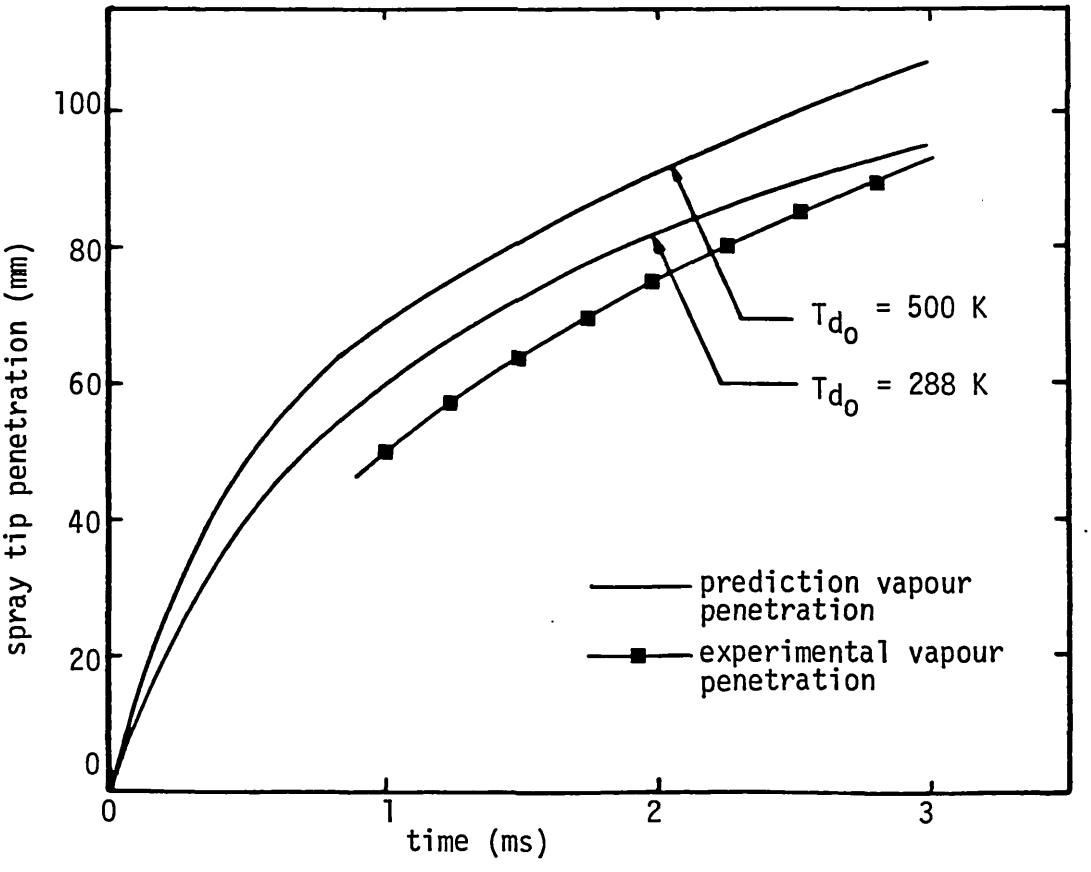
Figures (7.34)(a) and (b) show that the nett effect of increasing T_{d_o} is enhanced droplet and vapour penetrations.

The increase in vaporization rate shown in Fig. (7.35) can also be explained in terms of the above effects. (The individual effect of increasing the injection velocity will be isolated and dealt with later in this section).

Figures (7.36) and (7.37) display the axial and radial profiles of the equivalence ratio and gas temperature at t = 3 ms from the start of injection, corresponding to runs 1 and 2 of table (7.3). It is clear from Fig. (7.36) that as noted earlier,



(a) droplet penetration



(b) vapour penetration

Fig. (7.34) Effect of droplet introduction temperature on spray penetration

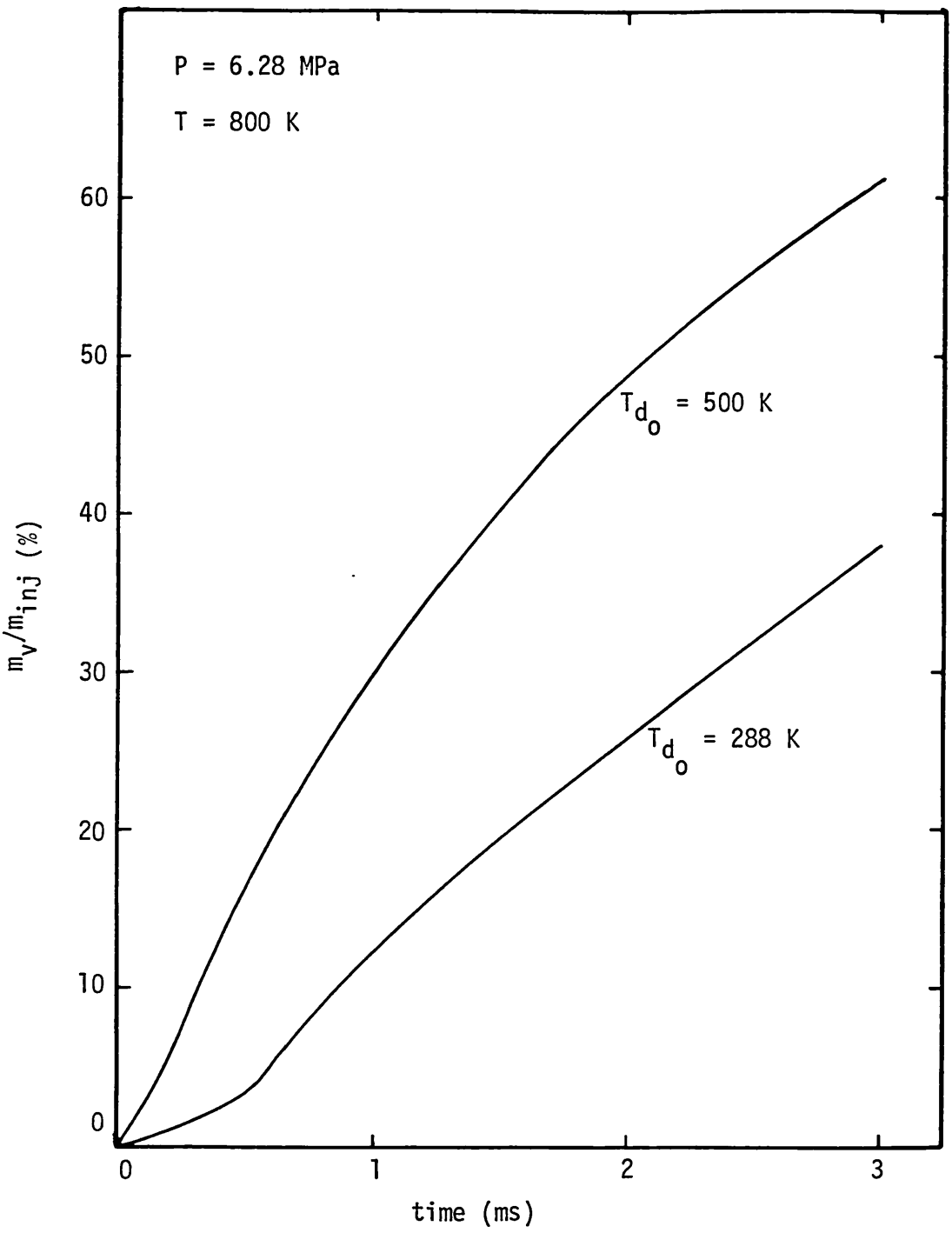


Fig. (7.35) Effect of droplet introduction temperature on the spray vaporization rate

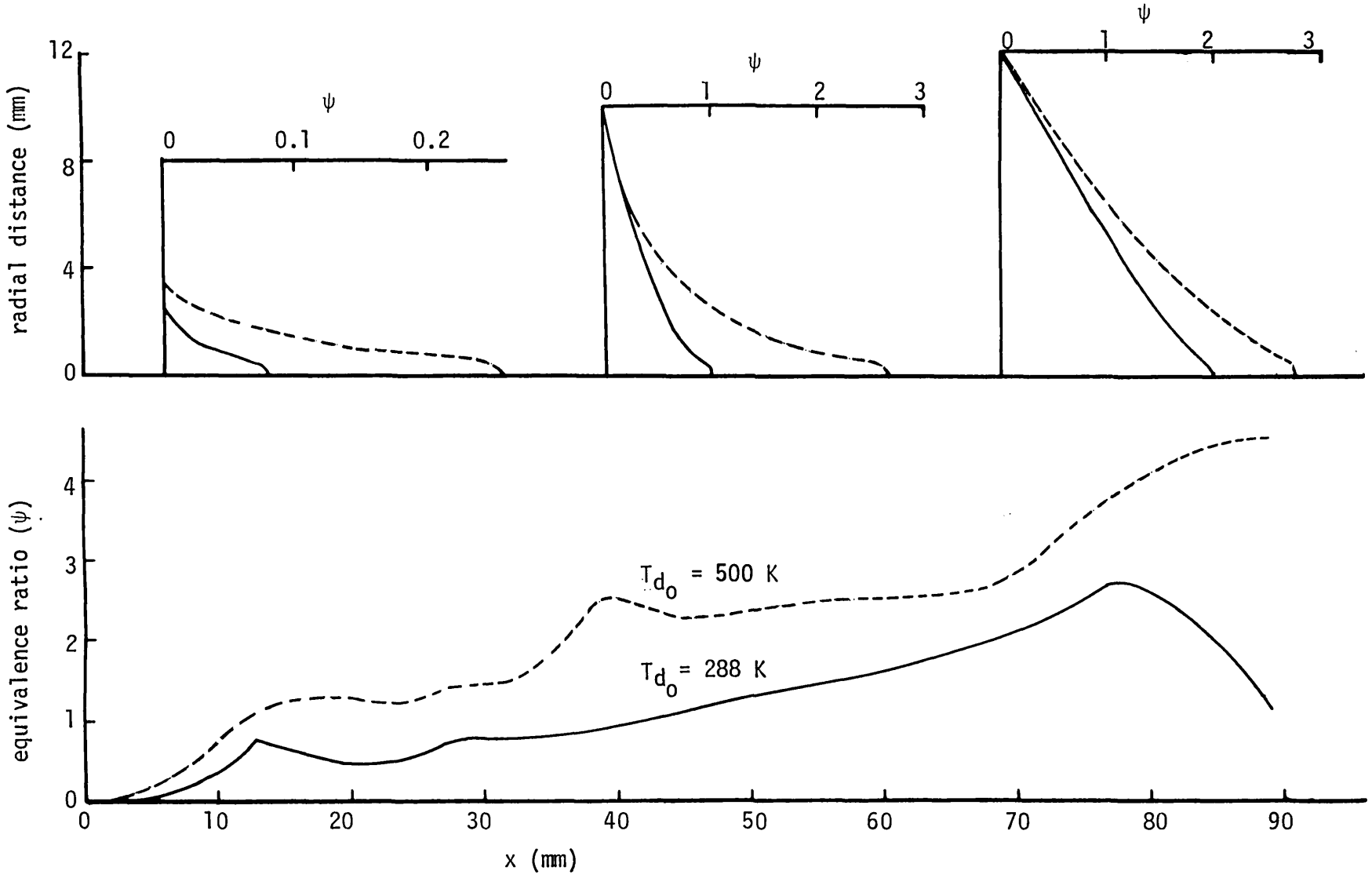


Fig. (7.36) Effect of droplet introduction temperature on the equivalence ratio (profile and distribution) at t = 3 ms. (P = 6.28 MPa, T = 800 K)

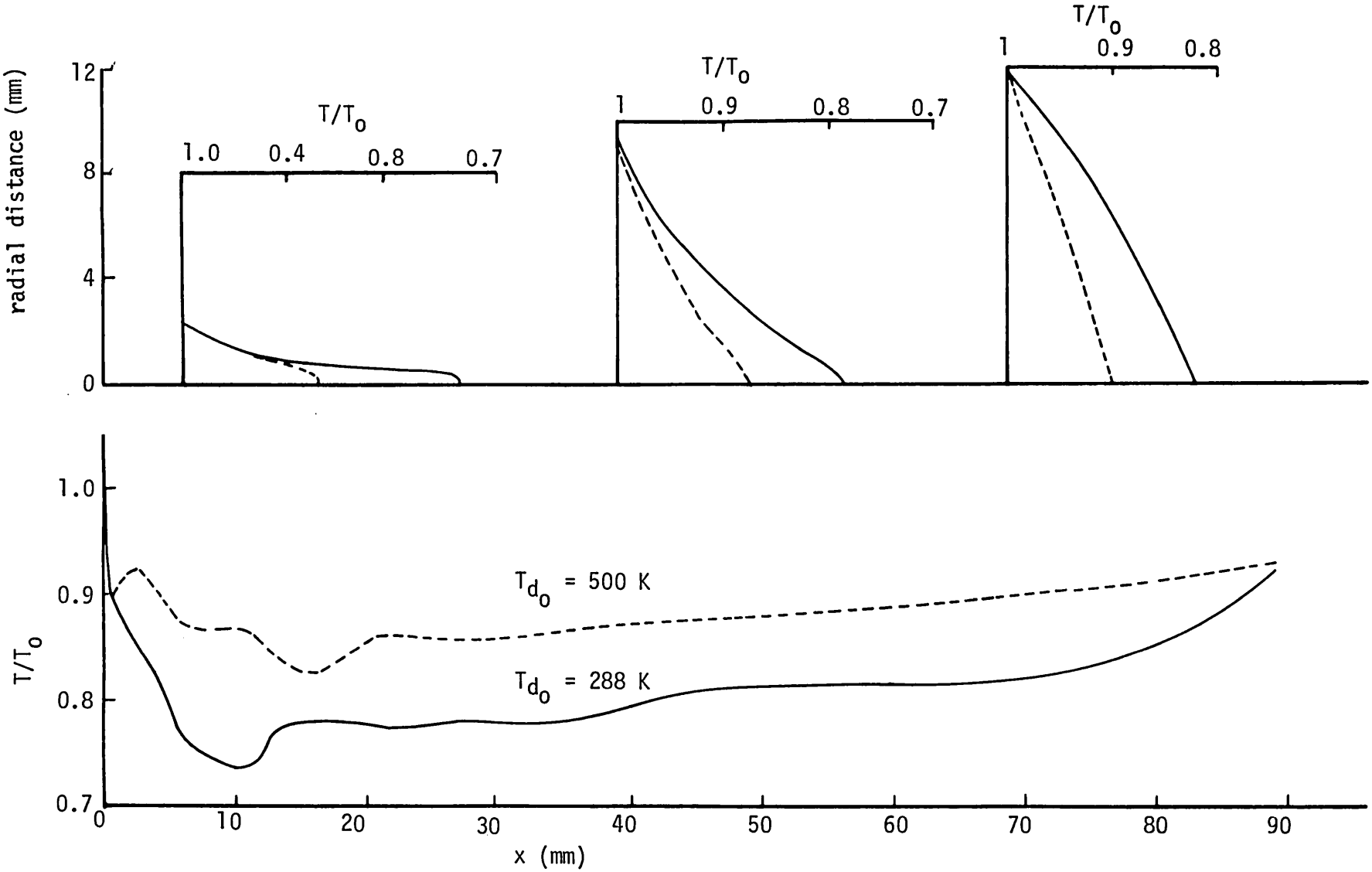


Fig. (7.37) Effect of droplet introduction temperature on the gas temperature at t = 3 ms.

(P = 6.28 MPa, T = 800 K)

the amount of vaporization of the droplets near the injector is less than that near the tip of the spray i.e. as the droplets are injected into the chamber, the liquid fuel is carried downstream before considerable evaporation takes place. This is clear from Fig. (7.37), which shows that the gas temperature decreases near the injector (due to the heat transfer to the relatively cold droplets) after which both gas and droplet temperatures reach an equal value. It should also be noted that the level of gas temperature for T_{d_o} = 500 K is higher than that corresponding to T_{d_o} = 288 K, which contributes to the higher evaporation rate.

2. Initial mean droplet size

Calculations were performed to investigate the effect of the initial mean droplet size to test the sensitivity to the assumption that the measured downstream droplet sizes can be used to represent those generated in the vicinity of the injector. For computational purposes, the Chi size distribution is retained and the Sauter mean diameter is reduced from D_{32} = 25 μm (Run 1) to 12 μm (Run 3). The outcomes are plotted in Figs. (7.38) and (7.39).

The droplet and vapour penetration histories displayed in Fig. (7.38) show that smaller droplet sizes result in a smaller penetration, as was also observed for isothermal sprays in section (7.2.3). The reduction here at t = 0.8 ms is about 6% as compared to about 4% for the isothermal case. This larger effect can be attributed to faster evaporation for the small droplets, as will be explained below.

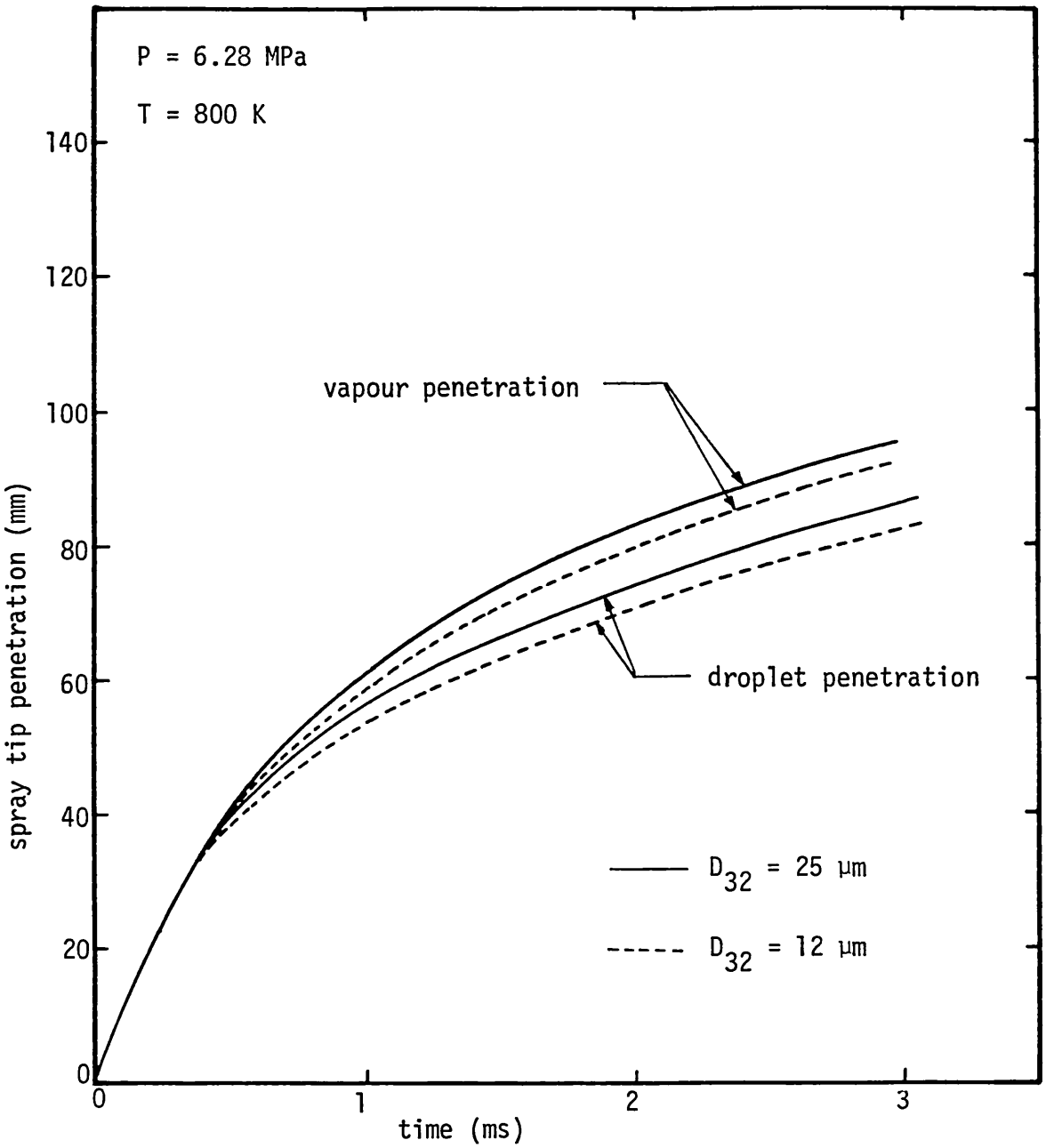


Fig. (7.38) Effect of droplet sizes on spray tip penetration of evaporating spray

Figure (7.39) illustrates the integrated evaporated masses for the two droplet size ranges considered. This figure is very significant in showing that the smaller droplets produce substantially higher rate: e.g. at t = 3 ms from the start of the injection, the total vaporization increases from 38% of the injected liquid for D_{32} = 25 μm to 60% for D_{32} = 12 μm. This can be attributed to the fact that smaller droplets heat up faster than the larger ones*, and once again the associated rapid increase in surface vapour concentration overshadows other effects.

3. Initial size distribution function

The influence of the initial size distribution is examined by performing the calculations using the two size distribution functions illustrated in Fig. (7.23) with the Sauter mean diameter equal to 25 μm corresponding to Run 1 and Run 4 of table (7.3).

Figure (7.40) shows a comparison of the droplet and vapour penetrations for the two distributions and as might have been expected, the Rosin-Rammler version gives slightly slower penetration, because it contains a higher proportion of finer droplets. For the same reason, the Rosin-Rammler distribution results in a higher evaporation rate as shown in Fig. (7.41).

*It can be shown from the droplet energy equation (3.73) that $\frac{dT_d}{dt} = \frac{f_1}{D_d} + \frac{f_2}{D_d^2}$, where f_1 and f_2 are functions of the film properties.

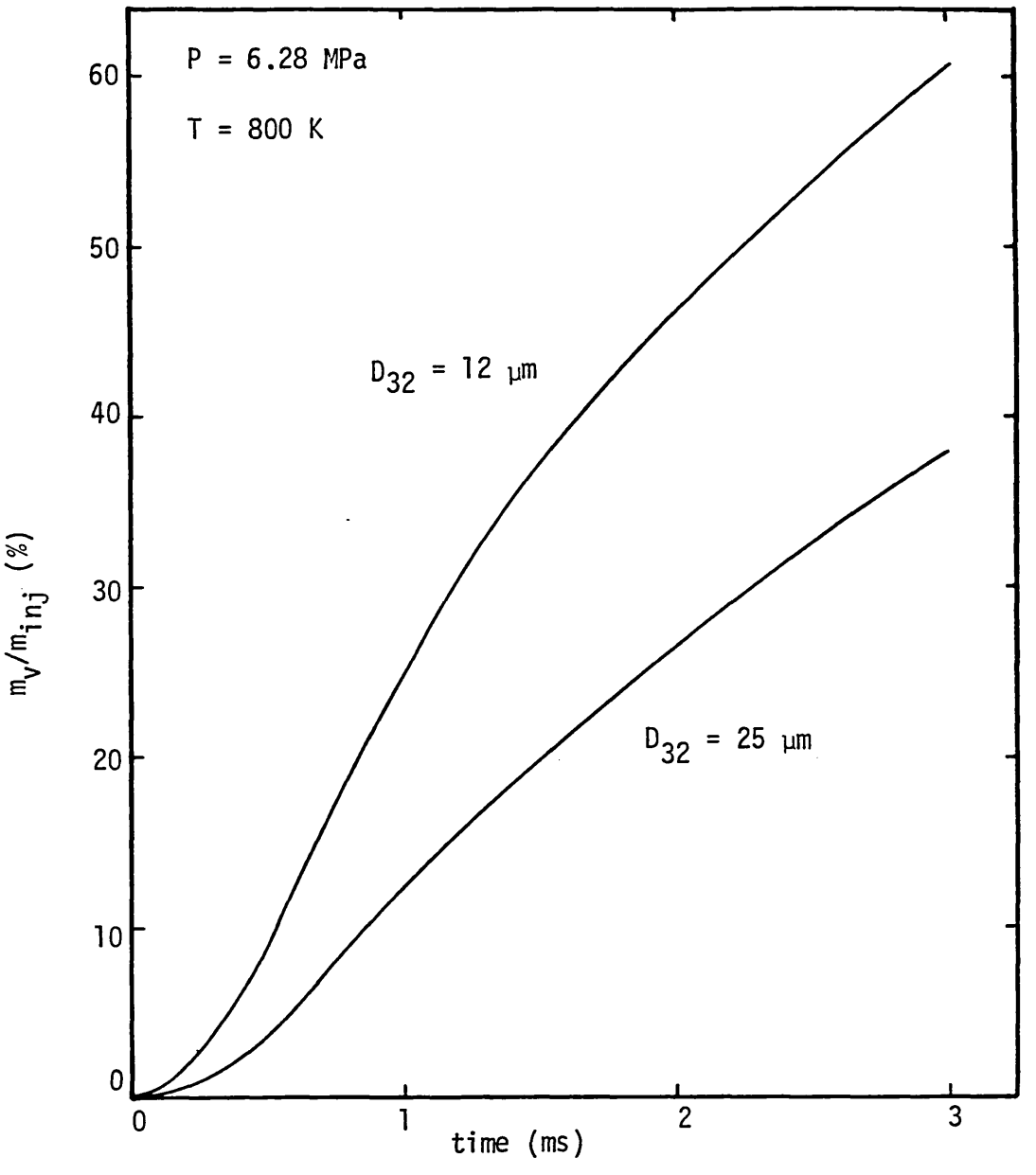


Fig. (7.39) Effect of initial droplet sizes on the vaporization rate

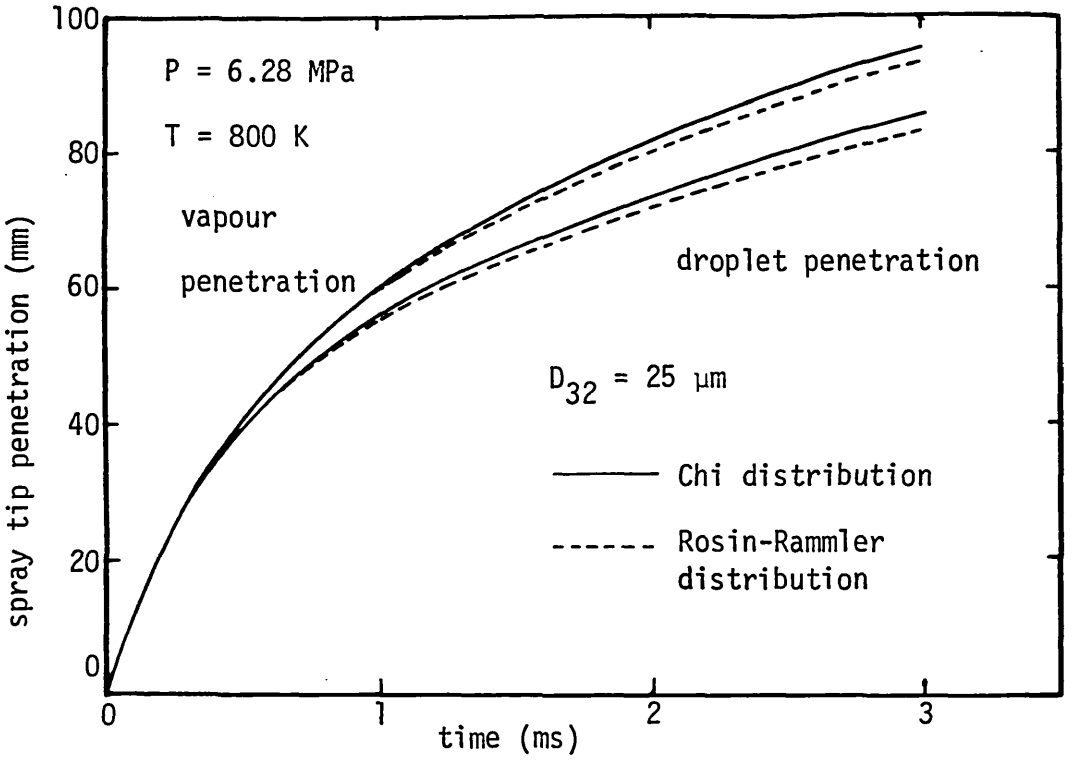


Fig. (7.40) Effect of droplet size distribution function on spray tip penetration

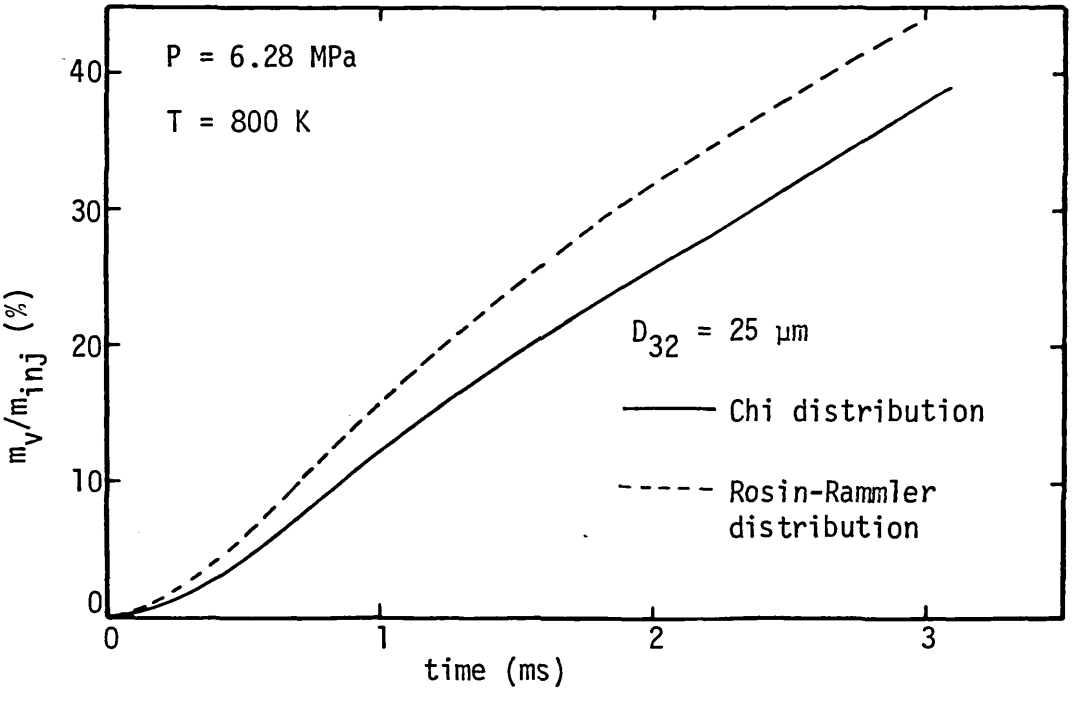


Fig. (7.41) Effect of droplet size distribution function on the vaporization rate

4. Injection rate history

Calculations were performed to explore the effect of the injection rate history using the two rate diagrams depicted in Fig. (7.42). The constant rate case (Run 1) closely resemble the measured one (Kuniyoshi et al (1980)) up to t = 3 ms from the start of injection and the hypothetical trapezoidal diagram (Run 5) produces, as the constant rate diagram, the measured total mass of fuel injected over the pulse duration (9 ms).

The penetrations for the two histories are plotted in Fig. (7.43) from which it is clear that the trapezoidal rate variation gives a drastic decrease in tip penetration in the early phase. This can be attributed to the reduced velocity (and hence momentum) of the injected droplets up to t = 1.25 ms from the start of injection. Note that the penetration rates (i.e. the slopes of the penetration curves) corresponding to the trapezoidal diagram are initially small and start to increase from t = 0.25 ms to t = 1.0 ms due to droplet overtaking, after which they start decreasing. However, the latter decrease is less than that exhibited by the constant injection rate case.

Figure (7.44) shows the integrated evaporated masses corresponding to the above two injection rate diagrams. The lower vaporization associated with the trapezoidal injection rate is attributed to the lower injection velocity which gives lower values of Reynolds number and hence lower values of Sherwood numbers.

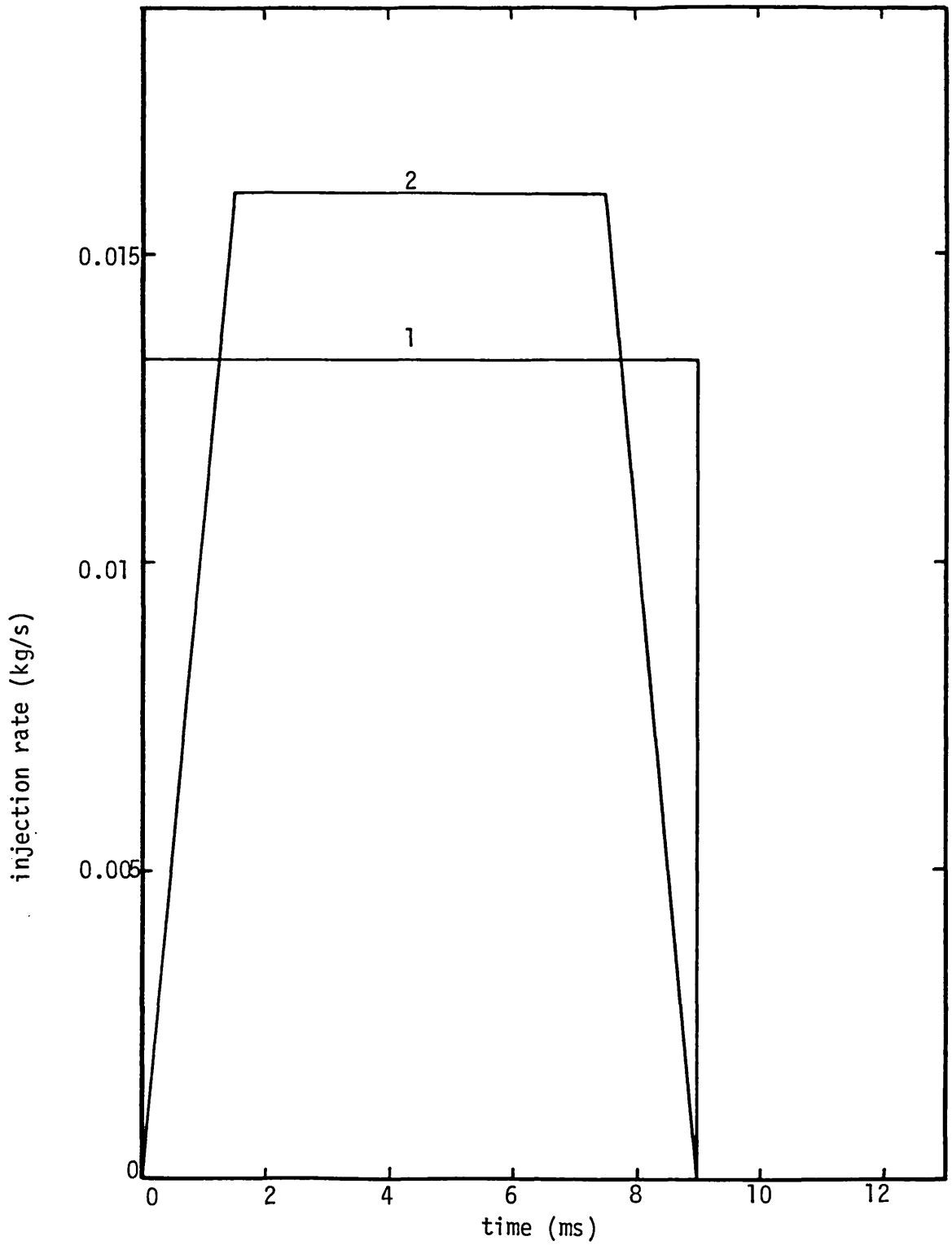


Fig. (7.42) The injection rate diagrams

1. Constant injection rate

2. Trapezoidal injection rate

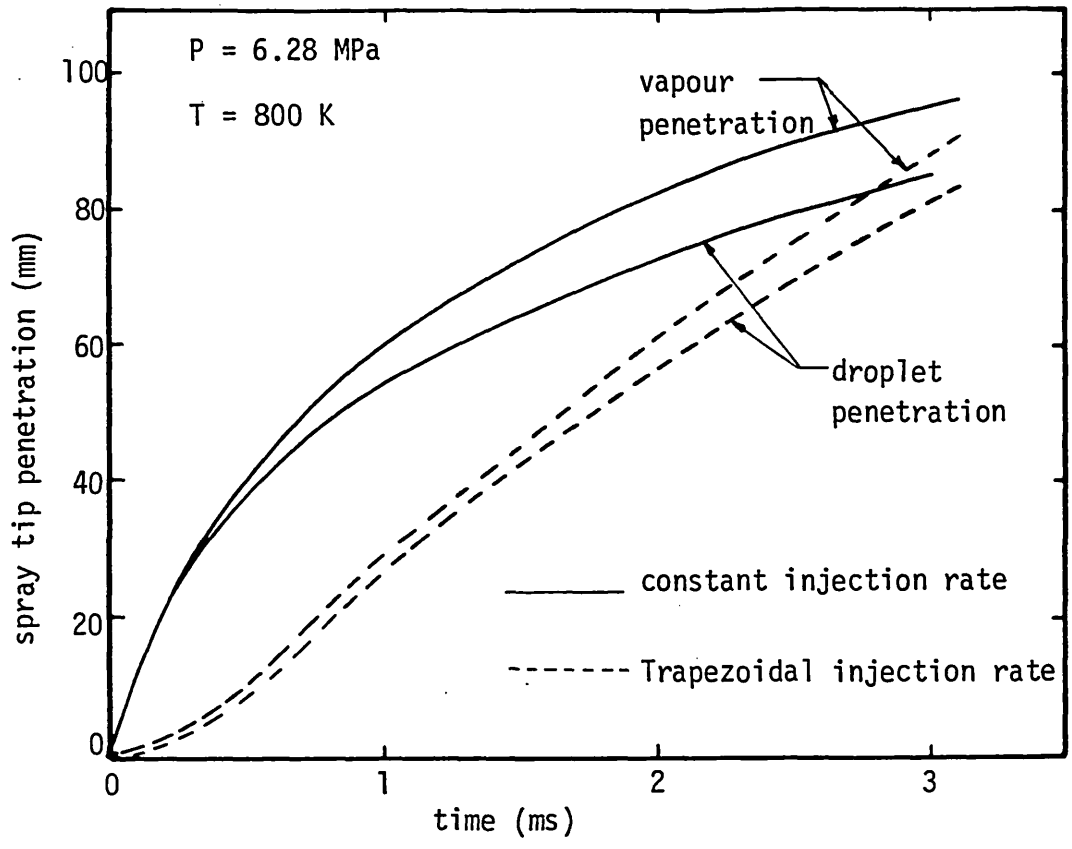


Fig. (7.43) Effect of the injection rate history on the spray penetration

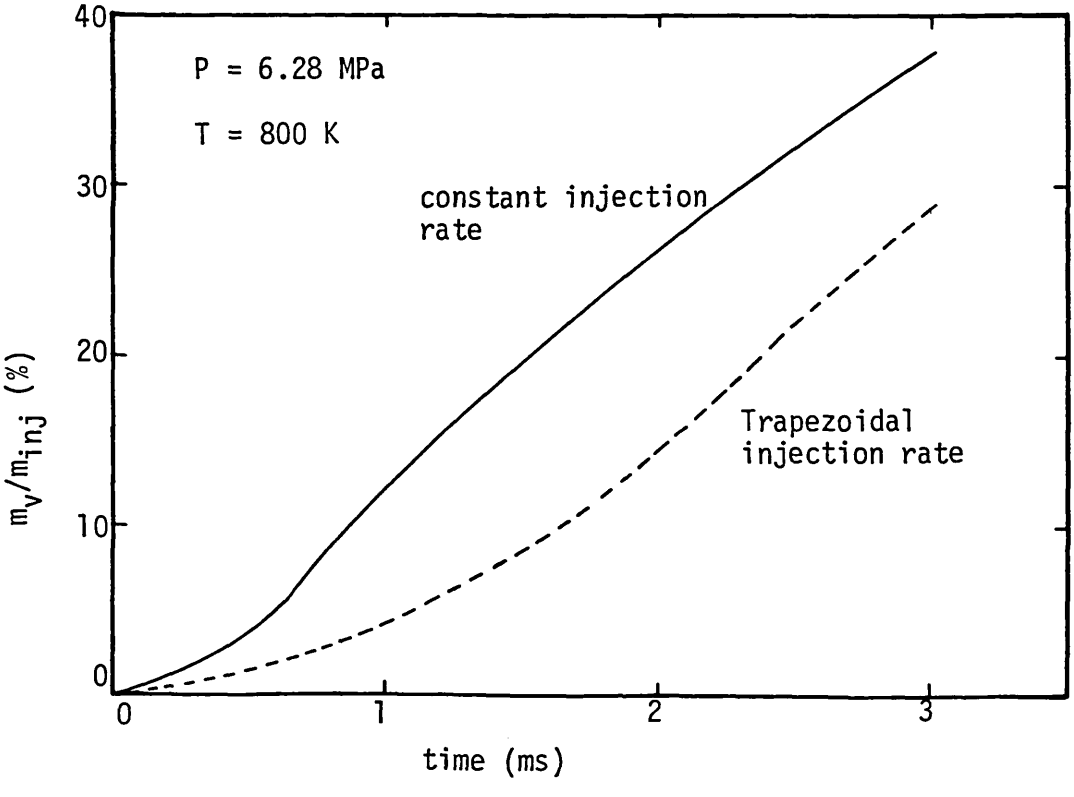


Fig. (7.44) Effect of the injection rate history on the vaporization rate

5. Injection velocity

Finally, the effect of the injection velocity was examined by performing calculations using nozzle diameters of 0.3 mm (Run 1) and 0.24 mm (Run 6) keeping the mass flow rate the same, in both cases.

Figure (7.45) shows the comparison between the droplet penetrations. The results indicate an increase with increasing injection velocity generated as would be expected. The vaporization rate is similarly augmented, as shown in Fig. (7.46).

Summary

From the above parametric study, the order of importance of the parameters influencing the vaporization rates of the non-isothermal sprays is written in descending order of importance as (i) fuel introduction temperature (being the most influential); (b) initial mean droplet size; (c) injection rate diagram; (d) initial size distribution and (e) injection velocity (being the least influential). The effects of those parameters on the spray tip penetration are given earlier in the summary of section (7.2).

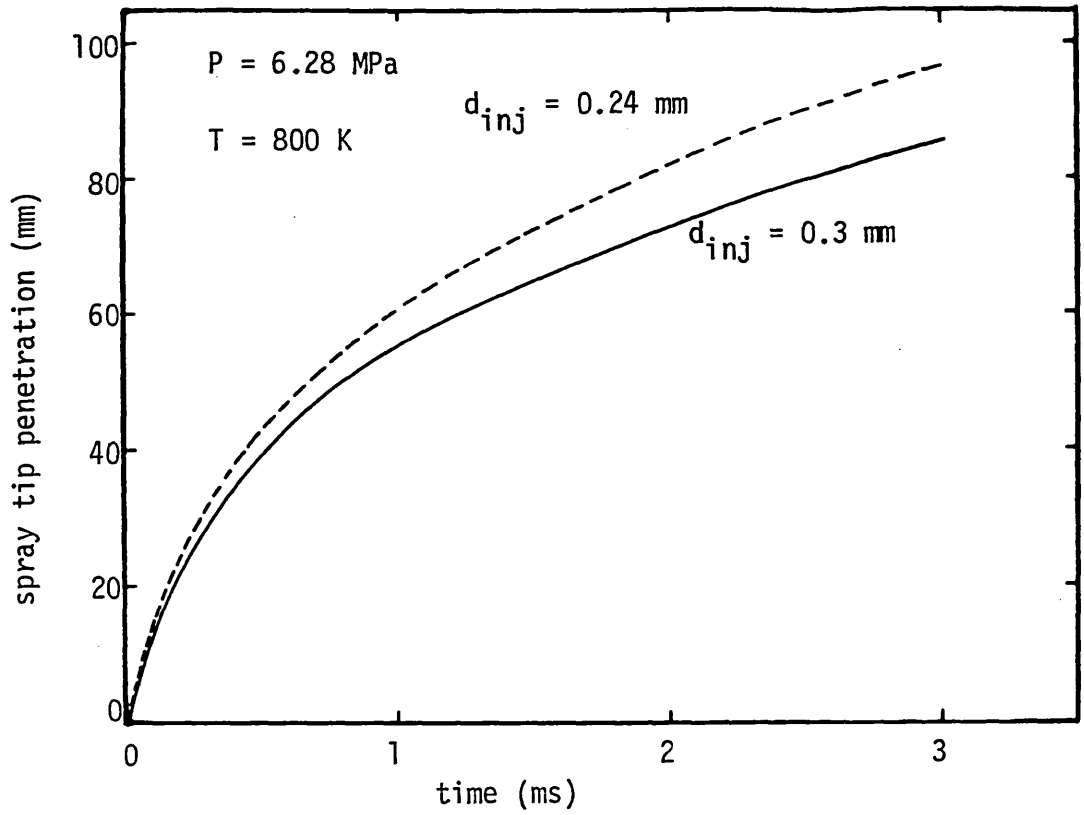


Fig. (7.45) Effect of the nozzle diameter (for the same mass flow rate) on the droplet penetration

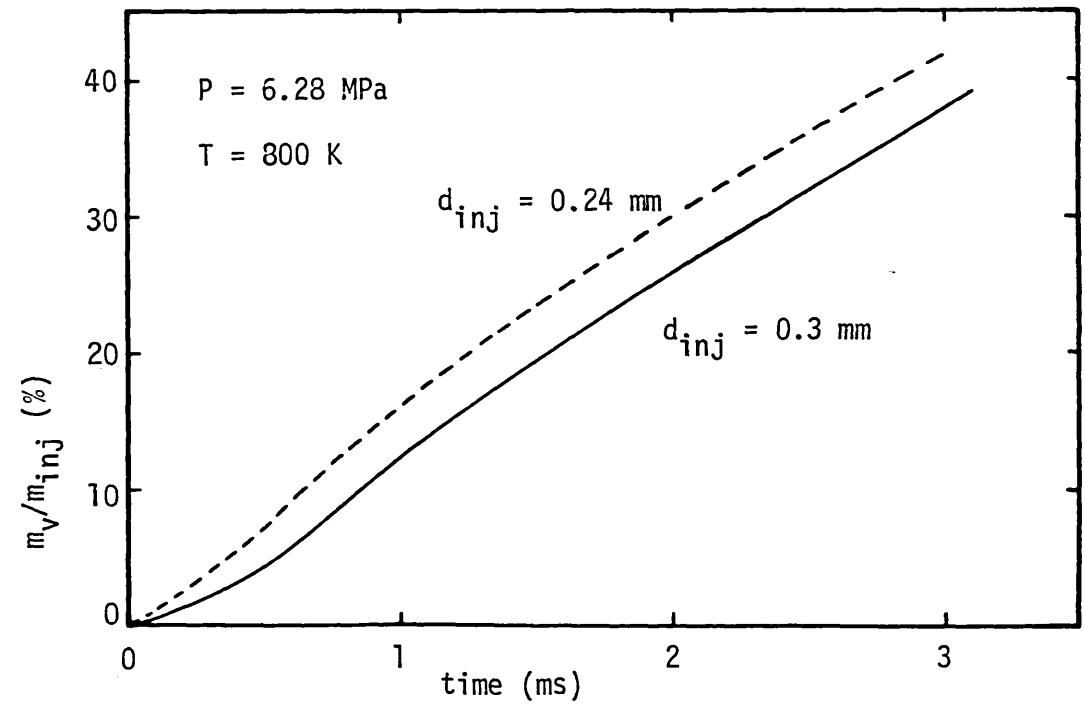


Fig. (7.46) Effect of the nozzle diameter (for the same mass flow rate) on the vaporization rate

7.4 Concluding Remarks

In this chapter the stochastic discrete droplet model has been applied and assessed against four sets of experimental data in which diesel fuel is injected into a chamber containing an inert gas at various pressures and temperatures.

The assessment of the procedure against the experiments of Yule et al (1985b) confirms the necessity to include a 'ligament' and 'break-up' regimes in the model for the low pressure cases to match the experimental observation, while the simulation of the evaporating spray of Kuniyoshi et al (1980) shows good qualitative and reasonable quantitative agreement with the measurements.

The results of the parametric study and sensitivity analysis reveal the following:

1. The spray shape depends mainly on the turbulent dispersion of the droplets and contrary to intuition, it is independent of the initial spray cone angle.
2. The factors which have the most appreciable effect on the spray tip penetration under isothermal conditions are: droplet injection velocity; injection rate history while other factors such as initial velocity profile of the droplets; initial spray cone angle; initial droplet sizes and size distribution, have a secondary (small) affect on penetration.
3. The total vaporized mass of non-isothermal sprays is appreciably influenced by; the fuel introduction temperature; initial mean droplet size and the injection

rate history while the initial droplet size distribution and the initial droplet velocities have smaller effect on the integrated vaporization rates.

CHAPTER 8

SUMMARY AND CONCLUSIONS

8.1 Summary of Achievements and Findings

A computational procedure has been developed to predict the unsteady behaviour of axisymmetric liquid sprays injected into a vessel containing quiescent inert gas at various pressures and temperatures. This has been achieved by solving (i) The Eulerian differential equations governing the conservation of mass, momentum and energy of the gas phase and the transport equation of the mass fraction of the vapour component of the gas. The two-equation k-ε turbulence model has been used to model the Reynolds stresses and the turbulent fluxes. (ii) The Lagrangian ordinary differential equations for the trajectory, velocity, temperature and size of individual droplets passing through and interacting with the gas phase. Each computational droplet represents a 'parcel' of spherical non-interacting droplets possessing the same size, velocity, temperature and position. The droplet equations have been combined with the gas-phase equations to enable simultaneous solution for the gas and droplet velocities. A method has been developed to solve the droplet mass and energy equations simultaneously. Turbulent droplets dispersion has been modelled in a stochastic way in which the instantaneous gas velocity within an eddy and the turbulent interaction time have been obtained from the mean gas velocity, turbulent kinetic energy and its dissipation rate. Furthermore, a provision has been made to improve the accuracy

of the spray calculation (to prevent it from producing non-physical overshooting or undershooting) results, by combining the momentum and continuity equations of the gas phase.

The accuracy and reliability of a fully implicit scheme used for gas jet calculations have been examined and the effects of grid size and time step on its performance have been tested. The accuracy of the semi-implicit scheme used to obtain gas-phase properties in the full spray calculations has been assessed by comparing its predictions with those of the fully implicit formulation for transient laminar and turbulent round free gas jets.

The accuracy and stability of the spray calculation procedure have also been examined. However, it must be stated that solutions independent of the effects of grid size could not be obtained since below some limiting cell size, the droplets cluster locally giving zero or negative void fractions. Under such conditions, the procedure fails to give physically stable solution, thus effectively puts a constraint on the minimum allowable cell size.

The main results of the assessment tests may be summarized as follows:

a. Gas Jets

The fully implicit numerical scheme has been applied to steady and transient laminar round free gas jets; steady and transient isothermal turbulent round gas jets and impulsively started non-isothermal turbulent jet.

The predicted steady state centreline velocity decay and the transient jet tip penetration of the incompressible impulsively started laminar round free gas jet were in a good agreement with

the experimental measurements of Abramovich and Solan (1973) and the characteristic length and time scales were $d_j Re$ and d_j/ν respectively, as recommended by Kuo and Bracco (1982a).

Comparison with Witze's (1980) measurements of steady and transient turbulent round free gas jets showed that the calculations were generally in reasonable agreement with the measurements although, on occasion, significant errors were observed and reasons have been suggested, in chapter 6, to account for the discrepancies. The length and time scales of the impulsively started turbulent jet have been obtained as $d_j Re^{0.053}$ and $d_j Re^{0.053}/U_o$ respectively, in accordance with the findings of Kuo and Bracco (1982a).

Finally, the transient calculation of Phillips (1971) turbulent hot jet produced satisfactory agreement, in spite of the uncertainty about the turbulence level at nozzle exit.

b. Sprays

The spray calculation method was assessed against four sets of data, all involving experiments in which diesel fuel is injected into a high pressure/high temperature chamber containing a quiescent inert gas. The predicted spray tip penetrations for the isothermal and evaporating sprays of Yule et al (1985b) were generally in qualitative agreement, although quantitatively, there were substantial differences especially at the low pressure case (P = 0.5 MPa). Some of the discrepancies could be ascribed to experimental error and to the difficulty of specifying the initial conditions for the droplets. The calculations of the evaporating sprays of Kuniyoshi et al (1980) produced the measured trend of increasing penetration with increasing temperature, however the

levels are over-estimated during the early stages of injection, where the discrepancies reached a maximum value of 20% at t = 1 ms from the start of injection. At later times the sets of curves approached each other, reducing the maximum discrepancies to only 5% at t = 3 ms.

The effects of the various parameters of the mathematical model on the behaviour of both isothermal and evaporating sprays were examined in chapter 7. The results of the computational and modelling sensitivity of the isothermal spray calculations showed that the penetration decreases with increasing the initial level of the turbulent viscosity while it increases when injecting the liquid with a power law velocity profile (but the two curves approach each other towards the middle of the injection period). The penetration was found to increase by only 6% when using half the measured spray cone angle and it was also found to be changed slightly when the turbulent droplets dispersion model was incorporated, although the spray shape did change appreciably (increasing the lateral spread of the spray).

The results of the parametric study on the isothermal spray behaviour revealed that the tip penetration is greatly increased by increasing the droplet injection velocity and using a constant injection rate diagram while increasing the initial droplet sizes from 10 μm to 50 μm produced only 7% increase in the penetration and the droplet size distribution has a minimum effect.

As far as the effects of the different parameters on the behaviour of the evaporating sprays are concerned, it was found that increasing the fuel introduction temperature increases both the levels

of the charge temperature and the fuel vapour mass fraction, enhances the penetration and appreciably increases the integrated vaporized mass. The initial mean droplet size and the injection rate history also have an appreciable effect on the vaporization rate while the size distribution function and the injection velocity have smaller effects.

8.2 Recommendations for Future Work

a. Droplet atomization and breakup

The spray calculations in the present study relies on the assumption that the spray is fully atomized and consists of spherical droplets. It also relies on the initial conditions ascribed to the individual droplets such as the droplet size and velocity distributions. Real progress towards the development of practical spray modelling procedures, useful for design, depends on the development of convenient methods of completely characterising the spray injection condition. Therefore, this point requires detailed measurements of the distributions of the droplet size and velocity at nozzle exit.

However, there is a growing body of evidence that sprays contain a liquid core surrounded by fully atomized regions. Comprehensive measurements at different pressures and temperatures are needed to clarify and assess this issue. As Yule et al (1985b) indicated that the photographs of the 0.5 MPa spray showed that it has a continuous central bulk liquid core extending over the first 40 mm from the

exit nozzle while the high pressure sprays have a dense and very poorly atomized core, adequate calculations of which necessitate the inclusion of breakup regime in the mathematical model (at least for the low pressure cases). This could be done by calculating the flow in the liquid core by a time-marching boundary layer procedure with a self-adjusting grid to conform to the nominal shape of the free surface. Instabilities of this liquid surface caused by air drag and other effects would have to be modelled, probably by some empirical approach, to give the initial sizes and velocities of the droplets formed.

b. Effect of droplets on turbulence

It seems intuitively reasonably that, in a turbulent flow, droplet inertial effects and fluctuating phase volume (void fraction) effects should influence the transport of turbulence energy, dissipation and scale. Droplet number density and size distribution are expected to be significant parameters in droplet/turbulence interaction. In the present study the form of the k-ε turbulence model employed does not contain any provision for the presence of the droplets. An attempt to model the effect of droplets on turbulence was performed by Buckingham et al (1981). They modified the k-ε turbulence model by considering added dissipation of droplet interactions in the governing equations for k and ε. The computations were not compared directly with measurements, however, the results suggested, as the complimentary experimental results for droplet laden flow, that droplets tend to damp turbulent motion primarily due to inertial effects. More extensive evaluation is required,

however, in order to adequately establish empirical coefficients appearing in terms representing droplet/turbulence interactions, which were employed in the model.

c. Limit on cell size

The present and previous Lagrangian formulation contain no provision for recognizing that an assembly of droplet parcels cannot occupy more volume than available and preventing overfilling of the cells. In situations where the injection cell radius falls below some limiting value the calculation scheme fails because the droplets cluster locally giving negative void fractions, which is non-physical. This is an important drawback, because it effectively prevents grid independent solution from being achievable and thereby introduces errors into the calculation. Overcoming this drawback represents useful avenues for research.

d. Evaporation at elevated pressures

At high charge pressures such as those encountered in diesel engines at the time of injection, a higher vapour pressure at the droplet surface is required to provide a given fuel mass fraction. Therefore, the boiling temperature during evaporation increases as the ambient pressure increased. Eventually conditions are reached where a drop approaches or exceeds its thermodynamic critical point during its lifetime. Near the critical point, several aspects of the conventional low pressure model must be modified; the solubility of the liquid phase for the ambient gas increases (at the critical condition itself all characteristics of both phases are the same;

temperature, enthalpy, pressure and composition); the radial regression velocity of the liquid surface becomes comparable to the radial gas velocity since the densities of the two phases are the same and liquid circulation and droplet secondary breakup become important due to reduced values of surface tension (Faeth (1977)).

Also required are detailed measurements of the thermodynamic properties of the diesel fuel at high charge pressure and temperature.

e. Ignition and combustion

The modelling of spray combustion must be prerequisited by modelling of the ignition process. It is well known from high-speed photography (Shiozaki et al (1980)) that combustion is often initiated simultaneously in different regions of the cylinder and a model that claims to be realistic must therefore allow for this. Also, the combustion model should allow for the effects of both the chemical kinetics and the rate-of-mixing of the fuel and oxygen on the rate of reaction. The time taken from the start of fuel injection until a detectable combustion is known as the ignition delay. It is thought to consist of a physical delay; during which spray evaporates and mixes with the surrounding air, and a chemical delay; in which time the fuel undergoes complex chemical reactions. Analysis of both delays is complicated by the fact that the two overlap. Hence, the ignition model should incorporate both the chemical and physical components of the delay period.

REFERENCES

Abbas, A.S., Koussa, S.S. and Lockwood, F.C. (1980)
"The Prediction of the Particle Laden Gas Flows"
18th Symp. (Int.) on Combustion, William and Wilkins Co.
Baltimore, pp. 1427-1438.

Abbas, A.S., Lockwood, F.C. and Koussa, S.S. (1981)
"The Prediction of a Variety of Heavy Oil Flames"
ASME 81-WA/HT. - 48.

Abramovich, S. and Solan, S. (1973)
"The Initial Development of a Submerged Laminar Round Jet"
J. Fluid Mech., vol. 59, part 4, pp. 791-801.

Anderson, T.B. and Jackson, R. (1967)
"A Fluid Mechanical Description of Fluidized Beds"
Ind. Eng. Chem. Fundamentals, vol. 6, pp. 527-534.

Bendat, J.S. and Piersol, A.G. (1967)
"Measurement and Analysis of Random Data"
Wiley, New York.

Bergwerk, W. (1959)
"Flow Pattern in Diesel Nozzle Spray Holes"
Proc. Instn. Mech. Engrs., vol. 173, No. 25, pp. 655-660.

Bermhorst, K. and Harch, W.H. (1977)
"Near Field Velocity Measurements in a Fully Pulsed Subsonic Air Jet"
Symp. of Turb. Shear Flows, Penn. State Univ. Park.

Bilger, R.W. (1975)
"A Note on Favre Averaging in Variable Density Flows"
Comb. Science and Tech., vol. 11, pp. 215-217.

Bird, R.B., Stewart, W.A. and Lightfoot, E.N. (1968)
"Transport Phenomena"
John Wiley & Sons Inc.

Borman, G.L. and Johnson, J.H. (1962)
"Unsteady Vaporization Histories and Trajectories of Fuel Drops Injected into Swirling Air"
SAE 598C National Powerplant Meeting.

Borodin, V.A., Dityakin, Yu F., Klyachko, L.A. and Yagodkin, V.I. (1967)
"Atomization of Liquids"
Izd-VO Mashinostroenie Moscow.

Boulderstone, R., Ahseng, C., Yule, A.J., Felton, P.G. and Chigier, N.A. (1981)
"The Structure of Diesel Injector Sprays"
CARL IM 81-01.

Boussinesq, J. (1877)
"Analysis Concerning the Theory of Flowing Water"
Memoires Presentes par Divers Savants a L'Acadmie des Sciences vol. 23, p. 46.

Boyson, F., Ayers, W.H., Swithenbank, J. and Pan, Z. (1981)
"Three-Dimensional Model of Spray Combustion in Gas-Turbine Combustors"
AIAA paper No. 81-0324R, J. of Energy, vol. 6, p. 368.

Bracco, F.V. (1974)
"Application of Steady State Spray Equations to Combustion Modelling"
AIAA Journal, vol. 12, pp. 1534-1540.

Bracco, F.V., Gupta, H.C., Krishnamurthy, L., Santavicca, D.A., Steinberger, R.L. and Warshaw, V. (1976)
"Two-Phase Two-Dimensional, Unsteady Combustion in Internal Combustion Engines; Theoretical and Experimental Results"
SAE paper no. 760114.

Bradshaw, P. and Ferriss, D.H. (1971)
"Calculation of Boundary-Layer Development Using the Turbulent Energy Equation: Compressible Flow on Adiabatic Walls"
J. Fluid Mech., vol. 46, part 1, pp. 83-110.

Brown, D.J. and Hutchinson, P. (1979)
"The Interaction of Solid or Liquid Particles and Turbulent Fluid Flow Fields - A Numerical Simulation"
ASME, J. of Fluid Engineering, vol. 101, pp. 265-269.

Buckingham, A.C. and Siekhaus, W.J. (1981)
"Interaction of Moderately Dense Particle Concentrations in Turbulent Flow"
AIAA 81-0346.

Burt, R. and Troth, K.A. (1970)
"Penetration and Vaporization of Diesel Fuel Sprays"
Proc. Instn. Mech. Engrs, vol. 184, Pt 3J.

Butler, T.D., Cloutman, L.D., Dukowicz, J.K., Ramshaw, J.D. and Krieger, R.B. (1980)
"Towards a Comprehensive Model for Combustion in a Direct-Injection Stratified-Charge Engine"
Combustion Modelling in Reciprocating Engines (J.N. Mattavi and C.A. Amann, ed.) pp. 231-264, Plenum Press, New York.

Carnahan, B., Luther, H.A. and Wilkes, J.O. (1969)

"Applied Numerical Methods"

John Wiley & Sons, Inc.

Carretto, L.S., Gosman, A.D., Patankar, S.V. and Spalding, D.B. (1972)

"Two Calculation Procedures for Steady, Three-Dimensional Flows with Recirculation"

Proc. Third Int. Conf. on Numerical Methods in Fluid Mechanics.

Castleman, R.A. (1931)

"Mechanism of Atomization of Liquids"

U.S. National Bureau Std. J. Res., vol. 6, p. 281.

Chorin, A.J. (1968)

"Numerical Solution of the Navier-Stokes Equations"

Math. Comp., 22, pp. 745-762.

Crowe, C.T. (1978)

"A Numerical Model for the Gas-Droplet Flow Field Near an Atomizer"

ICLASS-78.

Crowe, C.T., Sharma, H.P. and Stock, D.E. (1977)

"The Particle-Source-In Cell (PSI-Cell) Model for Gas-Droplet Flows"

ASME, J. Fluid Engineering, pp. 325-332.

Courant, R., Friedrichs, K. and Lewy, H. (1967)

"On the Partial Difference Equations of Mathematical Physics"

IBM Journal, 2.

Courant, R., Isaacson, E. and Rees, M. (1952)
"On the Solution of Non-Linear Hyperbolic Differential Equations by Finite-Differences"
Comm. Pure Appl. Math., vol. 5, p. 243.

Dehaye, J.M., Giot, G. and Riethmuller, M.L. (1981)
"Thermohydraulic of Two-Phase Systems for Industrial Design and Nuclear Engineering"
Hemisphere Publishing Corp., Washington, pp. 95-179.

DeJuhasz, K.T. (1931)
"Dispersion of Sprays in Solid Injection Oil Engines"
Trans. ASME, vol. 53, p. 65.

Dent, J.C. (1971)
"A Basis for the Comparison of Various Experimental Methods for Studying Spray Penetration"
SAE Trans., vol. 80, paper no. 710571.

Dukowicz, J.K. (1980)
"A Particle-Fluid Numerical Model for Liquid Sprays"
J. of Computational Physics, 35, pp. 229-233.

Eisenklam, P., Arunachalam, S.A. and Weston, J.A. (1967)
"Evaporation Rates and Drag Resistance of Burning Drops"
11th Symp. (Int.) on Comb., The Comb. Inst., pp. 715-728.

ElBanhawy, Y.H. and Whitelaw, J.H. (1980)
"The Calculation of the Flow Properties of Confined Kerosene-Spray Flames"
AIAA J., vol. 18, p. 1503.

ElKotb, M.M. (1982a)
"Spray Modelling for Multifuel Engines"
Second Annual T.R., European Research Office, U.S. Army.

ElKotb, M.M. (1982b)

"Fuel Atomization for Spray Modelling"

Prog. Energy Combustion Sci., vol. 8, pp. 61-91.

ElKotb, M.M. and Abdalla, M.M. (1982)

"Atomization of Multifuel Sprays"

ICLASS-82 paper no. 9.3, pp. 237-244.

El Wakil, M.M., Ueyhara, O.A. and Myers, F.S. (1954)

"A Theoretical Investigation of the Heating-up Period of Injected Fuel Droplets Vaporizing in Air"

NACA, TN 3179.

Faeth, G.M. (1977)

"Current Status of Droplet and Liquid Combustion"

Prog. Energy Combust. Sci. 3, pp. 191-224.

Faeth, G.M. (1979)

"Spray Combustion Models - A Review"

AIAA paper no. 79-0293, 17th Aerospace Sciences Meeting.

Faeth, G.M. (1983)

"Evaporation and Combustion of Sprays"

Prog. Energy and Combustion Science, vol. 4.

Favre, A. (1969)

"Statistical Equations of Turbulent Gases"

Problems of Hydrodynamics and Continuum Mechanics, Soc. Indust. Appl. Math., pp. 231-266.

Fujimoto, H., Kuniyoshi, H., Sato, G.T., et al (1977)

"Investigation on Combustion in Medium-Speed Marine Diesel Engines Using Model Chambers"

12th CIMAC, p. 1853.

Fujimoto, H., Tanabe, H., Sato, G.T. and Kuniyoshi, H. (1979)
"Investigation in Combustion in Medium-Speed Marine Diesel Engines Using Model Chambers"
13th CIMAC, D25.

Fujimoto, H., Sugihara, H., Tanabe, H. and Sato, G.T. (1981)
"Investigation on Combustion in Medium Speed Marine Diesel Engines Using Model Chambers"
14th CIMAC, D38.

Giffen, E. and Muraszew, A. (1953)
"The Atomization of Liquid Fuels"
John Wiley & Sons, New York.

Goldstein, S. (1957)
"Numerical Development in Fluid Dynamics"
Oxford University Press.

Gosman, A.D. and Harvey, P.S. (1982)
"Computer Analysis of Fuel Air Mixing and Combustion in an Axisymmetric D-I Diesel"
SAE paper no. 820036.

Gosman, A.D. and Ioannides, E. (1981)
"Aspects of Computer Simulation of Liquid-Fuelled Combustors"
AIAA 81-0323.

Gosman, A.D., Ioannides, E., Lever, D.A. and Cliffe, K.A. (1980a)
"A Comparison of Continum and Discrete Droplet Finite-Difference Models Used in the Calculation of Spray Combustion in Swirling Turbulent Flows"
AERE Harwell Report TP 865.

Gosman, A.D. and Johns, R.J.R. (1980b)
"Computer Analysis of Fuel Air Mixing in Direct-Injection Engines"
SAE paper no. 800091.

Gosman, A.D., Li, K.H. and Samaraweera, S. (1976a)
"A Numerical Calculation Procedure for Two-Phase Recirculating Flows"
Proc. Fifth Int. Conference on Numerical Methods in Fluid Dynamics. Twente Univ., Enschede.

Gosman, A.D., Lockwood, F.C. and Sayed, S.A. (1976b)
"Prediction of a Horizontal Free Turbulent Diffusion Flames"
Sixteenth Symp. (Int.) on Combustion.

Gosman, A.D. and Pun, W.M. (1974)
Lecture Notes for Course Entitled "Calculation of Reciprocating Flows"
Imperial College, Mech. Eng. Dept. Report.

Gosman, A.D., Pun, W.M., Runchal, A.K., Spalding, D.B. and Wolfstein, M. (1969)
"Heat and Mass Transfer in Recirculating Flows"
Academic Press, London.

Graves, C.C. and Scull, W.C. (1960)
"Mixing Processes"
Design and Performance of Gas Turbine Power Plant,
Oxford Univ. Press.

Gupta, H.C. and Bracco, F.V. (1978)
"Numerical Computations of Two-Dimensional Unsteady Sprays for Application to Engineers"
AIAA Journal, vol. 16, pp. 1053-1061.

Haenlein, A. (1932)

"Uber den Zerfall eines Flussigkeitsstrahls"

"On the Disruption of Liquid Jets"

NACA TM 659.

Harlow, F.H. and Amsden, A.A. (1971)

"A Numerical Fluid Dynamics Calculation Method for All Flow Speeds"

J. Computational Physics, 8-2, pp. 197-213.

Harlow, F.H. and Amsden, A.A. (1975)

"Numerical Calculation of Multiphase Fluid Flow"

J. Computational Physics, 17, pp. 19-52.

Harlow, F.H. and Nakayama, P.I. (1967)

"Transport of Turbulence Energy Decay Rate"

Los Alamos Scientific Lab., Univ. of Calif. Report no. LA-3854.

Haselman, L.C. and Westbrook, C.K. (1978)

"A Theoretical Model for Two-Phase Fuel Injection in Stratified Charge Engine"

SAE paper no. 780318.

Hay, N. and Jones, P.L. (1972)

"Comparison of the Various Correlations for Spray Penetration"

SAE paper no. 720776.

Henein, N.A. (1976)

"Analysis of Pollutant Formation and Control and Fuel Economy in Diesel Engines"

Prog. Energy and Combustion Science, vol. 1, pp. 165-207.

Hengrussamee, D. (1975)

"Mixing of Hot Starting-Jets with Cold Surroundings"

Ph.D. thesis, Univ. of London.

Hilsenrath, J. (1960)

"Tables of Thermodynamic and Transport Properties"

Pergamon Press, London.

Hinze, J.O. (1959)

"Turbulence"

McGraw Hill, New York.

Hiroyasu, H. and Kadota, T. (1974)

"Fuel Droplet Size Distribution in Diesel Combustion Chamber"

SAE paper number 740715.

Hiroyasu, H., Kadota, T. and Arai, M. (1980)

"Fuel Spray Characterisation in Diesel Engines"

Combustion Modelling in Reciprocating Engines (J.N. Mattavi and C.A. Amann, ed.) Plenum Press, New York.

Hiroyasu, H., Shimizu, M. and Arai, M. (1982)

"The Breakup of High Speed Jet in a High Pressure Gaseous Atmosphere"

ICLASS-82, paper no. 2.5, p. 69.

Hotchkiss, R.S. and Hirt, C.W. (1972)

"Particle Transport in Highly Distorted Three-Dimensional Flow Fields"

Los Alamos Scientific Lab. Preprint LA-DC72-364.

Ideriah, F.J.K. (1974)

"The Prediction of Turbulent Jets and Plumes"

M.Sc. thesis, Univ. of London.

Ioannides, E. and Gosman, A.D. (1978)

"A Survey of the Literature Relating to Oil Spray Combustion"

UKAEA Report HTFS RS 254.

Ingebo, R.D. (1956)

"Drag Coefficient for Droplets and Solid Spheres in Clouds Accelerating in Airstream"

NACA TN 3762.

Ishikawa, M. and Murakami, T. (1982)

"Characteristic of Intermittent Sprays Generated by an Orifice Atomizer"

ICLASS-82, paper number 3.1, p. 85.

Jahanbaksh, A. (1984)

Private Communication.

Johns, R.J.R. (1980)

"Prediction of Flow in Diesel Engine Cylinders"

Ph.D. thesis, University of London.

Jones, W.P. (1980)

"Models for Turbulent Flows with Variable Density and Combustion"

Lecture series 1979-2. Von Karman Inst. for Fluid Dynamics.

Jones, W.P. and Launder, B.E. (1972)

"The Calculation of Low-Reynolds Number Phenomena with a Two-Equation Model of Turbulence"

Int. J. Heat and Mass Transfer, vol. 16, p. 1119.

Jong-Yul Ha, Hayashi, A., Tanabe, H. Sato, G.T. et al (1983)

"Investigation on the Initial Part and the Spray Formation Delay of Diesel Spray"

SAE paper no. 830451.

Kadota, T. and Hiroyasu, H. (1976)

"Evaporation of a Single Droplet at Elevated Pressures and Temperatures"

Bulletin of the JSME, 19, no. 138, pp. 1515-1521.

Karasawa, T. and Kurabayashi, T. (1982)
"Coalescence of Droplets and Failure of Droplets to Impact the Sampler in the Immersion Sampling Technique"
ICLASS-82, paper 11.1, pp. 285-291.

Khalil, E.E., Spalding, D.B. and Whitelaw, J.H. (1975)
"The Calculation of Local Properties in Two-Dimensional Furnaces"
Int. J. Heat and Mass Transfer, vol. 18, pp. 775-791.

Khalil, E.E. and Whitelaw, J.H. (1977)
"Aerodynamic and Thermodynamic Characteristics of Kerosene Spray Flames"
16th Symp. (Int.) on Combustion, The Comb. Inst.,pp. 569-576.

Kuniyoshi, H., Tanabe, H., Sato, G.T. and Fujimoto, H. (1980)
"Investigation on the Characteristics of Diesel Fuel Spray"
SAE paper no. 800968.

Kuo, T.W. (1982)
"On the Scaling of Transient Laminar, Turbulent and Spray Jets"
Ph.D. thesis, Faculty of Princeton University, U.S.A.

Kuo, T.W. and Bracco, F.V. (1982a)
"On the Scaling of Transient Laminar, Turbulent and Spray Jets"
SAE paper no. 820038.

Kuo, T.W. and Bracco, F.V. (1982b)
"Computations of Drop Sizes in Pulsating Sprays and of Liquid-Core Length in Vaporizing Sprays"
SAE paper no. 820133.

Lapple, C.E., Henry, A. and Blake, D.E. (1967)
"Atomization Survey and Critique of the Literature"
Stanford Research Institute Report, no. 6, AD831-314.

Launder, B.E. and Morse, A. (1977)

"Numerical Prediction of Axisymmetric Free Shear Flows with Reynolds Stress Closure"

1st Int. Symp. on Turb. Shear Flows, Penn. State Univ.

Launder, B.E., Reece, G.J. and Rodi, W. (1975)

"Progress in the Development of a Reynolds-Stress Turbulent Closure"

J. Fluid Mech., vol. 68, part 3, pp. 537-566.

Launder, B.E. and Spalding, D.B. (1972)

"Lectures in Mathematical Models of Turbulence"

Academic Press, London.

Launder, B.E. and Spalding, D.B. (1973)

"The Numerical Computations of Turbulent Flows"

Imperial College, Mech. Eng. Dept. Report HTS/73/2.

Levich, V.G. (1962)

"Physicochemical Hydrodynamics"

Prentice Hall.

Libby, P.A. (1973)

"A Provisional Analysis of Two-Dimensional Turbulent Mixing with Variable Density"

NASA SP-321, 421.

Libby, P.A. and Bray, K.N.C. (1977)

"Variable Density Effects in Premixed Turbulent Flames"

AIAA J., vol. 15, no. 8, p. 1186.

Looney, M.K. (1982)

"Numerical Modelling of the Transport Equations for Two-Dimensional Free and Impinging Jet Flows"

Ph.D. thesis, University College, Dublin.

Lumley, J.L. (1975)

"Prediction Methods for Turbulent Flows"

Lecture series, No. 76, Von Karman Inst., Belgium.

Lyshevskiy, A.S. (1956)

"The Coefficient of Free Turbulence in a Jet of Atomized Liquid Fuel"

NASA TT-F351.

Maltosz, R.L., Leipziger, S. and Torda, T.P. (1972)

"Investigation of Liquid Drop Evaporation in a High Temperature and High Pressure Environment"

Int. J. Heat Mass Transfer, vol. 15, pp. 831-852.

Manrique, J.A. and Borman, G.L. (1969)

"Calculation of Steady State Droplet Vaporization at High Ambient Pressures"

Int. J. Heat Mass Transfer, vol. 12, pp. 1081-1095.

Matsouka,S. (1983)

"Creation of Image on Diesel Spray and Flame by Means of Rapid Compression Machine and DI Diesel Engine"

SAE paper no. 830447.

Maxwell, J.B. (1956)

"Data Book on Hydrocarbons"

Van Norstad.

McGuirk, J.J. and Rodi, W. (1977)

"The Calculation of Three-Dimensional Free Jets"

Symp. on Turb. Shear Flows, Penn. State Univ.

Megahed, A.M. (1979)

"The Prediction of Three-Dimensional Gas-Fired Combustion Chamber Flows"

Ph.D. thesis, Univ. of London.

Mongia, H.C. and Smith, K. (1978)

"An Empirical/Analytical Design Methodology for Gas Turbine Combustors"

AIAA paper no. 78-998.

Murray, J.D. (1965)

"On the Mathematics of Fluidization. Part 1: Fundamental Equations and Wave Propagation"

J. Fluid Mech., vol. 21, pp. 465-493.

Natarjan, R. and Brzustowski, T.A. (1970)

"Some New Observations on the Combustion of Hydrocarbon Droplets at Elevated Pressures"

Comb. Sci. Tech., 2, pp. 259-269.

National Bureau of Standards(1952)

Selected Values of Properties of Hydrocarbons Compiled Under American Petroleum Institute Research Project 44.

Negus, C. (1983)

"Droplet Formation in Diesel Sprays"

AERE-R11013 Harwell, U.K.

Ogasawara, M. and Sami, H. (1966)

"Study on the Behaviour of a Fuel Droplet Injected into the Combustion Chamber of a Diesel Engine"

SAE Trans., vol. 78, paper no. 670468.

O'Rourke, P.J. (1981)

"Collective Drop Effects on Vaporizing Liquid Sprays"

Ph.D. thesis, Faculty of Princeton University, U.S.A.

O'Rourke, P.J. and Bracco, F.V. (1980)

"Modelling of Drop Interactions in Thick Sprays and a Comparison with Experiments"

Stratified Charge Automotive Engines Conference, The Instn. Mech. Engrs.

Oz, I.H. (1969)

"Calculation of Spray Penetration in Diesel Engines"

Paper 690254 presented at SAE Automotive Engineering Congress, Detroit.

Parks, M., Polonski, C. and Toye, R. (1966)

"Penetration of Diesel Fuel Sprays in Gases"

Paper 660747 presented at SAE Combined Powerplant and Transportation Meeting, Chicago.

Patankar, S.V. (1980)

"A Numerical Heat Transfer and Fluid Flow"

McGraw Hill Book Company (Hemisphere Publishing Corporation).

Patankar, S.V. and Baliga, B.R. (1978)

"A New Finite-Difference Scheme for Parabolic Differential Equations"

Num. Heat Transfer, vol. 1, p. 27.

Patankar, S.V. and Spalding, D.B. (1972)

"A Calculation Procedure for Heat, Mass and Momentum Transfer in 3-D Parabolic Flows"

Int. J. Heat and Mass Transfer, 15.

Phillips, H. (1971)

"Theory of Suppression of Explosions by Narrow Gaps"

4th Symp. on Chemical Process Hazards with Special Reference to Plant Design.

Pope, S.B. (1976)

"The Calculation of the Flow Behind Bluff Bodies With and Without Combustion"

Ph.D. thesis, Univ. of London.

Prandtl, L. (1925)

"Bericht Uber Untersuchungen Zur Ausgebildeten Turbulenz"

ZAMM, 5, 136.

Prandtl, L. (1945)

"Uber en Neus Formelsystem fur die Ausgebildete Turbulenz"

Nochrichten von der Akod. der Wissenschaft in Gottingen.

Rabin, E., Schallenmuller, A.R. and Lawhead, R.B. (1960)

"Displacement and Shattering of Propellant Droplets"

Final Summary Report, AFOSR TR 60-75.

Raithby, G.D. and Torrance, K.E. (1974)

"Upstream-Weighted Differencing Schemes and their Applications to Elliptic Problems Involving Fluid Flow"

Computers and Fluids, 2, pp. 191-206.

Rajaratnam, N. (1976)

"Turbulent Jets"

Elsevier Scientific Publishing Company, Amsterdam.

Ranz, W.E. and Marshall, W.P. (1952)

"Evaporation from Drops"

Chem. Eng. Prog. Part 1, vol. 48, no. 3, pp. 141-146.

Rayleigh, W.S. (1878)

"On the Instability of Jets"

Proc. Lond. Math. Soc., vol. 4, p. 10.

Reitz, R.D. (1978)

"Atomization and Other Breakup Regimes of a Liquid Jet"

Ph.D. thesis, Faculty of Princeton University, U.S.A.

Reynolds, W.C. (1976)

"Computation of Turbulent Flows"

Annual Review of Fluid Mechanics, 8, p. 183.

Rizk, W. (1958)

"Experimental Studies of the Mixing Process and Flow Configuration in Two-Cycle Engine Scavenging"

Proc. Instn. Mech. Engrs., vol. 172, p. 417.

Roache, P.J. (1972)

"Computational Fluid Dynamics"

Hermosa Publishers.

Rose, J.W. and Cooper, J.R. (1977)

"Technical Data on Fuel"

Published by The British National Committee of the World Energy Conference and Distributed by Scottish Academic Press.

Rowe, P.N., Claxton, K.T. and Lewis, J.B. (1965)

"Heat and Mass Transfer from a Single Sphere in an Extensive Flowing Fluid"

Trans. Instn. Chem. Engrs., vol. 43, T14-T31.

Runchal, A.K. (1977)

"Comparative Criteria for Finite-Difference Formulations for Problems of Fluid Flow"

Int. J. Numerical Methods in Eng., 11, p. 1667.

Rusinov, R.V. (1963)

"Length of Atomized Fuel Jet in a Diesel Engine"

Russian Engrg. J. 43.

Salooja, A.P. (1978)

"Mathematical Modelling of, and Experimental Studies in Axisymmetric Combustion"

Ph.D. thesis, Univ. of London.

Sato, G.T., Tanabe, H. and Fujimoto, H. (1982)

"An Investigation of Diesel Sprays"

ICLASS-82, pp. 229-235.

Sayed, S.A. (1977)

"Experimental and Theoretical Investigation of a Horizontal Free Turbulent Diffusion Flames"

Ph.D. thesis, Univ. of London.

Schweitzer, P.H. (1937)

"Penetration of Oil Sprays"

Penn. State Coll. Bull. No. 46.

Shearer , A.J. and Faeth, G.M. (1977)

"Combustion of Liquid Sprays at High Pressures"

NASA CR-135210.

Shearer , A.J., Tamura, H. and Faeth, G.M. (1978)

"Evaluation of a Locally Homogeneous Flow Model of Spray Evaporation"

AIAA paper no. 78-1042 R.

Shiozaki, T., Suzuk, T. and Shimoda, M. (1980)

"Observation of Combustion Process in D.I. Engine via High Speed Direct and Schlieren Photography"

SAE paper no. 800025.

Sirignano, W.A. (1983)

"Fuel Droplet Vaporization and Spray Combustion Theory"

Prog. Energy Combust. Sci., vol. 9, pp. 291-322.

Sitkei, G. (1964)

"Kraftstoffaufbereitung und Verbrennug bei Dieselmotoren"

Springer-Verlag.

Soo, S.L. (1967)

"Fluid Dynamics of Multiphase Systems"

Blaisdell.

Spalding, D.B. (1972)

"A Novel Finite-Difference Formulation for Differential Expressions Involving Both First and Second Derivatives"

Int. J. for Numerical Methods in Eng., vol. 4, pp. 551-559.

Takeuchi, K., Senda, J. and Shikuya, M. (1983)

"Transient Characteristics of Fuel Atomization and Droplet Size Distribution in Diesel Fuel Sprays"

SAE paper no. 830449.

Tanasawa, Y. and Tesima, T. (1958)

"On the Theory of Combustion Rate of Liquid Fuel Spray"

Bulletin of ISME, vol. 1, no. 1.

Tate, R.W. (1969)

"Sprays"

Encyclopaedia of Chem. Technology, vol. 18, p. 634.

Taylor, D.H. and Walsham, B.E. (1970)

"Combustion Processes in a Medium Speed Diesel Engine"

Diesel Engine Comb., Proc. Instn. Mech. Engrs., vol. 184 part 3J.

Tiskoff, J.M. (1982)

"Measurements of Particle Size and Velocity in a Fuel Spray"

ICLASS-82 paper no. 10.1, pp. 245-252.

Tham, S.Y. (1982)

"Diesel Spray Penetration"

Transfer Report, UMIST.

Travis, J.R., Harlow, F.H. and Amsden, A.A. (1976)

"Numerical Calculation of Two-Phase Flows"

Nuclear Science and Engineering, 61, pp. 1-10.

Varde, K.S. and Pope, D.M. (1983)

"Diesel Fuel Spray Penetration at High Injection Pressures"

SAE paper no. 830448.

Wakuri, Y., Fujii, M., Amitani, T. and Tsuneya, R. (1960)

"Studies on the Penetration of Fuel Spray in a Diesel Engine"

JSME, vol. 3, no. 9, pp. 123-130.

Wallis, G.B. (1969)

"One-Dimensional Two-Phase Flow"

McGraw Hill Book Company.

Watkins, A.P. (1973)

"Calculation of Flow and Heat Transfer in the Combustion Chamber of a Reciprocating Engine"

M.Sc. thesis, Univ. of London.

Watkins, A.P. (1977)

"Flow and Heat Transfer in Piston Cylinder Assemblies"

Ph.D. thesis, Univ. of London.

Westbrook, C.K. (1976)

"Three-Dimensional Numerical Modelling of Liquid Fuel Sprays"

16th Int. Symp. on Comb., Cambridge, Massachusetts.

Westbrook, C.K. (1977)

"Numerical Solution of Spray Equation"

Lawrence Livermore Lab. Report UCID 17361, Univ. of Calif.

Williams, F.A. (1962)

"Progress in Spray-Combustion Analysis"

8th Symp. (Int.) on Combustion, Williams and Wilkins Co., Baltimore, p. 50.

Williams, F.A. (1965)

"Combustion Theory"

Addison-Wesley Publishing Co. Inc., London.

Witze, P.O. (1980)

"The Impulsively Started Incompressible Turbulent Jet"

SAND 80-8617.

Wolfhard, H.G. and Bruszak, A.E. (1960)

"The Passage of Explosions Through Narrow Cylinderical Channels"

Comb. and Flame, vol. 4, p. 149.

Wu, K.-J., Su, C.-C., Steinberger, R.L., Santavicca, D.A. and Bracco, F.V. (1983)

"Measurements of the Spray Angle of Atomizing Jets"

ASME 83-WA/FE-10 Journal of Fluid Engineering.

Wygnanski, I. and Fiedler, H. (1969)

"Some Measurements in the Self-Preserving Jet"

J. Fluid Mech., vol. 38, part 3, pp. 577-612.

Yuen, M.C. and Chen, L.W. (1976)

"On Drag of Evaporating Liquid Droplets"

Comb. Science and Tech., vol. 14, pp. 147-154.

Yuen, M.C. and Chen, L.W. (1978)

"Heat Transfer Measurements of Evaporating Liquid Droplets"

Int. J. Heat Mass Transfer, vol. 21, pp. 537-542.

Yule, A.J. (1984)

"A Review of Diesel Spray Research at UMIST Supported by the J.R.C.

Presented to a meeting of J.R.C. at UMIST, 24th May, 1984.

Yule, A.J., Aval, S.M., Mo, S.L. and Ereaut, P.R. (1985a)

"Measurement Techniques for High Density Sprays Including Diesel Sprays"

ICLASS (to be presented).

Yule, A.J., Mo, S.L., Tham, S.Y. and Aval, S.M. (1985b)

"Diesel Spray Structure"

ICLASS (to be presented).

Yuu, S., Yasukouchi, N., Hirosawa, Y. and Jataki, T. (1978)

"Particle Turbulent Diffusion in Dust Laden Round Jet"

AIChE J. 24, p. 509.

Zubar, N. (1964)

"On the Dispersal Two-Phase Flow in the Laminar Flow Region"

Chem. Eng. Sci., vol. 19, pp. 897-917.

NOMENCLATURE

A	coefficient of finite-difference equation
A_d	surface area of the droplet
a	area of cell faces
a_1, a_2, a_3	constants
B_d	drag function
C_D	drag coefficient
C_Q	discharge coefficient
C_R	Courant number
c_p, c_v	specific heats
c_1, c_2, c_μ	turbulence model constants
D	diffusivity
D_d	droplet diameter
D_{32}	Sauter mean diameter
dD	increment of droplet diameter
dV	increment of droplet volume
d_j	jet diameter
F	cell face flux
f	fuel vapour mass fraction or spatial weighting factor
G_t	generation rate of turbulence energy
g	acceleration of gravity
h	stagnation enthalpy, coefficient of heat transfer
h'	coefficient of mass transfer
k	turbulent kinetic energy or number of droplets
L	latent heat of vaporization
ℓ	penetration length or length scale
Ma	Mach number

m_d	mass of droplet
$\dot{m}$	mass flow rate
m	molecular weight
Nu	Nusselt number
N_d	number of droplets in the parcel
n	exponent of Rosin-Rammler distribution
P	pressure
Pe	Peclet number
Pr	Prandtl number
Q	$(\frac{\partial \rho}{\partial P})_T$, volume flow rate
q	heat flux
R	gas constant
Re	Reynolds number
r	radial distance or radial co-ordinate
Sc	Schmidt number
Sh	Sherwood number
S_ϕ	source term in gas-phase equation
$S_{\phi,d}$	droplet interaction source term
T	temperature
t	time
t_e	eddy life time
t_R	droplet transit time
t*	non-dimensional time
U_{inj}	injection velocity
U_o	axial velocity at nozzle exit
u	axial velocity
u_r	axial velocity relative to the co-ordinate frame
V	volume

V_{rel}	relative velocity
v	radial velocity
v_r	radial velocity relative to co-ordinate frame
We	Weber number
x	axial distance, axial co-ordinate
x_B	breakup length

Greek Symbols

α	spacial weighting factor
β	spray cone angle
Γ	turbulent diffusivity
∇	divergence operator
δ	increment
ε	dissipation rate of turbulence energy
ξ	time varying distance
η	temporal weighting factor
θ	void fraction
κ	thermal conductivity
μ	dynamic viscosity
ν	dynamic viscosity
ρ	density
Σ	summation
σ	surface tension or turbulent Prandtl or Schmidt numbers
τ	stress or relaxation time or interaction time
ϕ	a dependent variable
ϕ'	turbulent fluctuation of
$\overline{\phi}$	ensemble-averaged value

$\tilde{\phi}$	Favre-averaged value
χ	under-relaxation factor

Subscripts

a	air
d	droplet
f	fuel or flame
g	gas
m	mean
max	maximum
min	minimum
mix	mixture
o	initial
P,N,S,E,W n,s,e,w	points-of-the-compass notation for grid points
s	surface
t	turbulent
v	vapour

Superscripts

i	iteration
n	old time level
n+1	new time level
-	(overbar) ensemble averaged
'	fluctuating component
*	prevailing
→	vector